MICROSTRUCTURE AND THE DISTRIBUTION OF TENSILE PROPERTIES IN INJECTION MOLDED POLYETHYLENE

by

Francis H. Moy

A Thesis Submitted to the Faculty of Graduate Studies and Research in Partial Fulfillment of the Requirements for the Degree of Doctor of Philosophy

Department of Chemical Engineering
McGill University
Montreal

February 1980

ABSTRACT

Studies conducted by many workers in recent years have indicated substantial anisotropies in injection molded thermoplastics. These anisotropies have been associated with differences in morphology (crystallinity) and orientation (shrinkage and birefringences) at various positions in the molding. They are reflected by anisotropies in tensile properties measured at different points or in different directions. However, no work has been reported to quantitatively relate the distributions of morphology and orientation to distributions in tensile properties. The present work represents an attempt to meet this challenge.

Microstructure determination is achieved by making the following measurements on microtomed specimens at different positions in the polyethylene moldings: density, sonic speed, birefringence, wide-angle X-ray diffraction, dichroic ratio, and polarized light photomicrography. The above tests yield data relating to crystallinity and orientation functions for both the crystalline and amorphous phases. They also yield sufficient data to check the consistency of results obtained by the different techniques. Tensile properties are measured on microtomed samples obtained from the same regions tested for microstructure. Finally, the distributions of tensile and sonic moduli in the molding are estimated by employing some of the theoretical techniques proposed in the literature. The results

show very good agreement between theoretical predictions and experimental data relating to the distributions of both sonic moduli and tensile moduli.

RESUME

Des études faites ces dernières années par différents auteurs demontrent des anisotropies substantielles dans les pièces obtenus grâce au moulage par injection. Ces anisotropies ont été associées à la différence de morphologie (cristallinité) et d'orientation (biréfringence et retrait) en différents endroits de la pièce moulée. Elles sont reflétées par les anisotropies dans les propriétés en tension, mesurées à différents points ou dans différentes directions. Cependant aucun travail n'a été rapporté qui essaie de relier quantitativement les distributions de morphologie et d'orientation aux distributions des propriétés en tension. Ce travail est une tentative dans ce sens.

Afin de déterminer la microstructure de l'échantillon de polyéthylene les mesures suivantes on été faites sur des coupes minces découpées à différentes positions dans la pièce moulée: densité, vitesse sonique, biréfringence, diffraction aux grands angles par rayon-X, dichroïsme, et photomicrographie par lumière polarisée. Ces différentes méthodes nous permettent d'obtenir des données sur la cristallinité et l'orientation des phases cristallines ou amorphes du polymère. Ces données permettent aussi de vérifier la reproductibilité des résultats obtenus. Les propriétés en tension sont obtenues à partir des mêmes échantillons servant à l'analyse de la microstructure. Finalement les distributions des modules soniques et des modules en

tension à l'intérieur de la pièce moulée sont estimés avec l'aide de modèles théoriques proposés dans la littérature. Les résultats montrent un très bon recoupage entre les prédictions théoriques et les résultats expérimentaux pour les distributions des modules sonique et en tension.

ACKNOWLEDGEMENTS

I wish to express my gratitude to the following people who have contributed to the conception and completion of this work.

In particular, I am especially indebted to my research director, Professor M.R. Kamal, for his guidance, wisdom, and encouragement throughout the duration of this work.

I would also like to thank:

- Mr. A. Krish and the staff of the Chemical Engineering Machine Shop, for their assistance with equipment and instrumentation problems,
- Mr. J. Dumont, for his assistance in the purchase of experimental equipment,
- the members of my research group, Professor J.M. Dealy, Dr. V. Tan, and Mr. D. Kalyon, for contributing to many invaluable discussions and suggestions during the course of this work,
- my colleagues, J. Rhi Sausi, D. Kalyon, A. Garcia-Rejon, and R. Salcedo, for their advice and assistance with various aspects of the project,
- Professor J. Smith of the Department of Metallurgy, for the use of the X-ray equipment,
- Dr. R. St. John Manley and Miss Lydia Larrondo of the Department of Chemistry and Pulp and Paper Research Institute, for helpful comments and suggestions, as well as for the use of the microdensitometer during the X-ray work,

- the Faculty of Graduate Studies and Research, for financial assistance in the form of a McConnell scholarship, and to the Department of Chemical Engineering, for financial support in the form of a teaching assistantship,
- DuPont of Canada, for supplying the materials used in this study and financial support,
- the National Science and Engineering Research Council of Canada, and the Ministère de l'Education du Gouvernement du Québec, for financial support,
- Miss Pat Fong, for her meticulous typing of this thesis.

I am especially grateful to my family and my fiancée for their continued support and encouragement throughout this work.

TO

MY PARENTS

TABLE OF CONTENTS

	Page
ABSTRACT	i
ACKNOWLEDGEMENTS	v
TABLE OF CONTENTS	viii
LIST OF FIGURES	xii
LIST OF TABLES	xix
1. GENERAL INTRODUCTION	1
2. LITERATURE REVIEW	4
2.1 Crystallization Phenomena of Polymers	4
2.1.1 Quiescent Crystallization	4
2.1.2 Crystallization Under Stress	9
2.2 Studies of Deformation Behavior of Polymer Systems	15
2.3 Microstructural Studies in Polymer Processing	18
2.4 Summary	25
3. SCOPE AND OBJECTIVES	27
4. THEORETICAL BACKGROUND	31
4.1 Density and Crystallinity	31
4.2 Sonic Velocity Measurements	32
4.3 Birefringence Measurements	37
4.4 Wide-Angle X-Ray Diffraction	39
4.5 Infrared Spectroscopy	48
4.6 Tensile Properties	50
4.7 Integration of the Results of Experimental Measurements	54
5. EXPERIMENTAL	58
5.1 Materials	58
5.2 Preparation of the Moldings	65
5.2.1 Injection Molding Machine	65
5.2.2 Rectangular Mold Cavity	66

Page

5.2.3 Calibration of Transducers 70
5.2.4 Molding Procedure 72

5.3 Determination of Microstructure 77

5.3.1 Preparation of Microtomed Sections . . . 77
5.3.2 Photomicrography 84

5.3.2.1 Apparatus 84
5.3.2.2 Procedure 86

5.3.3 Density 88

5.3.3.1 Apparatus 88
5.3.3.2 Procedure 91

5.3.4 Sonic Velocity 94

5.3.4.1 Apparatus 94
5.3.4.2 Procedure 96

5.3.5 Intrinsic Sonic Moduli from Compression Molded Samples 98

5.3.5.1 Apparatus 98
5.3.5.2 Procedure 99

5.3.6 Birefringence 100

5.3.6.1 Apparatus 100
5.3.6.2 Procedure 101

5.3.7 Wide-Angle X-Ray Diffraction 103

5.3.7.1 Apparatus 104
5.3.7.2 Procedure 106

5.3.8 Infrared Spectroscopy 108

5.3.8.1 Apparatus 110
5.3.8.2 Procedure 111

5.3.9 Mechanical Properties 112

5.3.9.1 Apparatus 114
5.3.9.2 Procedure 114

6. RESULTS AND DISCUSSION 116

6.1 Molding Conditions 116

Page

6.2 Photomicrography 120
6.3 Density 130
6.4 Intrinsic Sonic Modulus from Compression Molded Samples 138
6.5 Sonic Modulus 143
6.6 Birefringence 152
6.7 Wide-Angle X-Ray Diffraction 159
6.8 Infrared Spectroscopy 183
6.9 Mechanical Properties 198
6.10 Correlation and Integration of Results Obtained by the Various Techniques 217

6.10.1 Amorphous Orientation 217
6.10.2 Crystalline and Amorphous Intrinsic Birefringences 224
6.10.3 Relative Contributions of Crystalline and Amorphous Phases to Total Orientation 232
6.10.4 Prediction of Sonic and Tensile Moduli Distributions 251

7. CONCLUSIONS, ORIGINAL CONTRIBUTIONS, AND FUTURE WORK 255

7.1 General Conclusions 255
7.2 Claims to Original Contributions 263
7.3 Suggestions for Future Work 265

LIST OF SYMBOLS 267

REFERENCES 270

APPENDIX 1 Calculation of Form Birefringence

APPENDIX 2 Calibration of Transducers

APPENDIX 3 Density

APPENDIX 4 Sonic Modulus

APPENDIX 5 Birefringence

APPENDIX 6 X-Ray Diffraction

APPENDIX 7 Infrared Spectroscopy

APPENDIX 8 Mechanical Properties

APPENDIX 9 Amorphous Orientation Function

Page

APPENDIX 10 Estimation of Intrinsic Birefringences

APPENDIX 11 Relative Contributions of Crystalline and Amorphous Phases to Total Birefringence

APPENDIX 12 Prediction of Sonic Modulus

APPENDIX 13 Prediction of Tensile Modulus

APPENDIX 14 Reproducibility Measurements

APPENDIX 15 Knife-Effects, Correction Factors, and Error Analysis

LIST OF FIGURES

Figure	Caption	Page
2.1	Schematic Representation of Polyethylene Single Crystals Showing Chain Folding and Orientation of Crystallographic Axes	6
2.2	Optical Micrograph of Polyethylene Spherulites	8
2.3	Schematic Representation of (a) Shearing Flow Field, (b) Extensional Flow Field	10
2.4	Effect of (a) Shearing and (b) Extensional Flow Fields on Flexible Macromolecules in Solution	11
2.5	Schematic Representation of the Shish-Kebab Model	14
4.1	Schematic Representation of Chair Orientation in an Amorphous Polymer. (a) Partial Parallel Orientation Along X, (b) Perfect Parallel Orientation, (c) Perfect Perpendicular Orientation	33
4.2	Unit Cell of Polyethylene	40
4.3	A Schematic Stress-Strain Curve	52
5.1	Shear Viscosity as a Function of Shear Rate	60
5.2	Shear Viscosity as a Function of Shear Rate	61
5.3	Crystallization of Resins EX 1 and EX 2 Under Shear at 140°C	63
5.4	Pressure-Volume-Temperature (P-V-T) Diagram	64
5.5	Danson Metalmec Reciprocating-Screw Injection Molding Machine	67
5.6	Schematic Drawing of Mold Assembly	69
5.7	Pressure Calibration Apparatus	71
5.8	Typical Pressure Transducer Calibration Curve	73
5.9	Position Designations on Molded Specimens	78

Figure	Caption	Page
5.10	Photograph of Reichert Microtome	80
5.11	Designated Positions for Microstructural Studies in the Depth Direction of the Moldings	83
5.12	Schematic Sequence of Measurements Performed on Microtomed Sections	85
5.13	Components of a Polarizing Microscope	87
5.14	Schematic Diagram of Setup Used for Preparing Density Gradient Column	90
5.15	Block Diagram of the Dynamic Modulus Tester PPM-5R	95
5.16	Schematic Representation of the Setup Used for Measuring Birefringence	102
5.17	Experimental Setup for Obtaining Flat-Film Photographs of Microtomed Sections	105
5.18	Examples of Stress-Strain Behavior	113
6.1	Typical Pressure Profiles in the Mold Cavity	117
6.2	Percent Frequency Polygon for the Distribution of Peak Pressures of the Molded Specimens	119
6.3	Morphological Zones in EX 1 Specimen, Molded at 176°C	123
6.4	Morphological Zones in EX 2 Specimen, Molded at 176°C	124
6.5	Morphological Zones in EX 2 Specimen, Molded at 205.9°C	125
6.6	Variation of Density (Crystallinity) in the Depth Direction	131
6.7	Variation of Density (Crystallinity) in the Depth Direction	132
6.8	Variation of Density (Crystallinity) in the Depth Direction	133
6.9	Typical Comparison of Density Distributions	136
6.10	Estimation of Intrinsic Transverse Sonic Moduli Values	140

Figure	Caption	Page
6.11	Plot of Sonic Modulus of Unoriented Samples Versus Volume Fraction Crystallinity	144
6.12	Variation of Sonic Modulus in the Depth Direction	145
6.13	Variation of Sonic Modulus in the Depth Direction	146
6.14	Variation of Sonic Modulus in the Depth Direction	147
6.15	Typical Comparisons of Sonic Modulus Distributions	150
6.16	Variation of Total Birefringence in the Depth Direction	154
6.17	Variation of Total Birefringence in the Depth Direction	155
6.18	Variation of Total Birefringence in the Depth Direction	156
6.19	Typical Comparison of Total Birefringence Distributions	158
6.20	Variation of the Crystallographic Axes in the Depth Direction	162
6.21	Variation of the Crystallographic Axes in the Depth Direction	163
6.22	Variation of the Crystallographic Axes in the Depth Direction	164
6.23	Variation of the Crystallographic Axes in the Depth Direction	165
6.24	Variation of the Crystallographic Axes in the Depth Direction	166
6.25	Variation of the Crystallographic Axes in the Depth Direction	167
6.26	Variation of the Crystallographic Axes in the Depth Direction	168
6.27	Variation of the Crystallographic Axes in the Depth Direction	169

Figure	Caption	Page
6.28	Variation of the Crystallographic Axes in the Depth Direction	170
6.29	Variation of the Crystallographic Axes in the Depth Direction	171
6.30	Variation of the Crystallographic Axes in the Depth Direction	172
6.31	Variation of the Crystallographic Axes in the Depth Direction	173
6.32	Variation of the Crystallographic Axes in the Depth Direction	174
6.33	Variation of the Crystallographic Axes in the Depth Direction	175
6.34	Variation of the Crystallographic Axes in the Depth Direction	176
6.35	Typical Comparison of the a-Axis Orientation Distributions	178
6.36	Wide-Angle X-Ray Pattern of Specimen Microtomed Near the Surface	181
6.37	Wide-Angle X-Ray Pattern of Specimen Microtomed from the Core Region	182
6.38	Variation of Dichroic Ratio in the Depth Direction	185
6.39	Variation of Dichroic Ratio in the Depth Direction	186
6.40	Variation of Dichroic Ratio in the Depth Direction	187
6.41	Variation of Dichroic Ratio in the Depth Direction	188
6.42	Variation of Dichroic Ratio in the Depth Direction	189
6.43	Variation of Dichroic Ratio in the Depth Direction	190
6.44	Variation of Dichroic Ratio in the Depth Direction	191

Figure	Caption	Page
6.45	Variation of Dichroic Ratio in the Depth Direction	192
6.46	Variation of Dichroic Ratio in the Depth Direction	193
6.47	Comparison of f_a Obtained by X-Ray Diffraction and Infrared Dichroism	195
6.48	Comparison of f_a Obtained by X-Ray Diffraction and Infrared Dichroism	196
6.49	Comparison of f_a Obtained by X-Ray Diffraction and Infrared Dichroism	197
6.50	Variation of Nominal Tensile Yield Stress in the Depth Direction	200
6.51	Variation of Nominal Tensile Yield Stress in the Depth Direction	201
6.52	Variation of Nominal Tensile Yield Stress in the Depth Direction	203
6.53	Typical Comparison of Nominal Tensile Yield Stress Distributions	204
6.54	Variation of Percent Elongation at Yield in the Depth Direction	205
6.55	Variation of Percent Elongation at Yield in the Depth Direction	206
6.56	Variation of Percent Elongation at Yield in the Depth Direction	207
6.57	Typical Comparison of Percent Elongation at Yield Distributions	209
6.58	Variation of Percent Elongation at Break in the Depth Direction	210
6.59	Variation of Percent Elongation at Break in the Depth Direction	211
6.60	Variation of Melting Temperature in the Depth Direction at the Indicated Location. Unpublished Results from Reference (121).	213

Figure	Caption	Page
6.61	Variation of Percent Elongation at Break in the Depth Direction	214
6.62	Typical Comparison of Percent Elongation at Break Distributions	216
6.63	Variation of Amorphous Orientation Function in the Depth Direction	219
6.64	Variation of Amorphous Orientation Function in the Depth Direction	220
6.65	Variation of Amorphous Orientation Function in the Depth Direction	221
6.66	Typical Comparison of Amorphous Orientation Function Distributions	223
6.67	Plot of $(\Delta_T/X_c\ f_{cr})$ Versus $(1 - X_c/X_c)(f_{am}/f_{cr})$ for Resin EX 1 Molded at 176°C	226
6.68	Plot of $(\Delta_T/X_c\ f_{cr})$ Versus $(1 - X_c/X_c)(f_{am}/f_{cr})$ for Resin EX 2 Molded at 176°C	227
6.69	Plot of $(\Delta_T/X_c\ f_{cr})$ Versus $(1 - X_c/X_c)(f_{am}/f_{cr})$ for Resin EX 2 Molded at 205.9°C	228
6.70	Plot of $(\Delta_T/X_c\ f_{cr})$ Versus $(\Delta_{am}/X_c\ f_{cr})$ for Resin EX 2 Molded at 176°C	231
6.71	Crystalline and Amorphous Phase Contributions to the Total Birefringence	235
6.72	Crystalline and Amorphous Phase Contributions to the Total Birefringence	236
6.73	Crystalline and Amorphous Phase Contributions to the Total Birefringence	237
6.74	Crystalline and Amorphous Phase Contributions to the Total Birefringence	238
6.75	Crystalline and Amorphous Phase Contributions to the Total Birefringence	239
6.76	Crystalline and Amorphous Phase Contributions to the Total Birefringence	240
6.77	Crystalline and Amorphous Phase Contributions to the Total Birefringence	241

Figure	Caption	Page
6.78	Crystalline and Amorphous Phase Contributions to the Total Birefringence	242
6.79	Crystalline and Amorphous Phase Contributions to the Total Birefringence	243
6.80	Crystalline and Amorphous Phase Contributions to the Total Birefringence	244
6.81	Crystalline and Amorphous Phase Contributions to the Total Birefringence	245
6.82	Crystalline and Amorphous Phase Contributions to the Total Birefringence	246
6.83	Crystalline and Amorphous Phase Contributions to the Total Birefringence	247
6.84	Crystalline and Amorphous Phase Contributions to the Total Birefringence	248
6.85	Crystalline and Amorphous Phase Contributions to the Total Birefringence	249
6.86	Typical Comparisons Between Predicted and Measured Sonic Modulus Distributions at the Indicated Location	252
6.87	Typical Comparisons Between Predicted and Measured Tensile Modulus Distributions at the Indicated Location	254
7.1	Distribution of Properties in the Depth Direction for Resin EX 1 Molded at 176°C	256
7.2	Distribution of Properties in the Depth Direction for Resin EX 2 Molded at 176°C	257
7.3	Distribution of Properties in the Depth Direction for Resin EX 2 Molded at 205.9°C	258
A.15.1	Plot of Sonic Modulus of Compression Molded Samples Versus Crystalline Volume Fraction	A15-4

LIST OF TABLES

Table	Title	Page
4.1	The Azimuthal Relative Intensity Distributions $I(\psi)$, for the (110), (200), and (020) Diffraction Arcs for a Sample Microtomed Near the Surface at the Location Midway from the Gate, Molded at the Higher Melt Temperature of 205.9°C	42
4.2	The Azimuthal Relative Intensity Distributions $I(\psi)$, for the (110), (200), and (020) Diffraction Arcs for a Sample Microtomed from the Core Region at the Location Midway from the Gate, Molded at the Higher Melt Temperature of 205.9°C	44
5.1	Physical Properties of Materials	59
5.2	Regression Coefficients for Transducer Calibration Equations	74
5.3	Molding Conditions	76
5.4	Band Assignments of Linear Polyethylene	109
6.1	Average Cavity Filling Times, Maximum Filling Pressures, and Maximum Packing Pressures for the Two Resins as Measured by Pressure Transducer Located Near the Gate. Standard Deviations Are in Brackets.	121
6.2	Sonic Modulus (E_u), Crystalline Volume Fraction (X_c), and Density (ρ_s) of Unoriented Compression Molded Polyethylene Films	139
6.3	Experimental Values Obtained for Elastic Modulus Transverse to the Chain ($E^o_{t,c}$) for Polyethylene	142
6.4	Spacing of Reflected Planes	161
6.5	Comparison of Intrinsic Birefringence Values	229
6.6	Comparison of Estimated Intrinsic Birefringence Values for Polyethylene	233
A.15.1	Summary of Results for Studying Knife-Effects	A15-3

CHAPTER 1

GENERAL INTRODUCTION

The general aim of most plastics processing operations is to transform a resin, originally in the form of random particles, such as pellets, powder or beads, into a commercial product of predetermined shape and dimensions. The products range from film, sheeting, coating, pipe, monofilament, various profiles to a multitude of articles such as bottles, cups, toys, household appliance parts, auto-body and furniture parts. These products are produced by a wide variety of polymer processing techniques which may be categorized into three broad groups, depending on the shaping operation: molding (including forming), extrusion, and calendering. Molding and extrusion account for the bulk of commercial plastics articles.

In general, processing or fabricating operations involve the following basic steps:

(a) Heating and melting of the resin.

(b) Forming the desired shape by filling a mold, pumping the melt through a die, or passing between rolls.

(c) Cooling of the formed article to a solid mass.

In the fabrication of thermoplastics, the above steps may be accomplished by continuous steady-state operations or by unsteady-state semi-batch processes. While extrusion is a steady continuous process and only allows a two-dimensional control of the product shape, molding is generally an unsteady-state

operation and thus permits three-dimensional control of the shape.

A variety of molding processes are used commercially, including compression and transfer molding, blow molding, and rotational molding. Among the molding processes, injection molding is the most important technique, since it is the most commonly used commercially to produce a broad range of intricately shaped end-products. In this process, raw material is melted, then it is injected under pressure into a cold mold. Cooling and solidification continue in the mold until the article is ejected without mechanical damage. Polyethylene is the most commonly used resin in injection molding. It accounts for more than half of the overall volume of injection molded materials in both Canada and the United States.

Because of its commercial importance, the study of injection molding has received increasing attention in recent years. Much effort has been directed to the modeling of the injection molding process, in order to throw some light on the thermo-mechanical history of the material during processing (1-13). The main thrust of mathematical modeling studies of the injection molding process has been associated with the effort to understand injection molding dynamics with the aim of improving moldability characteristics and/or mold design.

Another important area, which has received limited attention thus far, relates to the effects of thermo-mechanical history during the molding process on the microstructure and, consequently, the ultimate properties of injection molded

articles. The present work attempts to contribute to the filling of the existing gap by reporting the results of an extensive experimental study of the detailed microstructure of injection molding parts and the impact of this microstructure on the distribution of mechanical properties in simple injection molded polyethylene articles. Microstructure, in the context employed in this work, relates to the morphology and orientation and their distributions in injection molded articles. Polyethylene, as a partially crystalline polymer, represents a class of materials in which morphology and orientation are strongly influenced by processing conditions and resin characteristics. On the other hand, morphology and orientation themselves influence the ultimate behavior of the molded article. In view of the above, a detailed study of morphology and orientation in injection molded articles should be of significant value for the understanding and control of the injection molded process.

CHAPTER 2

LITERATURE REVIEW

In this chapter, it is desirable for completeness to divide the literature background into three broad sections. The first section reviews briefly the morphological and crystallization phenomena of crystalline polymers. The second section reviews the rheo-optical studies of the deformation behavior of crystalline polymers. The third section reviews the microstructural studies relating to commercial polymer processing operations.

2.1 Crystallization Phenomena in Polymers

Most of the main features associated with crystallization of polymers from quiescent solutions and melts are well understood, and the resulting morphologies are well documented. Extensive literature reviews are available concerning the subject (14-17).

2.1.1 Quiescent Crystallization

Keller (18) and Fischer (19) independently showed that single polymer crystals could be formed from dilute solutions and that the linear macromolecules crystallize into the form of thin platelets whose large upper and lower surfaces consist of an array of molecular folds. These folds are commonly referred to as "chain-folded crystals" or "chain-folded lamellae", the latter term usually being reserved for folded structures in

polymers crystallized from the melt. A schematic representation showing the chain-folding in a polyethylene single crystal is shown in Figure 2.1. The simple lamellar crystals are typically 100 A^{o} or so in thickness and a few microns in length and width. X-ray and electron diffraction of these single crystals have demonstrated that the chain axis is perpendicular to the broad surface (14, 15). Since each polyethylene molecule entering the crystal is of the order of 10^{4} A^{o} in length, this means that it must re-enter the flat surface many times by chain-folding.

The crystal structure of polyethylene was first studied by Bunn (20) by comparing the X-ray diffraction patterns from n-paraffins and from a (branched) polyethylene. He concluded that polyethylene basically had the same structure as did the shorter chain homologues of polyethylene. The unit cell is orthorhombic and the carbon atoms of each molecule form a planar zigzag arrangement. The chain axis lies along the crystallographic c-axis.

Furthermore, the appearance of polymer single crystals with chain folds from dilute solution is not a unique phenomenon of polyethylene. The evidence of chain-folding in other polymers has been reviewed by Hoffman et al. (17).

The crystallization of polymers from the melt is not fundamentally different from crystallization from solution. In both cases, the polymer molecules are driven to uncoil from high entropy configurations (15). The main difference between melt crystallization and crystallization from dilute solution is

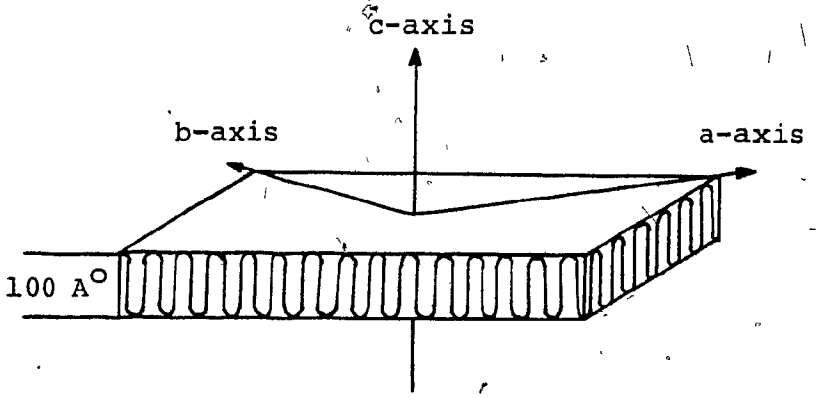
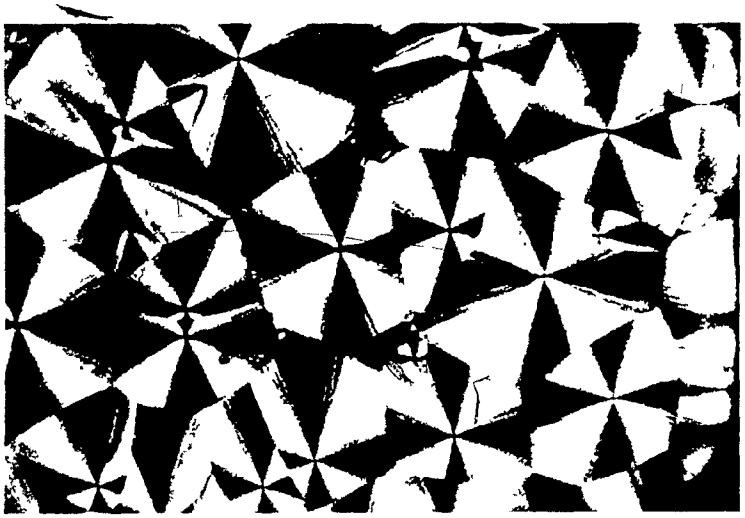


FIGURE 2.1. Schematic Representation of Polyethylene Single Crystals Showing Chain Folding and Orientation of Crystallographic Axes (Reference 21)

that in the former, the polymer molecules are in more intimate contact with each other in the coiled state. Consequently, the melt crystallized polymers are polycrystalline aggregates in which the crystals are intimately tied together. Keller (18) showed ample evidence to suggest that the principal crystalline unit in a melt crystallized linear polymer is ordinarily a thin chain-folded lamella similar in general character to a single crystal as regards the site of the folds and its thickness. The most commonly observed morphology in polymers crystallized from quiescent melts is the spherulitic one. The crystallization occurs by the nucleation of spherulitic centers and the subsequent creation and longitudinal growth of the concomitant ribbons or lamellae. The outward growth of a spherulite ceases when it has impinged upon the growing surface of another spherulite.

Figure 2.2 shows the specific symmetry and orientation of crystals within the spherulites. A spherulite becomes a three-dimensional spherical object by virtue of the fact that the lamellae occasionally branch. Furthermore, the lamellar ribbons are observed to grow in the direction of the crystallographic b-axis (parallel to the ribbon axis), which is the growth axis for polyethylene (14). Further details on the properties of melt crystallized polymers are discussed by Geil (14) and Schultz (15).

FIGURE 2.2. Optical Micrograph of Polyethylene Spherulites (Reference 21)



2.1.2 Crystallization Under Stress

A brief survey of the work in the field of oriented crystallization from flowing polymer solutions and melts is now presented. The accelerating influence of molecular orientation on the crystallization of polymeric materials can be readily illustrated by citing the example of crystallization in rubber. Andrews (22) and later Schuur (23) showed that butyl rubber in the relaxed state does not crystallize at all, or hardly at all, even at low temperatures, whereas it does crystallize rapidly at room temperature when highly stretched.

Molecular orientation can be readily achieved in polymer solutions or melts by imposing a flow field on the system, thereby influencing the crystallization. The flow fields that could be imposed may be classified into two main categories: elongational (extensional) flow and shearing flow. In many situations of interest, shearing and elongational fields are usually superposed. An extensional flow field is one in which the velocity gradient is parallel to the direction of flow and fluid elements are subjected to a stretching deformation, while for a simple shearing flow, the velocity gradient is perpendicular to the direction of flow and fluid deformations are mainly of a rotational nature (24). Figures 2.3 and 2.4 illustrate schematically the two types of flow and their effect on molecules in solution, respectively. The effect of an extensional flow field is to elongate a coiled molecule, while that of a shear field is to cause the molecule to rotate. However, in a molten polymer this distinction becomes blurred because of the

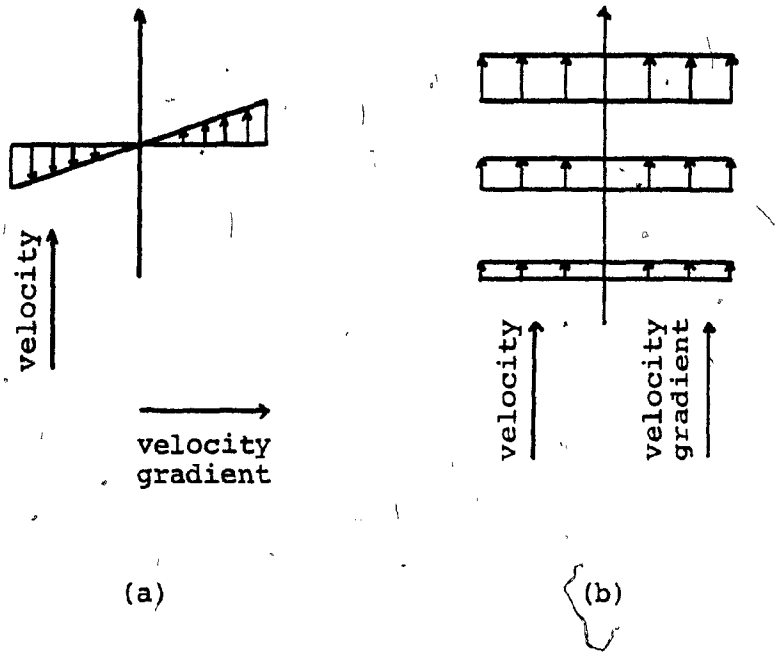
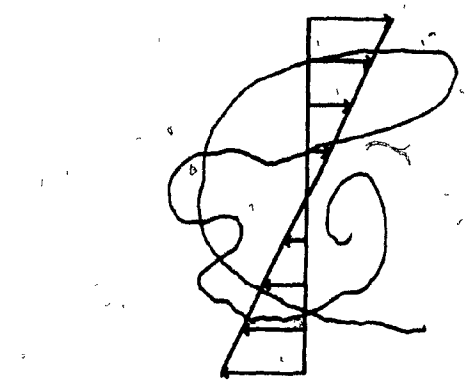
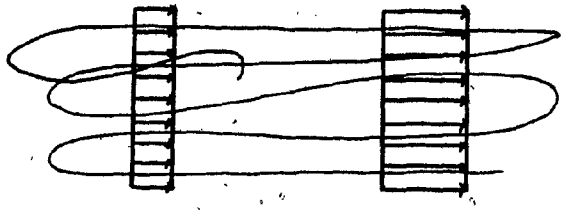


FIGURE 2.3. Schematic Representation of (a) Shearing Flow Field, (b) Extensional Flow Field



(a)



(b)

FIGURE 2.4. Effect of (a) Shearing and (b) Extensional Flow Fields on Flexible Macromolecules in Solution

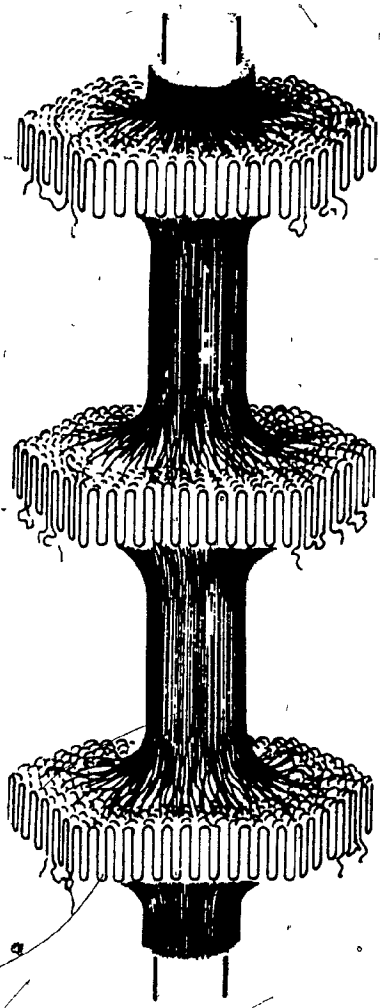
presence of molecular entanglements which prohibit free rotation of a molecule. A more rigorous fluid mechanical treatment of the flow fields can be found in standard textbooks on rheology (25, 26, 27) and relevant review articles (28).

The two most common systems used to date for studying the phenomenon of flow induced crystallization are simple Couette devices (flow caused by two concentric rotating cylinders) and paddle-stirred systems. The accelerating influence of a flow field on polymer crystallization was first dramatically demonstrated by Pennings and Kiel (29). They were able to grow fibrous crystals from a 5% (by weight) solution of linear polyethylene (Marlex 50) in xylene, which was mechanically stirred at 102°C. Furthermore, Pennings and co-workers (30) and recently Frank et al. (31) and McHugh and Schultz (32) demonstrated that the principal influencing factor for nucleation and growth of fibrous material from stirred solutions, is the presence of an extensional flow, and that simple laminar shearing flow alone is not capable of promoting nucleation in a dilute polymer solution.

Studies in oriented crystallization from dilute polymer solutions are not limited to polyethylene (29-33). The phenomenon has been reported for several polymers: isotactic polystyrene (34), isotactic polypropylene (35), ethylene-propylene copolymers (35), polyoxymethylene (36) and poly (ethylene oxide) (37).

Certain important features of oriented crystallization from polymer solutions have emerged from such investigations. First, the amount of supercooling needed to induce crystallization in a flowing polymer solution is greatly reduced. There is also some evidence to suggest that polymer chains of higher stiffness can be more readily oriented in a hydrodynamic field under comparable conditions and so crystallized at higher temperatures above the lower bound of the metastable area for quiescent crystallization (37). The second important feature is the fibrillar morphology of the crystals. Electron micrographs of these crystals show that they consist of a fibrous backbone with lamellar "beads" strung out at intervals of approximately 1000 A^{O} with thicknesses of about 200 A^{O} (32). Figure 2.5 schematically represents the so-called "shish-kebab" morphology observed in all cases of growth from flowing solutions. Finally, the significant improvement in the tensile strength of the polymer crystals as a result of fibrillar growth is experimentally documented. Pennings and co-workers (38) have measured the tensile properties of carefully grown fibrous polyethylene and have reported a maximum modulus of 20×10^4 kg/cm^2 and a fracture stress of 9×10^3 kg/cm^2. In contrast, the tensile strength values for single crystal mats grown from solution are about 100 kg/cm^2 and unoriented melt crystallized material exhibits a tensile strength of about 200 kg/cm^2 (39). A more detailed review of oriented crystallization from polymer solutions is given by Keller and Willmouth (33).

FIGURE 2.5. Schematic Representation of the Shish-Kebab Model (Reference 179)



Crystallization from a stressed polymer melt has been found to produce not the familiar randomly nucleated spherulitic structures, but instead a highly oriented "row nucleated" morphology. Polyethylene films stretched with pins during crystallization exhibit a shish-kebab structure (40, 41). Southern and Porter (42, 43) have reported the formation of a highly oriented section of polyethylene fiber which crystallizes exclusively in the entrance region of a capillary rheometer where an induced elongational flow exists. Wide angle X-ray diffractometry of the material shows that the chain-axis is oriented preferentially in the flow direction. Furthermore, DSC melting at various heating rates shows the material to be highly superheatable, similar to extended material (44). Haas and Maxwell (45) have reported similar temperature dependence of the melting of linear polyethylene samples crystallized under high stress. Studies on the crystallization of polymer melts in a Couette flow system indicate that the temperature at which crystallization could be observed increases significantly with increasing shear rate (46, 47). These observations are consistent with the general features of oriented crystallization from polymer solutions.

2.2 Studies of Deformation Behavior of Polymer Systems

The deformation of crystalline polymers has been a subject of keen interest for many years. A number of workers (48-65) have employed one or more of a variety of techniques such as X-ray diffraction, birefringence, polarized infrared spectros-

copy, and small-angle light scattering, in order to study the relationship between morphology and deformation mechanisms in crystalline polymers.

Stein and co-workers (51-55) in a series of papers employed the above-mentioned techniques to study the orientation of both the crystalline and amorphous portions in stretched polyethylene films. According to these workers, the crystal orientation may be readily studied by X-ray diffraction while birefringence and infrared dichroism may be used to characterize the total orientation, as well as that of the crystalline and of the less ordered regions. Furthermore, if the orientation contributions of both regions are assumed to be additive, the birefringence of the less ordered region could be estimated by subtracting the crystalline contribution as determined from X-ray diffraction data from the total measured birefringence. They concluded that when polyethylene samples were elongated between 0 and 400%, both the amorphous and crystalline regions oriented appreciably upon stretching.

Stein and co-workers (51-55) have also observed that the amorphous orientation is somewhat lower than that of the crystallites and that many of the amorphous chains appear to become completely stretched out. They suggest that the degree of crystallinity remains constant during stretching and that the oscillator strength of the CH_2 rocking vibration is also constant. Furthermore, by using any two of the three methods of X-ray diffraction, birefringence, and infrared dichroism, one may determine the individual contributions to the overall

orientation by the amorphous and the crystalline portions of the polymer. With the resulting data, it would be possible to predict the measurements obtained with the third method.

Samuels and co-workers (60-63) have used similar methods, including a sonic velocity technique to study the deformation of isotactic polypropylene films and fibers. These workers have developed a two-phase sonic modulus theory which makes possible the determination of the amorphous orientation function and the intrinsic sonic moduli of the polymer. Furthermore, they have proposed a technique for the experimental determination of the intrinsic birefringence values of the crystalline and amorphous regions of the polymer.

The mechanical properties of crystalline polymers are dependent upon the mechanisms of deformation available to their structures. These are related to morphological features such as degree of crystallinity, connectivity of crystals by amorphous chains, the size and shape of the crystallites and their participation in superstructure (66-70). The understanding of these properties is facilitated by the simultaneous observation of a number of properties of such materials during deformation. A number of workers (71-74) have observed the time dependence of changes in X-ray diffraction, birefringence, light scattering, and visible, infrared, and ultraviolet dichroism. Each method is primarily sensitive to a particular aspect of the morphology and the combined use of several methods serves to help resolve the relatively complex deformation process into constituent mechanisms. For more details on the deformation of

a polycrystalline polymer in terms of the changes in morphology, texture, crystalline structure, and chain conformation, the reader is referred to a review article by Stein (74).

Studies of deformation behavior are by no means limited to polyethylene (48-59). Other polymers include: nylon (64), polyester (64), polypropylene (60-64), poly (ethylene terephthalate) (65, 75, 76), high impact polystyrene (75), polyvinyl chloride (75), and poly (chlorotrifluorethylene) (77).

2.3 Microstructural Studies in Polymer Processing

In many polymer processing operations, molten polymers emerge from dies into a stress field which deforms the melt into a final fabricated shape. The properties of the fabricated parts are determined in crystalline polymers by the morphology and orientation which are in turn related to the deformation history and the crystallization process (78).

Ziabicki and Kedzierska (79-83) in the late 1950's and early 1960's studied the melt spinning process, and used birefringence as a measure of molecular orientation under various spinning conditions. They concluded that molecular orientation increased with spinline tension, the difference between the take-up and extrusion velocities, and the inverse of the filament diameter. More recently, Katayama *et al.* (84), Kitao *et al.* (85), and White and co-workers (78, 86-88) reported more quantitative details regarding the effects of melt spinning and drawing variables on the nature of the crystallinity and molecular orientation and, in turn, their influence on the mechanical

properties. Similar studies were reported by Sheehan and Cole (89) and Fung and co-workers (90, 91). Also, Dees and Spruiell (87) proposed a detailed model of the morphology developed in melt spun linear filaments based on the "row structure" concepts of Keller et al. (40, 92).

Spruiell and White (78) have pointed out that an integral part of the problem during melt spinning is the interaction of rheological factors (stretching of the melt), heat transfer from the running threadline, and the crystallization kinetics of the polymer. Furthermore, these factors not only control the morphology of the spun filament, but, indeed, they determine whether or not crystallization occurs during spinning. This was realized by Ziabicki (93) and later by Katayama et al. (84).

Katayama et al. (84) obtained X-ray patterns, and measured temperature, birefringence and diameter profiles on running spinlines of polyethylene, polypropylene and polybutene-1. They appear to be the first to have demonstrated that crystallization kinetics may be greatly enhanced during melt spinning, as compared to quiescent conditions, due to the molecular orientation caused by the stretching and cooling of the melt. Similar methods have been used by Dees and Spruiell (87) in their study of high density polyethylene. In more recent work, Nakamura et al. (94) have attempted to treat the relation between crystallization temperature, crystallinity and cooling conditions. Furthermore, Nadkarni and Schultz (95) have studied the crystallization induced by elongational flow during the melt spinning of polyethylene and employed a variety of techniques such as

wide-angle X-ray scattering, density, scanning electron microscopy and differential scanning calorimetry to characterize the microstructure of the as-spun fibers. They also attempted to correlate physical properties and structural features of the spun fiber samples with processing variables.

Recently, Porter and co-workers (96-100) and subsequently, Takaganagi and co-workers (101) and Ward with co-workers (102) have studied the solid-state extrusion of crystalline polymers (notably high density polyethylene). Many studies have been made to evaluate the influence of extrusion conditions on the physical, mechanical, and morphological properties of the ultra-drawn fibers (96-102). In particular, Porter et al. (100) have assessed the properties of the resulting fibers by a variety of techniques such as density, birefringence, thermal expansivity, differential scanning calorimetry, small- and wide-angle X-ray scattering, tensile modulus, strength, and recovery.

On the other hand, there have been relatively few similar studies on polymer processing operations other than melt spinning. Aggarwal et al. (103), in the earliest work, studied orientation in extruded polyethylene films by means of X-ray diffraction and infrared spectroscopy. Later Holmes and Palmer (104) employed X-ray diffraction and birefringence techniques to study the orientation of the crystalline and amorphous regions in tubular-blown polyethylene films. In more recent work, Lindenmeyer and Lustig (105) studied the crystallite orientation in tubular extruded polyethylene films, by means of X-ray diffraction, and attempted to correlate the orientation

of the crystallographic axes with the ultimate mechanical properties of the films.

In the area of thermoplastic injection molding, much of the effort has been directed to the modeling of the process, in order to throw some light on the thermo-mechanical history of the material during processing (1-13). Other work has concentrated on the study of the morphology and orientation in injection molded parts (106-122). Earlier work has concentrated on the measurement of internal (frozen-in) stresses in thermoplastic moldings mainly by means of polarizing optics such as birefringence (123-125), and analysis of X-ray scattering (111, 112) or indirectly by measuring thermal shrinkage (126) and by determination of mechanical anisotropy (127, 128).

Menges and Wubken (114) have studied orientation in polystyrene moldings by means of heat shrinkage measurements. They have concluded that the flow direction is the main direction of orientation in plane-shaped moldings and that maximum orientation is observed at the surface, while minimum orientation is observed at the centre of the moldings. Furthermore, increasing the melt and cavity wall temperatures tends to reduce the frozen-in orientation, while increasing the injection rate tends to marginally increase the orientation at the surface but significantly reduces the internal orientation. Similar results have been reported by Bakerdjian and Kamal (117) on the basis of birefringence measurements in polystyrene moldings. The latter workers have observed a more complex behavior of the orientation distributions in conjunction with polyethylene

moldings. They have attributed the complexity of polyethylene behavior to the interaction between orientation and crystallization phenomena.

Fleissner and Paschke (115) and Paschke (129) have studied the influence of melt temperature on the development of orientation as measured by birefringence and heat shrinkage measurements, and its effect on the mechanical properties of thin-wall (1 mm) injection moldings of high density polyethylene. These workers have separated high density polyethylene into high-flow and low-flow types. They have found that for high-flow materials, increasing the melt temperature in the range 140°C to 340°C tends to decrease the notched impact strength, while for low-flow materials, the notched impact strength tends to increase as the melt temperature is increased. Furthermore, the tensile yield stress is observed to decrease as the melt temperature is increased, due to the lower orientation. The elongation at yield tends to increase for high-flow materials, but decreases for low-flow materials. Fleissner and Paschke attribute the differences in mechanical properties to the lower orientation at higher melt temperatures, and to the molecular weight differences between the high-flow and low-flow materials. On the basis of their findings, they suggest that the optimum temperature range for injection molding of high density polyethylene is between 280-310°C.

Recently, a number of workers (106-113) have reported on the development of morphology in the injection molding process and its influence on the ultimate properties of the molded part.

Clark (107) and later Boehme (106) have studied the structure development of injection molded acetal homopolymer, under different molding conditions, and the influence on the mechanical properties of the molded part. These workers have observed by optical microscopy that the microstructure of injection molding consists of a composite of different morphologies forming a laminate structure. Three types of morphology occur: a skin of high molecular orientation, a less highly oriented intermediate "transcrystalline layer", and a spherulitic core. Clark (107) points out that the skin represents that portion of the melt crystallizing during the filling period with a structure interpreted as an overgrowth of folded-chain lamellae on fibril nuclei similar to the well-known "shish-kebabs" from stirred solutions, except for the less extended chain nature of the fibril domains. The transcrystalline and spherulitic regions result from crystallization under low melt stress. Furthermore, the variation in skin thickness in a molding is due to the expected decrease of melt velocity with distance from the gate and its corresponding influence on the creation of fibril nuclei. Further, the relative volumes of the transcrystalline and spherulitic regions are determined by the rate of heat transfer to the mold wall. Boehme (106) has observed that the thicknesses of the three developing zones are influenced both by the molding procedure and the mold temperature, which in turn, modifies the mechanical properties and the dimensional stability of the molded part.

The skin-core morphology of injection molded crystalline polymers has since been studied by several workers (111-113, 119, 121). Kantz, Newman and Stigale (111) studied the skin-core morphology and structure-property relationships in injection molded polypropylene. They evaluated the effects of melt temperatures and injection pressures on the morphology and crystalline orientation, using optical microscopy and X-ray diffraction, and their influence on the mechanical properties of the molded parts. Their studies revealed, by optical microscopy of microtomed thin sections of the tensile bars, the presence of three distinct crystalline zones, namely, a highly oriented non-spherulitic skin, a row or shear-nucleated spherulitic intermediate layer, and a typically spherulitic core. Furthermore, the thickness of the oriented skin layer was a function of the polymer melt temperature and varied inversely with temperature. The thickness of the intermediate layer varied with injection pressure, but in a complex manner. Also, the preferred crystallite orientation in the skin and intermediate layer exerted profound effects on mechanical properties. The tensile yield strength, impact strength and shrinkage increased with increasing combined thickness of the two oriented outer layers. Fitchmun and Mencik (112) and later Hobbs and Pratt (113) also made similar observations concerning the composite structure or skin-core morphology of injection molded crystalline polymers. The former workers used optical and scanning electron microscopy to characterize the morphology in injection molded polypropylene, while the latter workers

employed optical microscopy, X-ray diffraction and density measurements, to characterize the skin-core morphology in injection molded poly (butylene terephthalate).

Tan and Kamal (119) have studied the morphological zones and orientation in injection-molded polyethylene. A variety of experimental techniques have been employed, including density, polarized light microscopy, infrared measurements, and differential scanning calorimetry, with the aim of elucidating the orientation and morphological effects in polyethylene injection molding. They concluded that the properties of injection-molded plastics parts are affected by resin properties, molding geometry and molding conditions.

Woebcken and Heise (116) used the X-ray diffraction technique to relate crystallite orientation in polyethylene injection moldings to mechanical properties and processing conditions. In their work, they observed significant interactions between microscopic structure, on the one hand, and both processing conditions and the properties of the molded articles, on the other hand.

2.4 Summary

The above survey suggests that morphology and orientation and their distributions in plastics parts reflect the thermomechanical history of the resin resulting from the interactions between the resin and the process which incorporates the effects of equipment and processing conditions. In turn, the microstructure, as reflected by morphology and orientation and their

distributions, plays a major role in influencing the ultimate properties of plastics articles.

Some detailed studies have been reported for fiber spinning regarding the interactions between morphology and orientation, on the one hand, and other variables like resin properties, processing conditions, and ultimate properties of the spun fibers, on the other hand. Similar, but less detailed studies have been reported for partially crystalline polymers, in conjunction with blown films. In some cases, some theoretical concepts were employed to obtain quantitative correlations between fiber or film microstructural characteristics and macroscopic properties.

On the other hand, work relating to the study of the microstructure of injection molded partially crystalline polymers has tended to be fragmented and qualitative in nature. A variety of techniques have been employed to elucidate the nature of morphology and orientation and their distributions in these systems. These techniques indicate a complex skin-core structure with continuous variation of morphology and orientation throughout the molding. However, little has been done to integrate the results of various experimental techniques or to employ quantitative methods to relate results from various techniques to each other and to the ultimate properties of the moldings.

The present study attempts to fill some of the void in the fundamental understanding of the injection molding process and related products. Its scope and objectives are outlined in the following chapter.

CHAPTER 3

SCOPE AND OBJECTIVES

The present work offers a systematic approach for quantitatively describing the microstructure developed in the injection molding of crystalline polymers. The study represents a part of a more general and integrated program to study the injection molding behavior of both amorphous and crystalline polymers. It is intended that the results of the present work should yield techniques to describe the microstructural distributions in injection molded parts and at the same time, to be able to integrate these techniques so that a detailed description of both the crystalline and amorphous phases may be achieved. Furthermore, distributions of various mechanical properties are obtained so that an attempt will be made to relate the microstructural properties to the observed variations in mechanical properties of the molded part, as a result of processing conditions and resin behavior.

The main specific objectives of the study are the following:

(1) To obtain a suitable set of moldings using a Danson 2-1/3 oz Metalmec injection molding machine, for microstructural characterization.

(2) To develop techniques such that the morphological and orientation distributions developed in the molded part, as a result of processing, may be obtained.

(3) To integrate these techniques such that the relative contributions of both the crystalline and amorphous phases to the total orientation may be obtained.

(4) To obtain the distribution of mechanical properties in the moldings and to relate these properties to the microstructural characteristics of the moldings.

Two injection molding grade high density polyethylene resins (designated EX 1 and EX 2) were used in the study. Table 5.1 lists some properties of these two resins, which are representative of commercial resins employed in injection molding. The two resins used in the study were supplied by DuPont of Canada.

It should be pointed out that the present work incorporates the results of an extensive number of experimental measurements. As indicated above, it has been the intention, in this work, to produce an integrated set of experimental data based on the application of a multiplicity of experimental techniques, in conjunction with injection molded parts. In order to obtain a meaningful integration of the results, it is necessary to employ data obtained on the same set of samples produced at the same time under predetermined molding conditions. The possibilities of errors due to aging or sample variation have indicated the high desirability of a complete set of data obtained under the above conditions. This, in fact, represents a major hurdle, but also offers the opportunity, for the first time, to have at hand a complete set of data relating to molding conditions, molding microstructural characteristics, and molding ultimate

properties. These data will be employed in the analyses required for the purposes of the present work. Moreover, they should prove to be useful for other future studies.

Although an effort will be made, in this work, to explain qualitatively some of the observed phenomena, it should be emphasized that a complete quantitative explanation can be based only on the application of detailed mathematical models of the injection molding process and related phenomena. In fact, the main aim of the present work should be considered in the context of obtaining the detailed experimental data relating to the microstructure of injection molding parts, rather than the explanation of these data on the basis of an analysis of the complex thermo-mechanical history. The latter task will have to await the results of other work currently in progress at this laboratory.

The text is divided into seven chapters. Chapters 1 and 2 deal with the general background and a general literature review of crystallization and orientation phenomena in polymers and their relevance to polymer processing operations. Chapter 4 presents some of the theoretical background relevant to the techniques employed in the study. Chapter 5 describes the experimental procedures. Chapter 6 presents the distribution of the microstructural characteristics in the molded parts as measured by each technique. It also presents the results of the integration of these techniques to obtain the relative contributions of the various phases to the total orientation. Furthermore, the relationships between the observed mechanical properties

and the microstructural characteristics are discussed. Chapter 7 contains the claims to originality, general conclusions, and suggestions for future work.

An exhaustive list of references is presented. The numerical data representing the results obtained by the various experimental techniques are tabulated in the Appendices (3-14). Appendix 15 presents an analysis of errors associated with the various measurements, as well as the estimation of the magnitude of the knife-effect.

CHAPTER 4

THEORETICAL BACKGROUND

In this chapter, the quantitative relationships governing each of the techniques employed in the study are described. Furthermore, the relationships between the measurements obtained with these techniques and the morphology and orientation developed in injection moldings, will be indicated.

4.1 Density and Crystallinity

Density is linked directly to the unit cell parameters. However, density determinations on melt-crystallized polymers show that the experimental values do not reach the unit cell densities, but rather lie somewhere between the densities of the crystalline and amorphous phases. Based on these experiments, a fractional crystallinity is usually calculated. The crystallinity concept, in its simplest form, assumes that polymers crystallize only partially. The semi-crystalline sample is thought to consist of two portions: a crystalline portion, to be described by the ideal crystal structure, and an amorphous one, to be described by the ideal melt. The volume fraction of crystallinity (X_c) is then given by (130),

$$X_c = (\rho_s - \rho_a)/(\rho_c - \rho_a) \qquad (4\text{-}1)$$

where ρ_s is the sample density in g/cc. ρ_c and ρ_a are the crystalline and amorphous densities in g/cc, respectively. For

polyethylene, the values of ρ_c and ρ_a are taken to be 1.001 and 0.856 g/cc, respectively (131).

It should be pointed out that the calculation of crystallinity by measurement of sample density using the density gradient technique is just one of the many techniques available for the determination of crystallinity (130).

4.2 Sonic Velocity Measurements

One method used for studying the orientation of polymers which does not make use of electromagnetic radiation is that of sonic velocity or pulse propagation (132).

Figure 4.1(a) shows a schematic diagram where the polymer chains are oriented at some average angle θ to the stretch axis while in Figures 4.1(b) and (c), θ has values of 0° and 90°, respectively. Simple physical considerations suggest that sonic velocity (in the X direction) is orientation dependent since in Figure 4.1(b) the mechanism of propagation occurs along the polymer chain (intramolecular bond stretching), while in Figure 4.1(c) the mechanism must depend on the propagation across the chains, that is, via van der Waals bonds (intermolecular bond stretching) or other chain-chain interactions such as hydrogen bonding. Based on these different mechanisms, theoretical calculations utilizing the force constants of bond stretching have predicted that the rate of propagation will be much greater when directed along the chain, that is, along chemical bonds, than when directed perpendicularly to the chain (133). Utilizing the above, Moseley (134) proposed a semi-empirical treatment

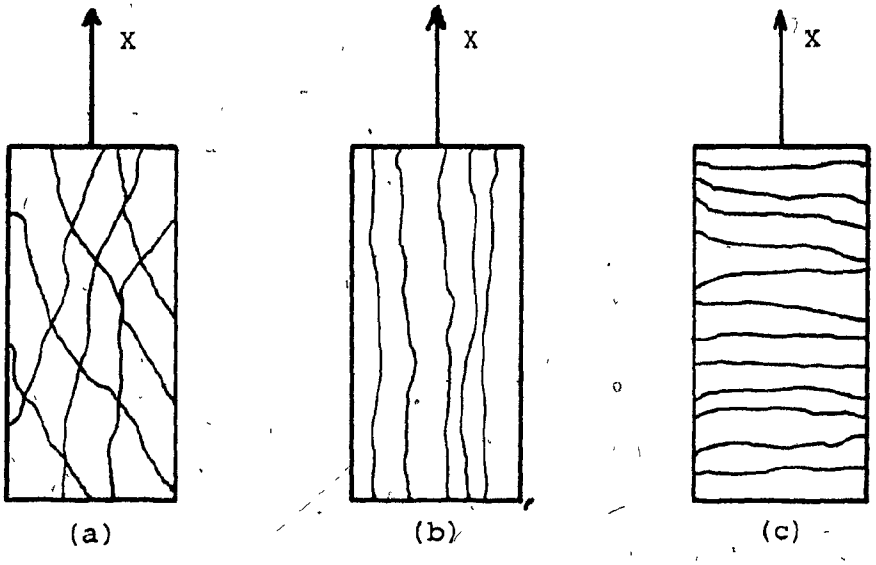


FIGURE 4.1. Schematic Representation of Chain Orientation in an Amorphous Polymer. (a) Partial Parallel Orientation Along X, (b) Perfect Parallel Orientation, (c) Perfect Perpendicular Orientation (Reference 132)

to relate the sonic velocity to orientation. He concluded that a series addition of the intra- and intermolecular force constants, weighted by an average orientation parameter, had to be used to represent the propagation of a sound pulse through the polymer. Moseley derived the following equation for the sonic velocity:

$$\frac{1}{C_s^2} = \frac{1 - \overline{\cos^2\theta}}{C_t^2} + \frac{\overline{\cos^2\theta}}{C_l^2} \qquad (4\text{-}2)$$

where C_s, C_t and C_l represent the sonic velocity for the sample having an average orientation angle θ, 90° (perpendicular orientation) and 0° (parallel orientation), respectively.

The sonic velocity is related to the sonic modulus, E_s, that is, Young's modulus measured at high frequency, via the expression (135)

$$E_s = \rho_s C_s^2 \qquad (4\text{-}3)$$

where ρ_s is the density of the material in g/cc. Hence, Equation (4-2) may be rewritten in terms of moduli rather than velocity, as

$$\frac{1}{E_s} = \frac{1 - \overline{\cos^2\theta}}{E_t^o} + \frac{\overline{\cos^2\theta}}{E_l^o} \qquad (4\text{-}4)$$

where E_t^o is the intrinsic lateral (transverse) modulus of a fully oriented sample (that is, where all of the chains are

aligned parallel to each other and perpendicular to the direction of sound propagation). Furthermore, because of the high longitudinal sound velocity along the chain axis of the molecule, the second term on the right in Equation (4-4) may be neglected (134). Thus, Equation (4-4) is reduced to

$$\frac{1}{E_s} = \frac{1 - \overline{\cos^2\theta}}{E_t^o} \qquad (4\text{-}5)$$

Samuels (136) has extended the treatment of Moseley to consider a two-phase system - specifically that of a semi-crystalline polymer. The two-phase model takes into account different intermolecular force constants for the crystalline and amorphous regions. Therefore, for an unoriented sample, $\overline{\cos^2\theta} = 1/3$ and Equation (4-5) becomes

$$\frac{3}{2\,E_u} = \frac{X_c}{E_{t,c}^o} + \frac{(1 - X_c)}{E_{t,am}^o} \qquad (4\text{-}6)$$

where E_u is the sonic modulus of the unoriented sample in pascals (Pa) and $E_{t,c}^o$ and $E_{t,am}^o$ are the intrinsic transverse moduli for the crystalline and amorphous phases, respectively. Thus, by studying the change in the sonic modulus of unoriented samples with crystallinity, the intrinsic lateral moduli of the crystalline and of the amorphous regions of the polymer may be determined.

For an oriented sample, Equation (4-5) is of the form

$$\frac{1}{E_{or}} = \frac{X_c(1 - \overline{\cos^2\theta_c})}{E^o_{t,c}} + \frac{(1 - X_c)(1 - \overline{\cos^2\theta_{am}})}{E^o_{t,am}} \qquad (4\text{-}7)$$

The orientation function for the individual phases is defined as

$$f_\chi = (3\,\overline{\cos^2\chi} - 1)/2 \qquad (4\text{-}8)$$

where χ is the angle between either the crystalline or amorphous phase and the reference direction which is also the direction of sound propagation. By combining Equations (4-6), (4-7) and (4-8), the equation for the sonic modulus of an oriented polymer becomes (136),

$$\frac{3}{2}(\Delta E)^{-1} = \frac{X_c\, f_{cr}}{E^o_{t,c}} + \frac{(1 - X_c) f_{am}}{E^o_{t,am}} \qquad (4\text{-}9)$$

where f_{cr} and f_{am} are the respective Herman's orientation functions for the crystalline and amorphous phases, respectively. $E^o_{t,c}$ and $E^o_{t,am}$ are the intrinsic transverse modulus values of the perfectly oriented crystalline and amorphous phases, respectively, and

$$(\Delta E)^{-1} = \left(\frac{1}{E_u} - \frac{1}{E_{or}}\right) \qquad (4\text{-}10)$$

where E_u and E_{or} are the respective moduli for an unoriented sample and the sample being measured, respectively.

It should be mentioned that the sonic technique, like the birefringence method, measures the average orientation of the total system. However, it is noteworthy that the orientation measured by the sonic method can be correlated directly with birefringence data on the same material (60). This ease of correlation has been suggested to lead to values of the intrinsic birefringence by extrapolation of the sonic data to perfect orientation (60, 64). Furthermore, the utility of Equation (4-9) is expanded when at least one of the f values is determined by another method, such as X-ray diffraction for the crystalline orientation.

4.3 Birefringence Measurements

Birefringence is a measure of the total molecular orientation of a system. It is defined as the difference between the principal refractive indices parallel ($n_{||}$) and perpendicular ($n_{\perp}$) to the stretch direction for a uniaxially oriented specimen. The refractive index, in turn, is a measure of the velocity of light in the medium and is related to the polarizability of the chains. Thus, the final measured birefringence is a function of contributions from polarizabilities of all of the molecular units in the sample (136).

In a partially crystalline material, the velocity of light in the crystalline region will be different from that in the amorphous region. Since the molecules are optically anisotropic, there is a difference in the principal polarizability parallel ($P_{||}$) and perpendicular ($P_{\perp}$) to the chain axis. If all of the

anisotropic molecules are randomly distributed in the specimen (unoriented sample), the average contribution to the refractive index will be the same in all directions and the birefringence, $\Delta_T = n_{\parallel} - n_{\perp}$, will be zero, that is, the specimen is optically isotropic. If all of the molecules are perfectly aligned parallel to the stretch direction, the birefringence will be a combination of the ideal polarizability anisotropy of each region. In other words, each region will have the birefringence of a fully oriented sample of that phase alone. The measured birefringence of oriented samples will have intermediate values between these extremes, depending on the orientation and amount of each phase present in the specimen.

By assuming a two-phase model for a uniaxially-oriented crystalline polymer, the measured birefringence is defined as (51)

$$\Delta_T = X_c \, f_{cr} \, \Delta_c^o + (1 - X_c) f_{am} \, \Delta_{am}^o + \Delta_f \qquad (4\text{-}11)$$

where X_c is the volume fraction of crystalline material; f_{cr} and f_{am} are the orientation functions for the crystalline and amorphous phases, respectively; Δ_c^o and Δ_{am}^o are the intrinsic birefringence values of the perfectly-oriented crystalline and amorphous phases, respectively; Δ_f is the form birefringence which expresses the deviation from additivity and arises from the deformation of the electric field at anisotropically-shaped phase boundaries. These may be boundaries of crystalline and amorphous regions, or may be boundaries of microvoids. The

form birefringence, Δ_f, is assumed to be negligible in this study. An expression for the determination of form birefringence contribution based on refractive indices is presented in Appendix 1. This expression was used by Porter and co-workers (100) in their study of solid-state extrusion of high density polyethylene. The relative contribution of the form birefringence was estimated to be 8% of the measured total birefringence.

4.4 Wide-Angle X-Ray Diffraction

The X-ray method is used to characterize the anisotropy of semi-crystalline polymeric materials or more specifically, to characterize the orientation of the various crystallographic axes a, b and c with respect to some specified set of sample axes. In the case of injection molded samples, the flow direction (X direction) is taken as the sample reference direction.

As with low molecular weight compounds, crystalline polymers may be characterized by specifying the unit cell parameters for the crystal lattice. Figure 4.2 shows the unit cell configuration for polyethylene (136). The c-axis lies parallel to the chain axis, although this is not true for all polymer crystals. Planes may be drawn through the crystal cell at various angles with respect to the axes and these planes are specified by the Miller indices (hkl) which are derived by forming the reciprocal of the intercepts of a given plane with the a, b and c axes. These reciprocals are then reduced to the smallest integer values resulting in the Miller indices for that set of planes.

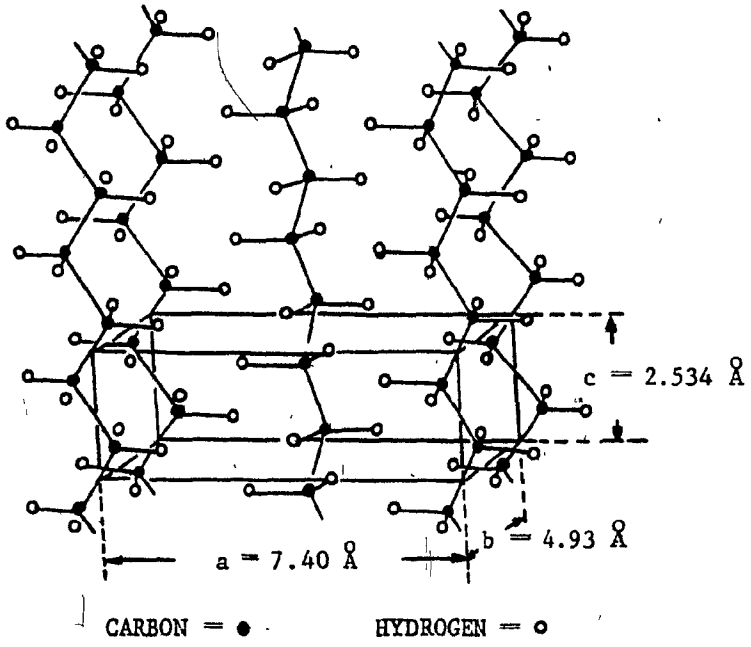


FIGURE 4.2. Unit Cell of Polyethylene (Reference 136)

In practice, several very elaborate experimental devices exist for studying orientation (137). There are also some very simple procedures that can be applied. In this study, the flat-film photographic technique (Laue method) is utilized. It is a simple and commonly used procedure for studying preferred orientation in polymers. It allows one to obtain average orientation values for a deformed crystalline polymer.

However, while photographic techniques may allow one to obtain some average orientation values for a deformed crystalline polymer, there is need for a quantitative measure of this orientation. In general, the distribution in orientation is determined for a single (hkl) plane - usually a (hoo), (oko) or (ool) plane, if sufficient diffraction exists. The data are then presented either in a pole figure or may be used to determine the Hermans' orientation function, which will be defined later.

Lindenmeyer and Lustig (105) in their studies on tubular extruded polyethylene films have described the use of pole figures as a means of representing orientation. However, this procedure would be rather cumbersome for the present study due to the sample thickness used. Instead, the procedure recommended and utilized by Nadkarni and Schultz (95) is employed. The use of the Hermans' orientation function as a quantitative means of representing orientation is justified in the following discussion.

Table 4.1 illustrates the relative intensity distributions for the (110), (200), and (020) reflections for a sample micro-

TABLE 4.1. The Azimuthal Relative Intensity Distributions $I(\psi)$, for the (110), (200), and (020) Diffraction Arcs for a Sample Microtomed Near the Surface at the Location Midway from the Gate, Molded at the Higher Melt Temperature of 205.9°C

ψ^{o}	$I(\psi)_{110}$	$I(\psi)_{200}$	$I(\psi)_{020}$
0	19.10	5.60	1.01
6	19.10	5.80	1.00
12	18.30	5.35	0.88
18	17.70	5.11	0.72
24	17.50	5.50	0.50
30	16.72	5.40	0.50
36	15.45	5.20	0.40
42	13.55	4.80	0.50
48	12.00	4.70	0.52
54	10.70	4.60	0.50
60	10.38	4.90	0.50
66	9.70	4.90	0.40
72	10.00	5.40	0.40
78	10.40	5.70	0.40
84	10.72	6.05	0.30
90	10.85	6.30	0.28

tomed near the surface of a typical molding at the location midway from the gate. The molding was obtained at a melt temperature of 206°C. The table shows that the (110), (200), and (020) reflections give rise to maxima at the equator, indicating a c-axis longitudinal type of symmetry where the c-axis tends to be oriented in the flow direction (95, 122).

Table 4.2 illustrates the relative intensity distributions for the (110), (200), and (020) reflections for a sample microtomed from the core region of the same molding. The table shows that the (110) reflection does not give rise to equatorial peaks about the equator, but rather a maximum at the equator. The relative intensity distribution of the (200) reflection gives rise to a maximum at the meridian. The (020) reflection gives rise to a maximum at the equator. The self-consistency of these (hkl) reflections is indicative of an a-axis longitudinal type of symmetry where the crystallographic a-axis tends to be oriented in the flow direction (95, 122).

In general, analysis of orientations from the azimuthal intensity distributions provided evidence for a c-axis longitudinal type of orientation near the surface and for an a-axis longitudinal type of orientation in the core region of the molding. Therefore, it appears that the use of the Herman's orientation function to represent the crystalline orientation in injection molded polyethylene samples, is reasonably justified.

For the X-ray diffraction pattern arising from the oriented orthorhombic type crystals of polyethylene, it is most convenient to work with the (200) and (020) reflections. The

TABLE 4.2. The Azimuthal Relative Intensity Distributions $I(\psi)$, for the (110), (200), and (020) Diffraction Arcs for a Sample Microtomed from the Core Region at the Location Midway from the Gate, Molded at the Higher Melt Temperature of 205.9°C

ψ°	$I(\psi)_{110}$	$I(\psi)_{200}$	$I(\psi)_{020}$
0	17.60	4.15	1.29
6	16.02	3.49	1.25
12	13.75	2.90	1.15
18	12.90	2.74	1.13
24	13.00	2.90	1.05
30	12.61	3.00	0.90
36	12.31	3.30	0.85
42	12.10	4.15	0.80
48	12.00	4.70	0.65
54	11.90	5.15	0.61
60	11.82	5.65	0.69
66	11.50	6.25	0.50
72	11.50	6.80	0.50
78	12.10	7.70	0.51
84	12.35	8.00	0.50
90	12.45	8.22	0.42

Herman's orientation functions for the a and b crystallographic axes of polyethylene are defined as (51, 138)

$$f_a = (3\,\overline{\cos^2\alpha} - 1)/2 \qquad (4\text{-}12a)$$

and

$$f_b = (3\,\overline{\cos^2\beta} - 1)/2 \qquad (4\text{-}12b)$$

The angles α and β are measured between the x-axis (the flow direction) and the a and b crystallographic axes, respectively. The c-axis orientation function, f_c, is obtained from the orthogonality relationship that exists among the three mutually perpendicular directions for an orthorhombic system. That is,

$$\overline{\cos^2\alpha} + \overline{\cos^2\beta} + \overline{\cos^2\varepsilon} = 1 \qquad (4\text{-}13)$$

and, therefore

$$f_a + f_b + f_c = 0 \qquad (4\text{-}14)$$

where ε is the angle between the x-axis (the flow direction) and the crystallographic c-axis. Since the average square cosines may vary between 0 and 1, the f's may vary between $-\frac{1}{2}$ and 1. In other words, the crystalline orientation function is +1 for perfect orientation, zero for random orientation, and -0.5 for perpendicular orientation relative to the x-axis.

It should be pointed out that, although f is a convenient index to characterize orientation, one must note that it is only an average value - specifically the second moment of the whole orientation distribution for the specific set of (hkl) planes utilized. Hence, for example, two different orientation distributions could exist having the same value of $\overline{\cos^2\alpha}$ and, therefore, identical f_a's. To separate these distributions and more fully characterize the orientation envelope would require higher moments of the total distribution and, in fact, all moments would be necessary for a complete description (132). However, this is outside the scope of this study.

In general, only the second moment is defined, such that (51, 138),

$$\overline{\cos^2\alpha} = \frac{\int_0^{\pi/2} I(\alpha)\cos^2\alpha \sin\alpha \, d\alpha}{\int_0^{\pi/2} I(\alpha)\sin\alpha \, d\alpha} \qquad (4\text{-}15)$$

A similar expression is evaluated for $\overline{\cos^2\beta}$. The angles measured from the equator to a point on the (200) and (020) diffraction arcs on the pinhole photographs are designated as ψ_{200} and ψ_{020}, respectively. Intensities for the (200) and (020) reflections on the pinhole photographs are determined as a function of ψ, the azimuthal angle. These intensities are used to calculate $\overline{\cos^2\alpha}$ and $\overline{\cos^2\beta}$, respectively, using the form of the Polanyi equation (51, 138, 139) for each reflected plane, such as

$$\cos\alpha = \cos\theta_{200} \sin\psi_{200} \tag{4-16a}$$

and

$$\cos\beta = \cos\theta_{020} \sin\psi_{020} \tag{4-16b}$$

where θ_{200} and θ_{020} are the Bragg angles for the two reflections. The mean of each of the two equations gives

$$\overline{\cos^2\alpha} = \cos^2\theta_{200} \overline{\sin^2\psi_{200}} \tag{4-17a}$$

and

$$\overline{\cos^2\beta} = \cos^2\theta_{020} \overline{\sin^2\psi_{020}} \tag{4-17b}$$

Since $I(\alpha)$ and $I(\beta)$ are not obtainable from the pinhole photographs for $\alpha = 0$ to $\alpha = \theta_{200}$ and for $\beta = 0$ to $\beta = \theta_{020}$, $I(\alpha)$ and $I(\beta)$ are set equal to $I(\alpha = \theta_{200})$ and $I(\beta = \theta_{020})$, respectively, in this range as suggested by Hermans et al. (138) and Garton et al. (139). The above assumption is reasonable considering the mild levels of orientation reported here.

The difficulty is that the photographic film method does not sample the entire orientation distribution, even for uniaxial orientation. The orientation population sampled comprises a small circle on a sphere rather than a great circle, and does not sample the region close to the longitudinal axis, X. The estimation of the correction factors pertaining to the intensity distributions for the two reflected planes is summarized in

Appendix 13. By applying this procedure, it is estimated that the polar region not sampled comprises 2% of the orientation sphere surface for the (200) reflection and 5% for the (020) reflection.

By following the simple procedure described above, orientation functions describing the orientations of the crystallographic axes with respect to the flow direction are obtained.

4.5 Infrared Spectroscopy

The position of infrared bands in the spectra of polymeric solids is determined by the normal modes of vibration of the molecules. Most dichroism studies of oriented polymers have so far been made in the infrared region, where the frequencies of absorption peaks measured in wave numbers, λ^{-1}, typically range from about 6000 cm^{-1} to about 200 cm^{-1}. The mechanism of infrared absorption by polymers can generally be described in terms of the normal resonance vibrations of groups of atomic nuclei which result in an increase in their vibrational energy (140). For partially crystalline polymers, infrared absorption peaks can arise from vibrations either within the crystalline phase or the amorphous phase or both.

For a uniaxially oriented polymer sample, the absorbance (A_L) measured with radiation polarized in the stretched or flow direction may differ from the absorbance (A_T) determined for radiation polarized perpendicular to this direction. The dichroic ratio (D) is given by (141)

$$D = \frac{A_L}{A_T} = \frac{\varepsilon_L}{\varepsilon_T} \qquad (4\text{-}18)$$

where ε is the absorbance per unit thickness of the deformed sample (142).

Dichroic measurements on crystalline absorption peaks can be employed to study the orientation of certain crystallographic axes, providing that the direction of the transition moment with respect to the axes is known. In the polyethylene crystal, the well-known CH_2 rocking vibrations yield absorptions at about 720 cm^{-1} and 730 cm^{-1}, respectively. The 720 cm^{-1} band contains components due to both the crystalline and amorphous phases (141, 143). The crystalline component arises from out-of-phase CH_2 rocking modes for the two chains in the unit cell (144) and in crystals of n-paraffins it is polarized along the b crystallographic axis (143). The amorphous component is assigned to CH_2 rocking modes of chain segments in the trans conformation, and according to Synder (145) it is associated with sequences of more than four trans bonds. The 730 cm^{-1} band arises from the crystalline phase and is assigned to in-phase CH_2 rocking modes for the two chains in the unit cell (144). In n-paraffin crystals, it has been found to be polarized along the a-axis of the crystal (143). Dichroic studies on the two absorption peaks have been used to study the orientation of the two crystal axes in polyethylene, although the presence of an amorphous absorption contribution at 720 cm^{-1} complicates the analysis of this peak and requires additional information on the orientation of the amorphous phase.

In this study, the infrared band at 730 cm^{-1} is used to yield information concerning the crystalline orientation of the a crystallographic axis (f_a). By measuring the dichroic ratio of the 730 cm^{-1} band, the crystalline orientation of the a-axis is given by (141)

$$f_a = \frac{D_{730} - 1}{D_{730} + 2} \qquad (4\text{-}19)$$

where D_{730} is the measured dichroic ratio of the 730 cm^{-1} band. A comparison is made between the crystalline orientation function of the crystallographic a-axis obtained both by X-ray diffraction method and infrared dichroism of the 730 cm^{-1} band. The dichroic ratios for the 720 cm^{-1} absorption band have also been measured in this study.

4.6 Tensile Properties

In many applications, the use of plastics, rubbers, and fibers is determined primarily by their mechanical properties rather than by their chemical behavior. Mechanical behavior involves the deformation of a material by applied forces (146). In the present study, it is important to know how the observed differences in molding behavior of the resins and in the microstructural characteristics of moldings are reflected by differences in the properties of the molded specimens. With the aim of understanding some of the effects, the tensile properties of microtomed sections of the moldings were measured.

Probably the most widely used mechanical test is the tensile stress-strain test. Tensile measurements are generally made by stretching the specimen at a uniform rate while simultaneously measuring the force on the specimen. The test is continued until the specimen breaks. Often, the change in length is determined from measurements of the separation of the jaws or clamps holding the specimen. Figure 4.3 illustrates a typical tensile stress-strain curve. The experimental curve gives a force F as a function of the time or the change in length $(l - l_o)$, since the time and amount of elongation are equivalent. The experimental curve must be replotted to give a curve of stress, σ against strain, ε. The strain as a function of time is given by

$$\varepsilon = \frac{l - l_o}{l_o} = \frac{kt}{l_o} \qquad (4\text{-}20)$$

where l is the length of stretched sample, l_o is the original length of specimen, k is the rate of extension and t is the time. Sometimes the strain is better replaced by the so-called "true strain" defined by

$$\varepsilon = \ln(l/l_o) \qquad (4\text{-}21)$$

which arises from

$$\varepsilon = \int_{l_o}^{l} \frac{dl}{l} = \ln(l/l_o) \qquad (4\text{-}22)$$

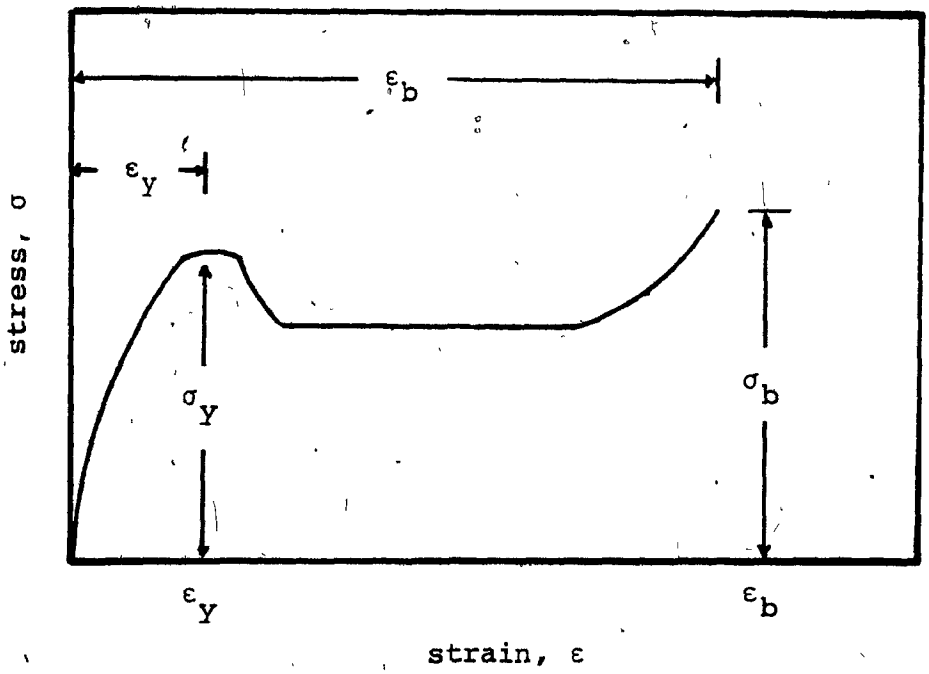


FIGURE 4.3. A Schematic Stress-Strain Curve (Reference 146)

Generally, the stress at any time during test is calculated on the basis of the original cross-sectional area. However, the cross-sectional area of a specimen decreases as it is stretched so that the true stress is greater than the ordinarily calculated nominal stress. The true stress is the force per unit of cross-sectional area at any time (or elongation). If the volume of the specimen remains constant during stretching, then the area at any time may be expressed as:

$$A = A_o l_o / l \qquad (4\text{-}23)$$

where A_o is the original area and A is the area at any time during elongation.

The tensile or Young's modulus, Y, for a material which obeys Hooke's law, is defined as the ratio of nominal tensile stress to nominal tensile strain, or

$$Y = \frac{\text{tensile stress}}{\text{tensile strain}} = \frac{\sigma}{\varepsilon} \qquad (4\text{-}24)$$

i.e.

$$Y = \frac{\sigma}{\varepsilon} \qquad (4\text{-}25)$$

therefore,

$$Y = \frac{F/A}{\Delta l / l_o} = \frac{\sigma}{\varepsilon} \qquad (4\text{-}26)$$

or

$$\sigma = \varepsilon Y \qquad (4\text{-}27)$$

Other terms such as yield stress σ_y, elongation at yield ε_y, ultimate strength or tensile strength σ_b, and ultimate elongation or elongation at break ε_b, which are useful terms in the discussion of stress-strain curves are illustrated in Figure 4.3.

4.7 Integration of the Results of Experimental Measurements

As already mentioned in Section 4.1, the polycrystalline material is not completely crystalline. From the density, one can deduce the volume fraction crystallinity. The variability of polyethylene density (volume crystallinity) is a good indicator of the crystallization phenomena during injection molding. Furthermore, during the molding cycle polymer melt elements are subjected to both shear and elongational stresses. The net effect of these stresses is to orient the polymer chains in the direction of the applied stress. The resulting combined morphology and orientation, in turn, markedly influence the end-use mechanical properties of the molded part. Since the resulting morphology and orientation developed in injection molded parts are rather complex such that a single technique cannot completely characterize the microstructure in such a system, the co-ordinated application of a number of the techniques is employed. Furthermore, it is intended that the techniques employed, will separate the orientation developed in polyethylene injection molded parts into crystalline and amorphous components.

The intrinsic sonic moduli are first determined by studying the change in the sonic modulus of compression molded samples with crystallinity as described in Section 5.3.5. The material constants are then determined by the use of Equation (4-6). Once the material constants for the material have been determined, the sonic modulus of injection molded samples is then examined, as described in Section 5.3.4. The sonic modulus of an oriented sample is a measure of the total orientation of the sample. It is a function of the orientation of both the crystalline and amorphous regions as well as that of the amount of each phase present in the sample (136).

Since the intrinsic lateral moduli are now established, the amorphous orientation function, f_{am}, is calculated for the injection molded samples by the use of Equation (4-9), from experimental values of the sonic modulus (E_{or}), density (X_c), and the crystalline orientation function (f_{cr}) determined by X-ray diffraction (as described in Section 4.2).

The f_{am} values, in turn, are used together with the birefringence expression (Equation (4-11)) to estimate the intrinsic birefringences for both the crystalline and amorphous phases. Once the intrinsic birefringence values are established, the combination of birefringence and X-ray diffraction may then be used to resolve the birefringence of injection molded polyethylene samples into its crystalline and amorphous components. Similar orientation studies have been carried out by Samuels and co-workers (60-63) and Stein and co-workers (51-55) on

isotactic polypropylene films and fibers and on low density polyethylene films, respectively.

Recently, a mechanical theory (147-149) has been presented which relates the material compliances to the same internal anisotropic structure. A consequence of the theoretical development is the emergence of a compliance equation which predicts the mechanical properties of an anisotropic polymer, once the crystallinity and orientation functions are known. It must be pointed out that only the final result of the model is presented here and that a more detailed description and derivation of the model is outlined in reference (149). The proposed two-parameter model is given as:

$$S_{33} = X_c A_c(1 - f_{cr}) + (1 - X_c)A_{am}(1 - f_{am}) \quad (4\text{-}28)$$

where S_{33} is the bulk compliance in the draw direction, X_c is the crystalline volume fraction, f_{cr} and f_{am} are the orientation functions for the crystalline and amorphous phases, respectively, and A_{cr} and A_{am} relate to the intrinsic compliances of the crystalline and amorphous phases, respectively.

Since the bulk compliance is the reciprocal of Young's modulus, then

$$S_{33} = (1/E_s) \quad (4\text{-}29)$$

where E_s is the Young's modulus of the oriented sample. Furthermore, the intrinsic compliances for the crystalline and amorphous phases are defined as

$$A_c = \frac{10}{15}\left(\frac{1}{E_c^o}\right) \tag{4-30}$$

and

$$A_{am} = \frac{10}{15}\left(\frac{1}{E_{am}^o}\right) \tag{4-31}$$

where E_c^o and E_{am}^o are the intrinsic modulus values for both the crystalline and amorphous phases, respectively.

The above model will be employed for predicting the distributions of mechanical properties in injection moldings by utilizing the quantitative orientation and crystallinity distributions, obtained by integrating the results of other non-mechanical techniques, as described earlier.

CHAPTER 5

EXPERIMENTAL

This chapter describes the materials used in the study and the preparation of the moldings which will be used for the determination of microstructure. A detailed description of the experimental apparatus and the procedure for each of the techniques employed for microstructure determination, are presented in the following sections.

5.1 Materials

In this study, two commercial and readily available injection molding grade thermoplastic resins were used. The two high density polyethylene resins, designated as EX 1 and EX 2, were supplied by DuPont of Canada Limited. Some of the properties of the resins are tabulated in Table 5.1. Figures 5.1 and 5.2 show the dependence of the true shear viscosities of the two resins on both the true shear rate and temperature (121). The shear viscosity data were obtained with an Instron Universal Testing Instrument, floor model (TT-CM-L) in conjunction with an Instron capillary rheometer type MCR, designed for use with the floor model of the Instron Tester. For all temperatures and over the entire range of true shear rates, but especially at higher shear rate levels, resin EX 2 exhibits slightly higher shear viscosity values than resin EX 1. These results suggest that resin EX 2 will fill the mold cavity more slowly than resin

TABLE 5.1. Physical Properties of Materials

Physical Properties	Resin Material		Source
	EX 1	EX 2	
$\bar{M}_W$ (g/mole)	8.92×10^4	7.45×10^4	(1)
$\bar{M}_N$	1.75×10^4	2.23×10^4	(1)
$\bar{M}_W/\bar{M}_N$	5.09	3.33	(1)
Density (g/cm^3)	0.959	0.962	(1)
Melt Index (g/10 min)	8.07	7.40	(1)
Melting Range (^oC)	113-146^oC	113-146^oC	(2)
Average Specific Heat			(3)
c_p solid, cal/g/^oC	0.569	0.607	
c_p melt, cal/g/^oC	0.589	0.587	
Average Thermal Conductivity			(3)
k_s solid, cal/cm/^oC/s	8.64×10^4	8.24×10^4	
k_m melt, cal/cm/^oC/s	6.24×10^4	6.25×10^4	
Average Thermal Diffusivity			(3)
α_s solid (cm^2/s)	20.6×10^4	18.9×10^4	
α_m melt (cm^2/s)	12.7×10^4	12.9×10^4	
Power Law Index, n	0.800	0.822	(2)
$\Delta E/R$ ($1/^oK$)	2338	2167.4	
A ($g/cm/s^{n-2}$)	92.76	139.9	

Note: $\eta_T = A \exp(E/RT) \dot{\gamma}_T^{n-1}$

where η_T is in poise, $\dot{\gamma}$ in s^{-1} and T in ^oK

Sources: (1) DuPont of Canada Limited
(2) Reference (121)
(3) Measurements made in this laboratory, not reported elsewhere.

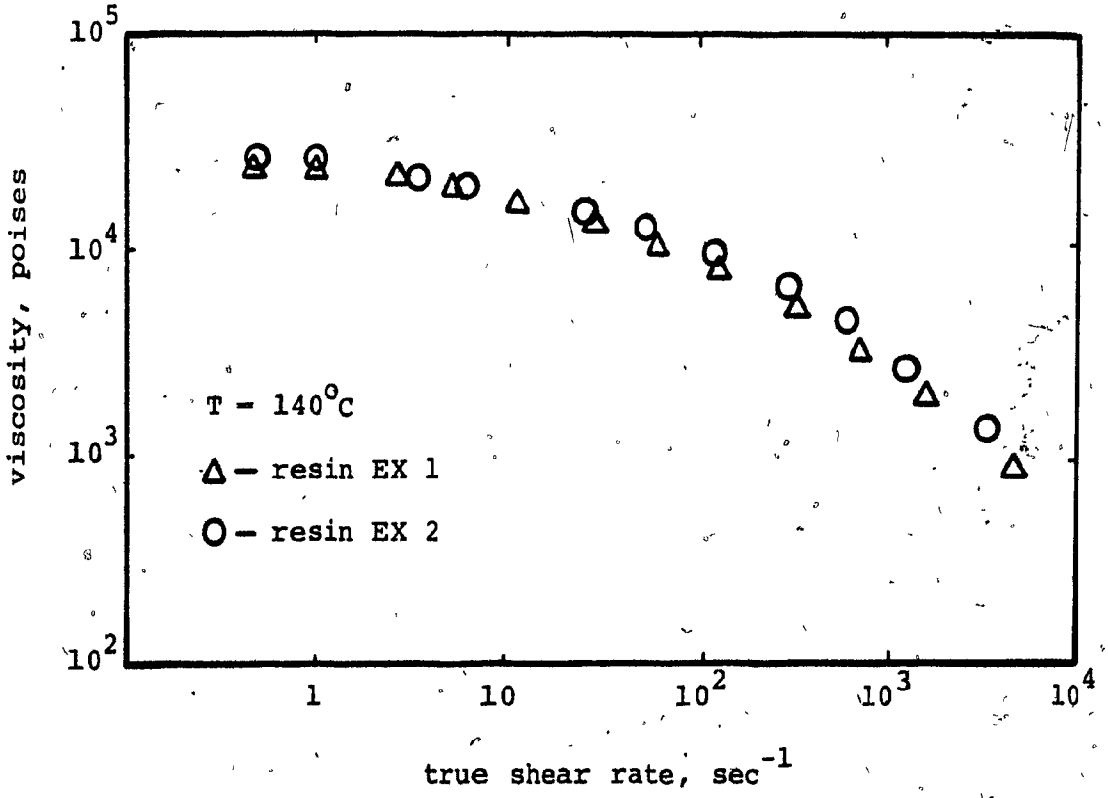


FIGURE 5.1. Shear Viscosity as a Function of Shear Rate

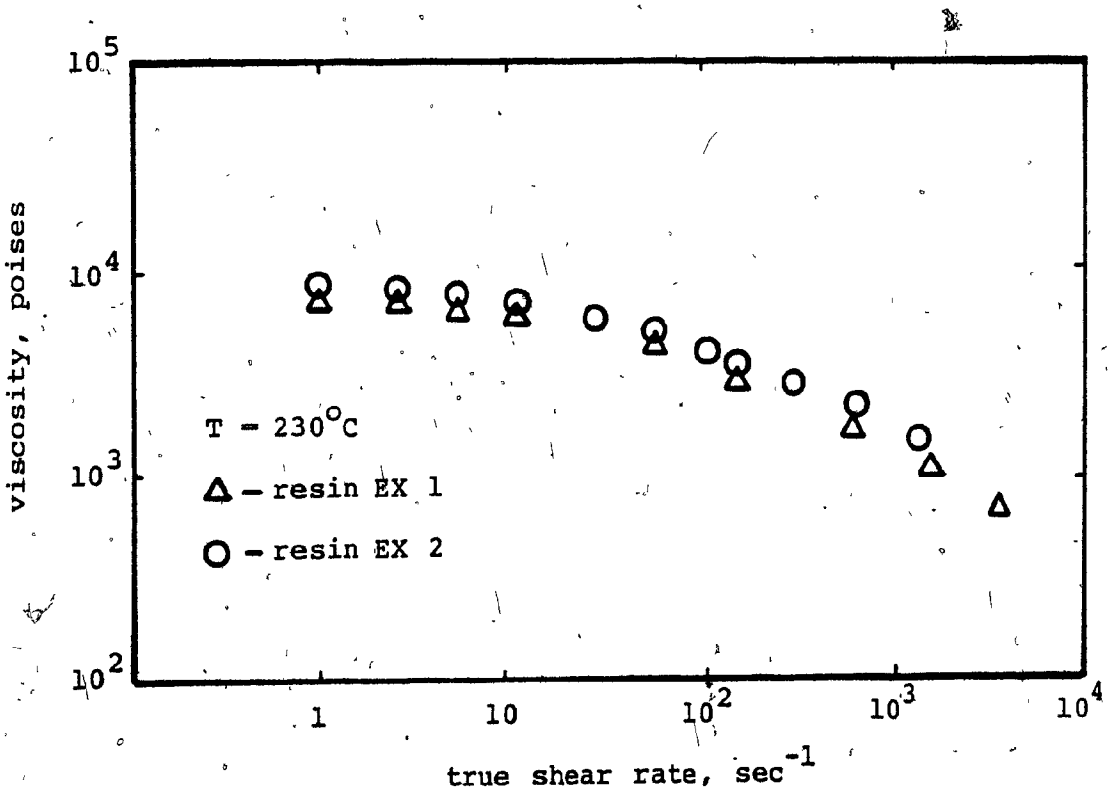


FIGURE 5.2. Shear Viscosity as a Function of Shear Rate

EX 1 and alternately, resin EX 2 will require higher injection pressures to achieve the same filling rate. This is consistent with the pressure-time profiles obtained for the two resins molded under identical conditions, presented in Section 6.1.

The shear viscosity behavior of the two resins under a constant shear rate of 10 sec^{-1} at 140°C is shown in Figure 5.3 (150). The increases in viscosity at long durations of time, that is, 100 to 200 seconds or at large strains may be attributed to the crystallization of the molten samples under shear. The comparison of the shear-induced crystallization behavior of the resins shows that resin EX 2, which has the higher shear viscosity, tends to exhibit a higher tendency for crystallization under shear. Thus, it is expected that resin EX 2 would show a larger tendency for crystallization during the filling stage. Since the highest shear rates and lowest temperatures occur near the wall, shear crystallization effects would predominate in this region. Thus, it would be expected that the enhanced cooling, due to the higher thermal conductivity of the thin crystalline skin of resin EX 2 would contribute to increasing the viscosity difference between the two resins. Ultimately, this should contribute to a widening of the gap between the filling times for the two resins.

The pressure-volume-temperature (P-V-T) characteristics of the two resins are shown in Figure 5.4 (121). Generally, the density values for resin EX 1 are higher than those observed for resin EX 2, for the recorded pressure range. The sudden changes in density observed may be associated with the crystal-

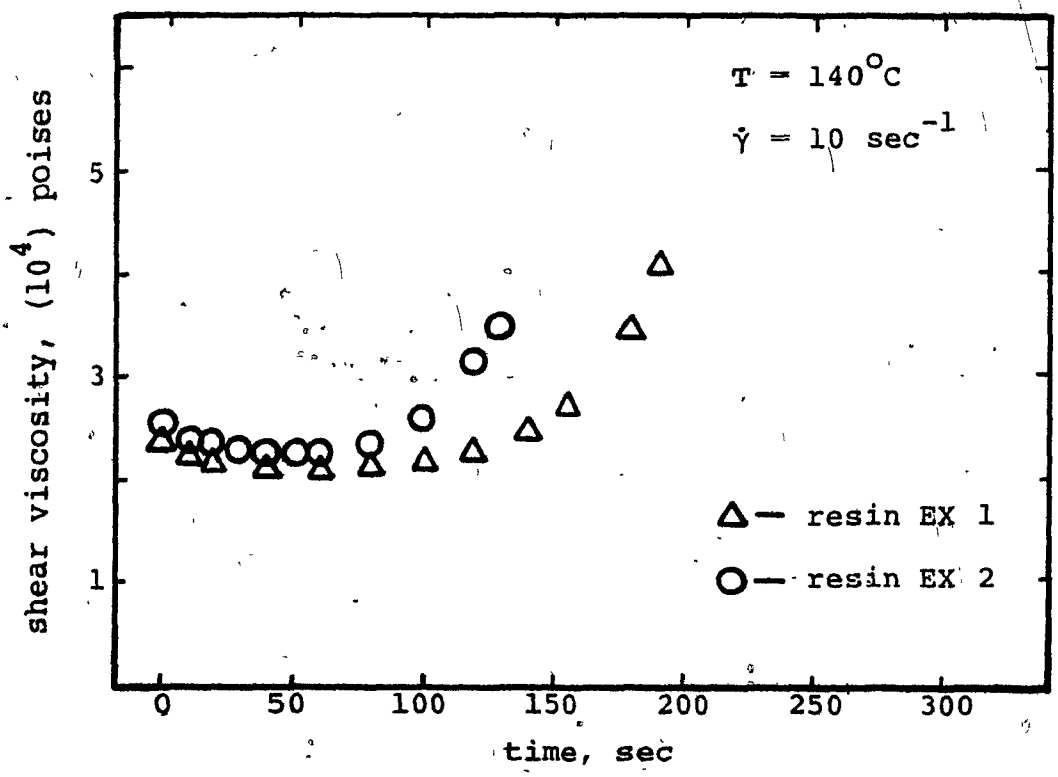


FIGURE 5.3. Crystallization of Resins EX 1 and EX 2 Under Shear at 140°C

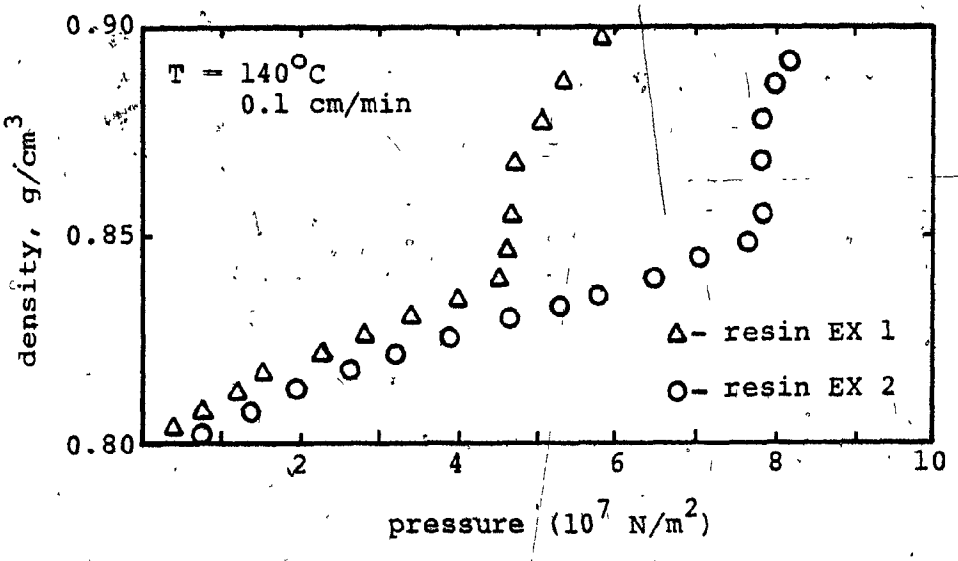


FIGURE 5.4. Pressure-Volume-Temperature (P-V-T) Diagram

lization of the melt under pressure at a temperature of 140°C, which is higher than the temperature for the onset of crystallization at atmospheric pressure. Furthermore, as shown in Figure 5.4, the crystallization of resin EX 1 commences at a pressure level of 4×10^7 Newtons/m^2 whereas resin EX 2 begins to crystallize at 7.8×10^7 Newtons/m^2. These results suggest that resin EX 1 will crystallize more readily than resin EX 2 under identical packing and cooling conditions in the injection molding process.

It should be noted that the observed differences in the crystallization behavior of resins EX 1 and EX 2 are typical and in accordance with the following generalization. Resins with higher viscosity tend to crystallize more readily under shear, but less readily under pressure than resins with lower viscosity (150).

5.2 Preparation of the Moldings

Moldings were prepared with the dual purpose of obtaining suitable moldings for microstructure characterization and at the same time to acquire molding data needed to supplement the work being carried out simultaneously in the mathematical modeling of the injection molding process.

5.2.1 Injection Molding Machine

The moldings were prepared with a Danson Metalmec (Model 60-SR, 2-1/3 ounce, 68 ton) reciprocating screw injection molding machine. The barrel is divided into two heating zones.

Each zone is independently heated by an electrical heating band. The two zone temperatures are controlled within $\pm 3^{o}C$ with respect to the set temperatures. Although the machine is equipped for operation in automatic, semi-automatic and manual modes, only the manual mode of operation was used in the preparation of the moldings. The injection molding machine is shown in Figure 5.5.

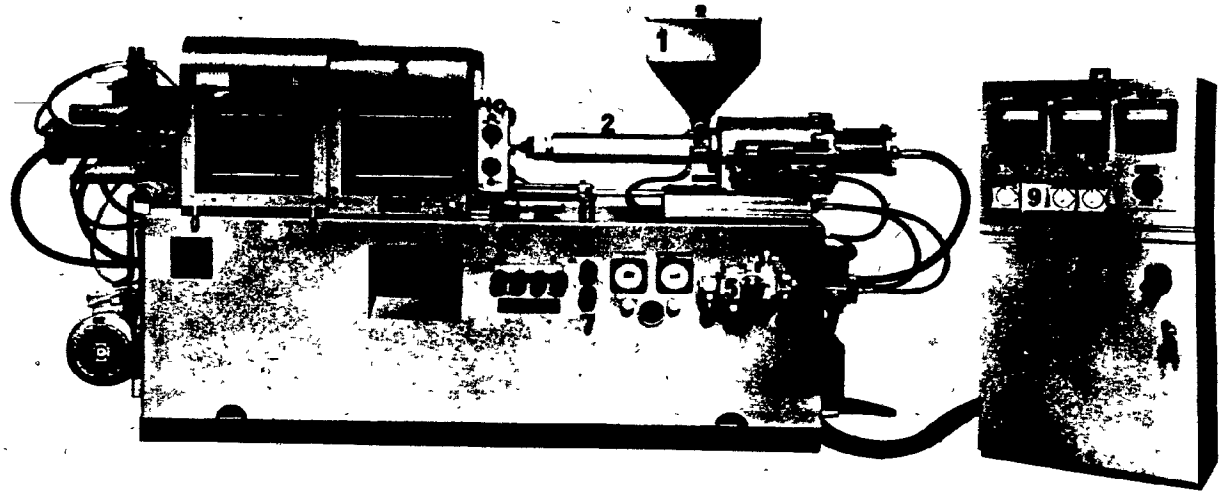
The injection pressure during filling is regulated by the injection speed and injection pressure valves. These valves regulate the hydraulic pressure which is applied to the screw. The injection pressure depends upon the dimensions of the runner and cavity as well as upon material properties. The maximum pressure which is developed during the packing stage is regulated by means of the holding pressure valve and the shot-size limit switch.

A linear displacement transducer, Model 4709, manufactured by Markite, was installed on the injection molding machine to monitor the displacement of the screw during the injection molding cycle. The transducer was excited by a 10 volts excitation voltage supplied by a Sensotec signal conditioning unit.

5.2.2 Rectangular Mold Cavity

The rectangular mold with cavity dimensions 12.5 cm x 2.5 cm x 3.18 mm, was employed to mold the rectangular test specimens. The cavity had a rectangular gate which was 3.18 mm wide and 1.59 mm deep.

FIGURE 5.5. Danson Metalmec Reciprocating-Screw Injection Molding Machine



1. HOPPER
2. SCREW BARREL
3. CLAMPING UNIT
4. SHOT SIZE SWITCHES
5. INJECTION SPEED VALVE
6. INJECTION PRESSURE VALVE
7. HOLD PRESSURE VALVE
8. TEMPERATURE CONTROL
9. AUTOMATIC TIMERS
10. MANUAL INJECTION SWITCHES

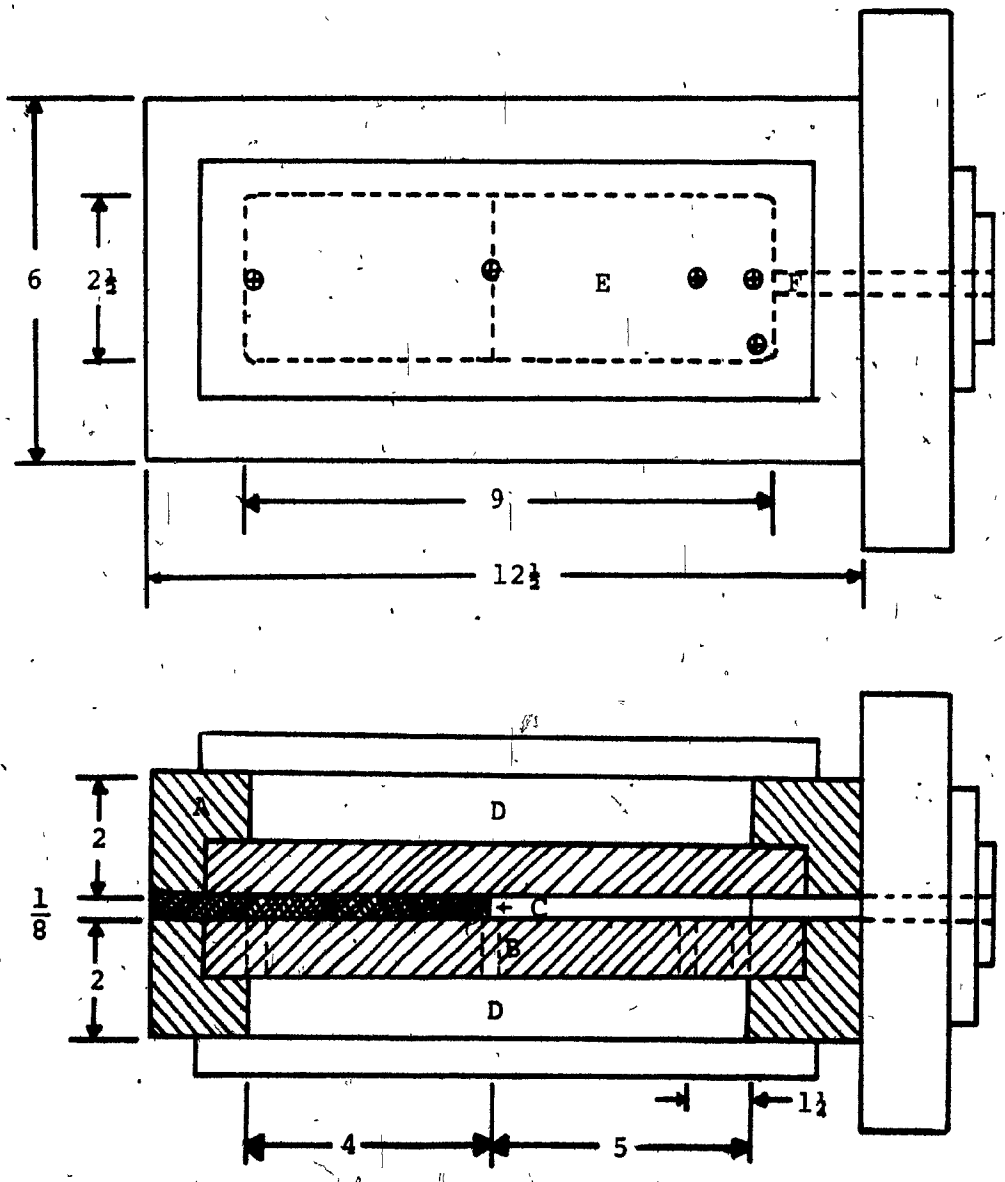
The mold assembly, as shown in Figure 5.6, essentially consisted of an inner stainless steel plate (shim), 3.18 mm thick, from which the rectangular cavity was cut out and two stainless steel cover plates each of which being 2.54 cm thick. The inner surfaces of the two cover plates were highly polished and served as the mold walls. The plate/shim/plate assembly in turn was placed between two heavy mounting frames and the whole assembly was fastened together by twelve 5/8 inches diameter allen-cap screws. The design of the mounting frames was such that the 2.54 cm thick plates, when mounted, remained recessed and permitted the attachment of two rectangular Plexiglas plates over them. The mold assembly, originally designed by Doan (151), was to be cooled by water circulation. However, the high water pressures required to circulate the water caused leakage into the mold cavity. Instead, high pressure air, 55 ± 5 psig, was circulated through the Plexiglas plates to maintain the mold at a constant temperature. The fluctuations in the air temperature (±5°C) made it necessary to heat the air supply by means of circulation through an electrical heater. The air temperature was kept constant at 35 ± 0.5°C.

An Iron-Constantan thermocouple was used to measure the temperature of the surface of the mold cavity. The thermocouple was calibrated by immersion in an ice-distilled water mixture and in boiling distilled water.

Four threaded holes were drilled into the mold to permit the attachment of melt pressure transducers flush with the inner wall of the mold. As shown in Figure 5.6, three of the

FIGURE 5.6. Schematic Drawing of Mold Assembly (dimensions in inches)

A. Frame
B. Steel Wall
C. Shim
D. Cooling Jacket
E. Mold Cavity
F. Gate
⊕ Transducer Location
● Thermocouple Location



holes were located along the centreline from the gate. The fourth was located at the off-centre position, near the gate.

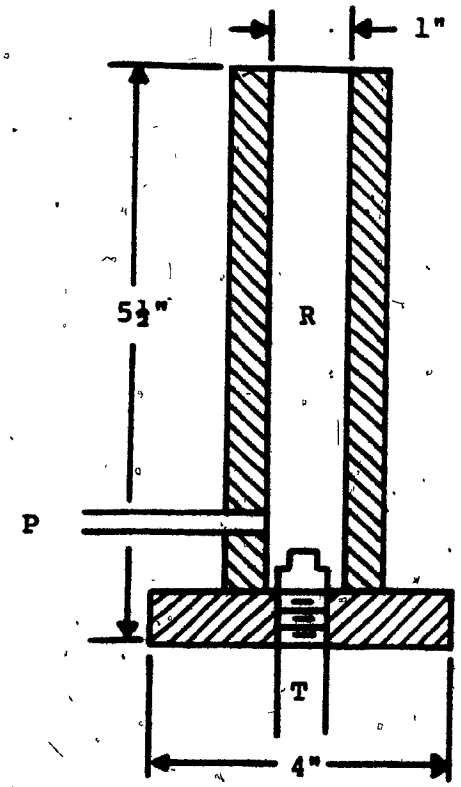
5.2.3 Calibration of Transducers

As mentioned in the previous section, transducers were mounted flush with the inner surface of the mold cavity in order to monitor the melt pressure at various locations within the mold cavity during the entire molding cycle. The four strain gauge transducers, Model PT4-22A-20M-6/18, manufactured by Dynisco, were capable of measuring melt pressures up to 1.38×10^{10} N/m^2 (20,000 psi). The sensing tip of each transducer has an active diameter of 0.80 cm, and detects pressure through four foil strain gauges connected in a wheatstone bridge-type arrangement. It has an input resistance of 346.5 ohms, an output resistance of 360 ohms, and requires a 6 volts excitation. The system incorporates a temperature compensating resistance to compensate for effects of temperature variation on pressure measurements. The transducers were used in conjunction with two signal conditioning units, Model SCA-43, manufactured by Sensotec. The signal conditioning units have variable resistors for balancing the transducer strain gauges, variable gain for signal amplification, an internal calibration shunt resistance, and supply excitation voltages to the transducers.

Calibration of the pressure transducers was performed with the aid of a specially designed pressure calibration apparatus shown in Figure 5.7. The transducer was mounted to the base of the cylindrical reservoir which was filled with Duckhams

FIGURE 5.7. Pressure Calibration Apparatus

P. Pressure Gauge
T. Transducer



Hypoid 80 gear oil. The oil was compressed by a piston which was driven by the crosshead of the Instron Universal Testing machine. The transducer output was recorded on a Hewlett-Packard strip-chart recorder (Model 7100B). The pressure was also measured independently by means of the Instron load cell and by means of a pressure gauge. A typical calibration curve is shown in Figure 5.8. The calibration data are tabulated in Appendix 2. For each transducer, the calibration data were correlated by means of a linear regression using a Texas Instruments calculator (Model TI 58). The regression equations are given in Table 5.2.

5.2.4 Molding Procedure

Each run was commenced by setting the barrel temperatures at the desired levels on the controllers, and allowing one hour for complete thermal stabilization of the injection unit. At the same time, cool air at the desired temperature and flow rate was circulated through the Plexiglas cover plates so as to achieve uniform temperature of the mold. Cold water was circulated around the hopper assembly to prevent preplasticizing of the resin pellets. Polymer pellets were then fed from the hopper into the barrel where they were plasticized and conveyed forward to the melt reservoir section. A few injections were made into the open air to clean the barrel from any old material, and to test the injection system.

While the barrel temperature was stabilizing during start-up, the strip-chart recorders and the signal conditioning units

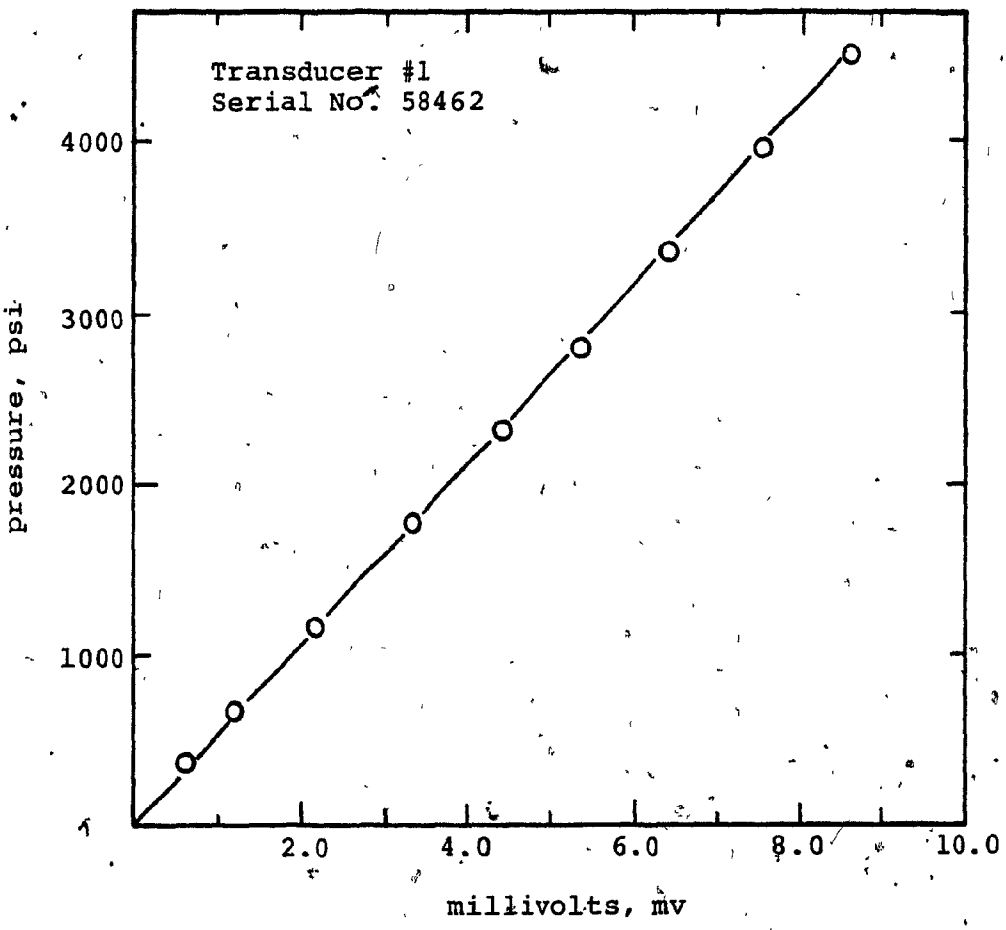


FIGURE 5.8. Typical Pressure Transducer Calibration Curve

TABLE 5.2. Regression Coefficients for Transducer Calibration Equations

Serial Number	Equation
58462	P_1 = 531.3 x (mV) psi
68470	P_2 = 1062.5 x (mV) psi
62849	P_3 = 523.4 x (mV) psi
65016	P_4 = 1043.7 x (mV) psi

were also switched on to allow one hour of warming up.

The control valves for injection pressure, holding pressure, screw rotational speed and the cam for the shot size control were set at predetermined positions and were kept constant throughout the molding experiments.

When all the components of the system were ready, the material was then plasticized and injected again several times into the open air to purge the barrel. The recorders were then run at the appropriate speeds (0.2-2 in/sec) and the melt was injected into the mold using the manual mode. During the whole mold cycle, the packing pressure was held until the pressure in the cavity dropped to zero. There are two reasons for maintaining the packing pressure during the molding cycle. Firstly, since there was no check valve available in the nozzle, reverse flow would be prevented. Secondly, a sudden drop in cavity pressure could lower the crystallization temperature of the melt inside the cavity, thus giving rise to the remelting of some portions of the already solidified polymer. This would have added to the complexity of the microstructural analysis.

For each resin at a given molding condition, about 40 rectangular specimens were molded. After the required number of specimens were molded from a resin, the hopper was emptied and the barrel was purged thoroughly. Table 5.3 summarizes the pertinent operating conditions for moldings made from the two resins EX 1 and EX 2. The moldings thus made were stored for at least 24 hours in an air-conditioned laboratory at 23°C ± 2°C and 50% ± 5% relative humidity for conditioning prior to testing.

TABLE 5.3. Molding Conditions

Resin	Barrel Temperature °F (°C)		Mold Temperature (°C)
	Front Zone	Rear Zone	
EX 1	380 ± 5 (193)	320 ± 5 (160)	35
EX 2	380 ± 5 (193) 420 ± 5 (216)	320 ± 5 (160) 320 ± 5 (160)	35 35

The output voltage response of the pressure and displacement transducer, recorded on the strip-chart recorder, were converted into actual pressures and displacement, through the calibration equations tabulated in Table 5.2.

5.3 Determination of Microstructure

Microstructure developed in an injection molded article is reflected by morphological characteristics and orientation distributions. A variety of techniques are employed to quantitatively study the microstructure with the purpose of providing the link between molding behavior and the ultimate properties of the injection molded parts.

5.3.1 Preparation of Microtomed Sections

A molded specimen from each resin or a particular set of molding conditions, was chosen on the basis of exhibiting a molding behavior similar to the average characteristics of the population of the moldings from each resin or from the particular set of molding conditions.

Two different rectangular pieces were marked off with a felt pen, as shown in Figure 5.9. The small rectangular pieces (8.0 mm x 8.0 mm x 3.18 mm), as shown in Figure 5.9, indicate the positions from which thin sections are microtomed in the perpendicular-to-flow direction along the transverse axis (YZ-plane) of the molding, for photomicrography. The dotted sections (4.0 cm x 4.0 mm x 3.18 mm) indicate the positions from which thin sections are microtomed in the parallel-to-flow direction

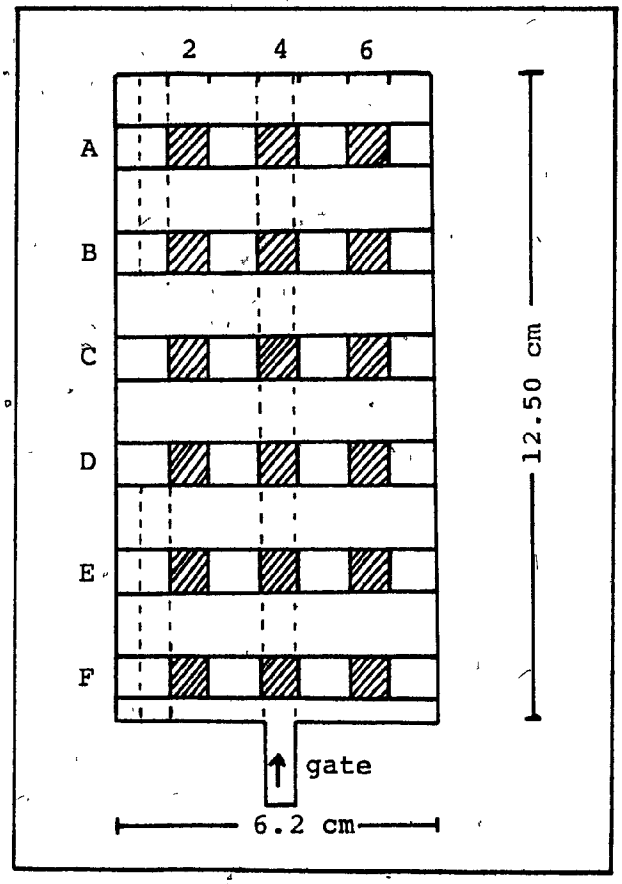


FIGURE 5.9. Position Designations on Molded Specimens

along the longitudinal axis (XY-plane). Prior to microtoming, the rectangular pieces were cut out by means of a fine-tooth coping saw. In order to avoid possible disorientation of the polymer chains, care was taken to minimize heat generation during cutting.

Microtoming was carried out on a large Sliding Reichert Microtome, Model OmE. The knives were supplied by American Optical Co. The block, onto which the knife was clamped, was constructed so that it permitted both a planar rotational adjustment (cutting angle), and a vertical angular adjustment (knife angle) of the knife. The specimen mounting clamp was the "Naples" type which permitted a three-way adjustment of the position of the sample, that is, vertically, north-south angularly, and east-west angularly. Figure 5.10 is a photograph of the Reichert Microtome used in the study.

The microtomed thicknesses may be adjusted automatically or manually. For a microtomed thickness of 1-30 microns, the automatic specimen feed may be utilized. The section thickness is adjusted by means of a pin, in 1-micron steps over the 1-30 microns range. After each section is cut, the knife block is moved to press on the pin at the end of the knife track and is moved vertically down by a distance, corresponding to the set thickness on the pin. For section thicknesses greater than 30 microns, the section thickness is adjusted by rotating a calibrated drum.

In order to microtome thin sections in the YZ-plane from the small rectangular pieces (8.0 mm x 8.0 mm x 3.18 mm) as

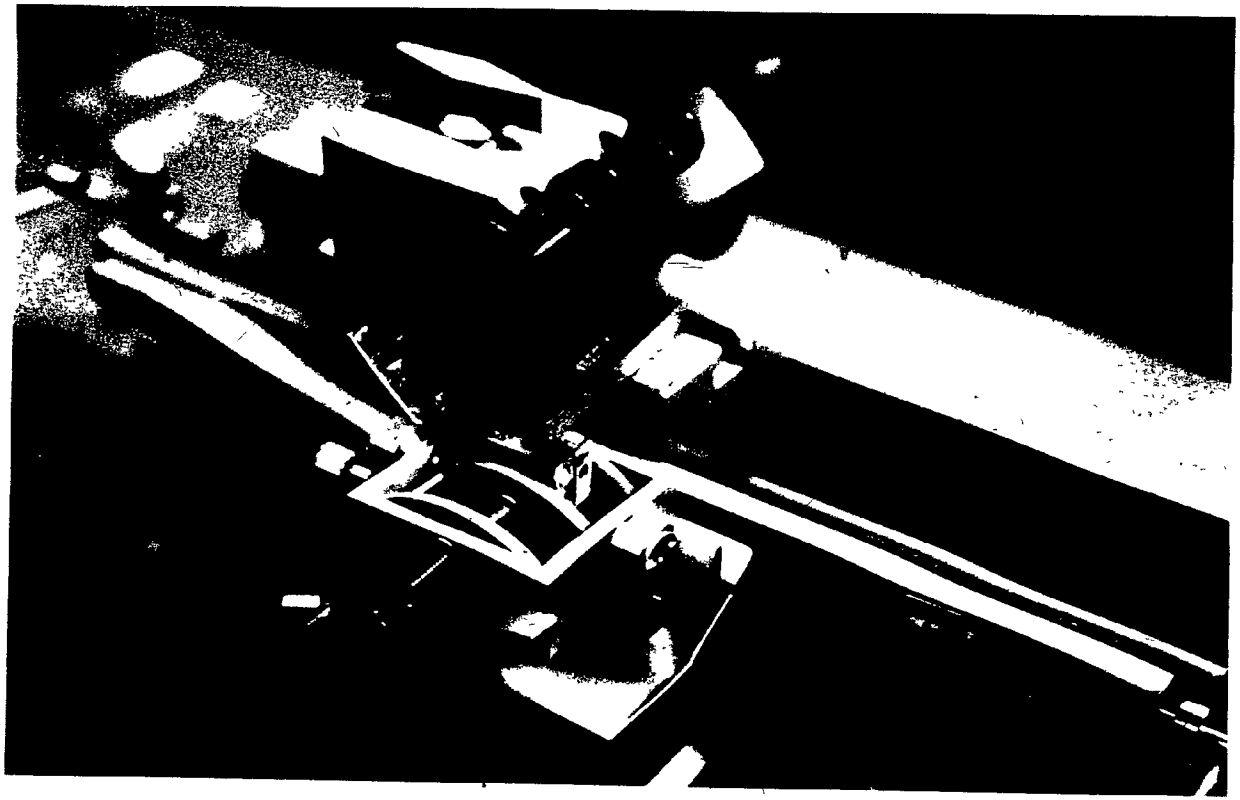


FIGURE 5.10. Photograph of Reichert Microtome

shown in Figure 5.9, these pieces were large enough to be fastened onto the Naples clamp without requiring any special mounting procedures. The microtomed sections were 20 microns thick employing the automatic feed of the microtome.

However, in the case of microtoming in the direction parallel to the XY-plane, the long rectangular pieces (4.0 cm x 4.0 mm x 3.18 mm) cut from the moldings (as shown in Figure 5.9) were glued onto smooth-faced rectangular Plexiglas pieces (5 cm x 0.7 cm x 1.0 cm). The glue used was Duro Super Glue-3, manufactured by Loctite Canada Inc.

After lubricating the microtome tracks, both the knife and the specimen were securely mounted on their respective microtome clamps. The knife position was adjusted such that, with respect to the specimen, the cutting angle was 90°, and the knife angle was 30°. The specimen position was adjusted such that during microtoming the sections cut would be in the desired plane rather than at some random angle to that plane. For this purpose, it was sufficient to have the specimen surface parallel to that of the knife block. In turn, the surface of the latter had the same horizontality as the knife edge. First, a course adjustment was made by balancing a small surface leveler on the specimen. Then one end of a highly polished bar magnet was placed on the steel knife block such that one end was protruding directly above the specimen. The final adjustment was made by making the surface of the specimen flush with the bottom surface of the bar magnet.

In the case of sections being microtomed in the XY-plane, it was necessary to keep accurate measure of their position as a function of depth from the surface of the specimen. After cutting the first 5-10 sections (200-400 μm), the thicknesses of the sections were measured using a Combimike Micrometer (No. 159-211) with an accuracy of 0.0025 mm, supplied by Mitutoyo MFG. Co., Ltd., Japan. These measurements, along with the initial thickness of the specimen, would then be used to calculate by linear interpolation the depth position of each of the microtomed sections.

Actual sectioning was accomplished by manually passing the knife block assembly over the specimen. For obtaining sections of uniform thickness, it was best to make the cutting motion as smooth and as continuous as possible. Simultaneous to the cutting action, a pair of fine-nosed tweezers were used to guide the section being cut against the flat portion of the knife. The microtomed sections were then stored between microscope slides for future testing.

As mentioned above, the sections microtomed in the YZ-plane were used for obtaining photomicrographs. The sections microtomed in the XY-plane were used first to measure sonic velocity, after which a small section (1.0 cm x 4 mm) was further cut from each of the long thin microtomed sections. The small sections corresponded to the positions as shown in Figure 5.11. The small sections were used in the measurements of birefringence, wide-angle X-ray diffraction, infrared dichroic ratio, and density. The sequence of measurements performed on the microtomed

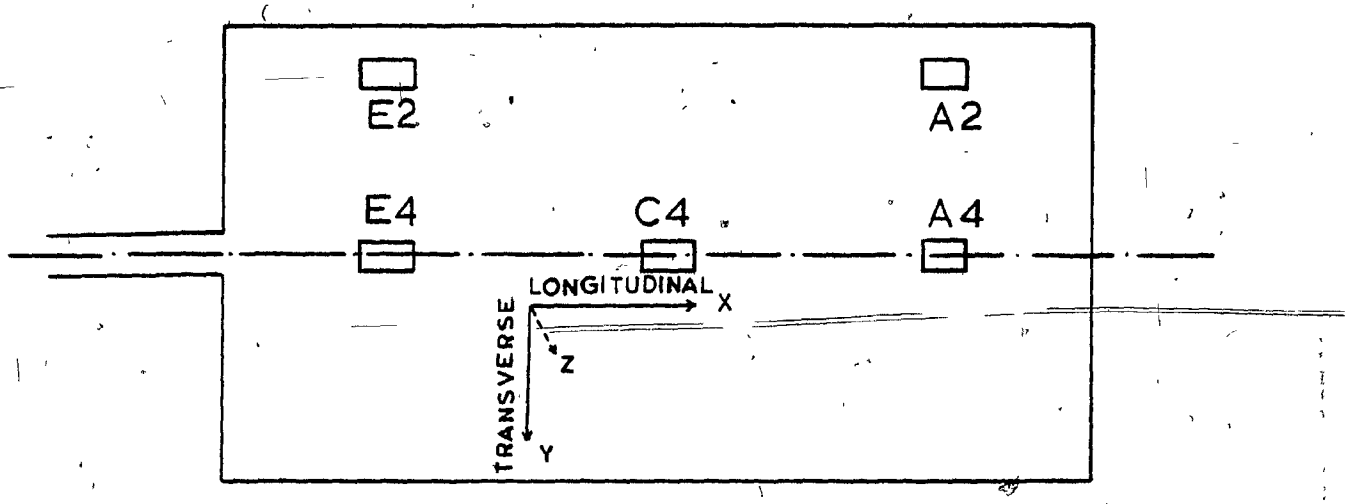


FIGURE 5.11. Designated Positions for Microstructural Studies in the Depth Direction of the Moldings

sections (XY-plane) is shown schematically in Figure 5.12. In the case of tensile measurements, long thin sections were microtomed from corresponding cut sections of another molding which exhibited a molding behavior similar to the average characteristics of the population of the moldings.

5.3.2 Photomicrography

When an electromagnetic beam, characterized by a sinusoidally varying electric field, $\vec{E}$, is incident on a sample, the electric field causes an electrical polarization, $\vec{P} \cdot \vec{P}$, and the electric field is parallel only if the material is isotropic. For an anisotropic material, the electrical polarization vector ($\vec{P}$) is related as $\vec{P} = K \vec{E}$, where K is a tensor, capable of rotating the direction of the electrical polarization vector ($\vec{P}$) with respect to the electrical field vector ($\vec{E}$). The direction of the polarization is determined by the bonding and symmetry of arrangement of atoms within the material. Measurement of optical anisotropy depends on the fact that a given material has associated with it unique optical properties determined by its polarizability. Different morphological aggregates give rise to different optical properties. That is, the spherulites when viewed under polarized light give rise to the characteristic Maltese cross pattern (15).

5.3.2.1 Apparatus

For the photomicrography study, a Reichert "Zetopan-Pol", large polarization microscope was employed. The basic compo-

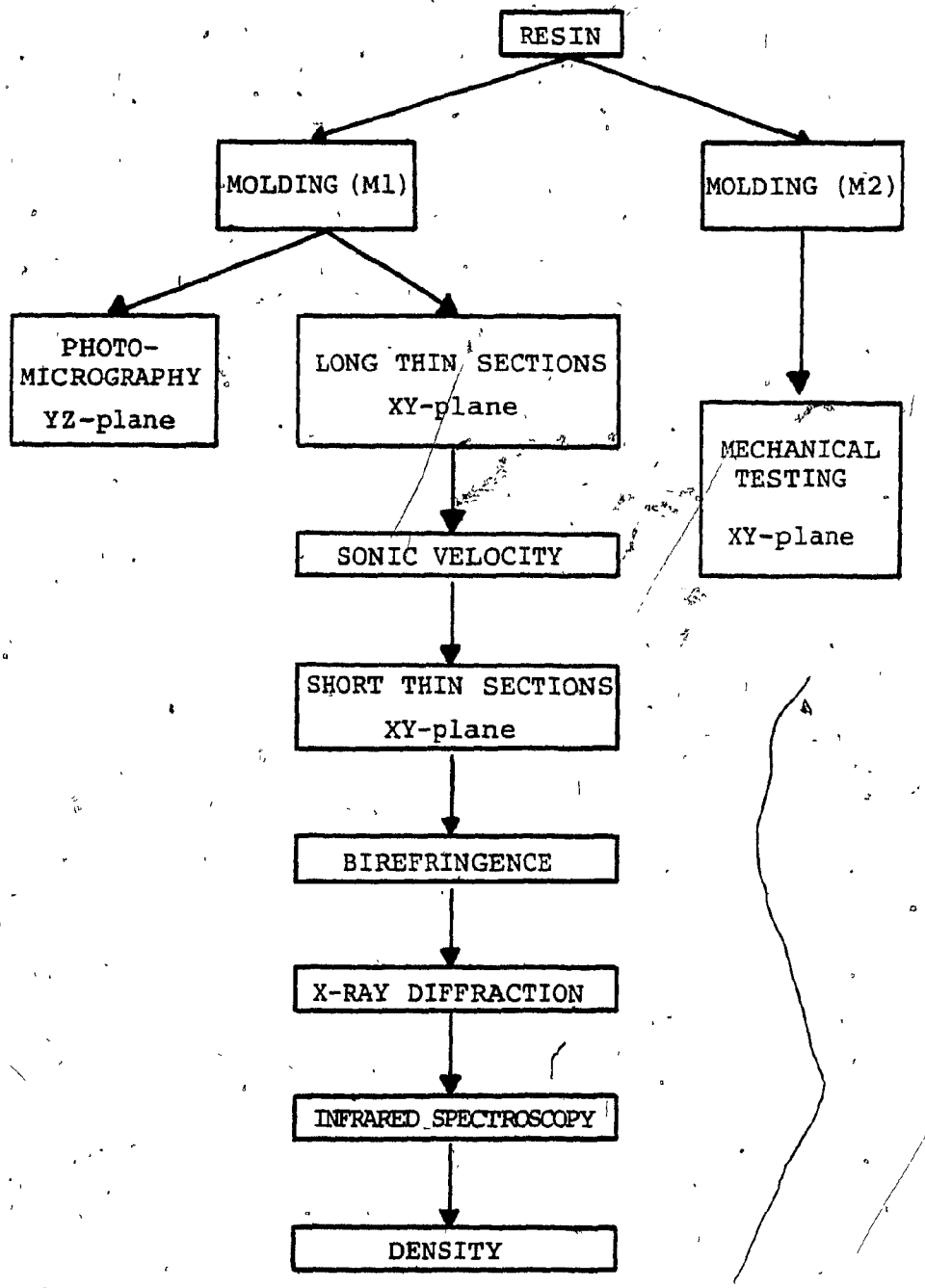


FIGURE 5.12. Schematic Sequence of Measurements Performed on Microtomed Sections

nents of a polarizing microscope are illustrated in Figure 5.13. The microscope is equipped with a large circular rotating stage, a polarization body fitted with a Bertrand lens and an iris diaphragm, a filter analyzer (which can be rotated 360^0), transmitted light and incident light objectives mounted in a slide, and a transmitted light filter polarizer which can be rotated 360^o in increments of 5^o. The magnification capability is between 11 and 630 times the original area. A Reichert polaroid camera is attached for photography.

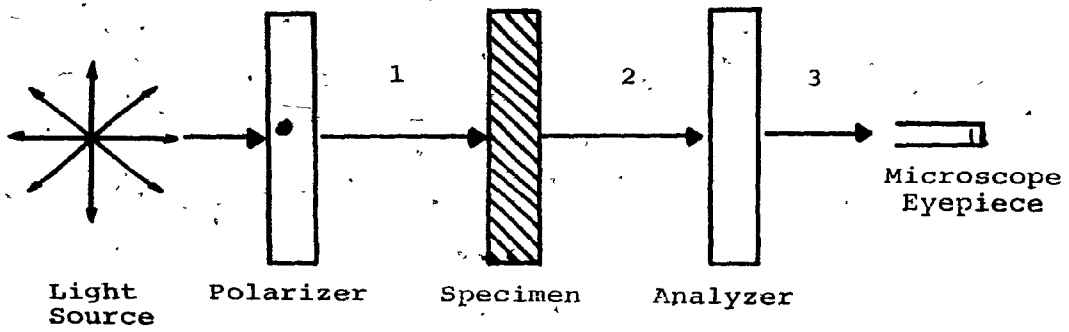
5.3.2.2 Procedure

Since each of the polarizing plates, polarizer and analyzer has the property that only a specific component of polarization of the incident beam can penetrate the plate, then if the polarization directions of the two polarizing plates are set at 90^o to each other, there will be no light passing through the two plates without any sample present. However, if a crystal sample is placed between the two plates (polarizer and analyzer), then the polarization plane of the light emerging from the crystal will, in general, no longer be normal to the polarization direction of the analyzer and some light will pass through the analyzer. If several crystals are present in a diversity of orientations, as in the case of a spherulite, the light transmitted through the various crystallites would appear lighter and darker.

The procedure used for obtaining polarized-light photomicrographs is as follows:

(1) The sections were microtomed and mounted on microscope

FIGURE 5.13. Components of a Polarizing Microscope



1. Plane-Polarized Light
2. Retardation Exhibiting Light
3. Plane-Polarized Light

slides as described in Section 5.3.1. These sections were microtomed in the perpendicular-to-flow direction along the transverse axis (YZ-plane) with thicknesses of 20 microns.

(2) The magnification on the Reichert microscope was set at 10 x 10 = 100.

(3) The polarizer and analyzer were set at right angles to each other.

(4) The sample was placed on the rotating stage of the microscope and viewed between the crossed polaroids.

(5) The stage was rotated until extinction was achieved.

(6) From a position of maximum darkness, the stage was rotated by $\pm 45^{\circ}$, to a position of maximum brightness. This was easily done by using the built-in 45° click stop system of the stage.

(7) The sample was then photographed using the Reichert polaroid camera.

5.3.3 Density

In order to study the density distributions in polyethylene moldings, sections were microtomed in the three principal directions, and their densities were determined using the density gradient technique.

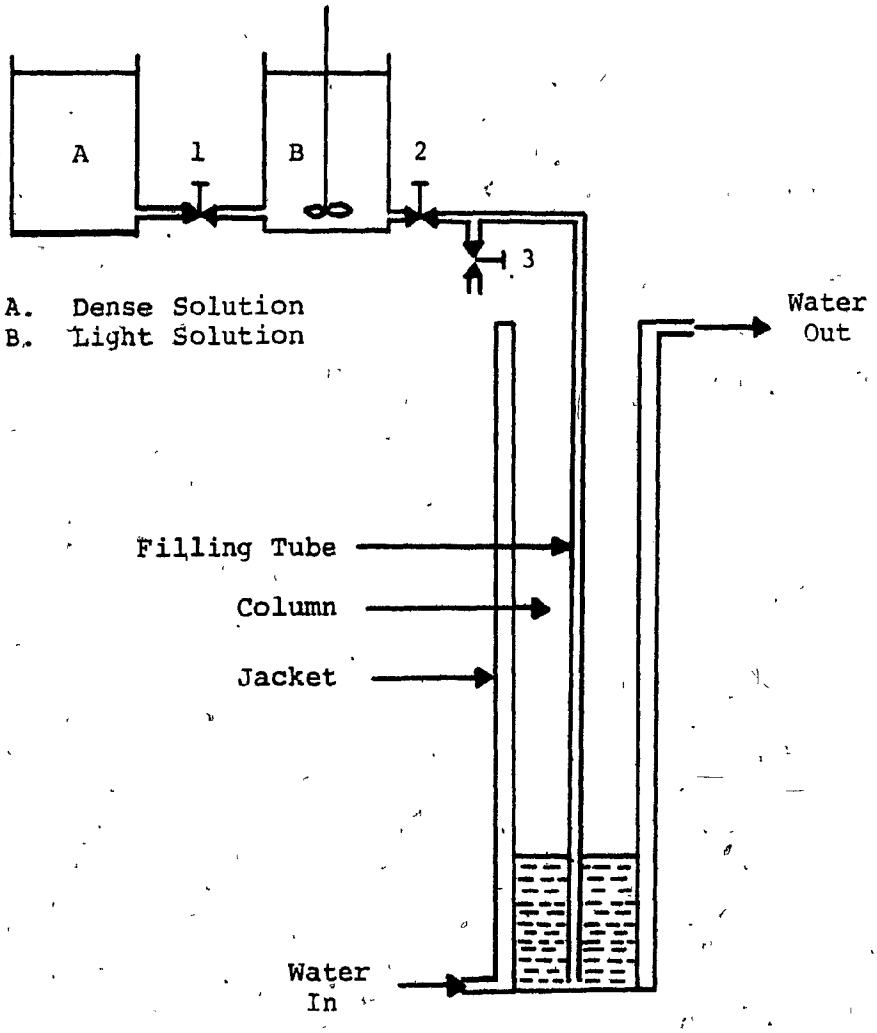
5.3.3.1 Apparatus

The technique (152) (ASTM D1505-68, Method C) employs a glass cylinder which is filled with a mixture of isopropanol

and water. The setup used was as shown in Figure 5.14. The inside diameter of the column and its height were 5 cm and 100 cm, respectively. The column was jacketed and maintained at 23 ± 0.1°C by circulating water from a constant temperature bath through the jacket at a rapid rate. To isolate the column from vibrations, a 2 ft x 2 ft x 1 ft high cement block was used as its base. The block in turn was placed over vibration absorbing felt pads. The filling tube had an inside diameter of ¼ inches. Each of the filling beakers had a capacity of 1000 ml. Filling of the column is carried out such that the liquid concentration varies continuously with cylinder height. The concentration of water and hence the density of the mixture would be higher towards the bottom of the cylinder. Further, a number of colored calibration glass floats of known density are placed such that the actual density variation with column height can be established. The colored glass floats of known density are supplied by the Scientific Glass Apparatus Company of Bloomfield, New Jersey, U.S.A.

A lift-line and basket are installed to permit the placing and removing of items in and out of the column without disturbing the density gradient. A clock motor was used to raise and lower the basket into the column at a slow speed of one cm/min. Thus, it would take about 80 minutes for the basket to traverse the column. The clock motor had a speed of 1/3 rpm and a torque capacity of 1.2×10^5 g-cm. This rotational speed was further geared down such that the final wind-up shaft speed was 1/4.5 rpm. The length of this grooved shaft was 3.2 cms

FIGURE 5.14. Schematic Diagram of Setup Used for Preparing Density Gradient Column



and the diameter was 1.43 cms. The spiral groove spacing was 0.16 cm. An electronic timer was hooked to the motor such that the duration of an operation could be set in advance. At the end of the operation the timer would automatically stop the motor.

5.3.3.2 Procedure

This section describes both the procedures for preparing the density gradient column and for density determinations using the density column prepared.

The step-by-step procedure for the preparation of the density column was as follows:

(1) Beaker A was filled with 900 ml of an isopropanol/water mixture. The density of this mixture was 0.978 g/cm^3 at 20°C.

(2) Beaker B was similarly filled with 900 ml of another isopropanol/water mixture. The density of the mixture was 0.900 g/cm^3 at 20°C.

(3) The stopcock #1 was opened and the magnetic stirrer was started in beaker B. The liquids were allowed to come to an equilibrium.

(4) The T-joint stopcock #3 was opened and stopcock #2 was adjusted until the flow rate was 13 ml/min.

(5) Stopcock #3 was closed and the column was allowed to fill. Filling the column would take approximately two hours.

(6) Upon completion, the filling tube was disengaged and attached to a lifting line. The line, which was in turn connected to a clock motor, would then lift the tube at a slow and non-disturbing rate of ½ cm/min. During this operation, the column was kept closed with a lid to prevent evaporation. A narrow slit in the lid allowed the passing of the line.

(7) When the tube was removed, the calibration floats were placed in a fine-meshed stainless steel basket.

(8) The basket was attached to the line and lowered into the column at 1 cm/min. The floats would leave the basket one by one as the proper density level was reached. In all, five colored floats were used ranging from 0.925 to 0.965 g/cm^3.

To determine the density of the microtomed sections, the samples are placed in the column and are allowed to settle to an equilibrium level. The density of the surrounding liquid would then be equal to that of the sample. The actual density of the sample is then determined by comparing its height, through linear interpolation, with those of the calibration floats, immediately above and below the sample.

The procedure used for measuring the density of the sections microtomed in the parallel-to-flow direction along the longitudinal axis (XY-plane), described previously in Section 5.3.1, was as follows:

(1) Up to twenty samples were placed into the column at

a time. Each of these samples was cut into a different shape for identification purposes.

(2) Using a pair of fine-nosed tweezers, each sample was wetted in the light density mixture of isopropanol and water as in beaker B.

(3) The sample was gently dropped into the column using the same fine-nosed tweezers. The relative position of each sample in the column was carefully noted.

(4) After twelve hours, the relative heights of each sample along with the heights of the floats immediately above and below each sample were measured using a cathetometer.

(5) The density of the samples was calculated by linear interpolation through the relation:

$$\rho_s = \rho_a + (\rho_b - \rho_a)(h_a - h_s)/(h_a - h_b)$$

where ρ = density

s = sample

a = float immediately above the sample

b = float immediately below the sample

h = height as measured by the cathetometer

(6) When the column became crowded with samples, the basket which was sitting at the bottom of the column was gently raised and the contents removed. After removing the samples, the floats and basket were again lowered into the column.

5.3.4 Sonic Velocity

In this study, a sonic velocity or pulse propagation technique was employed to characterize the microstructural distributions and in particular, the amorphous state, developed in injection molded products. The sonic modulus obtained is basically a mechanical measurement. It measures the Young's modulus of the specimen. The sonic pulse causes real displacements of the molecules from their equilibrium position as it passes through the sample. However, for the sonic method to be effective in quantitative microstructural studies, knowledge of the intrinsic transverse moduli for both the crystalline and amorphous phases must be available. The experimental determination of the two elastic constants, employing the sonic method, is described in Section 5.3.5.

5.3.4.1 Apparatus

The sonic velocity for each microtomed section was measured using a Dynamic Modulus Tester, Model PPM-5R, supplied by H.M. Morgan Co., Inc., Norwood, Mass. The PPM-5R is a complete system comprising the tester, strip-chart recorder, sample mount and transducers. The PPM-5R was internally calibrated to a laboratory standard by the manufacturer and the tester is accurate to ±1% in absolute sound velocity. The transducers contain a piezo-electric ceramic crystal with a natural frequency of 5 kHz. The temperature range of the transducers is from 0 to 45°C. A block diagram of the PPM-5R is shown in Figure 5.15. The velocity of a longitudinal wave in the material is deter-

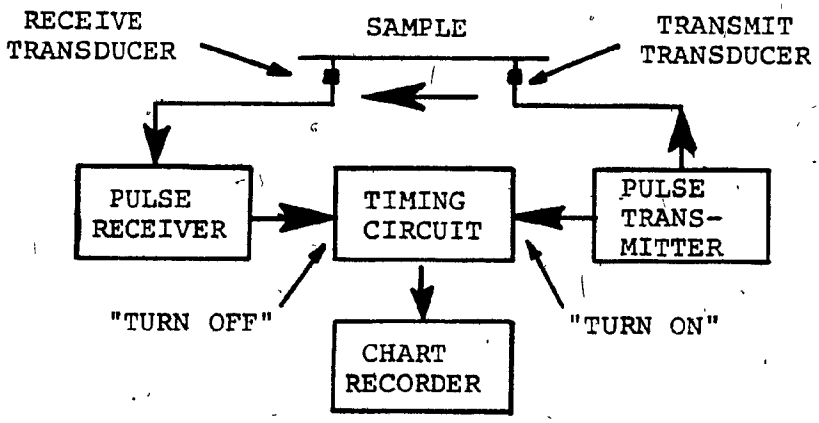


FIGURE 5.15. Block Diagram of the Dynamic Modulus Tester PPM-5R

mined by measuring the transit time of a sonic pulse between the two transducers in contact with the sample.

5.3.4.2 Procedure

The step-by-step procedure for the sonic velocity measurement in the microtomed sections from the injection moldings, was as follows:

(1) The sections were microtomed and mounted on microscope slides as described previously in Section 5.3.1. These sections were microtomed in the parallel-to-flow direction along the longitudinal axis (XY-plane).

(2) The power to the PPM-5R was switched on and a warm-up period of 1 minute was allowed.

(3) The sample was supported by taping the ends onto a 8½" x 2½" acetate sheet (Cat. No. FA-811), supplied by Concept Audio Visual, Montreal, Quebec, from which a 3.2 cms x 1.0 cm piece was cut off from the centre. This acetate sample-mount was convenient for easy positioning of the sample on the planar sample-mount of the PPM-5R.

(4) The PPM-5R Range Switch was set at 400 microseconds.

(5) The PPM-5R Zero Control switch was set in the extreme clockwise position.

(6) The Threshold Control switch was set in the extreme counter-clockwise position.

(7) The chart drive was set at 3/4 in/minute.

(8) The recorder was zeroed, if required, from the back of the recorder.

(9) The lever on the sample mount was pressed gently until the transducers were touching the sample and the switch was actuated. The switch was held steady either manually or with the insert hold-down rod.

(10) The Threshold Control switch was then turned slowly clockwise until the recorder pen moved sharply up scale and a steady reading was observed. At this stage, the PPM-5R threshold was set and the tester was ready for measuring the transit time of the sonic pulse in the sample as a function of distance between the transducers.

(11) This was done by moving one transducer (transmitter) in increments of 3 mm toward the other (receiver). Each time the actuator lever was pressed down for about 5 seconds to record the reading. The measurements were repeated, but this time the other transducer (receiver) was moved in increments of 3 mm toward the other (transmitter), so that an average of the two sets of readings was obtained. In the case of compression molded specimens, longer samples were employed and the transducer was moved in increments of 1 cm toward the other, instead of 3 mm.

(12) The sonic velocity was obtained by plotting the transit times as a function of distance between the transducers, the reciprocal of the slope of the straight

line gave the sonic velocity of the pulse in the sample.

(13) The sonic modulus of the sample was then calculated by multiplying the square of the sonic velocity by the measured sample density. The sample density was measured using the density column technique previously described in Section 5.3.3.

5.3.5 Intrinsic Sonic Moduli from Compression Molded Samples

The sonic method was employed to measure the sonic moduli of compression molded samples of different densities and hence of different crystallinities. Since the intrinsic transverse modulus is a mechanical measurement, the unoriented samples will have nonzero sonic modulus values. The films produced by the compression molding procedure had a uniform thickness of 125 ± 25 microns. For the sonic velocity measurements, long samples (10 cm x 4 mm x 125 μm) were employed. An average of three density measurements for each compression molded sample was taken. The procedures carried out for both the density determination and sonic velocity measurement were exactly as described previously in Sections 5.3.3 and 5.3.4, respectively.

5.3.5.1 Apparatus

The compression molded samples were produced using a "Dake" Molding Press (Model 44-325), supplied by "Dake" Corporation, Grand Haven, Michigan, together with two flat stainless steel plates (15 cm x 15 cm x 2 mm). The load exerted by the molding

press was calibrated by the manufacturer, based on a 3-5/8 inch diameter ram piston. The press-plates are equipped with cooling ducts through which tap water may be circulated to cool the plates quickly to room temperature.

5.3.5.2 Procedure

The step-by-step procedure for the preparation of compression molded samples with different densities, using resin EX 2, was as follows:

(1) The temperature of the top and bottom plates of the molding press was set at 180°C, and the power to the heaters was turned on.

(2) While the press-plates were heating up to the set temperature, a weighed amount (5 gms) of the resin material was placed between the stainless steel plates. Thin aluminum foils (15 cms x 15 cms) separated the resin material and the stainless steel plates.

(3) When the set temperatures of the heated plates were observed to be steady, by inserting thermometers into the side-pockets of the heated plates, the prepared resin material on the stainless steel plates was gently placed between the heated plates of the press.

(4) After two minutes, the load was increased to 5000 lbs and kept at that value for ten minutes.

(5) After ten minutes, the load between the press-plates was reduced and the stainless steel plates containing the still molten material were quickly quenched in

a liquid (water) bath at 20°C.

(6) After the sample has solidified, it was carefully removed from the aluminum foils and stored in an air-conditioned laboratory for 24 hours, at 23° ± 2°C and 50% ± 5% relative humidity, for conditioning prior to testing.

(7) The molding procedure was repeated using different bath temperatures. The other quenching conditions used were: tap water at 50°C, dry ice and acetone mixture at -50°C, and press-cooled by circulating tap water at 10°C through the cooling ducts of the press.

5.3.6 Birefringence

Injection molded parts invariably possess anisotropic physical properties. This is primarily due to variations in morphological microstructures and the orientation of the polymer chains in a preferred direction which is usually measured with respect to the direction of flow. It is found that injection molded parts are optically anisotropic and hence are birefringent.

5.3.6.1 Apparatus

The apparatus used for measuring birefringence is essentially the same as used for polarized-light photomicrography, previously described in Section 5.3.2. A Reichert "Zetopan-Pol", large polarization microscope was employed together with a compensator to measure the retardation produced between the light

waves after passing through the sample. The compensator used was an Ehringhaus rotary quartz crystal type, supplied by the Carl Zeiss Company. After passing through the compensator, the two retardation-free light waves are passed through the analyzer to produce again a plane polarized light wave. A schematic diagram of the experimental setup for measuring birefringence is shown in Figure 5.16.

5.3.6.2 Procedure

The procedure used for measuring the optical anisotropy or birefringence of the microtomed sections was as follows:

(1) The sections were microtomed and mounted on microscope slides as described previously in Section 5.3.1. These sections were microtomed in the parallel-to-flow direction along the longitudinal axis (XY-plane) with thickness of about 40 microns.

(2) The thickness of the sections was measured accurately using a Combimike Micrometer (No. 159-211) with an accuracy of 0.0025 mm, supplied by Mitutoyo MFG. Co., Ltd., Japan.

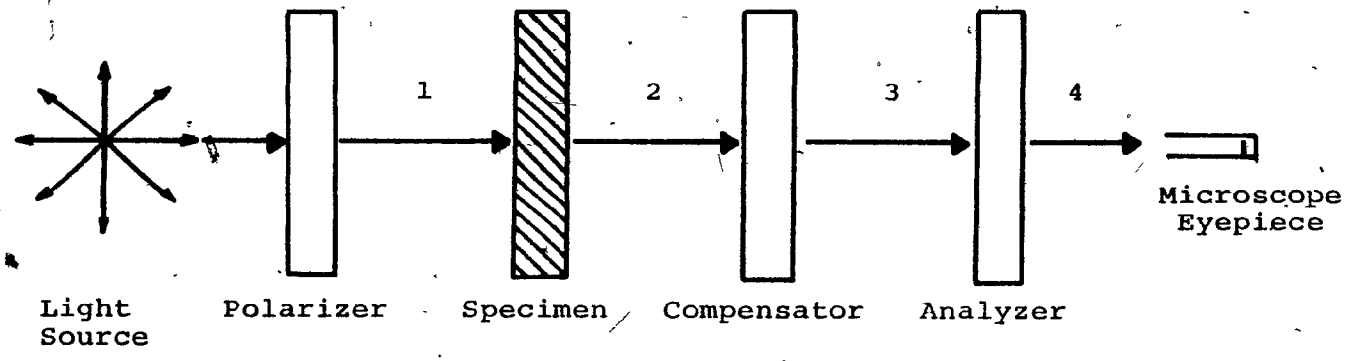
(3) The magnification on the Reichert microscope was set at 10 x 5.6 = 56.

(4) The polarizer and analyzer were set at right angles to each other.

(5) The sample was placed on the rotating stage of the microscope and viewed between cross polaroids.

(6) The stage was rotated until extinction was achieved.

FIGURE 5.16. Schematic Representation of the Setup Used for Measuring Birefringence



1. Plane-Polarized Light
2. Retardation Exhibiting Light
3. Retardation-Free Light
4. Plane-Polarized Light

(7) From a position of maximum darkness, the stage was rotated by $\pm 45^{\circ}$, to a position of maximum brightness. This was easily done by using the built-in 45° click stop system of the stage. The direction of rotation was determined by trial and error depending upon whether or not extinction was obtainable by use of the compensator.

(8) The compensator was inserted at a SE-NW direction and it was adjusted until extinction was achieved. The retardation was measured in both clockwise and counter-clockwise directions. The average of the two readings was recorded.

(9) The measured retardation (in degrees) was converted into a phase difference (in mμ) from a table containing the phase differences for light of the wavelength of the e-line of the solar spectrum and for inclinations of the quartz plate from 0 to 70 degrees in intervals of tenths of a degree.

(10) The measured birefringence of the sample was obtained by dividing the phase difference by the thickness of the sample.

5.3.7 Wide-Angle X-Ray Diffraction

In practice, several very elaborate experimental devices exist for studying orientation (137). However, it is the further purpose of this study to apply simple procedures for evaluating crystallite orientation in injection moldings. The

pinhole method, because of its simplicity and common use in studies of preferred orientation, was the method adopted in this study. The pinhole method employs monochromatic radiation to examine a polycrystalline specimen in a Laue camera. The X-ray beam passes through a sample film and falls on a flat photographic plate. The result is called a pinhole photograph. A schematic representation of the experimental setup is shown in Figure 5.17.

5.3.7.1 Apparatus

Pinhole photographs of the microtomed sections were obtained employing a Philips X-ray generator (Model PW 1120), supplied by Philips Electronics Industries Ltd., Toronto, Ontario, and a transmission pinhold camera. The Philips X-ray generator PW 1120 features 3 kW maximum power, a 4-80 mA continuously variable tube current, and 10-60 kv continuously variable high voltage. Minimum and maximum high voltage values are limited by an adjustable mechanical stop. A damping resistor prevents the high voltage tank from damage in case of short circuit in the X-ray tube. The cooling circuit contains a magnetic valve, filter and water switch. The switch causes the generator to be switched off in case the water flow decreases below a minimum level. Cu K_α radiation with Ni filter was used, at a current of 20 milliamps and a voltage of 40 kv. The samples were exposed for 48 hours. The camera was evacuated during exposure to minimize air scattering. Kodak medical X-ray film NS-54T, supplied by Eastman Kodak Company, Rochester, New York, was used. The

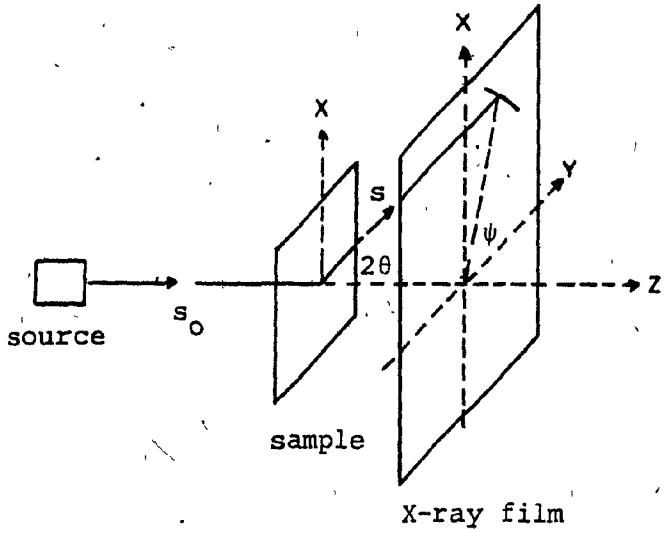


FIGURE 5.17. Experimental Setup for Obtaining Flat-Film Photographs of Microtomed Sections

pinhole photographs were scanned using a Joyce-Loebl Automatic Recording Microdensitometer, Model MK III C.S., supplied by Joyce, Loebl and Co., Ltd., England. The instrument incorporates a true double-beam system in which the two beams arise from a single light source and terminate in a single photoelectric receiver. This makes the instrument almost independent of its own parameters and complete reproducibility of record is possible, with the range of densities specified. The azimuthal intensity distributions of the (110), (200), and (020) reflections were determined from 0° to 90° in increments of 3°. In order to ensure consistency, all pinhole photographs were scanned under the same machine settings.

5.3.7.2 Procedure

X-ray diffraction experiments were carried out to study the crystalline characteristics of the microtomed sections from injection moldings. A step-by-step procedure for obtaining pinhole photographs of the microtomed sections, was as follows:

(1) The sections were microtomed and mounted on microscope slides as described previously in Section 5.3.1. These sections were microtomed in the parallel-to-flow direction along the longitudinal axis (XY-plane) with thickness of about 40 microns.

(2) The sample was then mounted on the sample holder with the longitudinal axis (x-direction) in the vertical plane.

(3) The X-ray diffraction patterns were recorded on 12.5 cms x 12.5 cms photographic film. The sample-to-film distance was 4.224 cms.

(4) The pinhole camera containing both the sample and photographic film was then mounted on the X-ray unit.

(5) The vacuum hose was connected to the pinhole camera and the pump activated, in order to minimize the scattering of the X-rays by the air.

(6) The power to the X-ray unit was turned on and both the current and voltage were increased slowly. The final current and voltage were 20 mA and 40 kv, respectively.

(7) The alignment of the pinhole camera should be such that the X-ray beam is incident in a plane normal to the XY-plane of the specimen. This was previously done without any photographic film in the camera by observing that the X-ray beam, which is seen as a bright spot, is in the centre of the beam-stop, viewed in a plane perpendicular to the incidence of the X-ray beam. The beam-stop was covered with a X-ray sensitive zinc sulphide based paper which permitted the X-ray beam to be "seen" from outside the camera. The final alignment of the camera was made using the adjustment screws of the camera mount.

(8) After the required exposure time, the X-ray unit and the vacuum pump were turned off.

(9) The camera was dismounted and taken to the darkroom for the processing of the photographic film.

(10) Before processing, the orientation of the photographic film was noted by cutting off a small piece from one of the corners.

(11) The marked film was then supported using a 12.7 cms x 17.8 cms film-and-plate developing hanger (No. 4A), supplied by Kodak Canada Ltd., Toronto, Ontario.

(12) The hanger containing the film was then placed in successive baths containing first D-19 developing solution for 4 minutes, then in a stop bath for 1 minute, and finally in a fixing solution for 20 minutes. After passing through the fixing solution, the film was left in cold running water for 4 hours after which it was hung to dry overnight. The developer D-19 (Cat. 146 4593) was supplied by Eastman Kodak Company, Rochester, New York. The Indicator Stop Bath (Cat. 146 4247) and the General Purpose Hardening Fixer (Cat. 123 8146) were supplied by Kodak Canada Ltd., Toronto, Ontario. All solutions were made up according to manufacturer's recommendations.

(13) The intensity distributions of the various reflections shown on the pinhole photograph were determined using the Joyce-Loebl Automatic Recording Microdensitometer described previously in Section 5.3.7.1.

5.3.8 Infrared Spectroscopy

The strongest absorption bands of linear polyethylene are listed in Table 5.4 together with the interpretation of the

TABLE 5.4. Band Assignments of Linear Polyethylene (Reference 119)

Frequency cm^{-1}	Type of Vibration of CH_2 Group	Contribution	Crystal Axis
2919	asymmetric stretching		
2851	symmetric stretching		
1473	bending	crystalline	
1463	bending	crystalline	
		amorphous	
731	rocking	crystalline	a-axis
720	rocking	crystalline	b-axis
		amorphous	

crystalline and/or amorphous contributions (154). As shown in Table 5.4, the well-known CH_2 rocking vibrations in the polyethylene crystal yield absorptions at about 720 cm^{-1} and 730 cm^{-1}, respectively. The two components correspond to in-phase and out-of-phase rocking modes, respectively; the 720 cm^{-1} component having a transition moment along the b crystal axis and the 730 cm^{-1} component being polarized along the a-axis (153).

In this study, dichroic measurements corresponding to both the 720 cm^{-1} and 730 cm^{-1} absorption peaks are made on the microtomed sections in order to study the microstructural distributions in injection moldings.

5.3.8.1 Apparatus

The dichroic ratio of each microtomed section was obtained by a Perkin-Elmer infrared grating spectrophotometer, Model 467, with the additional attachments of a sample space wire grid polarizer, a 4X beam condenser, and a demountable micro cell mount. The infrared grating spectrophotometer has the capability of scanning the frequency range from 4000 cm^{-1} to 250 cm^{-1}. It is equipped with four scan speeds plus a special high-speed forward and reverse modes, and a flowchart recorder for recording continuous, unbroken spectra. The wire grid polarizer (P-E Part No. 186-0243) contains a polarizing element which is a gold-wire grid, vapor-deposited on a silver bromide substrate for use in the 2.5 to 35 μm spectral range. The 4X refracting beam condenser (P-E Part No. 127-1271) is equipped with lenses that reduce the size of the sample beam image at the sample

position and then restore the beam to its original size. The optics are made of KBr and employ both cylindrical and spherical surfaces to eliminate residual aberrations. The demountable micro cell mount (P-E Part No. 186-0094), for use with the refraction beam condenser, facilitated the observation of very small samples.

5.3.8.2 Procedure

The step-by-step procedure for the measurement of the absorption in the longitudinal (A_L) and the transverse (A_T) directions of the molding, was as follows:

(1) The sections were microtomed and mounted on microscope slides as described previously in Section 5.3.1. These sections were microtomed in the parallel-to-flow direction along the longitudinal axis (XY-plane) with thickness of about 40 microns.

(2) The power to the infrared spectrophotometer (P-E, Model 467) was turned on and a period of fifteen minutes was allowed for warming up, according to the manufacturer's recommendations.

(3) The beam attenuator was set at 100% transmission at the 700 cm^{-1} band position before the sample was placed in the sample beam.

(4) The scan mode was set at "F" (fast mode) and the slit at "N" (normal).

(5) The sample was then placed at 45°, in the clockwise direction, to the slit.

(6) The polarizer was set at the 45° position to measure the absorption in the longitudinal (A_L) and at the 315° position to measure the absorption in the transverse (A_T) direction of the molding, respectively.

(7) The dichroic ratio, D, is then measured as $D = A_L/A_T$.

5.3.9 Mechanical Properties

In the majority of applications of polymers, there are three basic mechanical properties - stiffness, strength and toughness, which are of significant practical interest. To these one can add the phenomenon of creep, which becomes important in many engineering applications. Stiffness represents resistance to deformation, while strength and toughness relate to failure. Strength is the ultimate stress which a material can withstand before it fails, whether by fracture or by excessive deformation, whilst, toughness represents the work required to fracture a material (132).

One of the most commonly encountered tests in the quality control of molded products, is the tensile stress-strain measurement. The tensile stress-strain measurements are generally made by stretching the sample at a uniform rate while recording the forces required to stretch the sample. Figure 5.18 shows two representations of typical stress-strain behavior. It should be noted that the experimental data are usually recorded in terms of the forces registered and the times required for certain changes to occur. These values are then converted into stress and strain, according to procedures which are described

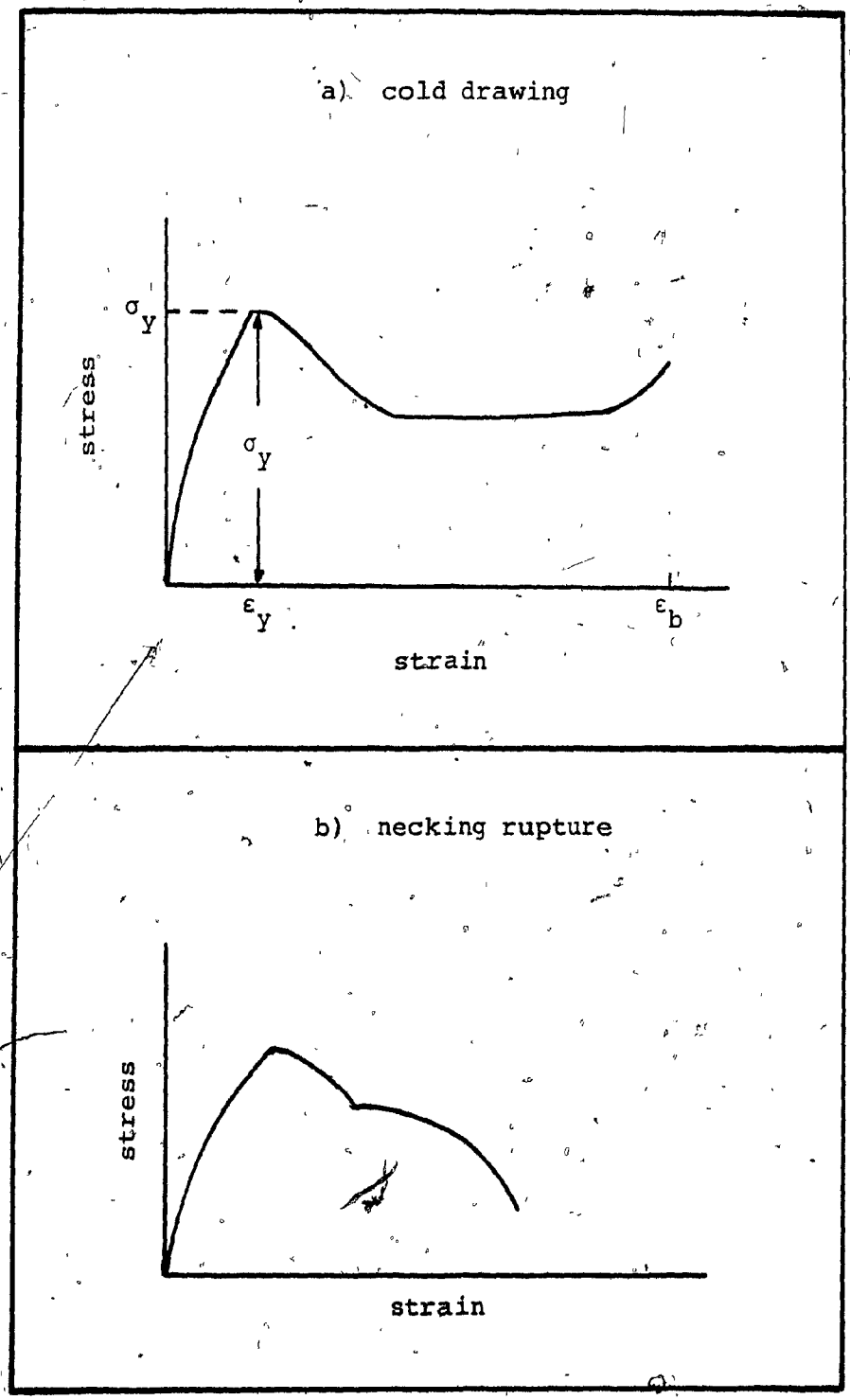


FIGURE 5.18. Examples of Stress-Strain Behavior

in detail by Nielsen (146).

5.3.9.1 Apparatus

An Instron Universal Testing Instrument, Model 1123, was used to determine the mechanical properties of the microtomed sections. The accuracy of the load weighing mechanism is ±0.5% of the indicated load or 0.25% of the recorder scale in use, whichever is greater. The positional servo-drive provides speed accuracy of ±0.1% of the set speed at any load and speed within the overall range of the instrument. A tensile load cell, type CM (Serial No. UK 282) manufactured by Instron, and having full scale ranges (normal) of 1, 2, 5, 10, 20 and 50 kgs was used in conjunction with the Instron Tester. Two pneumatic action grips, Model 3CA, manufactured by Instron, were used to hold the sample. The grips have a load capacity of 100 kg and the maximum sample thickness that may be used, is 0.64 cm. Laboratory compressed air was used as the power medium.

5.3.9.2 Procedure

The step-by-step procedure for the measurement of tensile properties of the thin microtomed sections, was as follows:

(1) The long thin sections for mechanical testing were microtomed and mounted on microscope slides as described previously in Section 5.3.1. These sections (about 4 cms x 4 mm x 0.04 mm) were microtomed in the parallel-to-flow direction along the longitudinal axis (XY-plane).

(2) For each of the microtomed sections to be tested, the width and thickness of each section were measured. The average of three width measurements along the gauge length was taken, using a Nikon Measurescope with an accuracy of 0.0025 mm, manufactured by Nippon Kogaku K.K., Japan. Similarly, an average of three thickness measurements along the gauge length was taken, using a Combimike Micrometer with an accuracy of 0.0025 mm, manufactured by Mitutoyo MFG. Co., Ltd., Japan.

(3) Before inserting the specimen into the grips, scotch-tape was stuck to the ends of the specimen to prevent any specimen slippage during mechanical testing.

(4) The load weighing mechanism of the Instron Tester was calibrated using a full-scale load of 1 kg.

(5) The distance between the grips was adjusted to 2 cms.

(6) The specimen was carefully placed between the grips.

(7) The specimen was then extended at a strain rate of 5 cm/min. The chart speed was also 5 cm/min.

(8) The chart recording showed the load as the abscissa and elongation as the ordinate. By knowing the initial cross-sectional area and gauge length of the test specimen, the yield stress and percent elongation at yield were calculated. "Maximum load criterion" was employed in determining the yield point. The percent elongation at break was obtained from knowledge of the original gauge length, chart speed and crosshead speed.

CHAPTER 6

RESULTS AND DISCUSSION

This chapter presents the results of each technique employed in the study. Furthermore, the results of the techniques are correlated and integrated to obtain quantitative information regarding the degree of orientation of the amorphous phase developed in the injection moldings. The measurements also afforded an estimation of the intrinsic birefringences for both the crystalline and amorphous phases. The estimated intrinsic birefringence values are used to calculate the relative contributions of the crystalline and amorphous phases to the total orientation as measured by birefringence. Furthermore, the results of crystallinity and orientation are combined to predict the distributions of sonic and tensile moduli measurements.

6.1 Molding Conditions

Figure 6.1 shows typical pressure profiles in the mold cavity for the two resins. It can be seen that resin EX 2 takes a longer time to fill the mold than resin EX 1, under identical molding conditions. At the higher melt temperature, the fill time is shorter due to the lower viscosity as exhibited by resin EX 2. The differences between the two resins in relation to their molding characteristics have been discussed previously in Section 5.1.

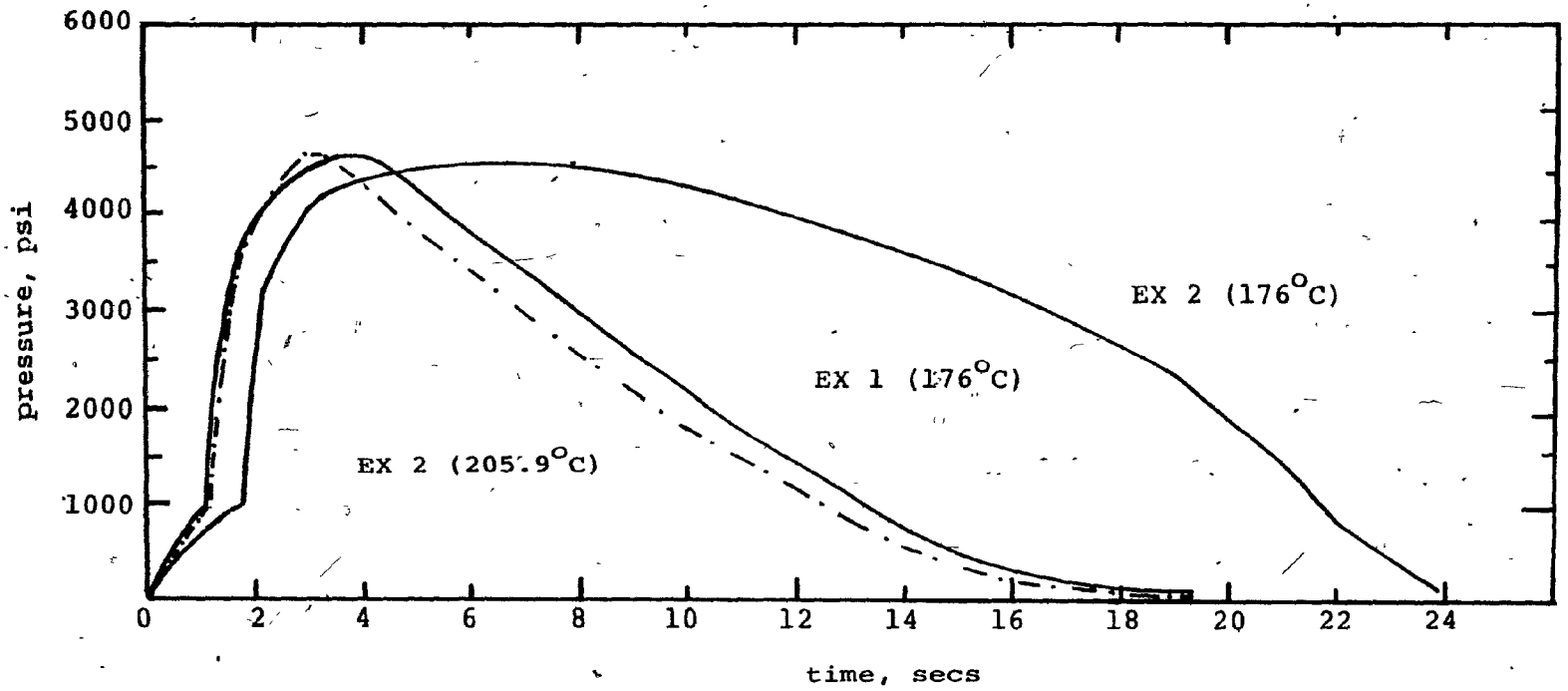


FIGURE 6.1. Typical Pressure Profiles in the Mold Cavity

It was observed that during injection molding of the rectangular specimens, variations from shot to shot in the injection molding behavior of each resin were observed. Figure 6.2 shows, as an example, the variations of the maximum cavity pressure for all samples molded from the two resins plotted in terms of a percent frequency polygon. Maximum pressure data are divided into 100 psi class intervals and are plotted against the percentages of moldings that were subjected to maximum pressures falling between these class intervals. The range of maximum pressures for the two resins molded at a melt temperature of 176°C, is 500 psi. In the case of resin EX 2 molded at a melt temperature of 205.9°C, the maximum pressure range is 600 psi. Generally, about 70% of the moldings were subjected to maximum pressures which fall within a pressure range of 200 psi. Furthermore, although the percent variation observed is not significant from molding to molding, it is obvious that there is a necessity for statistical analysis in characterizing the molding behavior of the resins (121). According to Rubin (155), it is a common observation that an injection molding machine will exhibit variations in its molding performance while a resin is being molded under the same operating conditions and geometry.

During the injection molding of the two resins, the barrel zone temperatures, the mold temperature, the injection speed and injection and holding pressure control valves, were kept constant. It is evident that the position of the control valves, which pertain to the hydraulic pressure of the oil delivered

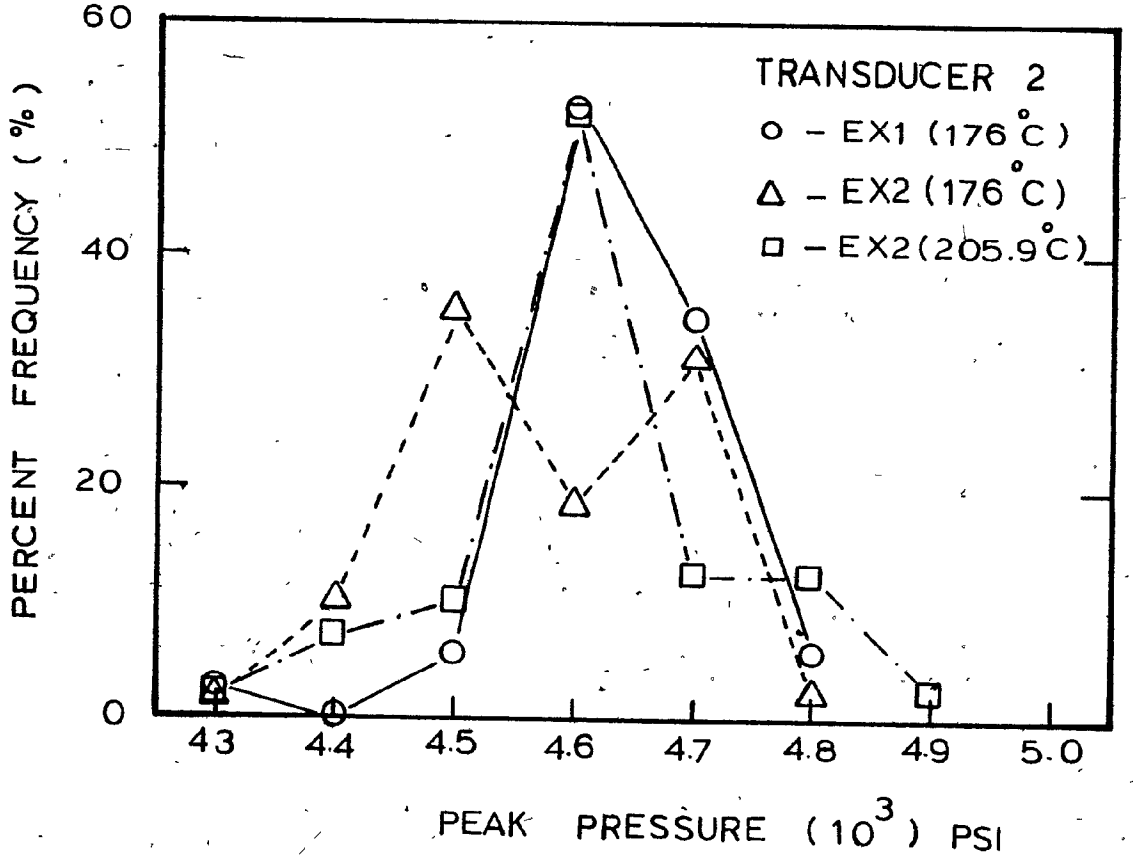


FIGURE 6.2. Percent Frequency Polygon for the Distribution of Peak Pressures of the Molded Specimens

to the back of the injection ram, cannot control the actual injection and holding pressures and the injection speed. The pressure in the mold cavity and the injection speed depend on the resin properties for a given molding geometry. With this in mind, the moldings chosen for microstructure characterization corresponded to those molded under the arithmetic averages of the molding conditions obtained for 35-50 moldings of each resin. Table 6.1 shows both the average values and standard deviations, of the cavity filling times, maximum filling pressures, and maximum packing pressures, for the two resins molded at a melt temperature of 176°C, and also for resin EX 2 molded at a higher melt temperature of 205.9°C. As shown in Table 6.1, resin EX 1 exhibited shorter filling time than resin EX 2. This is attributed to the lower viscosity of resin EX 1 at the corresponding temperatures (121). Furthermore, resin EX 2 exhibited shorter filling time at the higher melt temperature due to the lower viscosity at the higher melt temperature.

The dynamics of the molding cycle concerning the filling, packing, and cooling stages employing these two resins have been previously studied in detail, as part of an extensive injection molding program at McGill University. For more detailed information regarding these aspects, the reader is referred to the study made by Kalyon (121).

6.2 Photomicrography

All positions when viewed under the polarizing microscope revealed the presence of zones with different morphologies as

TABLE 6.1. Average Cavity Filling Times, Maximum Filling Pressures, and Maximum Packing Pressures for the Two Resins as Measured by Pressure Transducer Located Near the Gate. Standard Deviations are in Brackets.

Resin	Melt Temp. (°C)	Average Fill. Time (sec)	Maximum Fill. Press. (psi)	Maximum Pack. Press. (psi)
EX 1	176	1.11 (0.07)	1034 (24.4)	4675 (85.0)
EX 2	176	1.77 (0.33)	1023 (44.6)	4502 (227)
EX 2	205.9	1.12 (0.05)	968 (15.9)	4622 (258)

shown in Figures 6.3-6.5. Elucidation of the morphological structure of each resin is of basic interest, as it may cast light on the mode of formation of these layers. Generally, three distinct layers are discernible; however, these layers can in some cases be further subdivided (112, 118, 119, 121). These morphological zones are designated as the skin, the intermediate zone, and the core. The volumes of these three zones were proposed to correspond to the volumes crystallized during the three stages of the injection molding cycle (107). However, further experimental work by Tan and Kamal (118, 119) revealed that the thickness of the layer solidified during the filling stage is thicker than the skin layer and falls somewhere within the intermediate layer.

The layer next to the surface, which does not transmit polarized light, is designated as the skin layer (107, 111). The thickness range of the skin layer is 0.05-0.25 mm. Furthermore, the thickness range of the skin layer changes both with position on a molding and with the resin used in molding the specimens (107, 111, 119, 121). The skin layer is thought to consist of stacks of lamellae with the chain axes nucleated in the flow direction and growing in the depth direction, because of the very rapid nucleation rate resulting from the low temperatures prevailing near the mold wall (15, 119). Furthermore, in the early stages of the crystallization, the temperature gradient normal to the mold wall is very steep and the crystals once formed, tend to grow parallel to that gradient.

FIGURE 6.3. Morphological Zones in EX 1 Specimen, Molded at 176°C

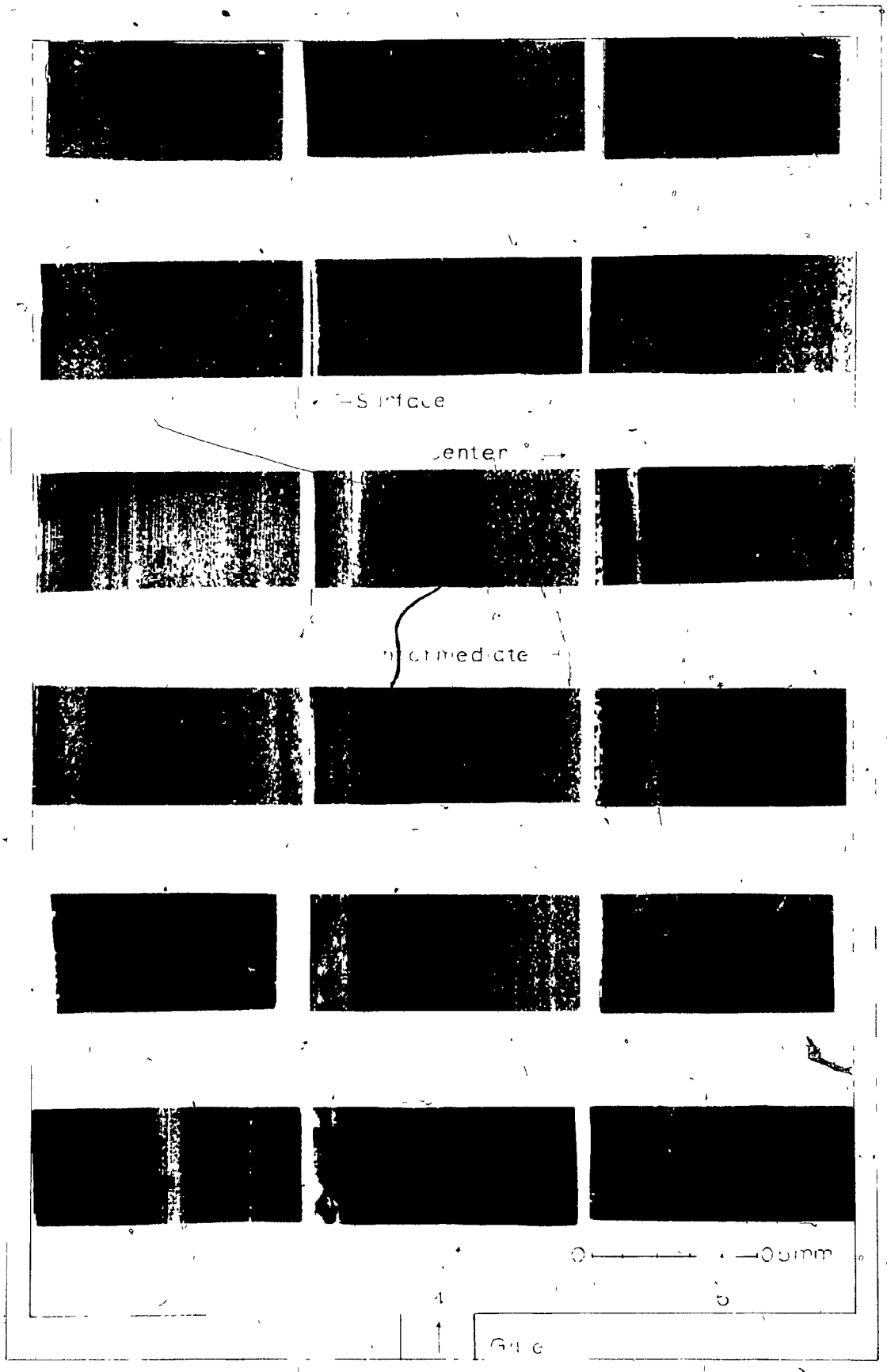

Surface
Center
Intermediate
0.5mm
a
b
Gage

FIGURE 6.4. Morphological Zones in EX 2 Specimen, Molded at 176°C

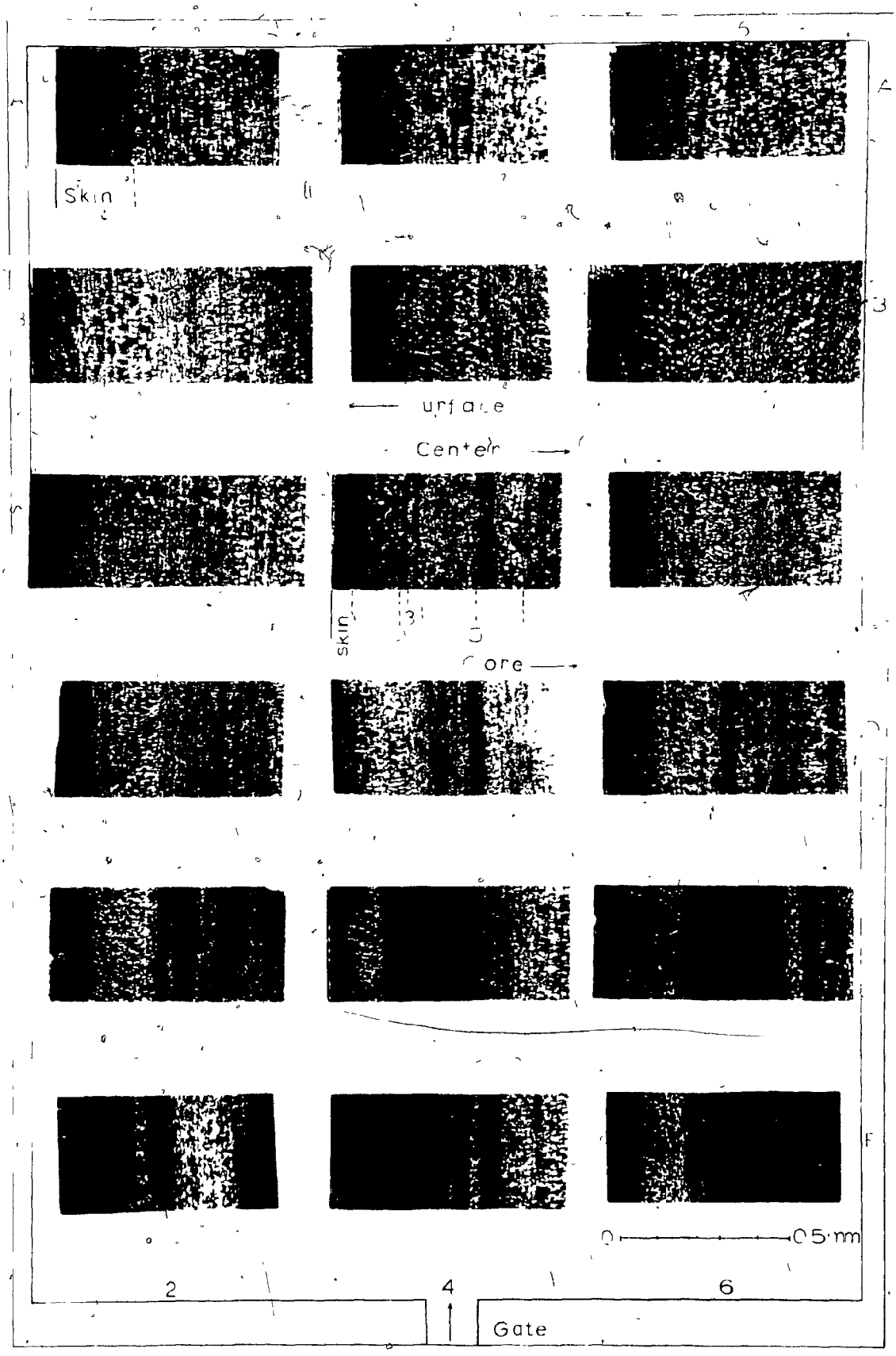
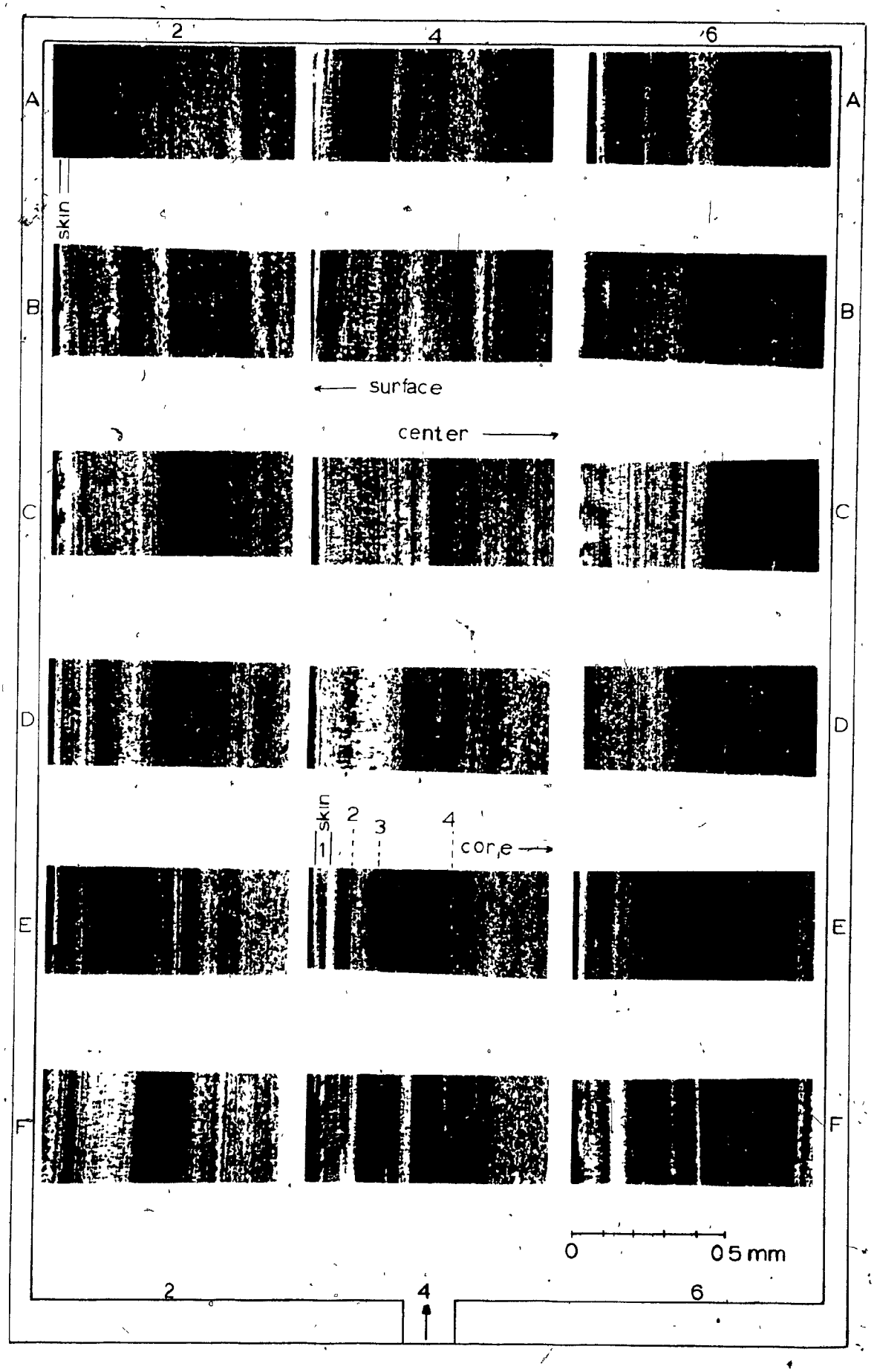

Skin
urface
Center
Core
0
0.5 mm
2
4
6
Gate

FIGURE 6.5. Morphological Zones in EX 2 Specimen, Molded at 205.9°C


2
4
6
A
skin
B
surface
center
C
D
skin
1
2
3
4
core
E
F
0
05 mm
2
4
6

The skin is followed by an intermediate layer with a thickness range of 0.25-0.80 mm, which changes in thickness with respect to position and resin. The intermediate layer is thought to consist of folded lamellae created by lower stress levels causing secondary nucleation on the surface of the linear row nuclei. If the growing lamellae exhibit a helical twist, the chain orientation in the chain direction is very soon replaced by the orientation of the axis of the maximum growth (b-axis in polyethylene) perpendicular to the strain direction (132). Thus, the spherulites discernible within the intermediate layer are formed and oriented in the direction of the thermal gradient. Furthermore, it is probable that the oblate spherulites oriented with their long axes perpendicular to the flow direction, is due to the prevailing steep temperature gradients (107).

The core constitutes the rest of the volume of the molding. Generally, the randomly nucleated spherulites in the core have grown under low rates of cooling and hence, the diameter of the spherulites increases as the centre of the core is approached.

The overall rate of crystallization is a function of the rates of spherulite nucleation and growth. Both the growth rate and the nucleation rate attain maximum values somewhere between the melting temperature and the glass transition temperature of the polymer (15). The rate of crystallization is strongly related to the undercooling, $(T_m - T_c)$, where T_m is the equilibrium melting point and T_c is the temperature at which the crystallization is carried out. Since the temperature of a melt element in the mold cavity is changing continuously, crystalli-

zation will occur at different rates with time.

Increasing the melt temperature, as shown in Figure 6.5, tends to decrease the combined thicknesses of both the skin and intermediate layers (107, 111, 156). At the high melt temperature, more heat must be removed to the cold mold wall and, other conditions being constant, more time is needed to reach the freezing point. Thus, at the higher melt temperature, less material crystallizes during the filling and packing stages and more spherulitic material is present (107).

A careful study of Figure 6.4 for resin EX 2 molded at a melt temperature of 176°C, shows that the thickness of the skin layer increases as distance from the gate increases. As mentioned earlier, the thickness of the skin layer is reported to increase as the injection temperature of the melt decreases. The observed increase in the thickness of the skin layer as distance from the gate increases, may be associated with the decrease of the average melt temperature as the melt element moves away from the gate during the filling stage.

The intermediate layer does not only change in volume, but also changes in nature as one moves towards the gate. Furthest away from the gate, it is composed mainly of medium-size spherulites, whereas closer to the gate it is composed of very small crystallites. It has been speculated that the intermediate layers have crystallized during the packing stage and have experienced high levels of pressure, which has affected the crystallization of lamellae (107, 121). The effect of an increase in pressure during crystallization is to increase the equilibrium

melting point and the rate of crystallization. The resulting lamellae will be thicker since the equilibrium crystallite thickness is proportional to the melting temperature (15).

As shown in Figures 6.3 and 6.4, the resulting microstructure for resin EX 1 exhibits significant differences from the distribution observed with resin EX 2. Firstly, the thickness of the skin layer is larger for resin EX 2 than for resin EX 1. This observation is attributed to the higher filling rate observed for resin EX 1 during the filling stage (12). The temperature drop of a melt element as it moves away from the gate for resin EX 1 will be less than the temperature drop for a similar element in resin EX 2, due to the difference in filling rates, and as mentioned before, a lower melt temperature gives rise to a thicker skin (111). Secondly, when the sizes of the spherulites are compared, according to Figures 6.3 and 6.4, resin EX 2 tends to exhibit larger spherulites than those observed for resin EX 1. The final mean spherulite diameter is dictated by a competition between the rate of nucleation and the subsequent rate of growth of the spherulites (15). It appears that the nucleation rate of resin EX 1 is so fast that subsequent growth of the spherulites is hindered by the impinging of the spherulite boundaries on each other. However, for resin EX 2, the number of active nuclei is lower, due to slower nucleation rates, and subsequent growth gives rise to spherulites with larger diameters.

The rate of nucleation can be affected by a variety of factors. A fast cooling rate increases the rate of nucleation

(157). Therefore, because of the higher thermal diffusivity and lower specific heat exhibited by resin EX 1, as shown in Table 5.1, it is highly likely that specimens molded from resin EX 1 will experience faster cooling rates which could have resulted in higher nucleation rates and smaller spherulites. Furthermore, the generally smaller spherulites observed for resin EX 2 molded at the higher melt temperature may again be attributed to the increased cooling rate and hence, to the increased rate of nucleation mentioned earlier. Tan and Kamal (156) have similarly observed a decrease in spherulite size as the melt temperature is increased.

Another factor that has to be considered is the probable presence of heterogeneous nuclei. If such special nucleating sites were present and were sufficiently more active than the sites formed spontaneously in the homogeneous melt, the total number of nuclei formed at any temperature would correspond to the number of heterogeneous nuclei available (15). In this case, the spherulite size depends mainly on the number of heterogeneous nuclei present per unit volume. It should be noted that the thermal history of the specimens plays a significant role, since different heterogeneities require different driving forces, such as undercooling, to induce nucleation.

One or both of the factors mentioned above, rate of cooling and concentration of nucleating agents, have affected the nucleation patterns of the resins to give rise to the different sizes of spherulites observed in molded specimens of resins EX 1 and EX 2 (121).

Generally, the distribution and the relative volumes of the zones differs from position to position within a molded specimen. As will be discussed in Section 6.9, this distribution may be very crucial in affecting the distribution of ultimate properties in an injection molded article (106, 107).

In summary, the results obtained from the study of morphology under polarized light have shown that heterogeneous morphological zones exist in the injection molded articles. Furthermore, the morphological characteristics of the zones are appreciably different and the distributions and the relative volumes of the morphological zones are dependent on resin properties and molding conditions. The relative volumes and some of the characteristics of the morphological zones differ from position to position in a molded specimen.

6.3 Density

The variation of polyethylene density (crystallinity) is an indication of the crystallization phenomena occurring during the injection molding process (118). The variations of the density and volume fraction crystallinity as a function of the distance from the surface for the two resins at the indicated locations along the molding, are shown in Figures 6.6 to 6.8. For the sake of clarity, the results of the two off-centre positions located near the gate and far from the gate are plotted together, but separately from the centreline positions. Furthermore, the density data at the various locations are presented in Appendix 3. The error analysis associated with the

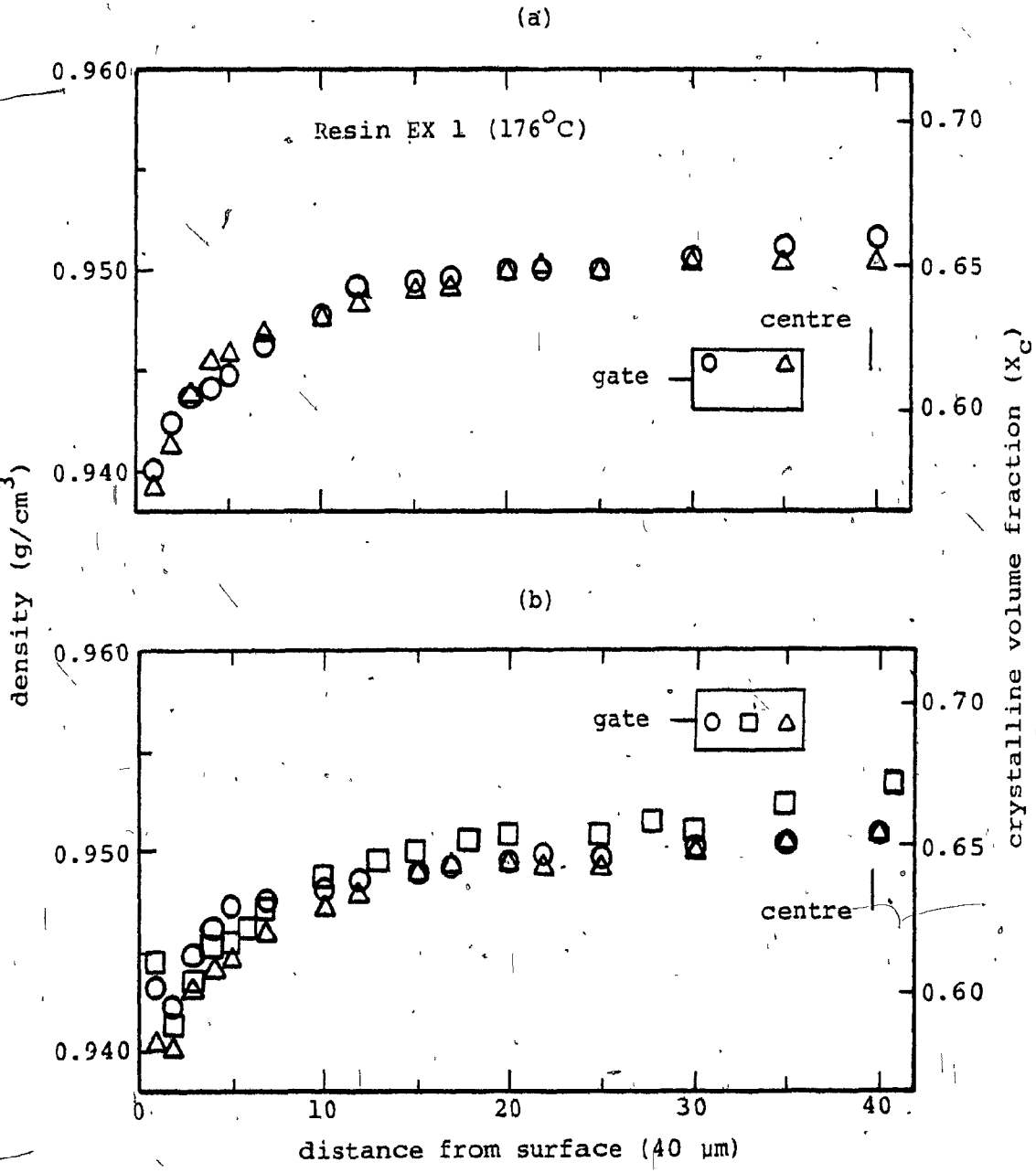


FIGURE 6.6. Variation of Density (Crystallinity) in the Depth Direction

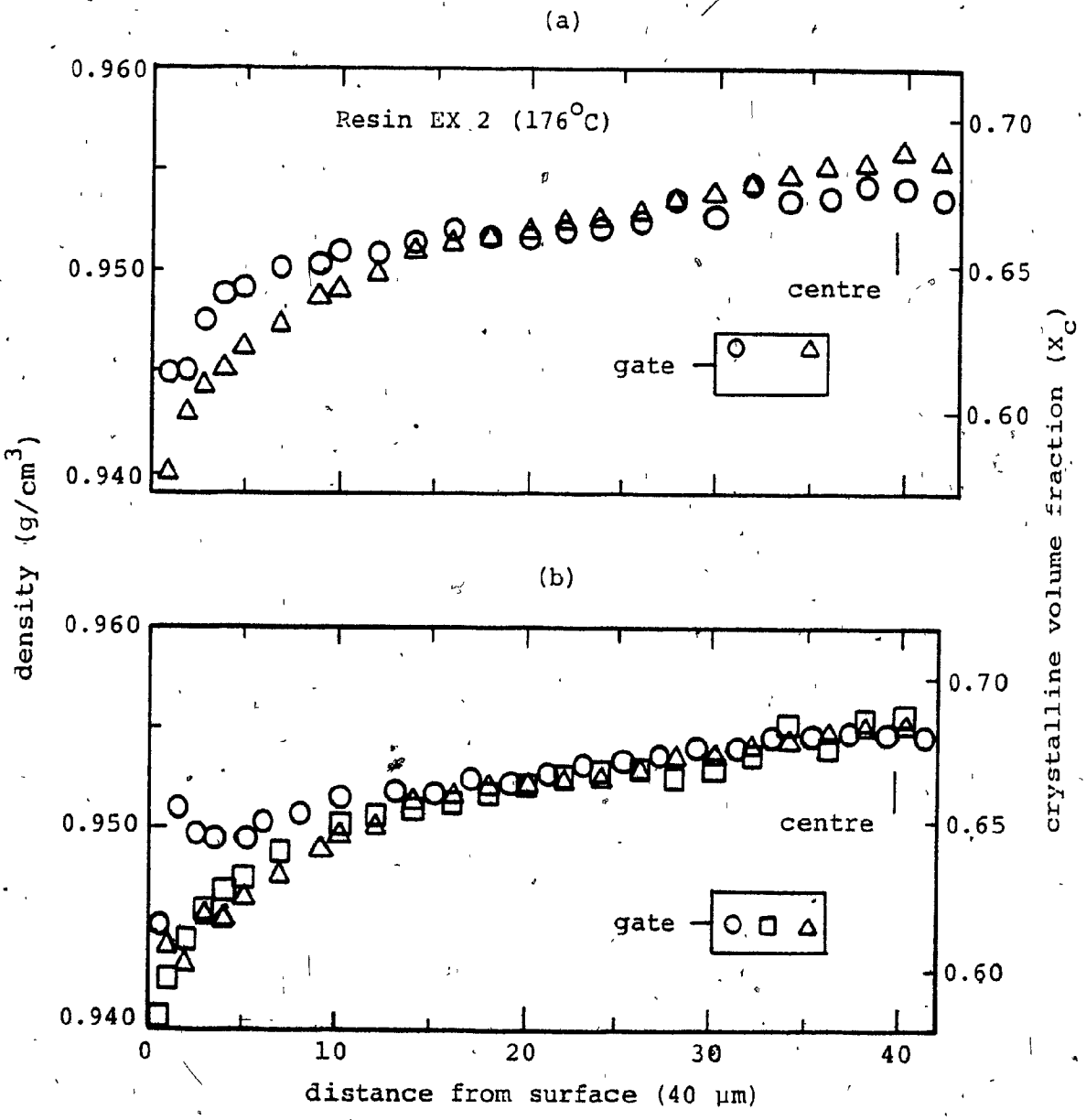


FIGURE 6.7. Variation of Density (Crystallinity) in the Depth Direction

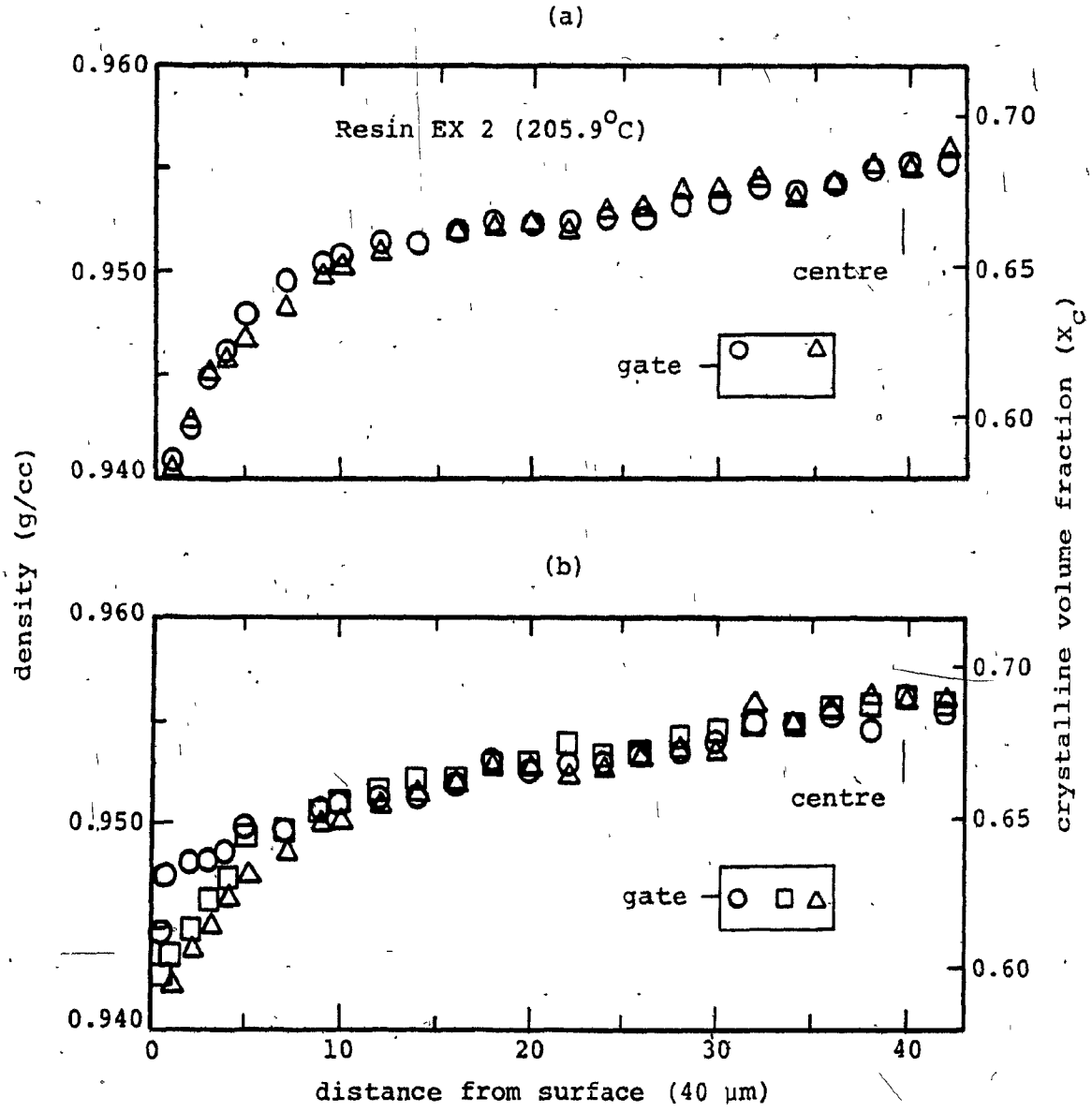


FIGURE 6.8. Variation of Density (Crystallinity) in the Depth Direction

measurement of density is presented in Appendix 15.

Generally, the density (crystallinity) increases monotonically, from a minimum value near the surface to a maximum towards the core region of the molding. Several workers (117, 118) have reported similar variations in the distribution of density in the depth direction of the molding. The lower crystallinity near the surface of the molding is attributed to the rapid cooling of the melt near the mold surface which reduces the extent of crystallization. Furthermore, the rapid cooling that melt elements experience near the cold mold surface causes the melt to incorporate more free volume than in the case of slow cooling. The higher densities observed towards the core of the molding are due to the lower thermal gradients and hence, lower cooling rates which enhance the growth of spherulites in this region.

Generally, the overall density is observed to be highest for the location near the gate and lowest for the location furthest from the gate. Similar differences in density distributions were reported by other workers (117, 118). This behavior is attributed to the longer cooling times and higher packing pressures that prevail near the gate (118, 122).

For the off-centre positions located both near the gate and far from the gate, there appears to be very little difference in the density distributions observed, as shown in Figures 6.6(a), 6.7(a), and 6.8(a). However, Figure 6.7(a) tends to show a difference between the two off-centre locations for resin EX 2 molded at a melt temperature of 176°C. The difference may

be attributed to the slightly longer cooling times and higher packing pressures in the region located near the gate, as mentioned earlier. Although Figures 6.6(a) and 6.8(a) do not exhibit as marked a difference, a similar tendency appears to be evident. Furthermore, there appear to be very little differences in the density distributions when the off-centre and centreline locations, except for the location near the gate, are compared.

As shown in Figure 6.9, generally resin EX 2 tends to exhibit higher densities (crystallinities) throughout the molded part than resin EX 1. This is due, in part, to the fact that resin EX 2 has a higher melt density to begin with.(121, 122). Furthermore, resin EX 2 probably experiences lower effective cooling rates than EX 1 since the former exhibits both a lower crystallization temperature, as shown by previous P-V-T and DSC data (121), and lower thermal diffusivity (158).

At the high melt temperature, as shown in Figures 6.8(a) and 6.8(b), the relative density distributions are similar to those observed for the two resins molded at the lower melt temperature. Generally, increasing the injection melt temperature tends to marginally increase the density (crystallinity) throughout the molded part. This is attributed to the generally longer cooling times associated with the higher melt temperature (118) and the resulting lower effective cooling rates due to the balance of the prevailing thermal properties of the system (158). However, when the density distributions for the off-centre and centreline positions, for the location near the gate, as shown

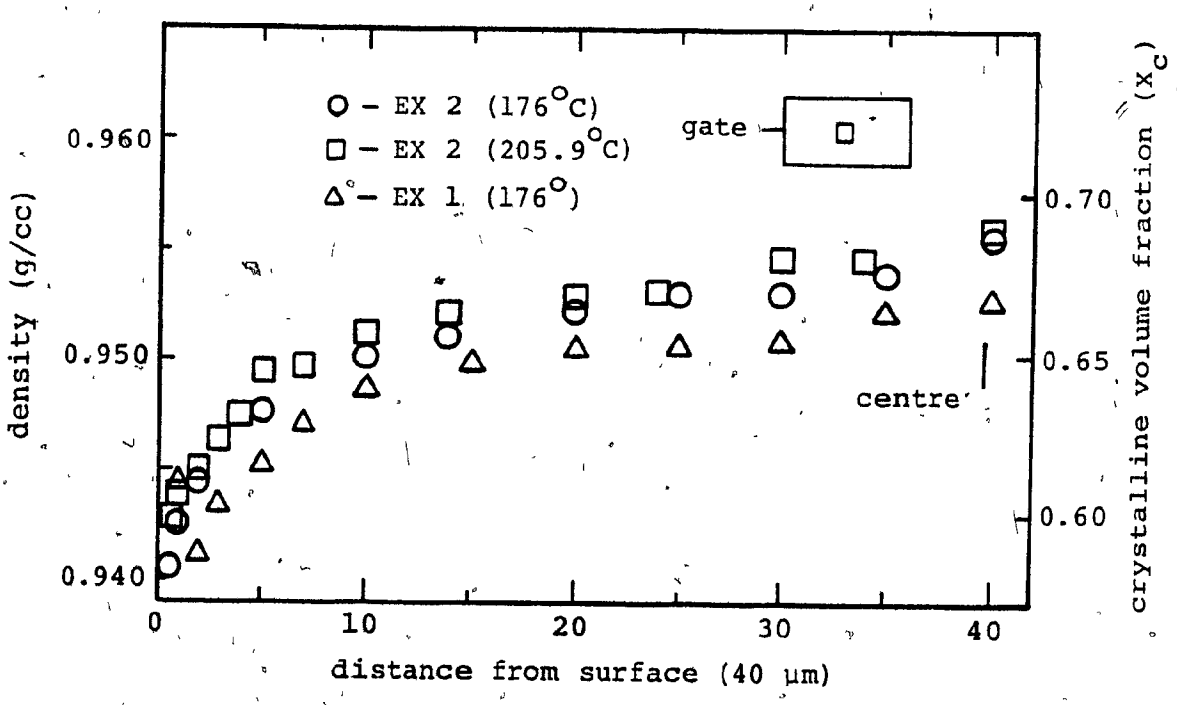


FIGURE 6.9. Typical Comparison of Density Distributions

in Figures 6.6 to 6.8, are compared, these locations tend to exhibit lower densities (crystallinities) at the higher melt temperature. This may be attributed to the faster crystallization rate that prevails in these zones as a result of increased cooling area near the cold mold surface, and hence, due to the higher cooling rates of the melt at the higher melt temperature. Furthermore, these locations near the gate tend to exhibit generally smaller spherulites caused by the rapid nucleation rates, discussed previously in Section 6.2.

Generally, the results of the density (crystallinity) measurements may be summarized as follows:

(1) There is a monotonic increase in density (crystallinity) from a minimum near the surface to a maximum in the core region of the molding.

(2) The density is highest for the location near the gate.

(3) Resin EX 2 tends to exhibit higher densities (crystallinities) throughout the molded part than those observed for resin EX 1.

(4) Increasing the injection melt temperature tends to marginally increase the density (crystallinity) throughout the molded part, except for locations near the gate which tend to exhibit lower densities at the higher injection melt temperature.

(5) It has been attempted to explain the above observations on the basis of qualitative arguments. Ideally, it would be desirable to obtain quantitative explanations on the basis of mathematical simulation of the

process with due consideration to the effects of resin characteristics, cooling rates, pressure, and hydrodynamic conditions on nucleation and crystalline growth in the system. Such a complex analysis is outside the scope of the present study.

6.4 Intrinsic Sonic Modulus from Compression Molded Samples

It is apparent from Section 4.2 that the application of Equation (4-9), which relates the orientation of both the crystalline and amorphous phases to the total orientation as measured by the sonic velocity method, requires knowledge of both the intrinsic transverse moduli for the crystalline ($E^o_{t,c}$) and amorphous ($E^o_{t,am}$) phases, respectively. Section 5.3.5 describes the procedure which was adopted to estimate the intrinsic sonic moduli (60).

Table 6.2 shows the values of the sonic modulus, crystalline volume fraction, and density, of unoriented compression molded polyethylene films using resin EX 2. The table shows that the sonic modulus increases as the density (crystallinity) of the unoriented material increases. Similar results were reported by Samuels (60) using isotactic polypropylene thin films. In Figure 6.10, the reciprocals of the y-intercept and the slope give the intrinsic transverse moduli for the crystalline and amorphous phases, respectively. By using the sonic method, the $E^o_{t,c}$ and $E^o_{t,am}$ values are estimated to be 0.570×10^{10} Pa and 0.043×10^{10} Pa, respectively.

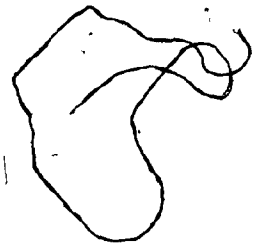


TABLE 6.2. Sonic Modulus (E_u), Crystalline Volume Fraction (X_c), and Density (ρ_s) of Unoriented Compression Molded Polyethylene Films

Sample	$E_u \times 10^{10}$ (Pa)	ρ_s (g/cc)	X_c
CM 1	0.129	0.9346	0.5461
CM 2	0.144	0.9429	0.6037
CM 3	0.168	0.9506	0.6570
CM 4	0.187	0.9598	0.7206

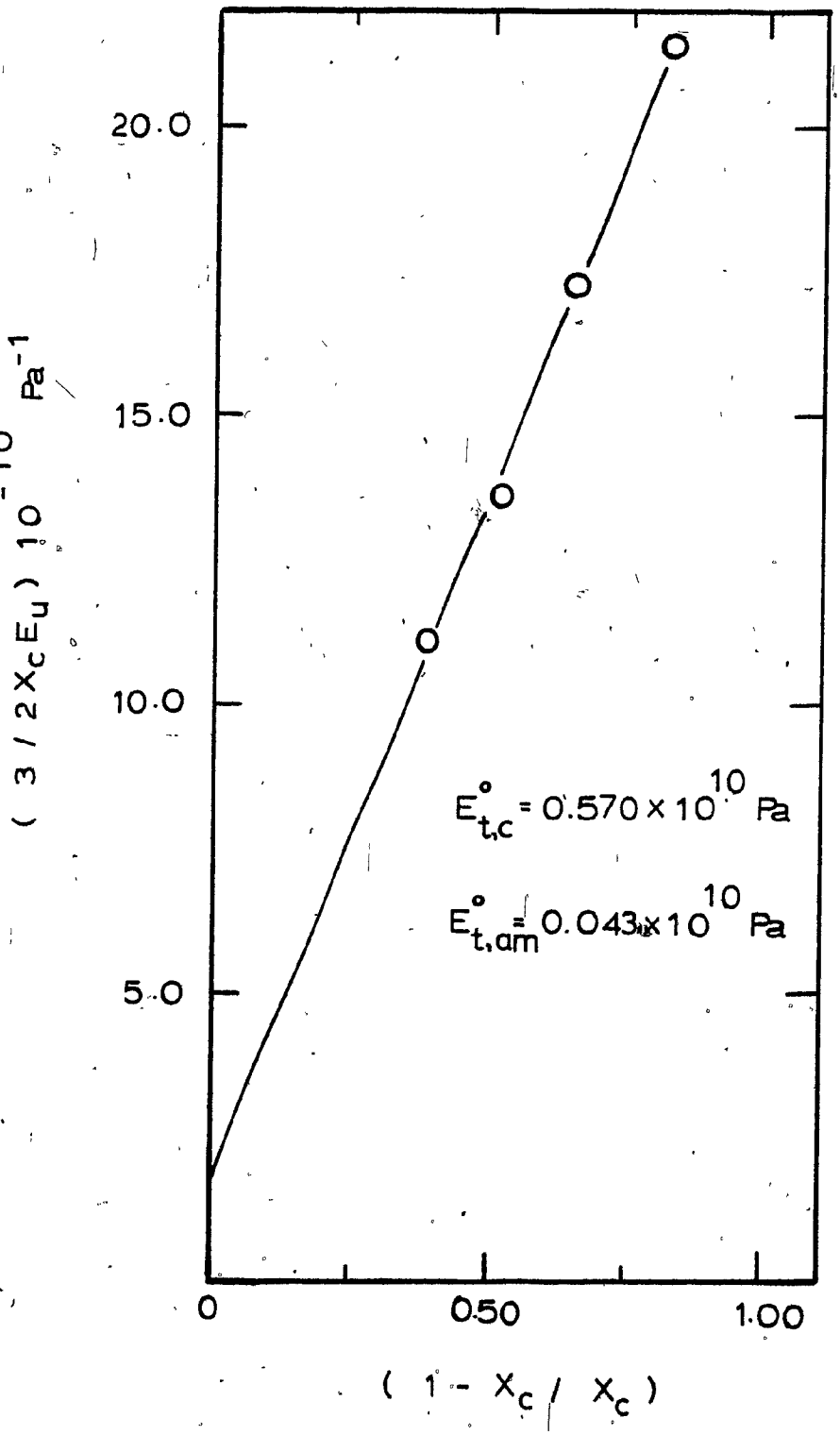


FIGURE 6.10. Estimation of Intrinsic Transverse Sonic Moduli Values

Table 6.3 compares the experimental values for the elastic modulus transverse to the chain ($E^o_{t,c}$) for polyethylene obtained by different techniques (132). Sakurada et al. (159) and Odajima and Maeda (160), each using the same stress X-ray technique, obtained values for $E^o_{t,c}$ for polyethylene ranging from 0.2 to 0.4×10^{10} Pa. Twisleton and White (161), using a neutron scattering technique, obtained a value of $E^o_{t,c}$ for polyethylene of 0.60×10^{10} Pa. The experimental values for $E^o_{t,c}$ show some differences depending on the experimental method employed. These differences will remain unresolved until further experimental work clarifies the situation (132). Thus, it appears that the $E^o_{t,c}$ value of 0.57×10^{10} Pa obtained by the sonic method employed in this study is in reasonable agreement with the results of different investigators (159, 160, 161).

As discussed in Section 4.2, the intrinsic sonic modulus of the amorphous region is defined as the transverse Young's modulus that the amorphous chains would have in a perfectly oriented sample. The lateral forces between amorphous chains in such a system would be expected to be lower than those in the crystal lattice (60, 132). The intrinsic lateral modulus of the amorphous region ($E^o_{t,am}$) for polyethylene was estimated in this work to be 0.043×10^{10} Pa, which is, as predicted, lower than the value of the intrinsic lateral modulus obtained for the crystal.

Once the material constants for the polymer have been estimated from sonic modulus studies on unoriented samples, the sonic modulus of the oriented injection molded samples can be

TABLE 6.3. Experimental Values Obtained for Elastic Modulus Transverse to the Chain ($E^{o}_{t,c}$) for Polyethylene. (Reference 132).

$E^{o}_{t,c}$ (measured) x 10^{10} Pa	Method	Authors (Reference)
0.38	X-ray	Sakurada *et al.* (159)
0.36 0.22 0.50	X-ray	Quoted by Odajima and Maeda (160)
0.60	Neutron	Twisleton and White (161)
0.57	Sonic	This work

determined from sonic speed measurements on oriented specimens. Furthermore, the isotropic reference state corresponding to the density (crystallinity) of each injection molded (oriented) specimen is obtained by the relationship shown in Figure 6.11, based on Equation (4-6).

6.5 Sonic Modulus

A detailed tabulation of the variation of the sonic modulus with position along the depth direction in the molding for the two resins is provided in Appendix 4. The error analysis associated with the measurement of sonic modulus is presented in Appendix 15.

The sonic modulus of an oriented film is a measure of the total orientation of the sample. It is a function of the orientation of both the crystalline and amorphous regions as well as the amount of each phase present in the sample (136). Figures 6.12 to 6.14 show the variation of sonic modulus as a function of distance from the surface at various locations along the molding.

Generally, it is observed that the main differences in the sonic modulus measurements occur within the first 0.30 mm (300 μm) from the surface beyond which very little change is observed. Furthermore, as shown in Figures 6.12(a) and 6.12(b), the lowest orientation for resin EX 1 occurs at the surface. Orientation gradually increases to a maximum near the surface, independent of location along the molding. Figures 6.13 and 6.14 show that the highest orientation for resin EX 2 occurs at the surface,

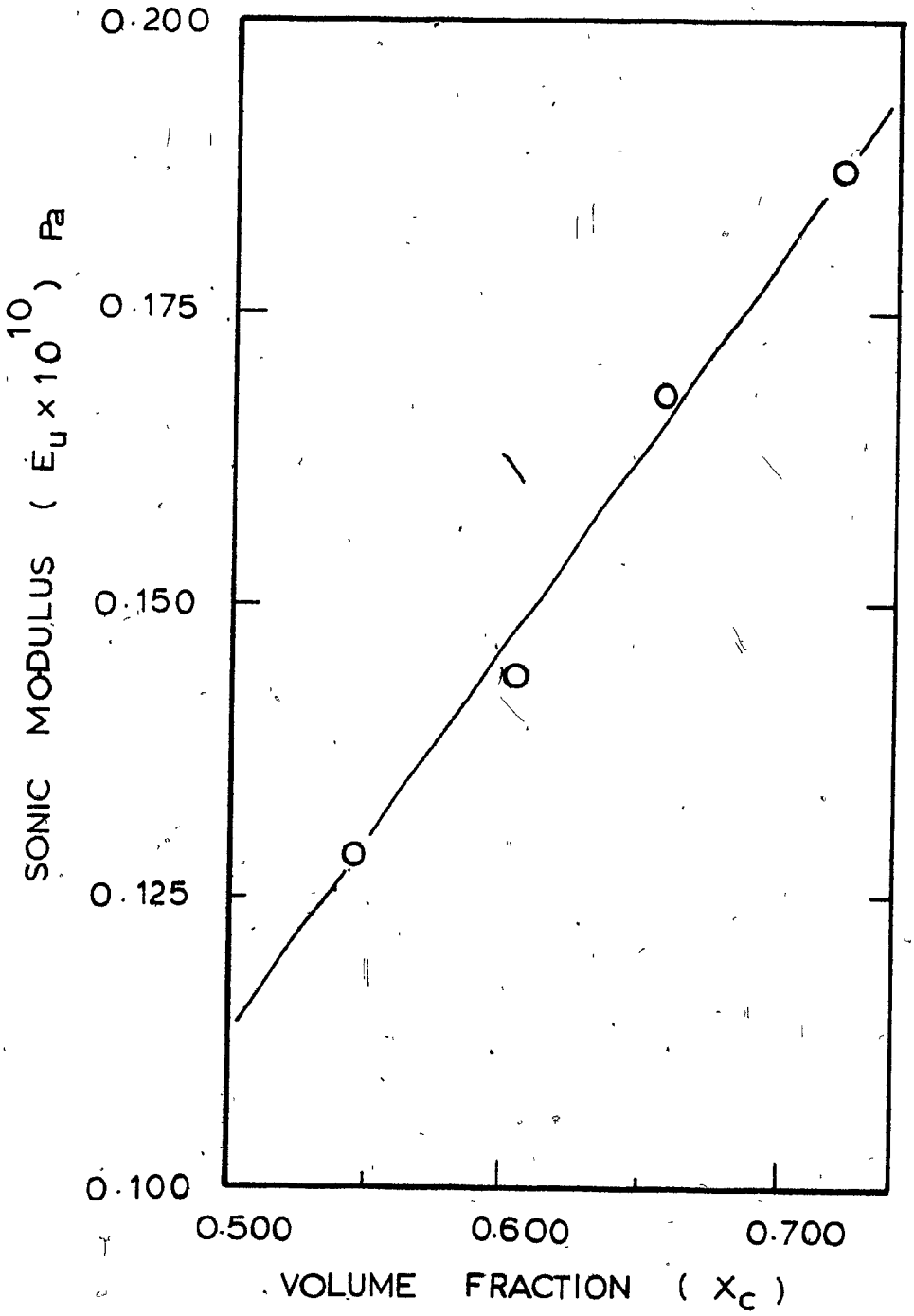


FIGURE 6.11. Plot of Sonic Modulus of Unoriented Samples Versus Volume Fraction Crystallinity

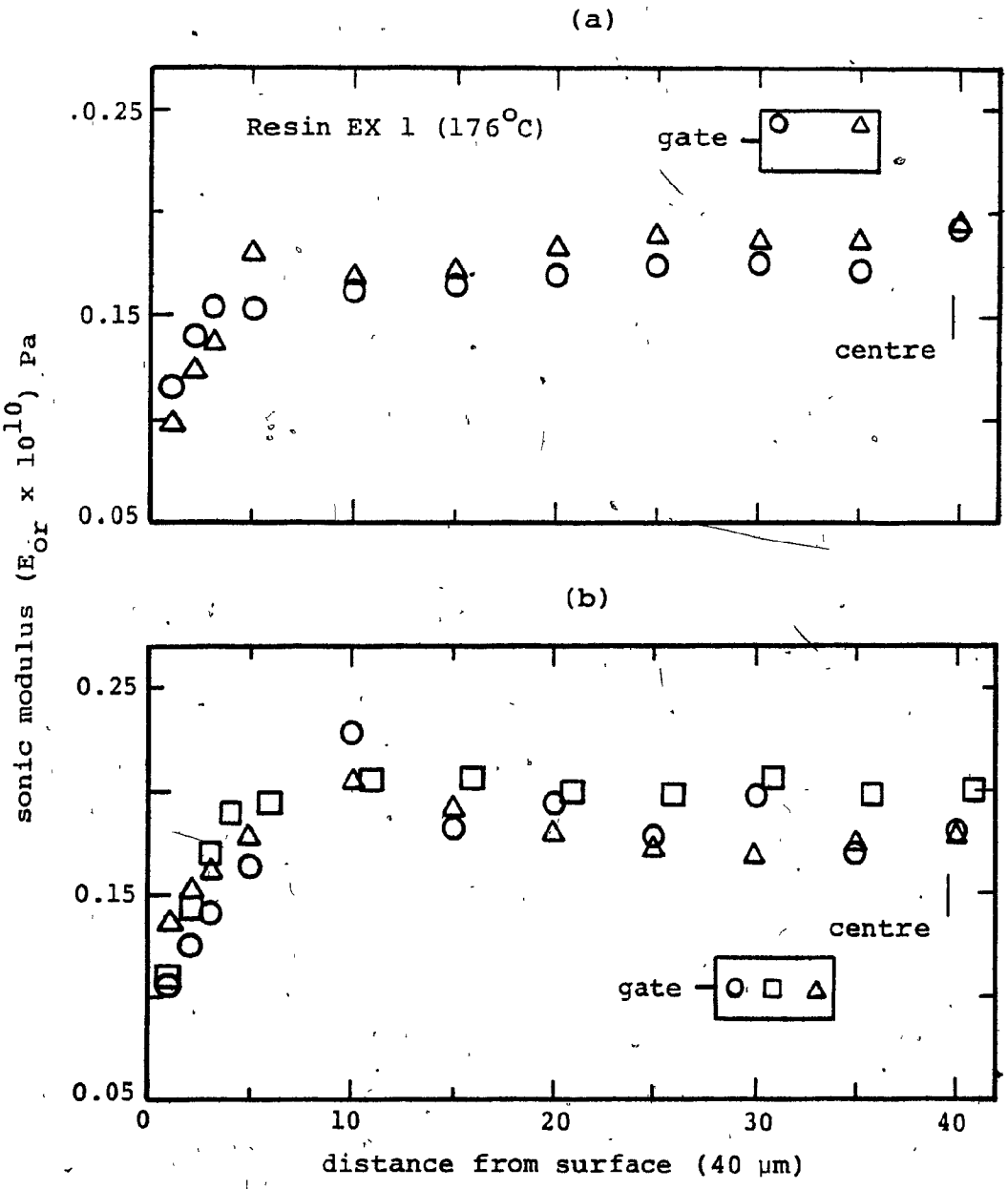


FIGURE 6.12. Variation of Sonic Modulus in the Depth Direction

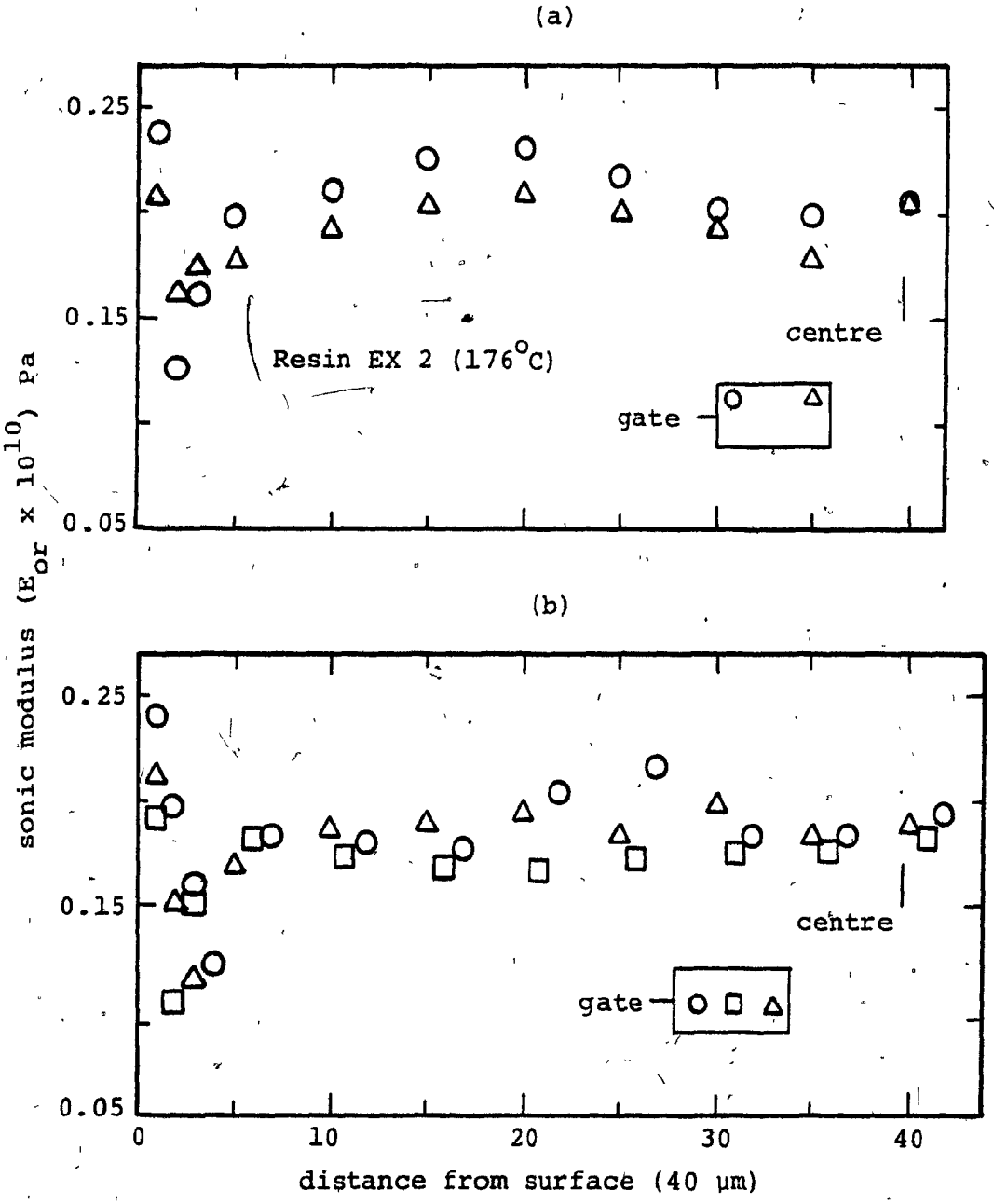


FIGURE 6.13. Variation of Sonic Modulus in the Depth Direction

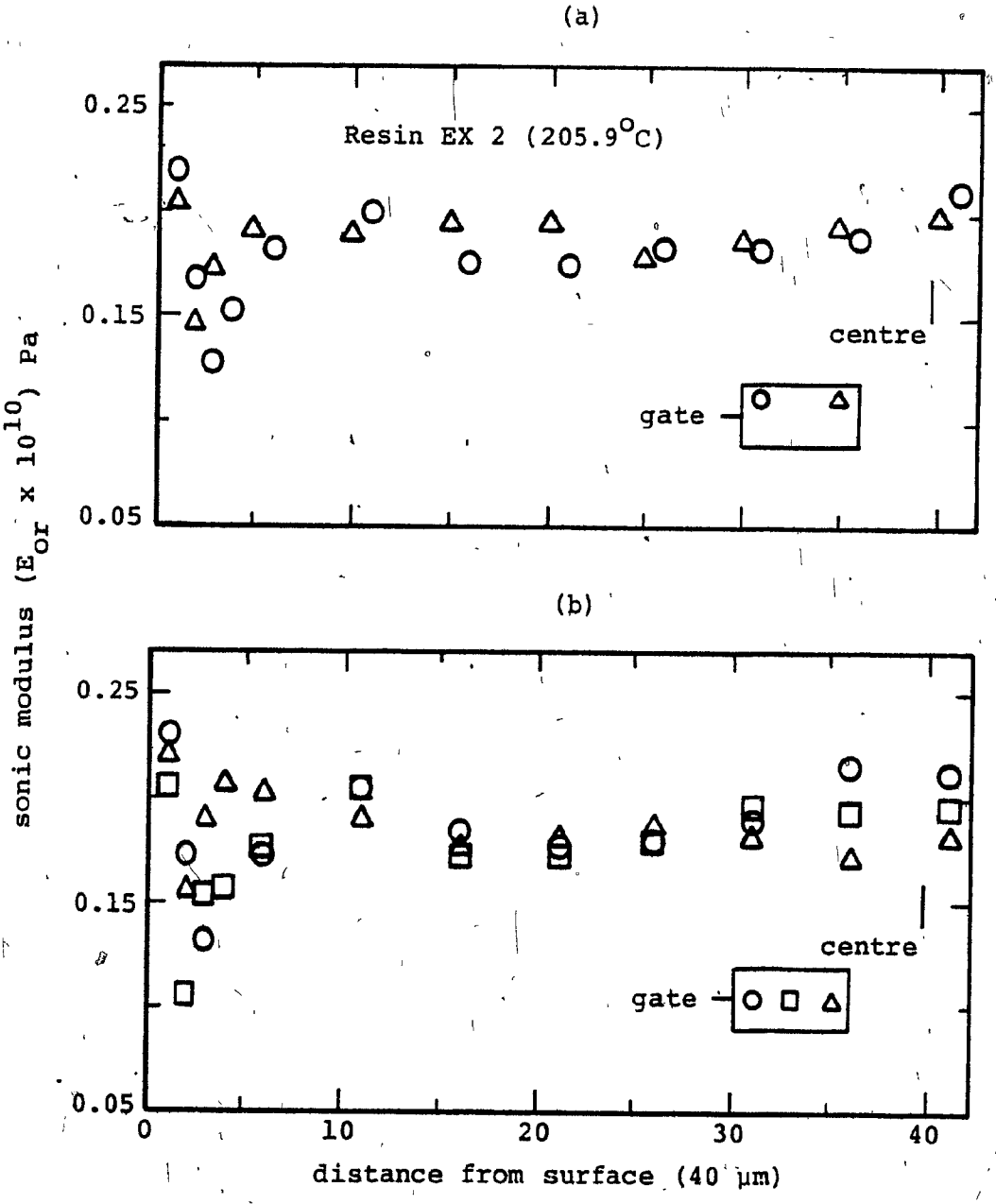


FIGURE 6.14. Variation of Sonic Modulus in the Depth Direction

but it decreases to a minimum near the surface and slowly increases to a constant value towards the core of the molding, regardless of injection melt temperature.

Published data on the distribution of orientation in the depth direction in injection molded articles have shown that the degree of orientation is a maximum at or near the surface of the molding and that orientation decreases as the centre of the molding is approached (114, 117, 118, 121). The relatively high degree of orientation at or near the surface has been attributed by Tadmor (162) to steady elongational flow in the advancing melt front. He argues that the source of the skin layer is the central region of the flow where the shear rates are very low and, therefore, it can be assumed that there is no prior deformation history of this layer except the elongational flow in the advancing front. The melt elements that contact the cold mold walls solidify instantaneously so that whatever orientation is induced during flow is retained in them.

The observation that resin EX 2 exhibits the highest orientation near the surface which decreases to a minimum towards the core whilst resin EX 1 exhibits the lowest orientation at the surface which increases to a constant value towards the core, may be explained by both the pressure dynamics and differences in the crystallization behavior of the two resins during the molding cycle. During the filling stage, melt elements of resin EX 2 experience higher fill pressures, as shown in Table 6.1, and consequently, higher shear stresses during this stage of the molding process. Furthermore, previous shear crystallization

studies (121) have indicated that resin EX 2 tends to crystallize more readily under the influence of shear. As a result, any orientation induced during flow is retained. The minimum is probably due to the existence of a maximum in temperature close to the wall, as a result of viscous heating. On the other hand, resin EX 1, which crystallizes more readily under pressure than resin EX 2 (121), will develop the maximum residual orientation in material solidified during the packing stage. This material will be located near, but not at, the surface. It is also interesting to note that, whereas the highest values of orientation in EX 2 moldings are observed at the surface near the gate, the lowest values of overall orientation in EX 1 moldings are observed at the same location, i.e. at the surface near the gate. These differences are probably attributable to the complex interactions between crystallization, pressure, shear stress, and cooling rates for the two resins. It would be difficult to offer a satisfactory explanation for these effects in the absence of a complete, detailed mathematical model of the process and relevant phenomena.

Figure 6.15 compares the sonic modulus distributions in the depth direction of the two resins molded at a melt temperature of 176°C and the effect of increasing the melt temperature of resin EX 2 to 205.9°C, for a location midway from the gate. As distance from the surface increases, resin EX 2 tends to exhibit lower overall orientation than resin EX 1 molded under the same conditions. The same relationship is also observed for the other locations. The higher orientation observed for resin EX 1

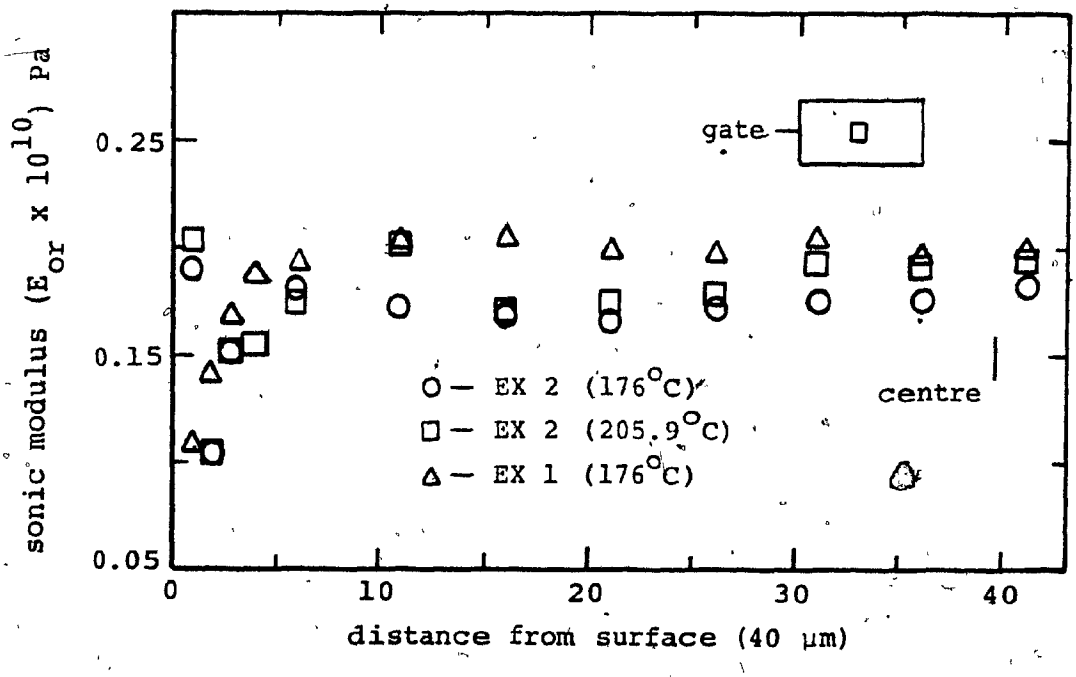


FIGURE 6.15. Typical Comparisons of Sonic Modulus Distributions

beyond 0.05 mm (50 μm) in the depth direction of the molding may be attributed to the fact that resin EX 1 tends to crystallize more readily under pressure, thus allowing shorter relaxation times. Most of the material away from the surface crystallizes under pressure during the packing and cooling segments of the molding cycle. Therefore, it is expected that resin EX 1 would exhibit higher levels of residual orientation away from the molding surface.

Figure 6.15 also shows that the injection melt temperature has a small influence on the overall sonic modulus measured, although the tendency is to marginally increase the overall orientation. The same observation may be made by comparing Figures 6.13(a) and (b) to Figures 6.14(a) and (b), respectively.

Generally, the results of the sonic modulus (overall orientation) measurements may be summarized as follows:

(1) Most of the differences between locations occur within the first 0.30 mm (300 μm) from the surface of the molding beyond which the sonic modulus decreases to a constant value towards the core region.

(2) Resin EX 2 tends to exhibit the highest sonic modulus at the surface which decreases as distance from the surface increases, whereas resin EX 1 tends to show the lowest sonic modulus at the surface, but increases to a maximum near the surface and gradually decreases as distance from the surface continues to increase.

(3) Except for near the surface, resin EX 1 tends to exhibit higher sonic modulus than that of resin EX 2,

at the corresponding locations.

(4) Whereas the highest values of overall orientation in EX 2 moldings are observed at the surface near the gate, the lowest values of overall orientation in EX 1 moldings are observed at the same location.

(5) Increasing the injection melt temperature seems to have little impact on the overall sonic modulus throughout the molded part.

(6) As in the case of crystallization phenomena, although some qualitative explanations might account for some of the observed effects and distributions, a dependable quantitative explanation must be based on a realistic mathematical model of the process and phenomena involved.

The total orientation in injection molded specimens, as measured by the sonic modulus method, has been discussed above. It is now worthwhile to compare the orientation distributions obtained by this method with those obtained from the birefringence technique, since the latter method is also a measure of the overall orientation. The results of the birefringence measurements are discussed in the next section.

6.6 Birefringence

A detailed tabulation of the variation of birefringence with position along the depth direction in the molding for the two resins, is provided in Appendix 5. The error analysis associated with the measurement of birefringence is presented in

Appendix 15.

As discussed in Section 4.3, the measured birefringence is a measure of the overall orientation in the sample. It is a function of the orientation of both the crystalline and amorphous regions as well as that of the amount of each phase present in the sample. Figures 6.16 to 6.18 show the variation of birefringence as a function of distance from the surface at various locations along the molding, for the two resins molded at a melt temperature of 176°C and for resin EX 2 molded at a high melt temperature of 205.9°C. Generally, as observed for the sonic modulus measurements, maximum birefringence is observed at or near the surface and gradually decreases as distance from the surface increases. Similar observations of birefringence distributions measured in the depth direction of injection molded articles have been reported previously (117, 118, 156).

In general, most of the birefringence differences occur within the first 0.30 mm (300 μm) of the molding, beyond which the birefringence remains constant. This observation is consistent with that obtained from the measurements of the sonic modulus distributions discussed in the previous section.

Figures 6.16(a) and 6.16(b) show that resin EX 1 tends to exhibit markedly lower birefringence near the skin layer than resin EX 2, shown in Figures 6.17(a) and 6.17(b), at the corresponding locations along the molding. It is interesting to note that negative birefringence is observed near the surface for the location near the gate for resin EX 1. Since polyethylene birefringence is inherently positive, the negative value

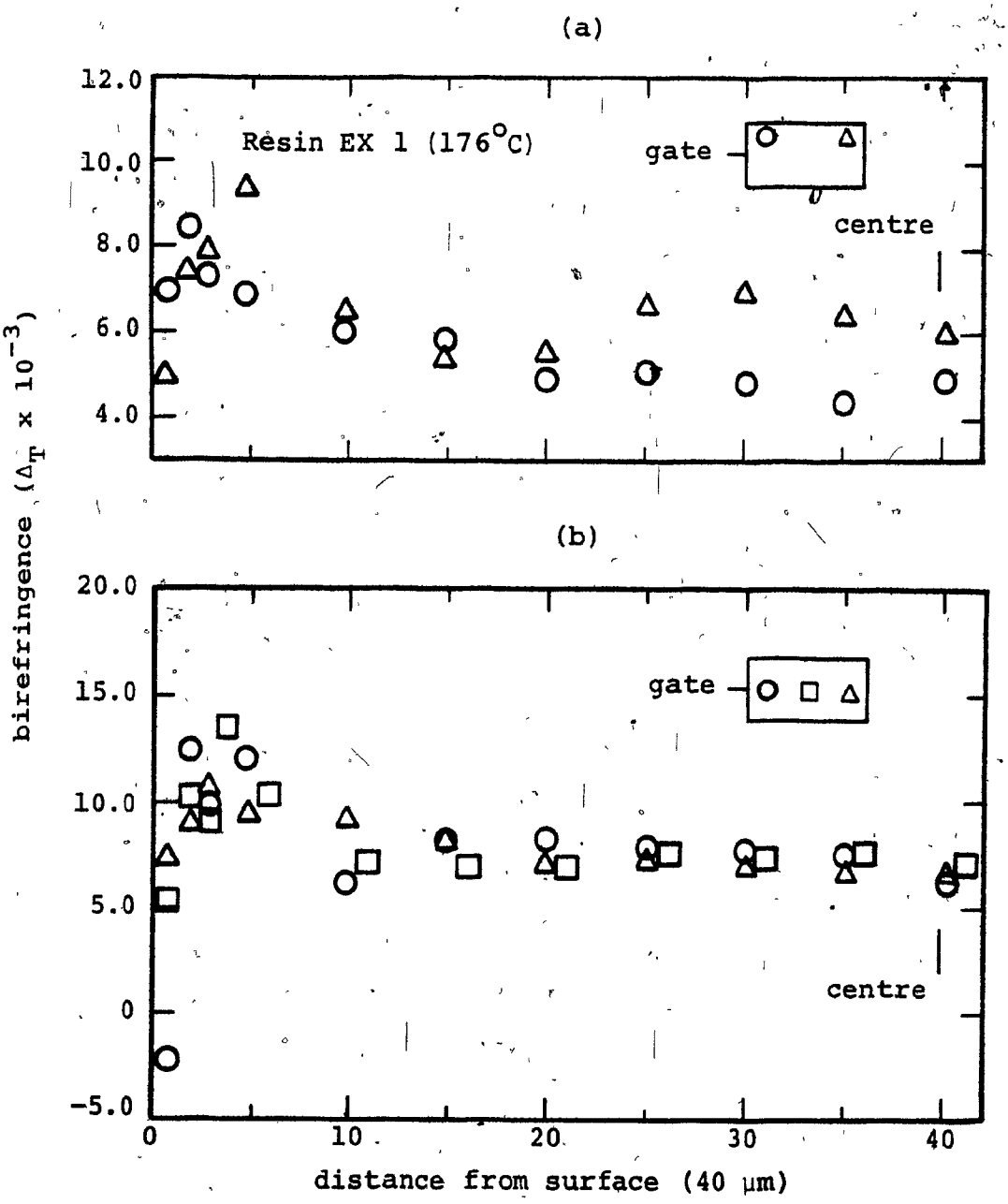


FIGURE 6.16. Variation of Total Birefringence in the Depth Direction

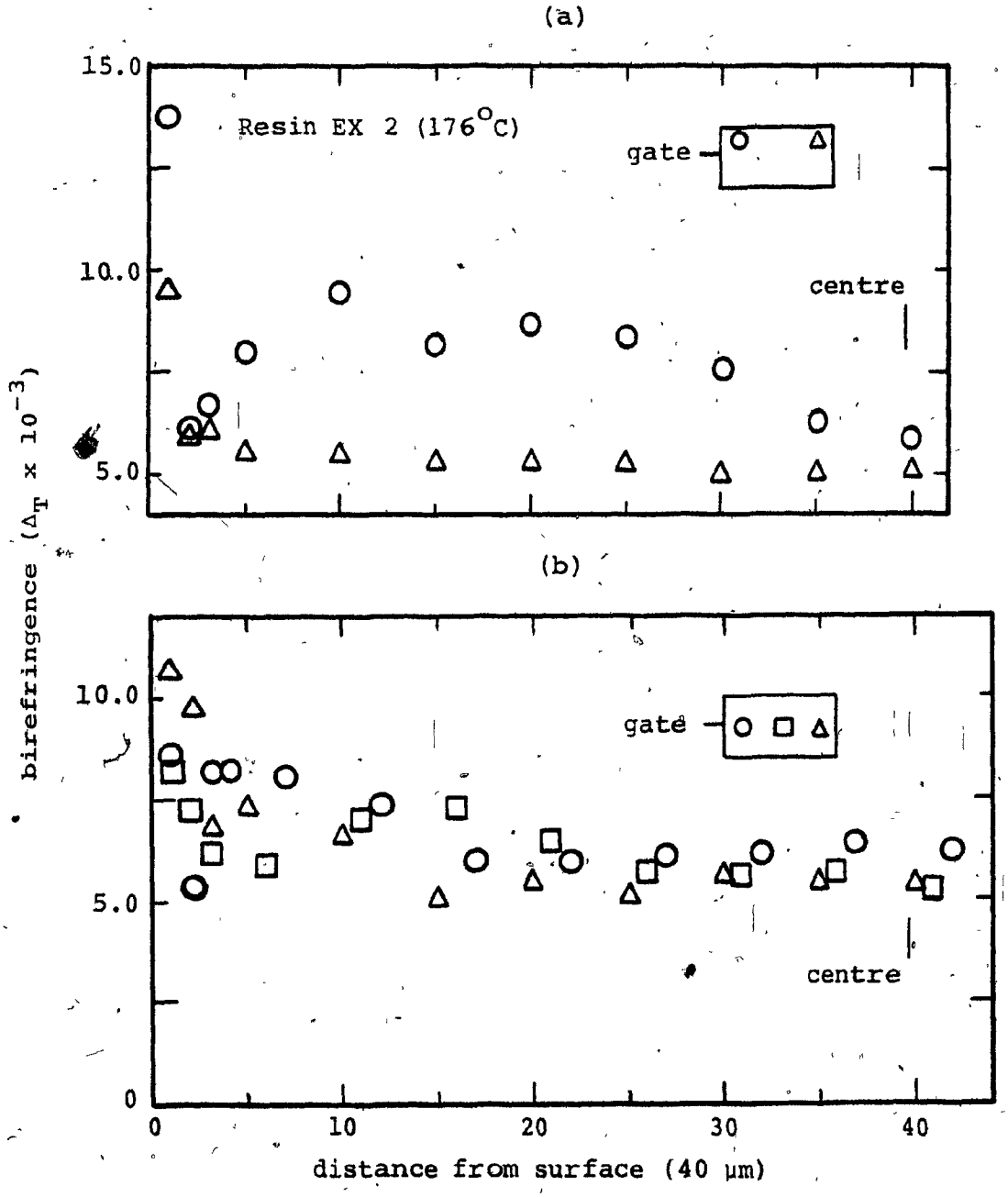


FIGURE 6.17. Variation of Total Birefringence in the Depth Direction

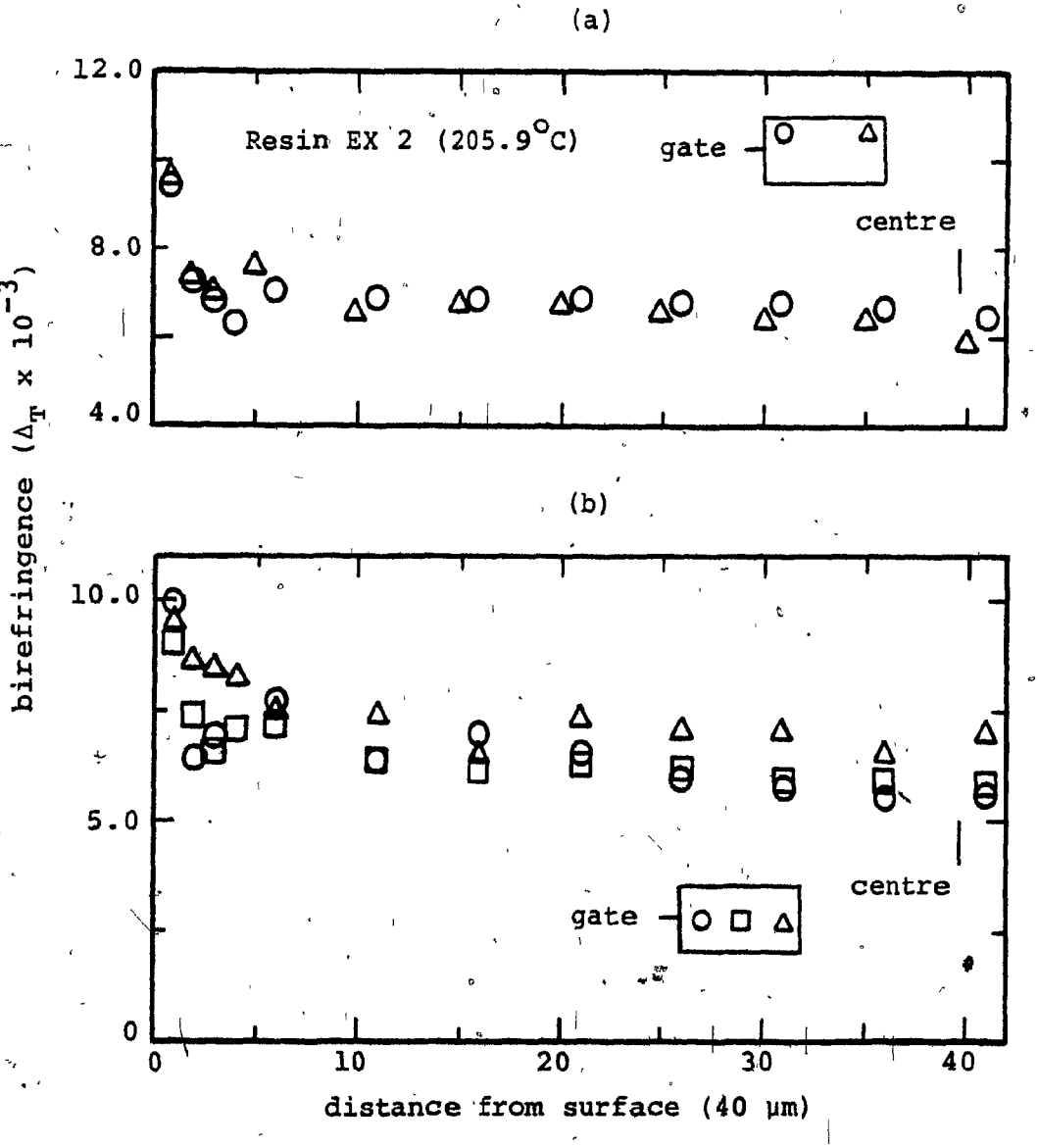


FIGURE 6.18. Variation of Total Birefringence in the Depth Direction

reported is an indication of the change in the principal direction of stress. The negative birefringence observed is thought to be a reflection of the fact that the layer near the surface experiences a hoop stress in the radial flow region (156). Other workers (163) have shown that when polyethylene crystallizes from an oriented amorphous network, the crystals form with their c-axes (chain axes), perpendicular to the direction of stretching of the amorphous material and since the c-axis of the polyethylene crystal is the axis of greatest polarizability (164), the measured birefringence at room temperature will have a negative sign. The maximum birefringence that is observed near the surface for resin EX 2 is independent of melt temperature, as shown in Figures 6.18(a) and (b), for the corresponding locations.

As an example, Figure 6.19 compares the birefringence distributions in the depth direction of the two resins molded at a melt temperature of 176°C and the effect of increasing the melt temperature of resin EX 2 to 205.9°C, for a location midway from the gate. It is observed that except near the surface, resin EX 1 tends to exhibit higher birefringence as distance from the surface increases. Generally, the higher birefringence is also observed for the other corresponding locations. Moreover, increasing the injection melt temperature tends to show very little change in the overall birefringence distribution.

Generally, the results of the birefringence (total orientation) measurements are consistent with those obtained from the sonic modulus method and hence, may be summarized as follows:

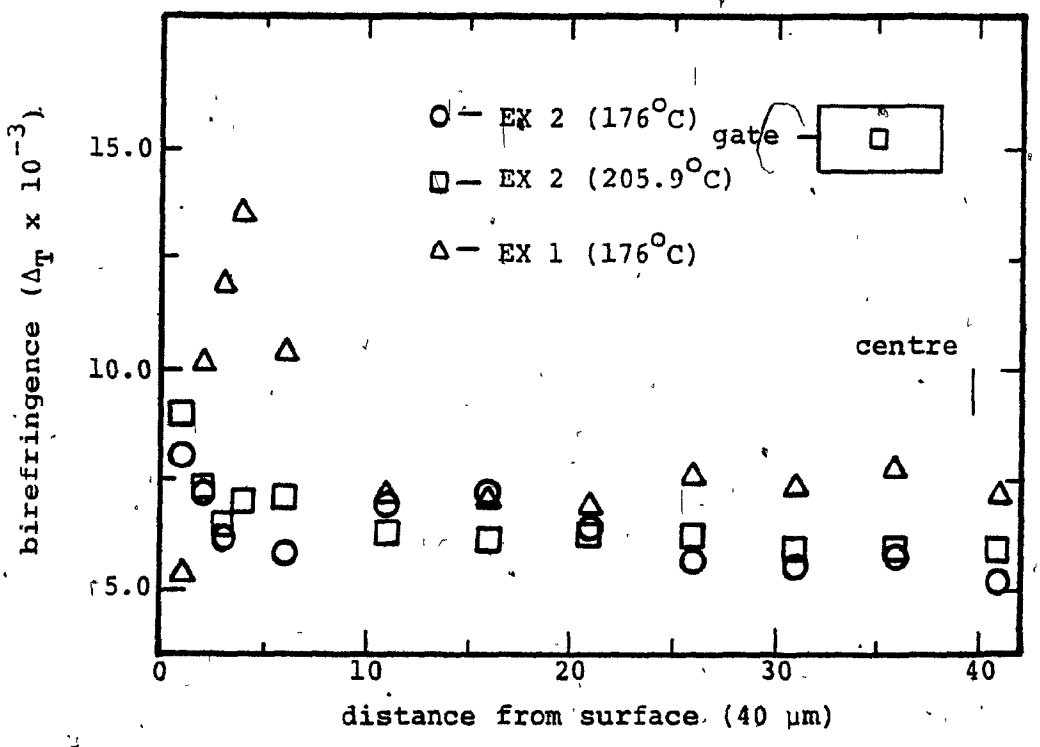


FIGURE 6.19. Typical Comparison of Total Birefringence Distributions

(1) Most of the differences occur within the first 0.30 mm (300 μm) from the surface of the molding beyond which the birefringence decreases to a constant value towards the core region.

(2) Resin EX 2 tends to exhibit the highest birefringence near the surface which decreases as distance from the surface increases, whereas resin EX 1 tends to show the lowest birefringence at the surface, but increases to a maximum near the surface and gradually decreases towards the core.

(3) Except for near the surface, resin EX 1 tends to exhibit higher birefringence than that of resin EX 2, at the corresponding locations.

(4) Increasing the injection melt temperature seems to have little impact on the overall birefringence throughout the molding.

It is apparent that the results of birefringence measurements discussed above are in reasonable agreement with those obtained with the sonic modulus measurements discussed in Section 6.5. The next stage in the characterization of microstructure in injection molded parts is to determine the degree of orientation of the crystalline phase. This is achieved by employing wide-angle X-ray diffraction technique, the results of which are discussed in the following section.

6.7 Wide-Angle X-Ray Diffraction

A detailed tabulation of the variations of the orientation

functions, f, for the crystallographic a, b, and c axes with the depth direction of the molding for resins EX 1 and EX 2 molded at the melt temperature of 176°C and for resin EX 2 molded at the high melt temperature of 205.9°C are provided in Appendix 6. The error analysis associated with the measurement of the crystalline orientation functions is presented in Appendix 15.

Table 6.4 shows the spacing of the (hkl) planes which is representative of all samples investigated by the X-ray diffraction method. There were no differences between the different samples analyzed. The reflections listed correspond to the region $15^{\circ} < 2\theta < 55^{\circ}$. Furthermore, the unit cell of the crystals is of the ordinary orthorhombic type (137).

Figures 6.20 to 6.29 show the variations of the orientation functions, f, for crystallographic a, b, and c axes in the depth direction at the various locations for the two resins molded at the melt temperature of 176°C. Figures 6.30 to 6.34 show the variations of the crystallographic a, b, and c axes in the depth direction at the corresponding locations for resin EX 2 molded at the high melt temperature of 205.9°C.

Generally, the a-axis tends to be oriented in the flow direction while the b and c axes vary symmetrically about this direction. Similar a-axis orientation has been observed in tabular blown films (103-105) and in the relaxation of stretched polyethylene films (48-50, 162). Furthermore, the variation of the orientations of the a, b, and c axes tends to be most pronounced within the first 0.30 mm (300 μm) from the surface, beyond which the distributions remain constant. The variations

TABLE 6.4. Spacing of Reflected Planes

Wide-angle X-ray Diffraction Pattern (Laue Method)

Cu K_α radiation $\lambda = 1.5418\ A^{o}$

Sample to film distance, L = 4.224 cms

Diameter of Ring D (cm)	$2\theta = \tan^{-1}(D/2L)$	$d_{hkl} = \frac{\lambda}{2 \sin\theta}$ (A^{o})	Miller Indices (hkl)
3.35	$21^{o}\ 38'$	4.10 (4.102)	(110)
3.78	$24^{o}\ 6'$	3.69 (3.696)	(200)
4.95	$30^{o}\ 22'$	2.94 (2.956)	(210)
6.25	$36^{o}\ 30'$	2.46 (2.467)	(020)
7.10	$40^{o}\ 3'$	2.25 (2.254)	(011)
7.40	$41^{o}\ 13'$	2.19 (2.203)	(310)
7.60	$41^{o}\ 59'$	2.15 (2.156)	(111)
7.95	$43^{o}\ 16'$	2.09 (2.089)	(201)
9.20	$47^{o}\ 26'$	1.92 (1.924)	(211)

The values of the interplanar spacing, d_{hkl}, in brackets refer to the calculated values obtained from reference (137).

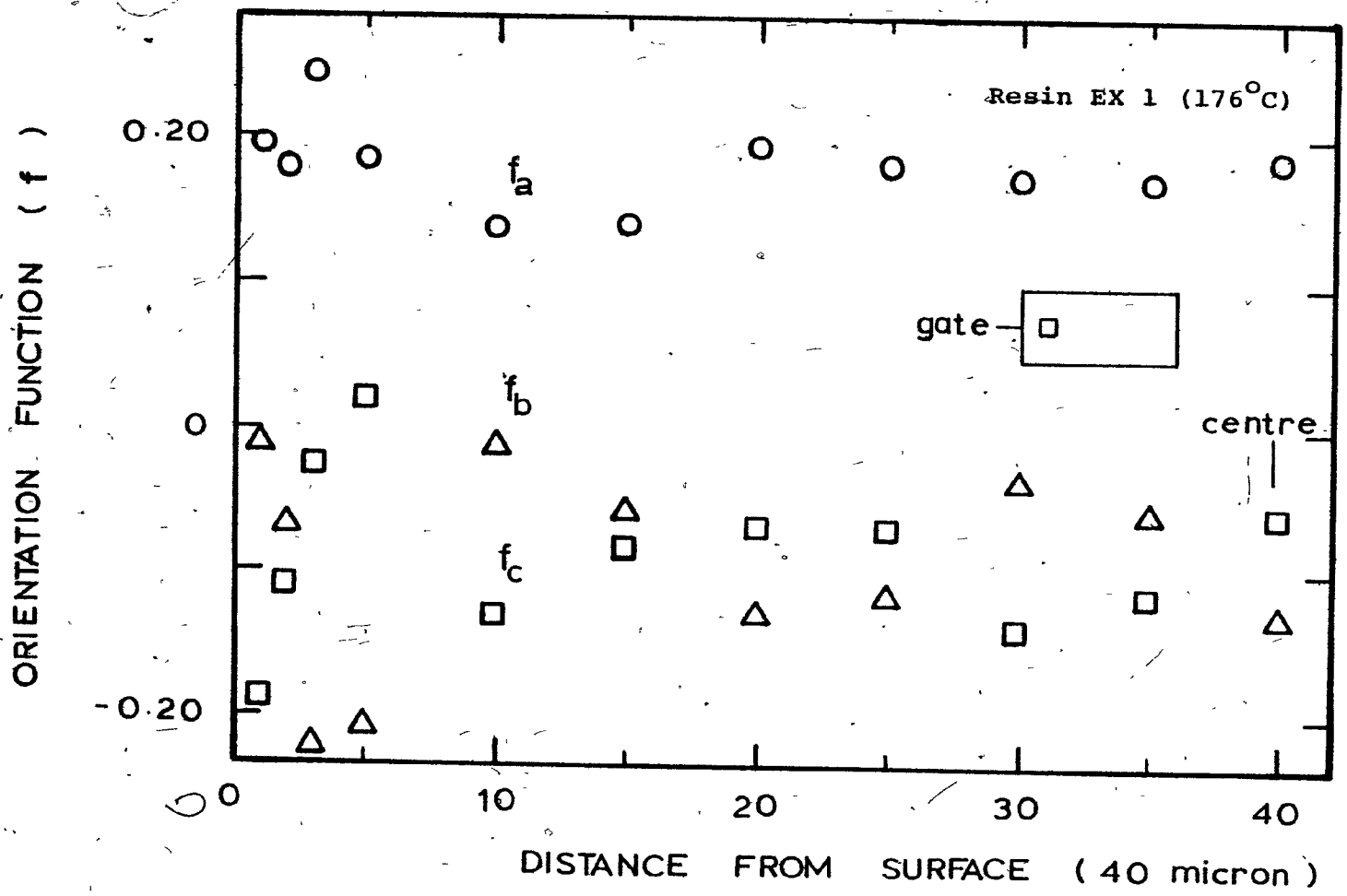


FIGURE 6.20. Variation of the Crystallographic Axes in the Depth Direction

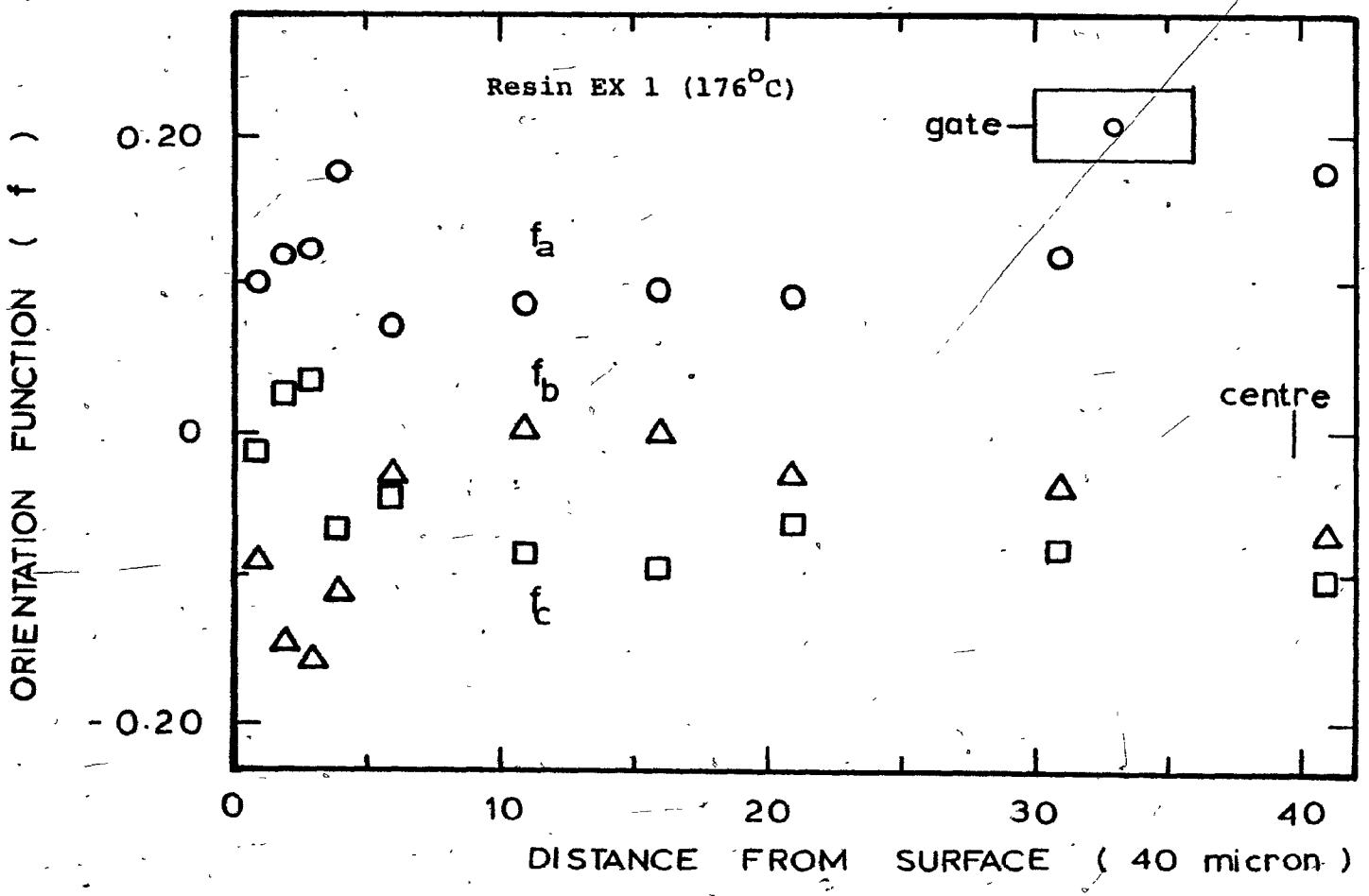


FIGURE 6.21. Variation of the Crystallographic Axes in the Depth Direction

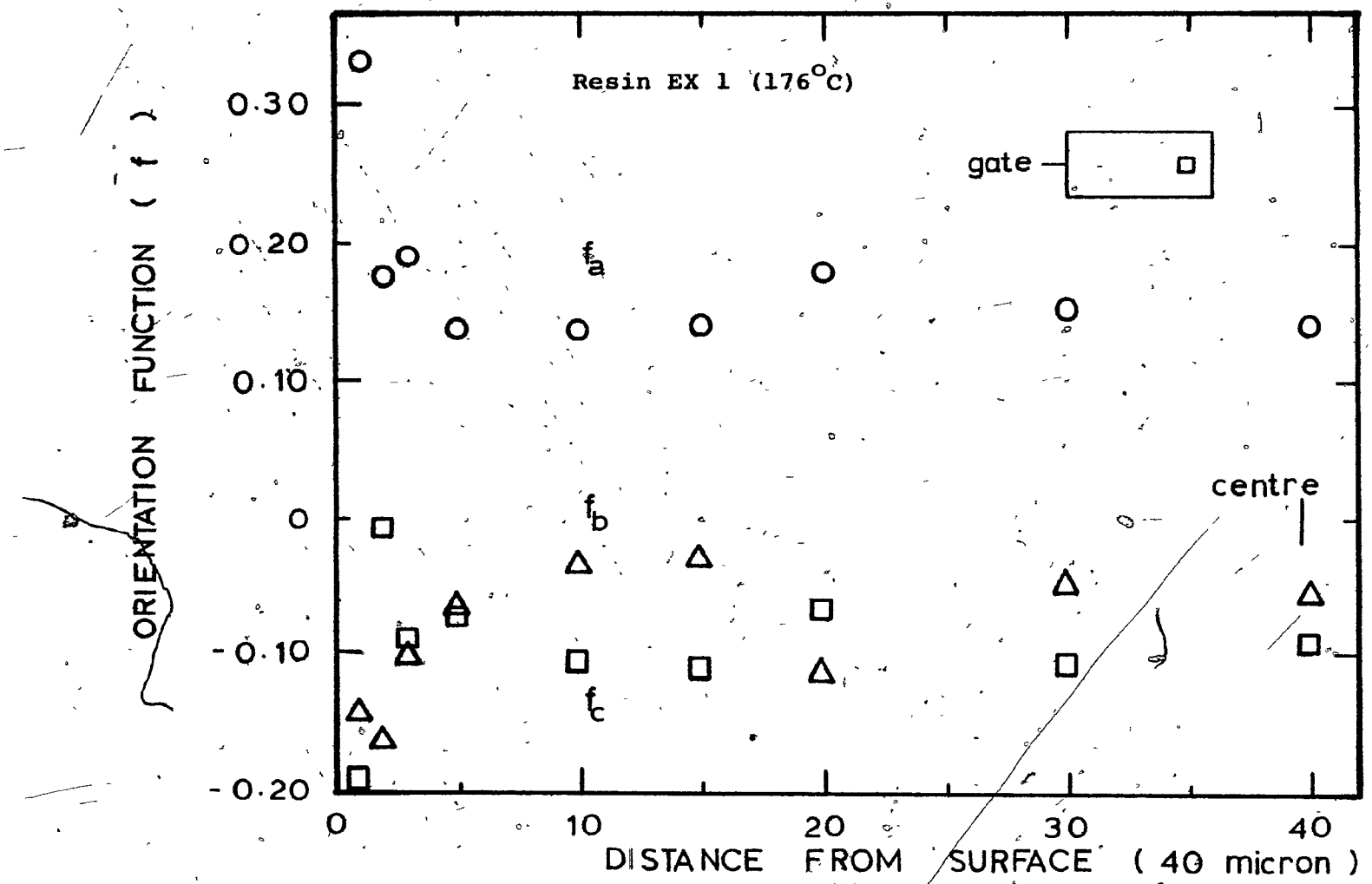


FIGURE 6.22. Variation of the Crystallographic Axes in the Depth Direction

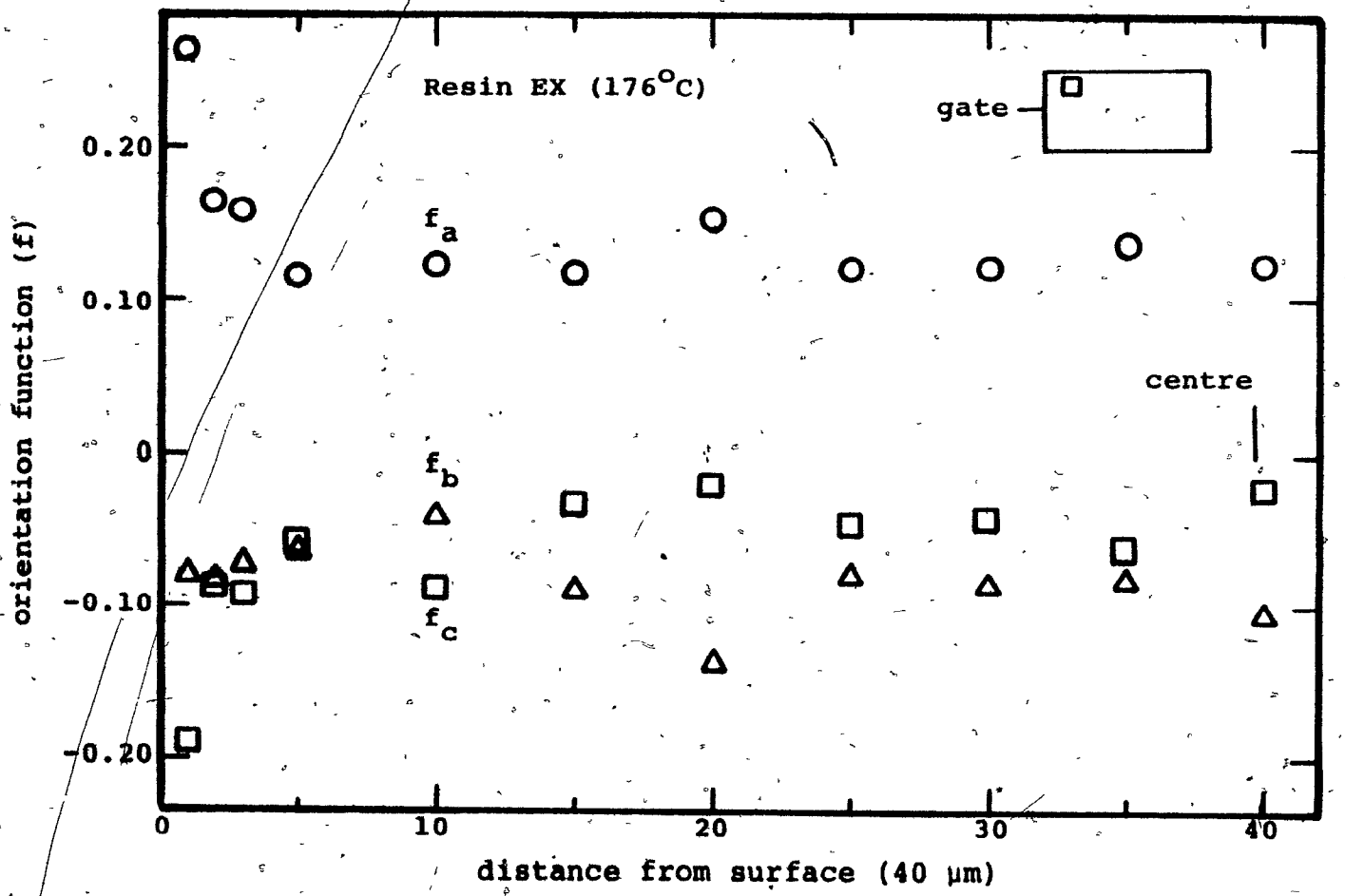


FIGURE 6.23. Variation of the Crystallographic Axes in the Depth Direction

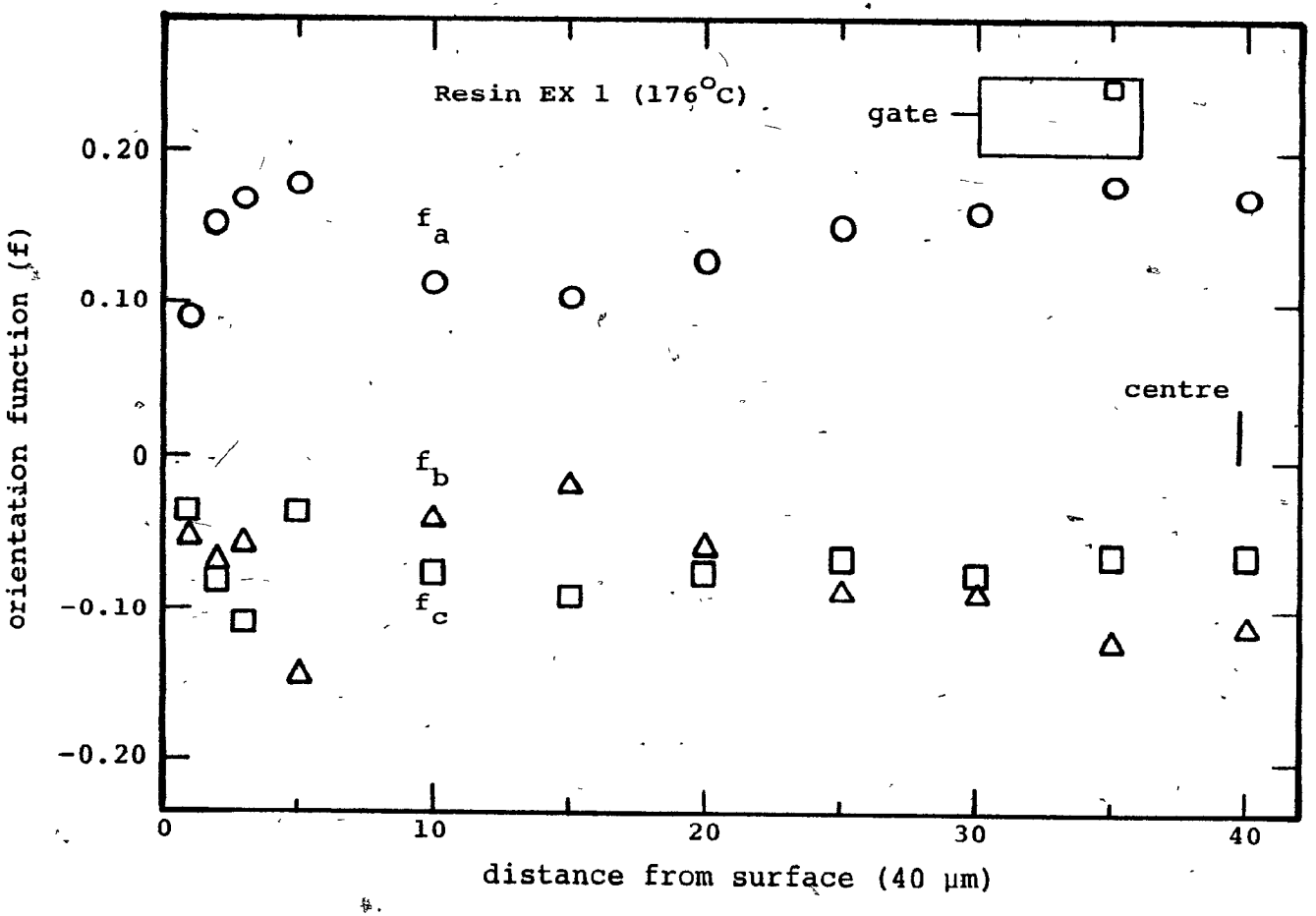


FIGURE 6.24. Variation of the Crystallographic Axes in the Depth Direction

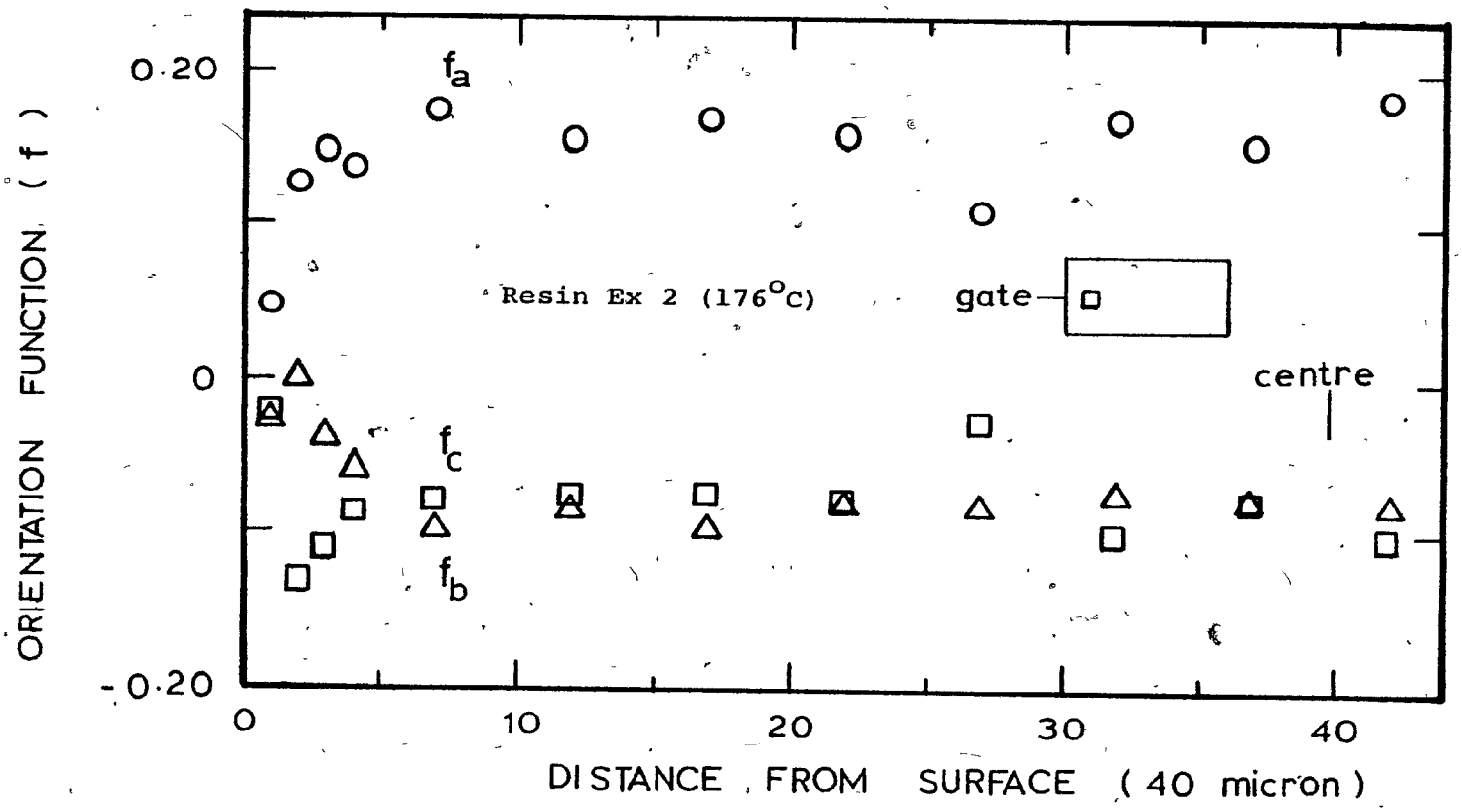


FIGURE 6.25. Variation of the Crystallographic Axes in the Depth Direction

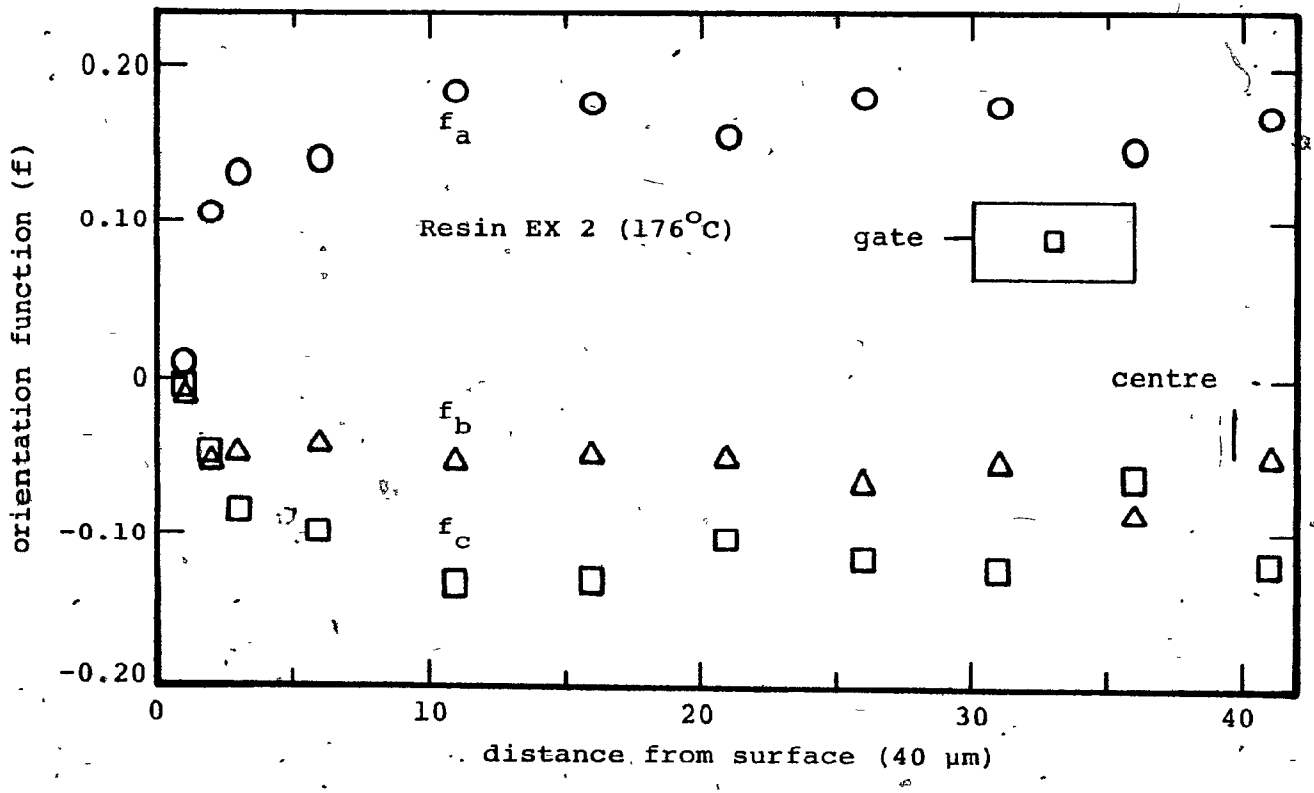


FIGURE 6.26. Variation of the Crystallographic Axes in the Depth Direction

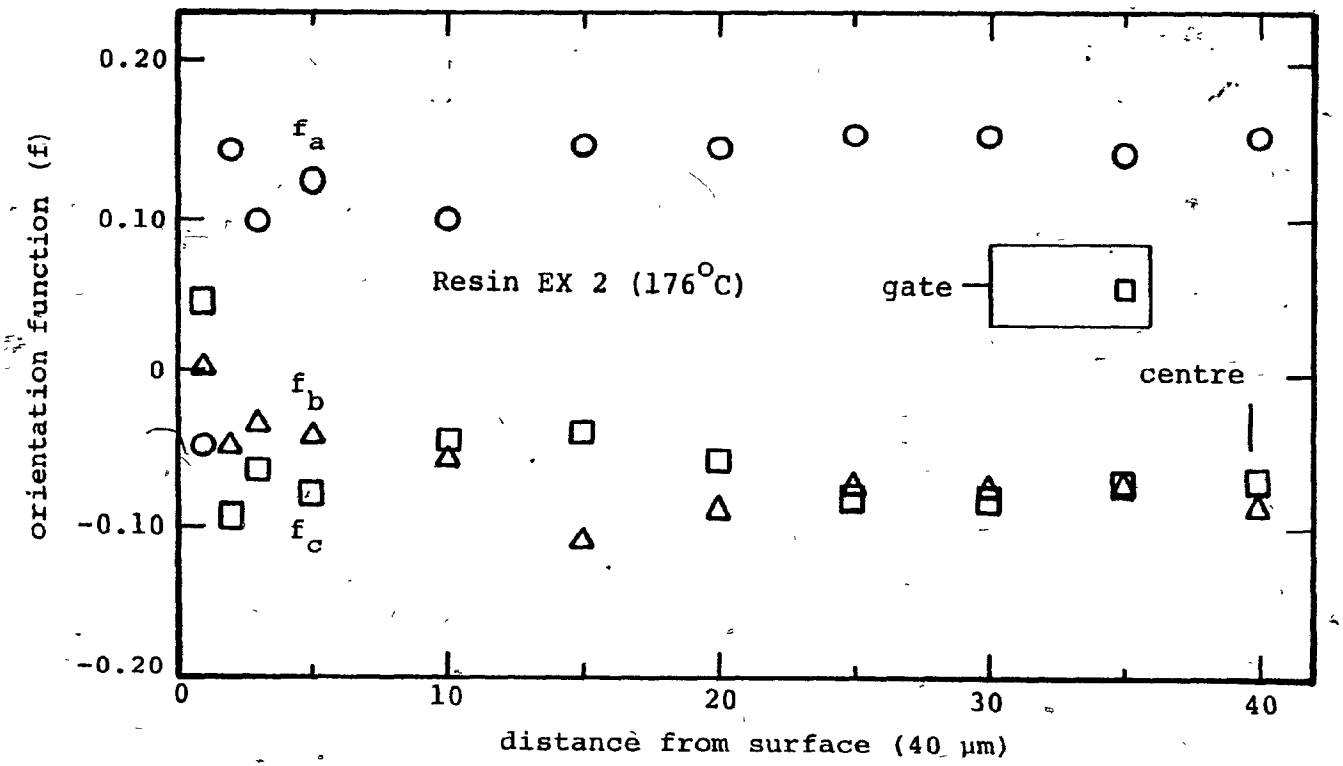


FIGURE 6.27. Variation of the Crystallographic Axes in the Depth Direction

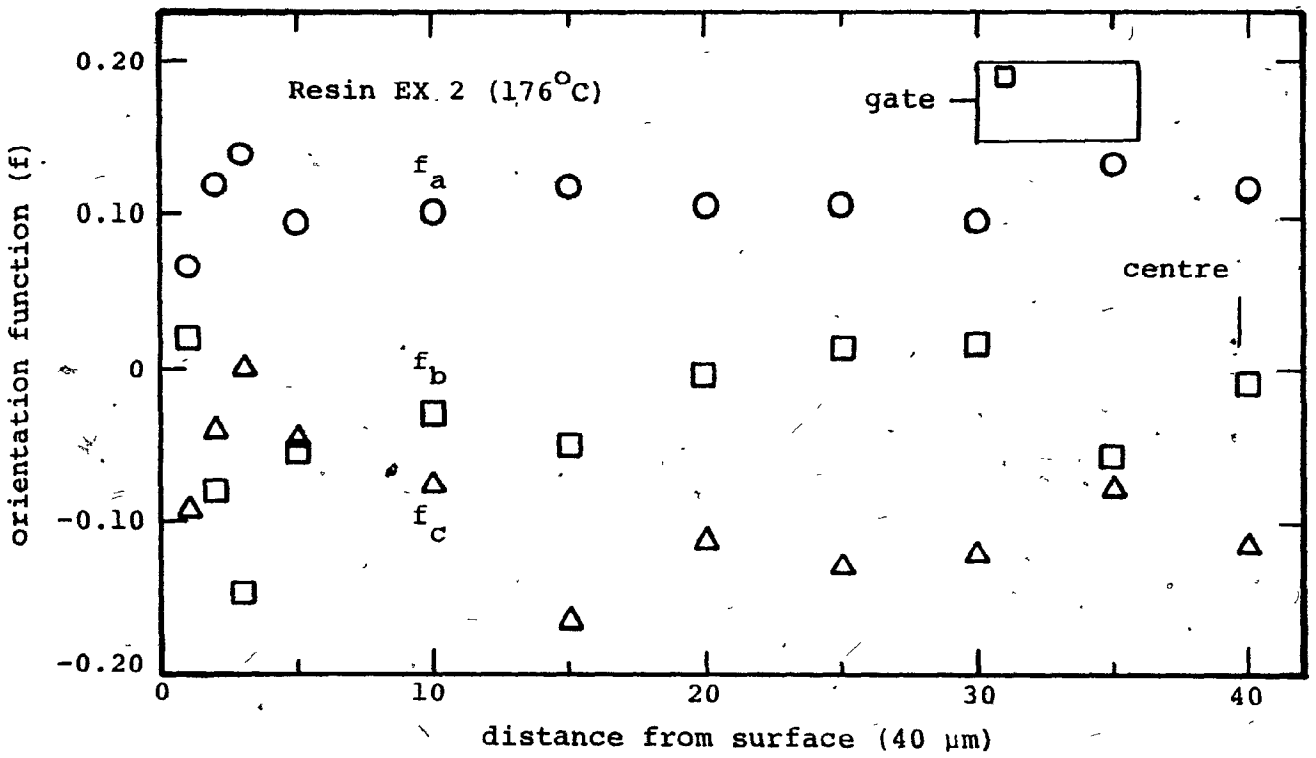


FIGURE 6.28. Variation of the Crystallographic Axes in the Depth Direction

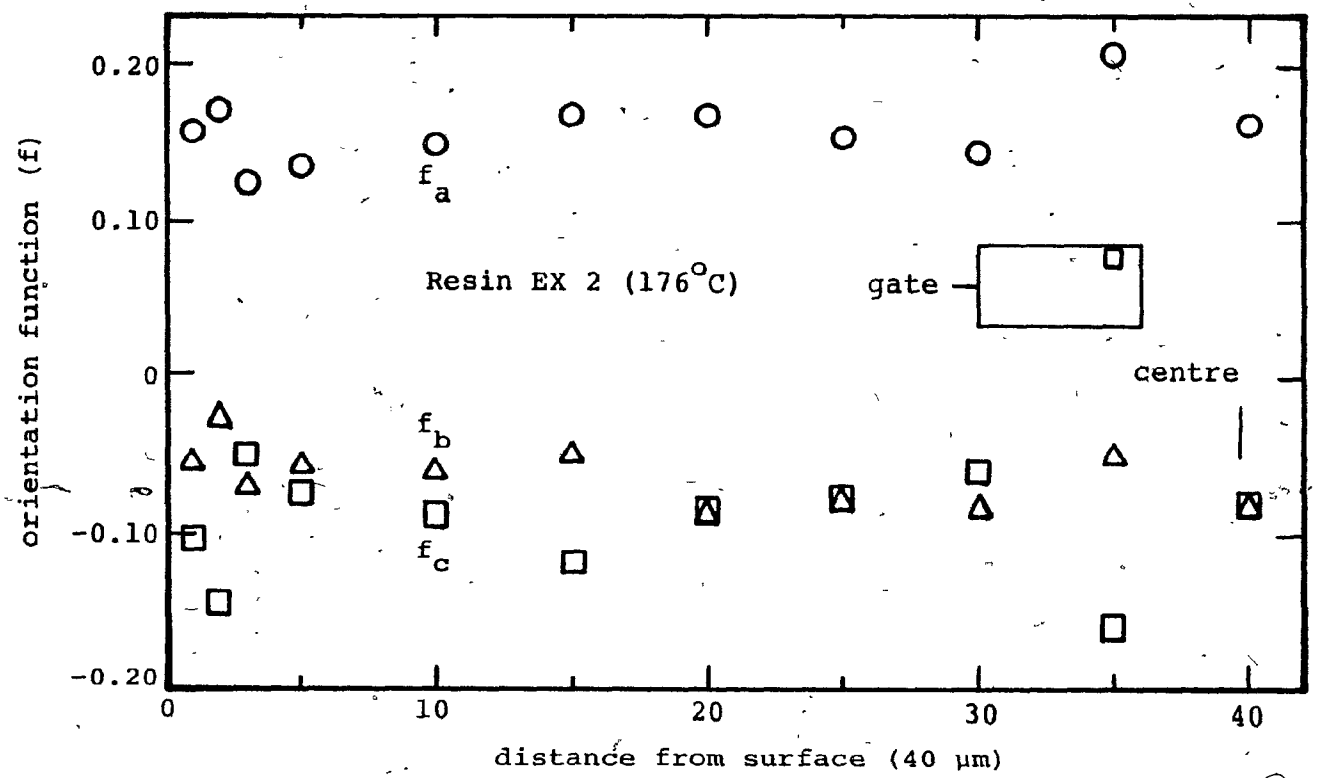


FIGURE 6.29. Variation of the Crystallographic Axes in the Depth Direction

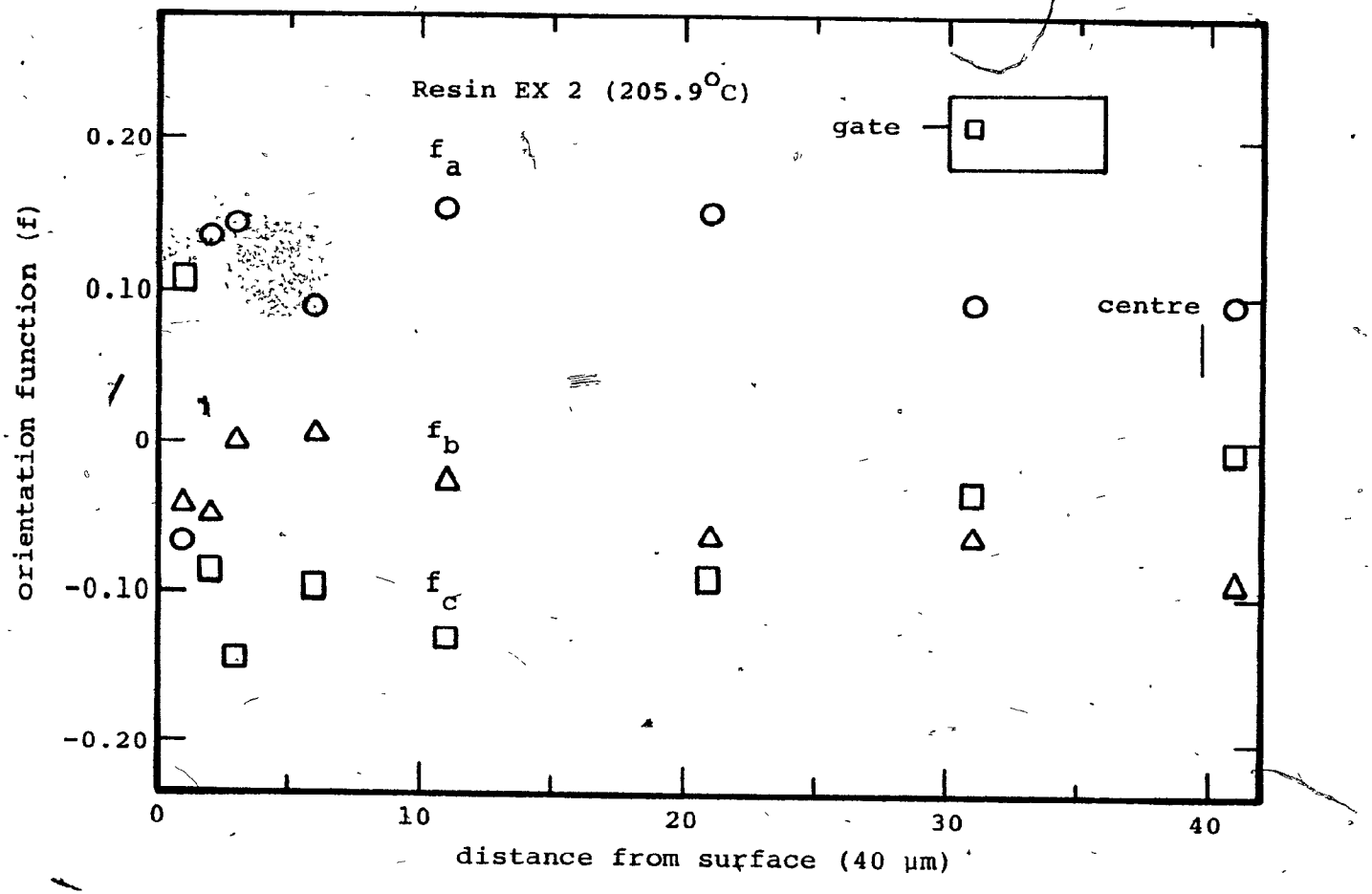


FIGURE 6.30. Variation of the Crystallographic Axes in the Depth Direction

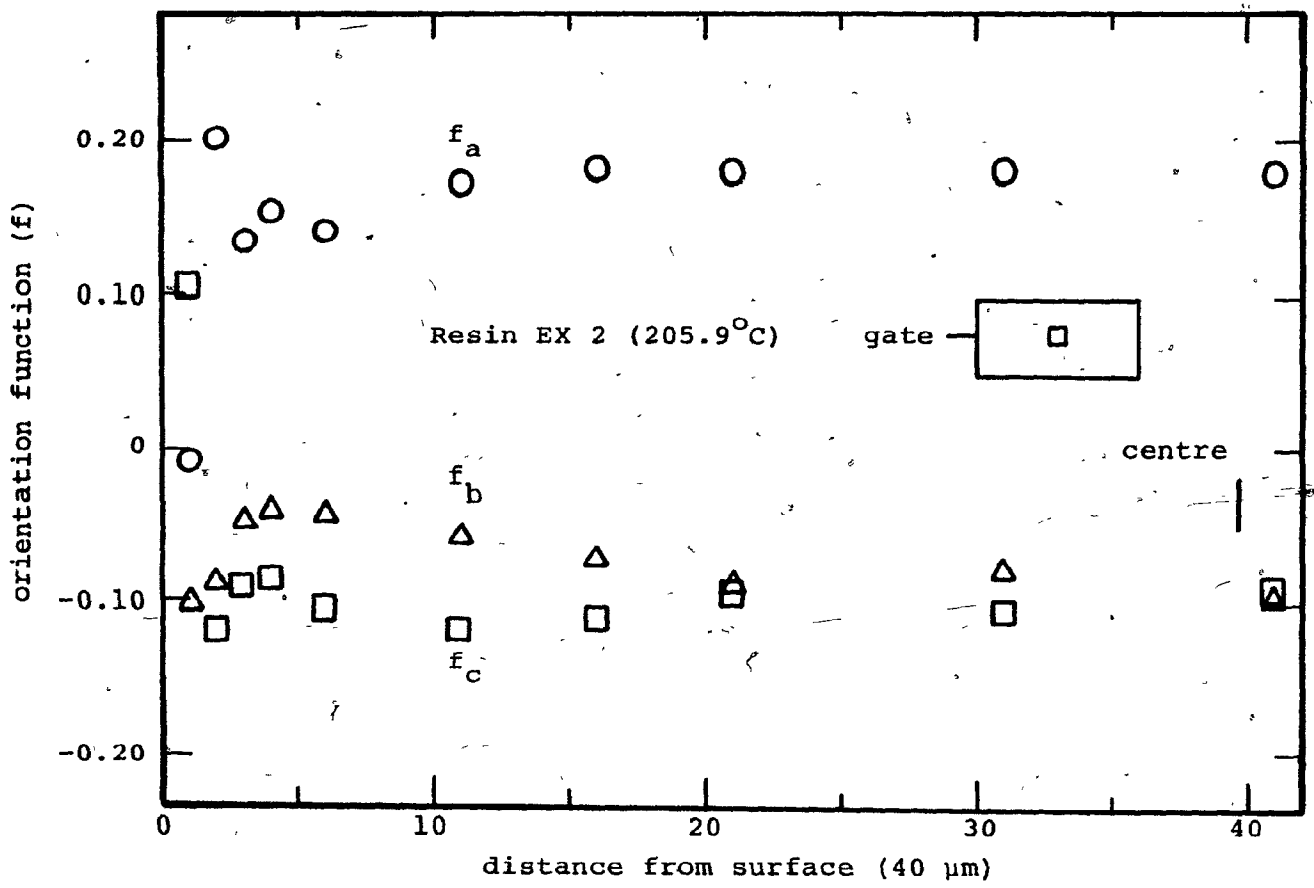


FIGURE 6.31. Variation of the Crystallographic Axes in the Depth Direction

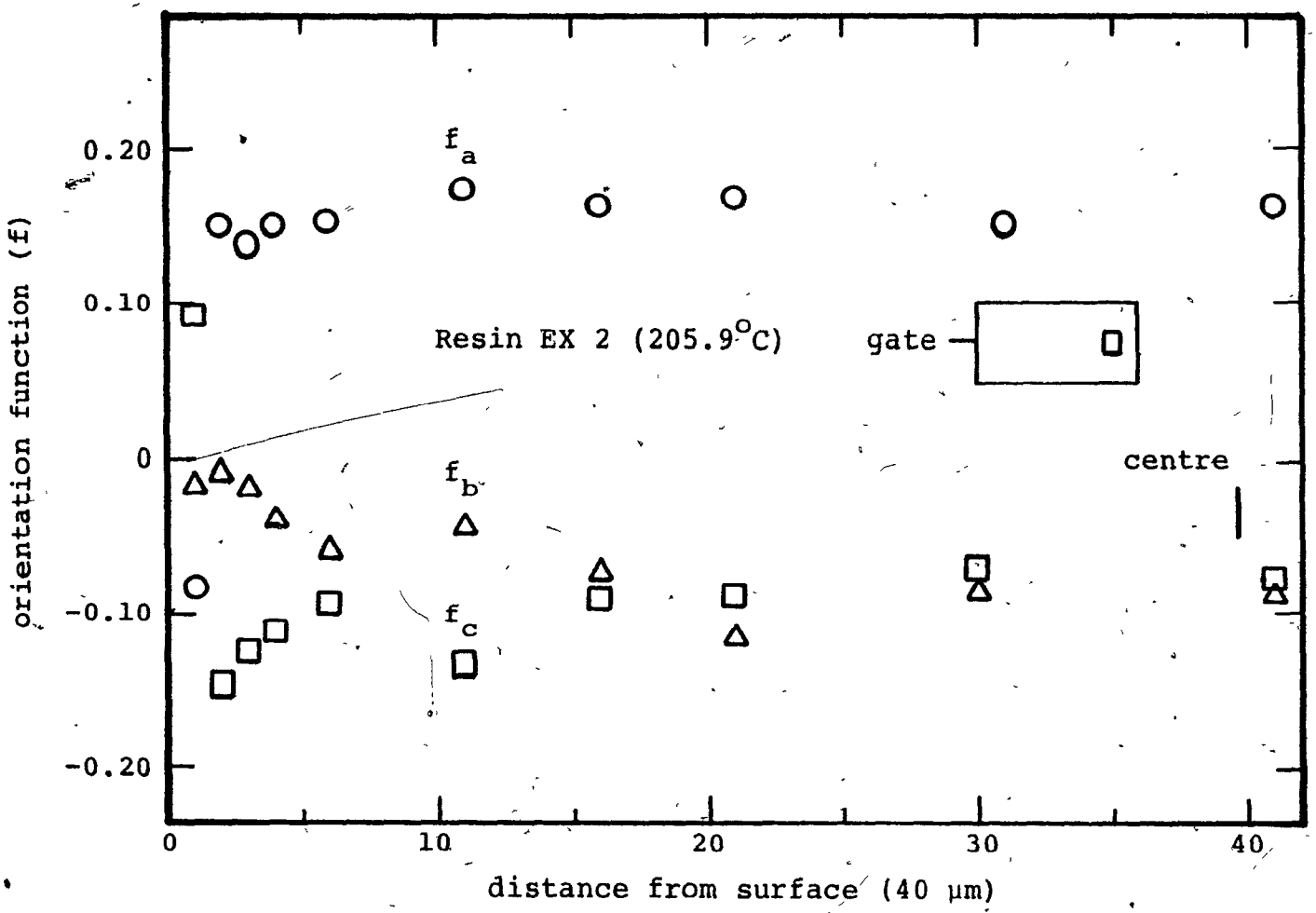


FIGURE 6.32. Variation of the Crystallographic Axes in the Depth Direction

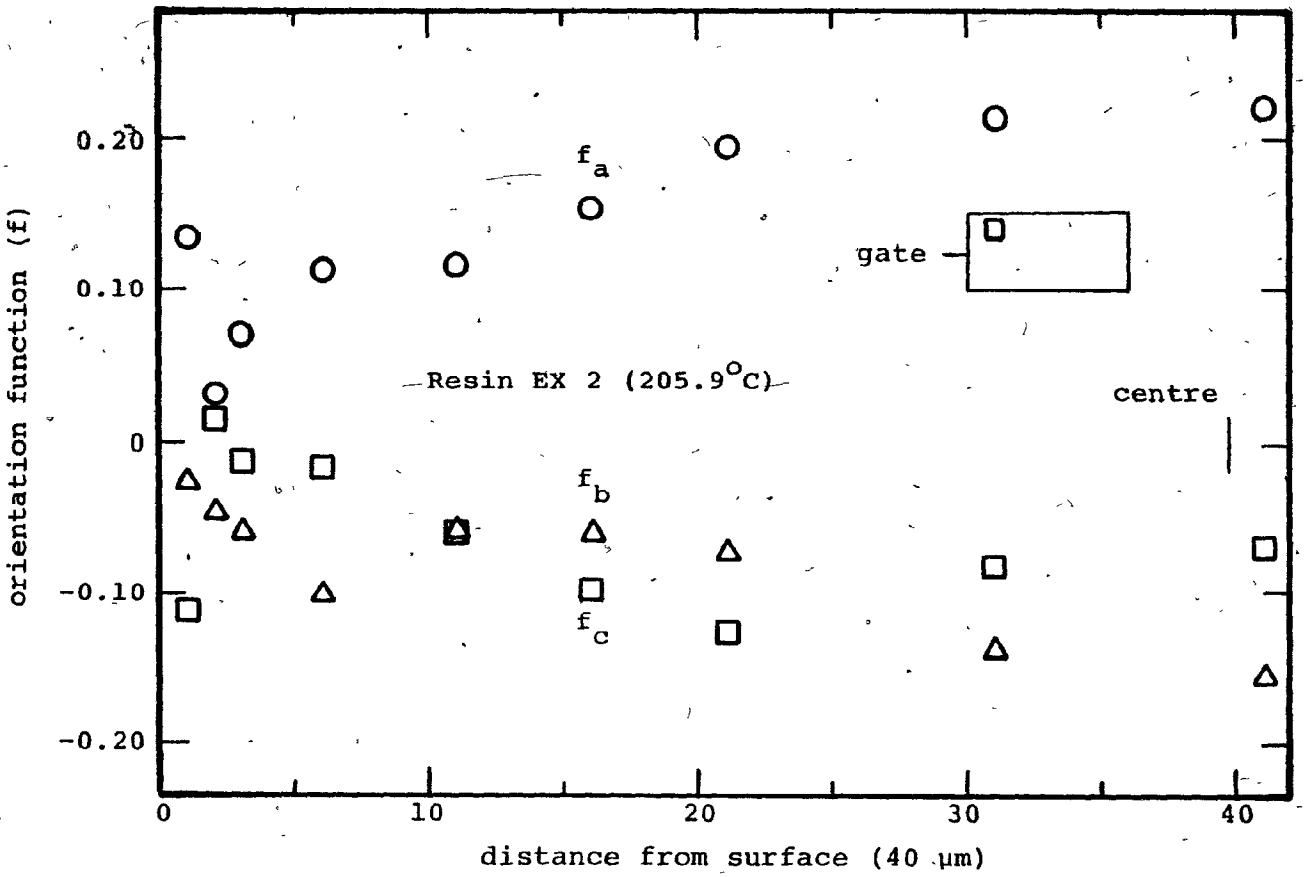


FIGURE 6.33. Variation of the Crystallographic Axes in the Depth Direction

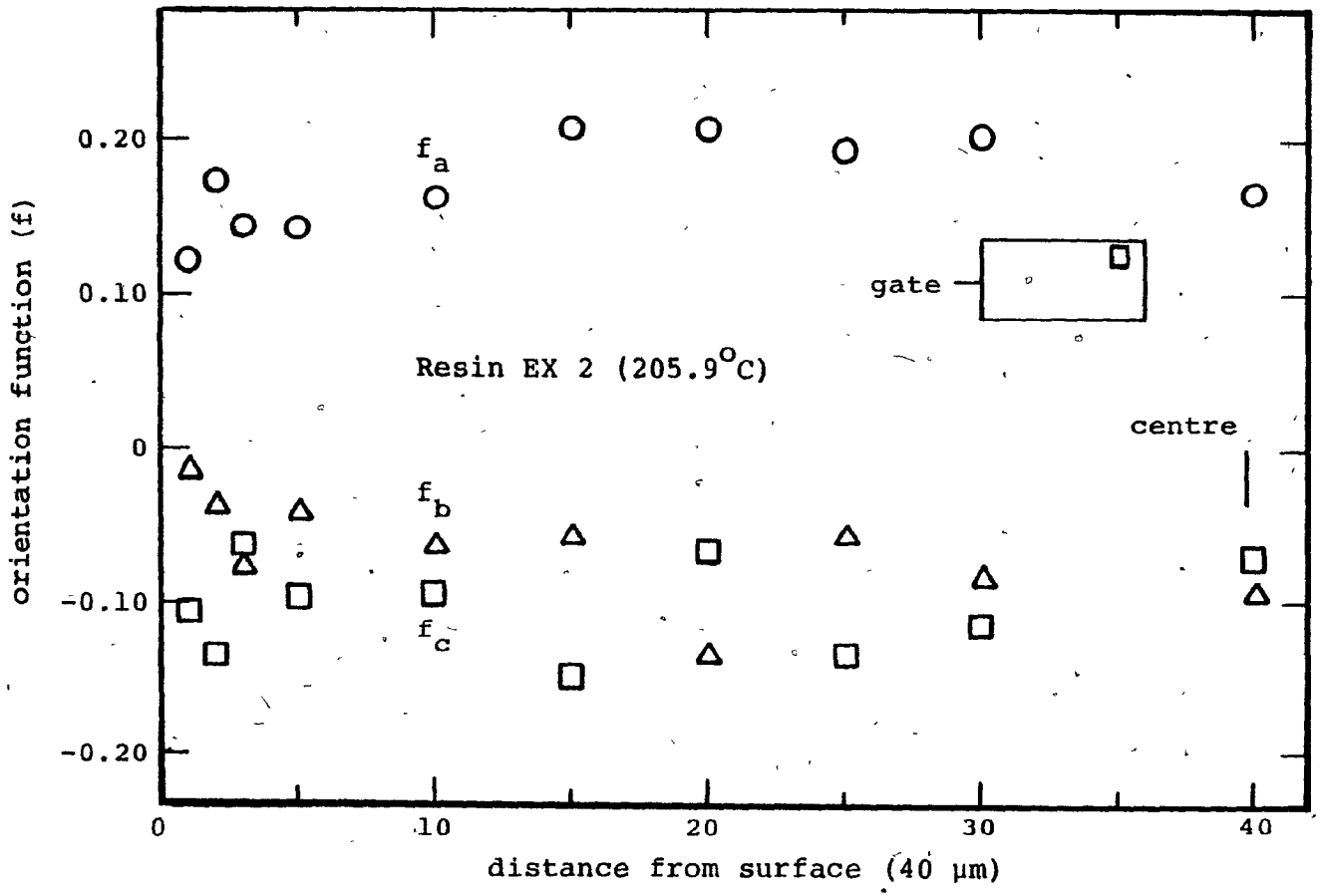


FIGURE 6.34. Variation of the Crystallographic Axes in the Depth Direction

of the orientations of the crystallographic axes are observed to be more pronounced for resin EX 1, as shown in Figures 6.20 to 6.24. The observation of a pronounced discontinuous type of distribution near the surface, especially for the locations near the gate, has been observed employing DSC and infrared dichroic ratio measurements (156). This region corresponds to the very dark area of the photomicrographs shown in Figures 6.3 to 6.5, and it may be attributed to the formation of a larger fraction of disordered molecular segments associated with the amorphous phase (156).

Generally, the crystallite orientation, as represented by the orientation of the crystallographic axis in the flow direction, tends to be maximum at or near the surface. This observation is consistent with the sonic modulus and birefringence measurements discussed earlier in Sections 6.5 and 6.6, respectively. Furthermore, Figures 6.20 to 6.24 show that resin EX 1 tends to exhibit a-axis orientation throughout the molding, while Figures 6.25 to 6.34 show that resin EX 2 tends to exhibit either relatively low a-axis orientation or high c-axis orientation in the skin layer and predominantly a-axis orientation towards the core of the molding.

Figure 6.35 compares the distribution of the crystallite orientation in the depth direction at the location midway from the gate for the two resins molded at the melt temperature of 176°C and for resin EX 2 molded at the high melt temperature of 205.9°C. Generally, the increase in degree of a-axis orientation as distance from the surface increases is attributed to the

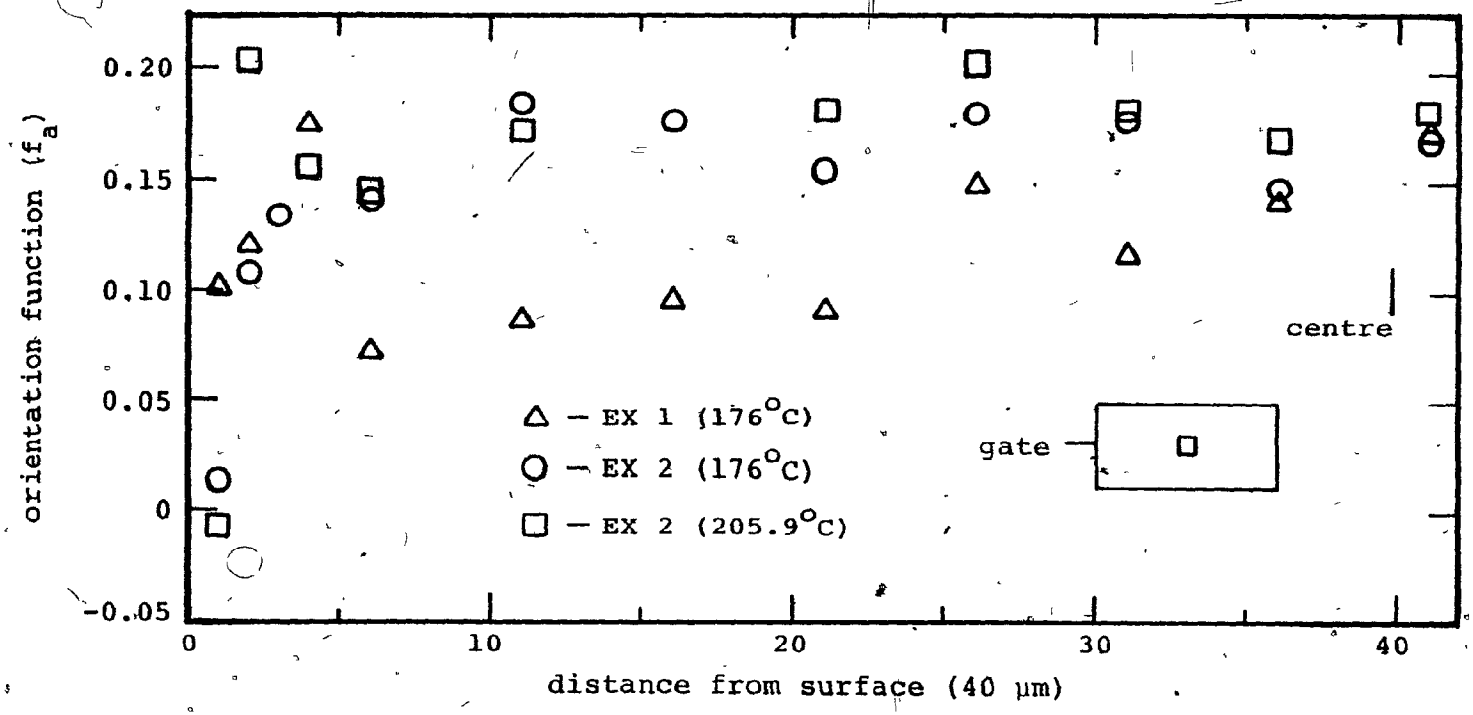


FIGURE 6.35. Typical Comparison of the a-Axis Orientation Distributions

increase in the time for the molecular chains to relax due to the longer cooling times towards the core region of the molding. When the crystalline orientation distribution is compared for corresponding locations shown as an example in Figure 6.35, it is observed that resin EX 1 tends to exhibit higher a-axis orientation near the surface (0-0.20 mm) than resin EX 2. This is attributed to the fact that resin EX 1 tends to crystallize later under shear and, therefore, experiences longer times for relaxation which give rise to higher orientation of the a-axis (48-50, 162). The lower orientation of the a-axis towards the core is similarly due to the shorter times to relax than that experienced by resin EX 2 since EX 1 tends to crystallize sooner under pressure, as discussed previously in Section 6.6. Furthermore, the observation that resin EX 2 generally tends to exhibit either relatively low a-axis orientation or high c-axis orientation near the skin layer is consistent with the shorter times to relax that resin EX 2 experiences since this resin tends to crystallize sooner under shear so that whatever orientation is induced during flow is retained (121).

As shown in Figure 6.35, generally increasing the injection melt temperature tends to either decrease the degree of a-axis orientation or increase the degree of c-axis orientation near the surface since the orientation of the b-axis is more or less fixed in the depth direction due to the direction of the thermal gradient. The higher injection melt temperature leads to a higher rate of crystallization near the surface. This results in a shorter time to relax and hence, give rise to either rela-

tively low degree of a-axis or high degree of c-axis orientation near the surface (46, 165, 166). The above agrees with the observation that resin EX 2 molded at the high melt temperature of 205.9°C exhibits a relatively high degree of c-axis orientation near the surface, as shown for the centreline locations in Figures 6.30-6.32.

Figures 6.36 and 6.37 show examples of X-ray diffraction patterns depicting slight c-axis orientation observed near the surface and a-axis orientation observed in the core region of the injection molding, respectively. As shown in Figure 6.36, the (110), (200) and (020) reflections give rise to maximum intensity at the equator which is indicative of c-axis longitudinal type of orientation (95). Figure 6.37 shows that both the (110) and (020) reflections give rise to maxima at the equator, whereas the (200) reflection is a maximum at the meridian. The self-consistency of the (hkl) reflections is indicative of the a-axis longitudinal type of orientation observed in the injection molded parts (95). Furthermore, reflections due to the presence of K_β radiation were observed in all samples analyzed.

Generally, the results of the X-ray diffraction measurements may be summarized as follows:

(1) The unit cell of the crystals after processing corresponds to the ordinary orthorhombic type for polyethylene.

(2) The crystallite orientation, as represented by the orientation of the crystallographic axis in the flow

FIGURE 6.36. Wide-Angle X-Ray Pattern of Specimen Microtomed Near the Surface

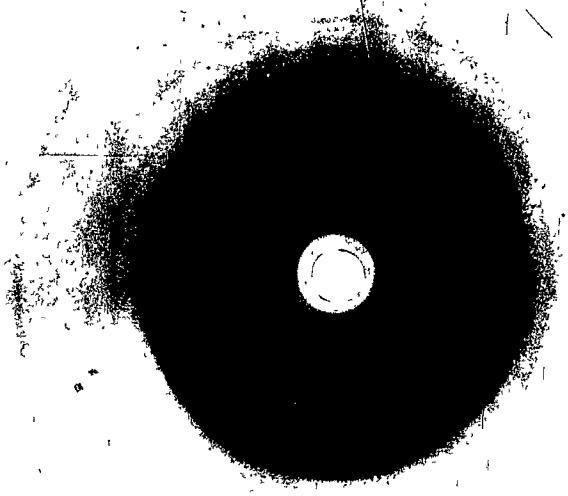
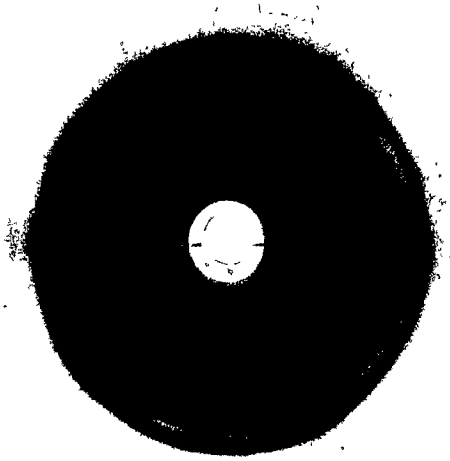


FIGURE 6.37. Wide-Angle X-Ray Pattern of Specimen Microtomed from the Core Region



direction (a-axis), is a maximum at or near the surface.

(3) The variation of the crystallite orientation is observed to be most pronounced in the region (0-0.30 mm) from the surface for the various locations analyzed.

(4) Resin EX 1 tends to exhibit higher a-axis orientation near the surface than resin EX 2. As distance from the surface increases, resin EX 2 tends to exhibit higher crystallite orientation.

(5) Increasing the injection melt temperature tends to cause the c-axis to be frozen-in in the flow direction near the surface, but marginally affects the a-axis orientation observed towards the core region.

The next section compares the results of dichroic ratio measurements, as measured by infrared spectroscopy, in the depth direction with the results of the techniques discussed thus far.

6.8 Infrared Spectroscopy

The anisotropy parameter used in infrared studies is the infrared dichroic ratio which is the significant factor in the interpretation of the optical anisotropy of the sample in terms of molecular orientation (136). In this study, the dichroic ratio measurements are compared with the distributions of orientation discussed in previous sections. Furthermore, the dichroic ratio measurements due to absorption of the 730 cm^{-1} band are used to deduce information regarding the orientation function of the crystallographic a-axis. Subsequently, these results

are compared to the results obtained by X-ray diffraction discussed in the previous section. A detailed tabulation of the variations of the dichroic ratios for both the 720 cm^{-1} and 730 cm^{-1} bands, as well as the distribution of the orientation function corresponding to the a-axis obtained from the 730 cm^{-1} band, with depth direction for the two resins molded at the melt temperature of 176°C and fof resin EX 2 molded at the high melt temperature of 205.9°C, are provided in Appendix 7. The error analysis associated with the measurement of the infrared dichroic ratio is presented in Appendix 15.

Figures 6.38 to 6.43 show the alternate distributions of the dichroic ratios for both the 730 cm^{-1} and 720 cm^{-1} bands, respectively, at the three centreline locations for the two resins molded at a melt temperature of 176°C. Similarly, Figures 6.44 to 6.46 show the alternate distributions of the two absorption bands at the corresponding locations for resin EX 2 molded at the high melt temperature of 205.9°C. A value of dichroic ratio lower than 1.0 signifies a preferred orientation in the transverse direction, while a value greater than 1.0 signifies a preferred orientation in the longitudinal direction.

As shown in Figures 6.38 to 6.40 for resin EX 1, the results of the dichroic ratio measurements for the CH_2 rocking vibration at the 720 cm^{-1} band absorption, which arises from both the crystalline b-axis and the amorphous phase, tend to exhibit a high value at the surface which decrease to a minimum near the surface and increases to a constant value towards the core. For resin EX 2, as shown in Figures 6.41 to 6.46, gen-

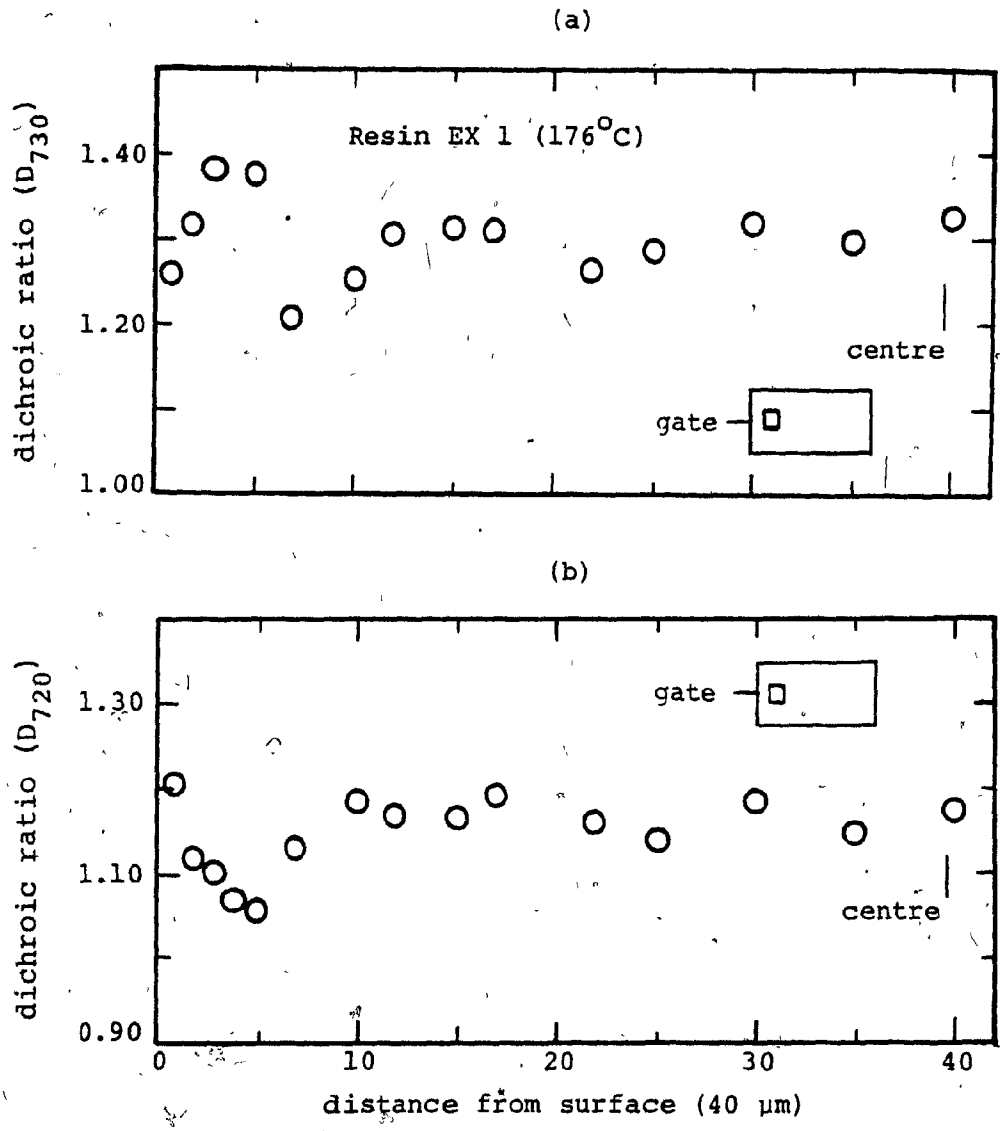


FIGURE 6.38. Variation of Dichroic Ratio in the Depth Direction

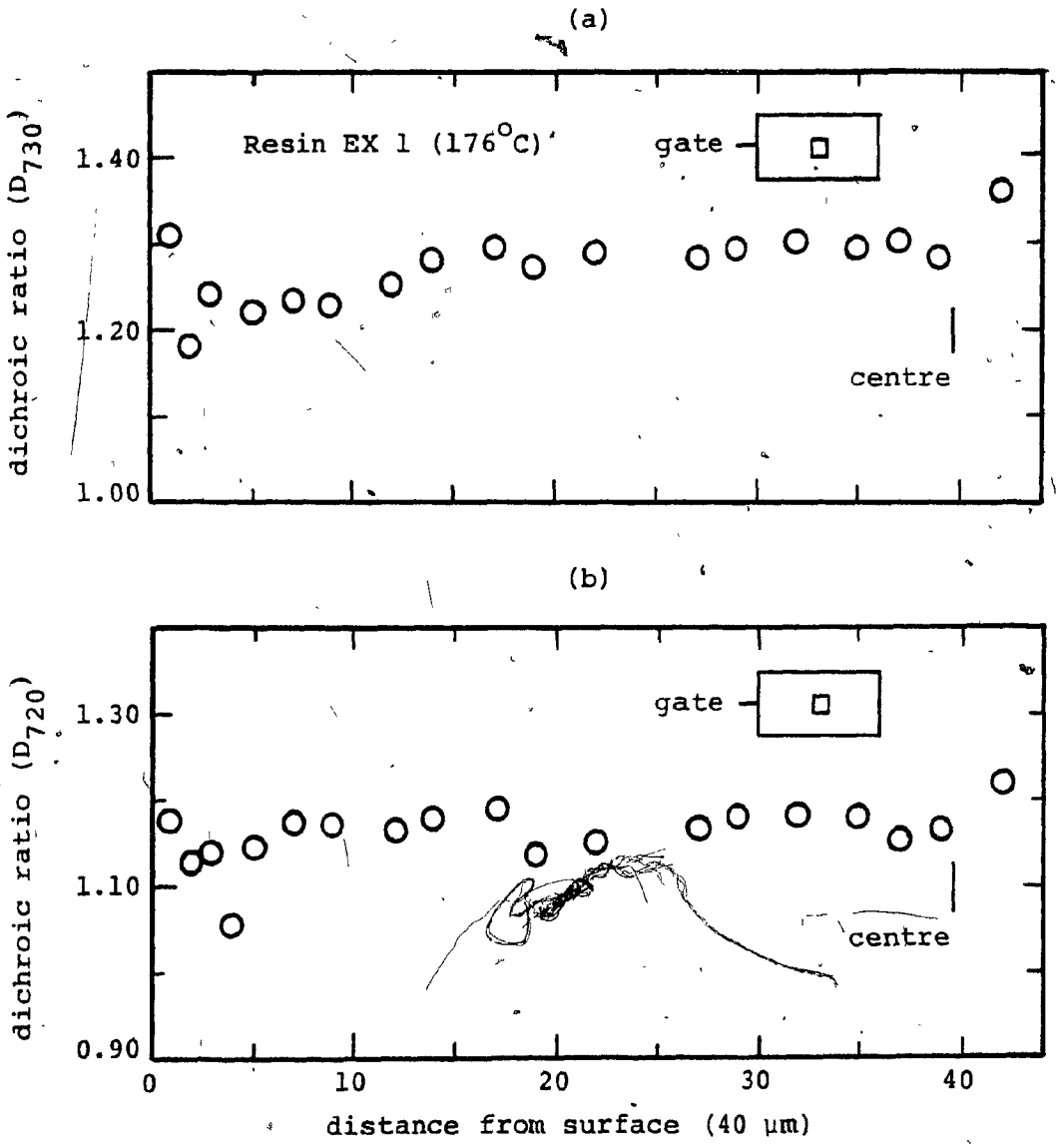


FIGURE 6.39. Variation of Dichroic Ratio in the Depth Direction

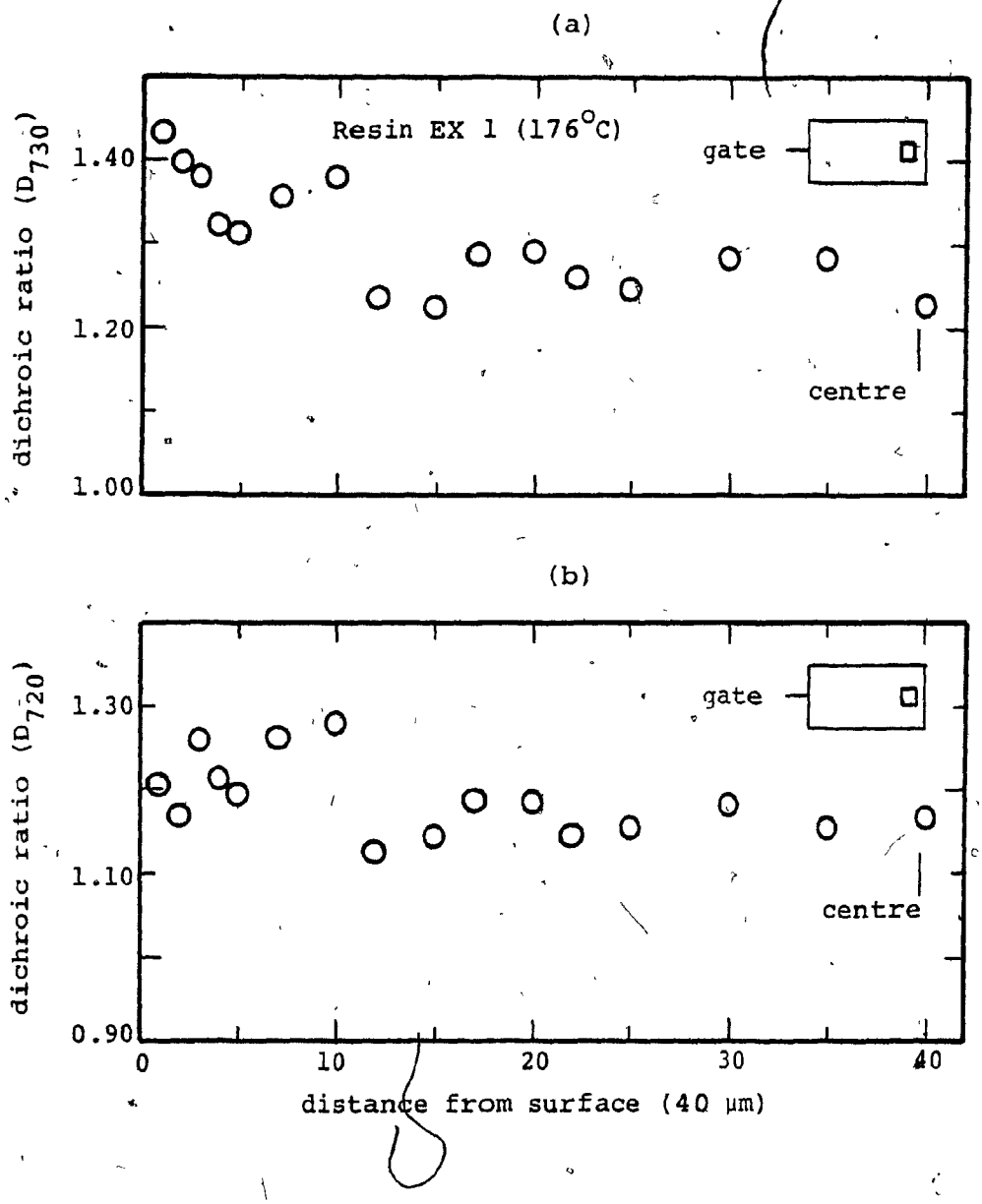


FIGURE 6.40. Variation of Dichroic Ratio in the Depth Direction

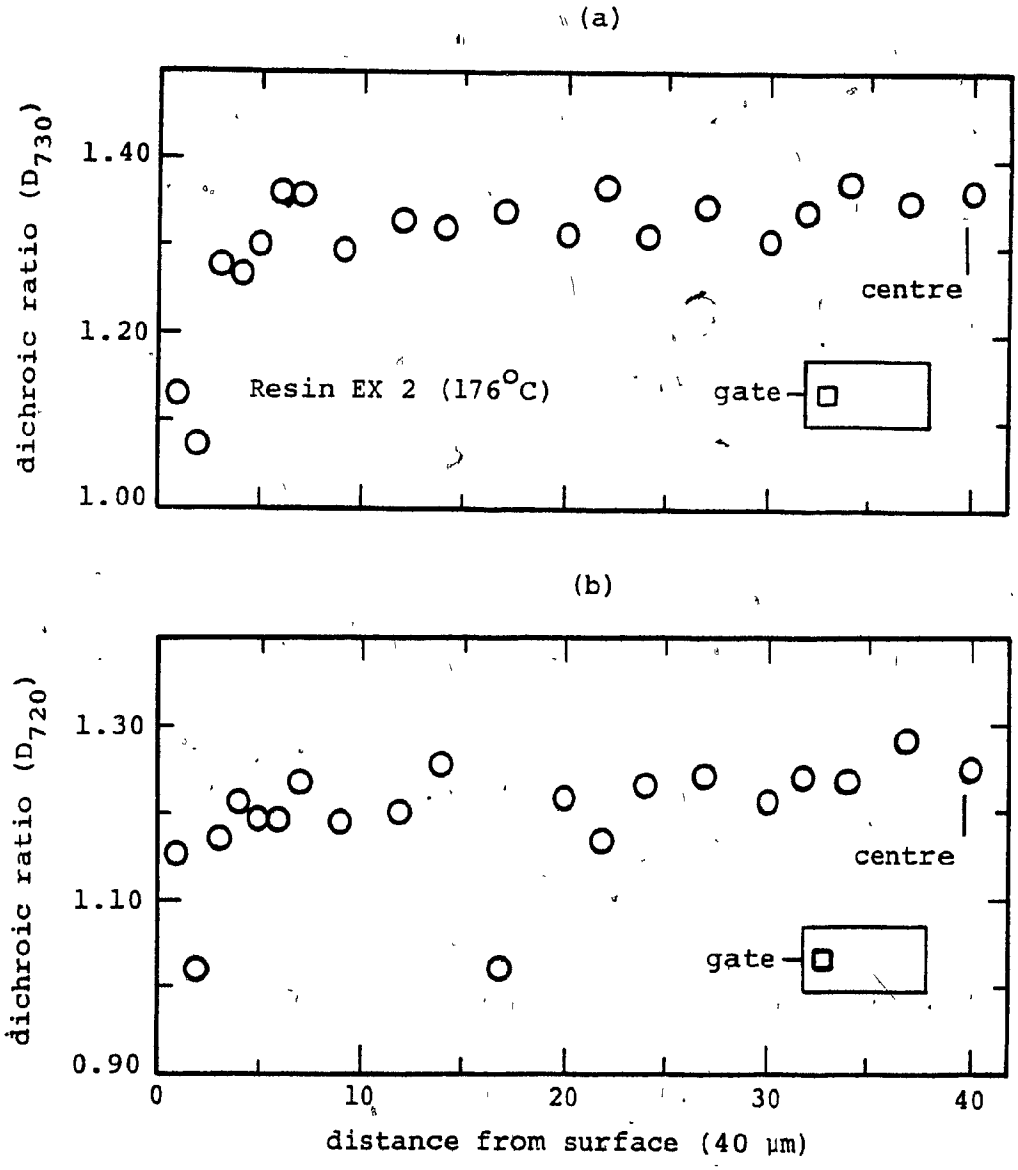


FIGURE 6.41. Variation of Dichroic Ratio in the Depth Direction

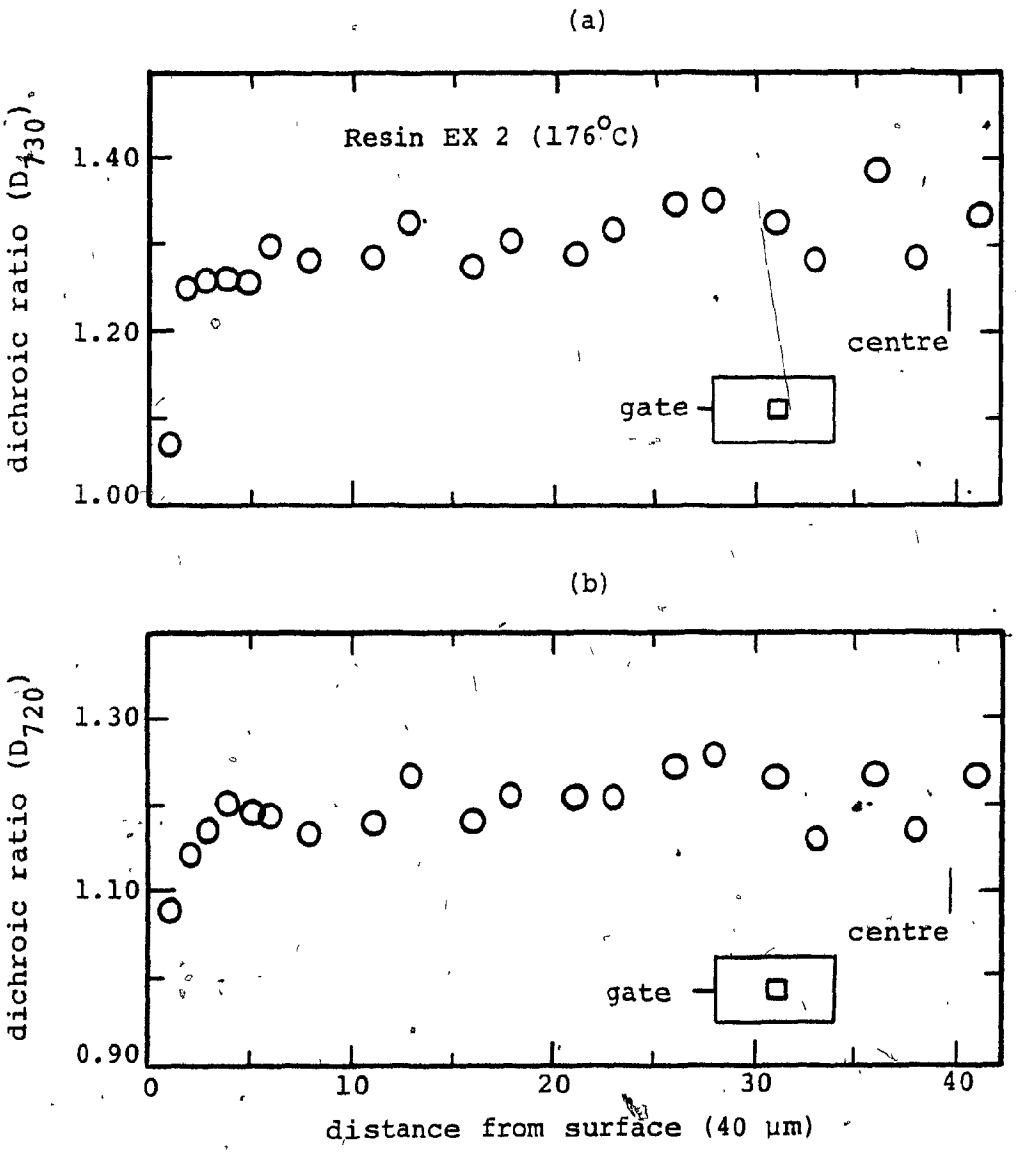


FIGURE 6.42. Variation of Dichroic Ratio in the Depth Direction

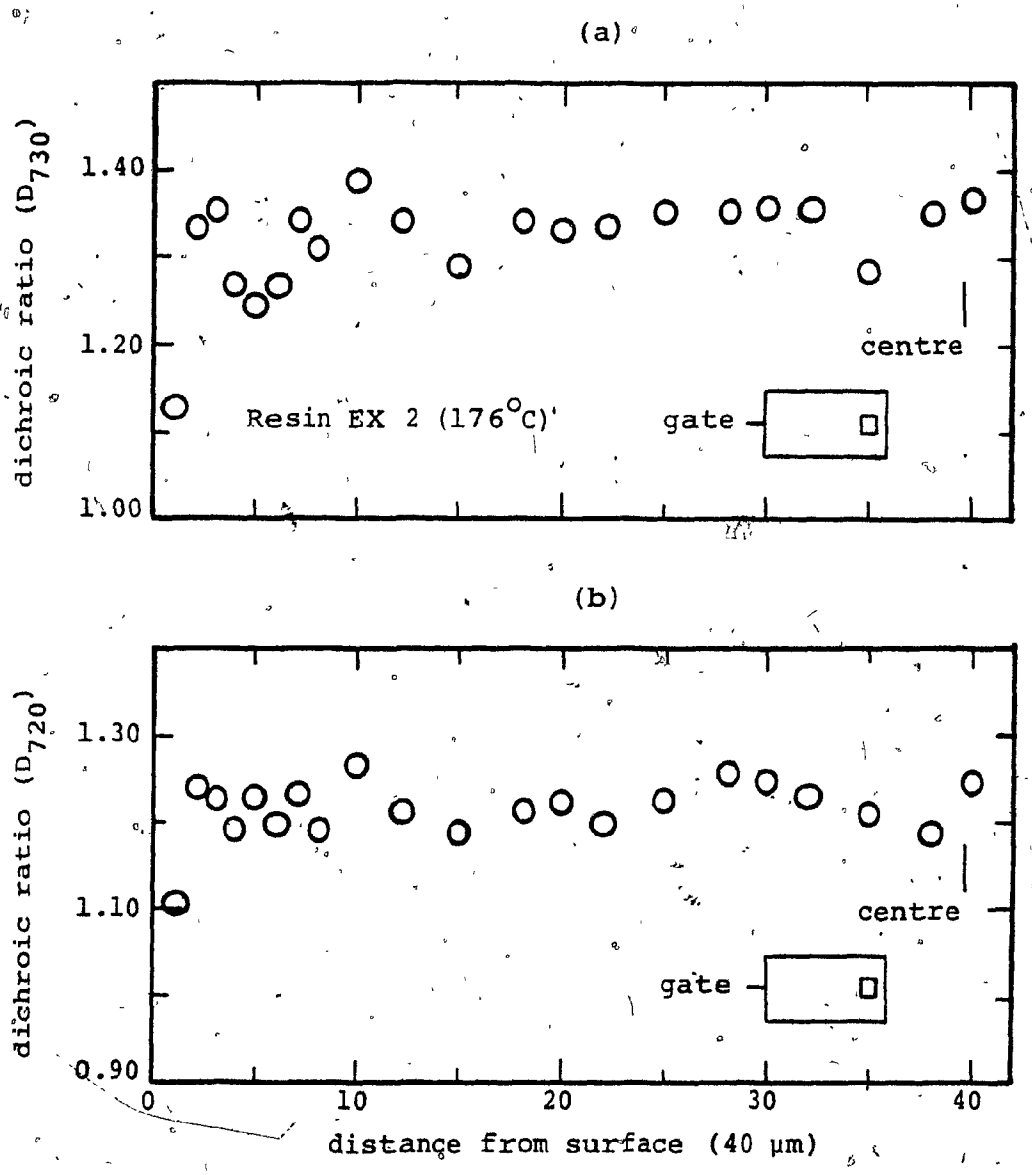


FIGURE 6.43. Variation of Dichroic Ratio in the Depth Direction

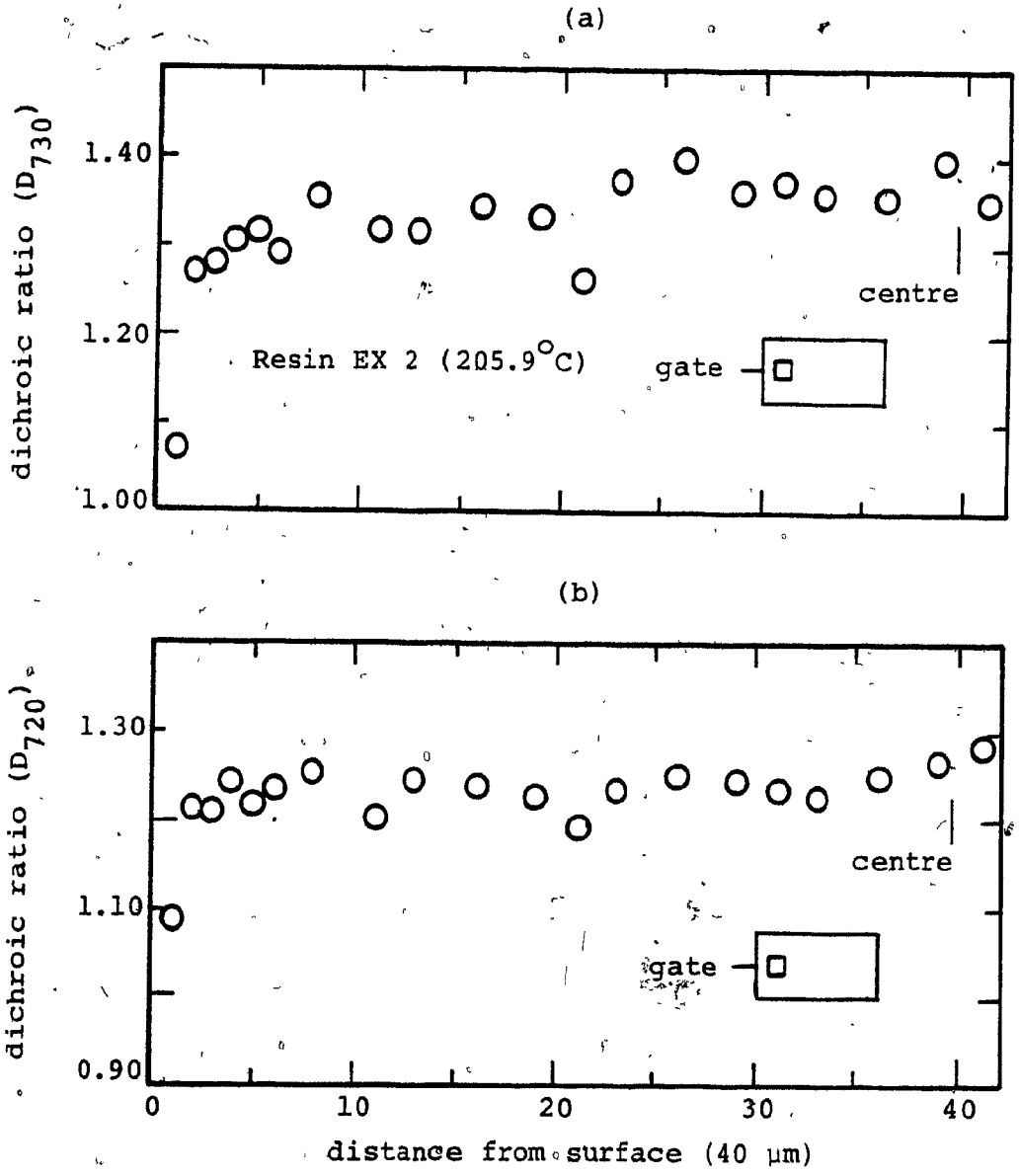


FIGURE 6.44. Variation of Dichroic Ratio in the Depth Direction

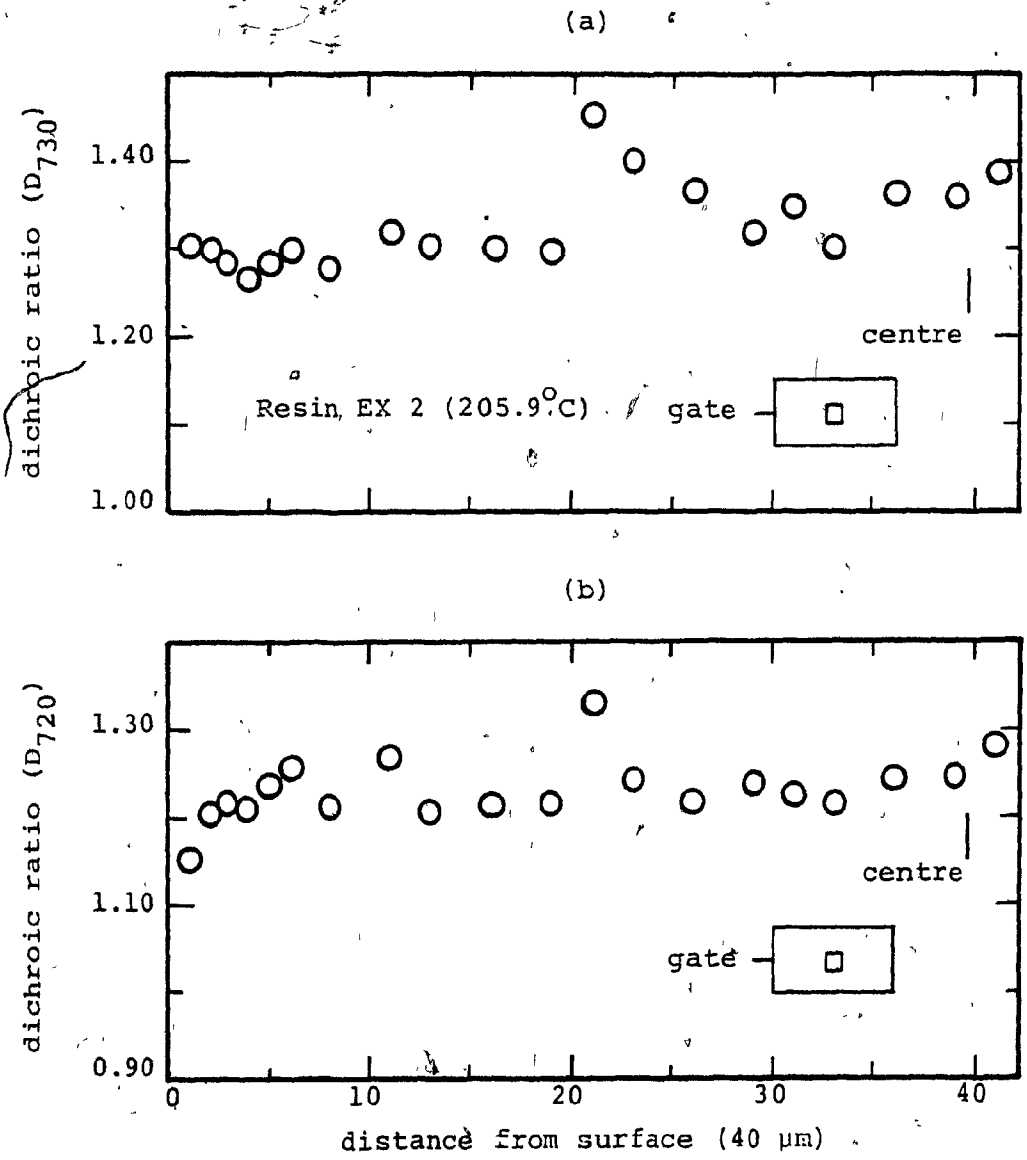


FIGURE 6.45. Variation of Dichroic Ratio in the Depth Direction

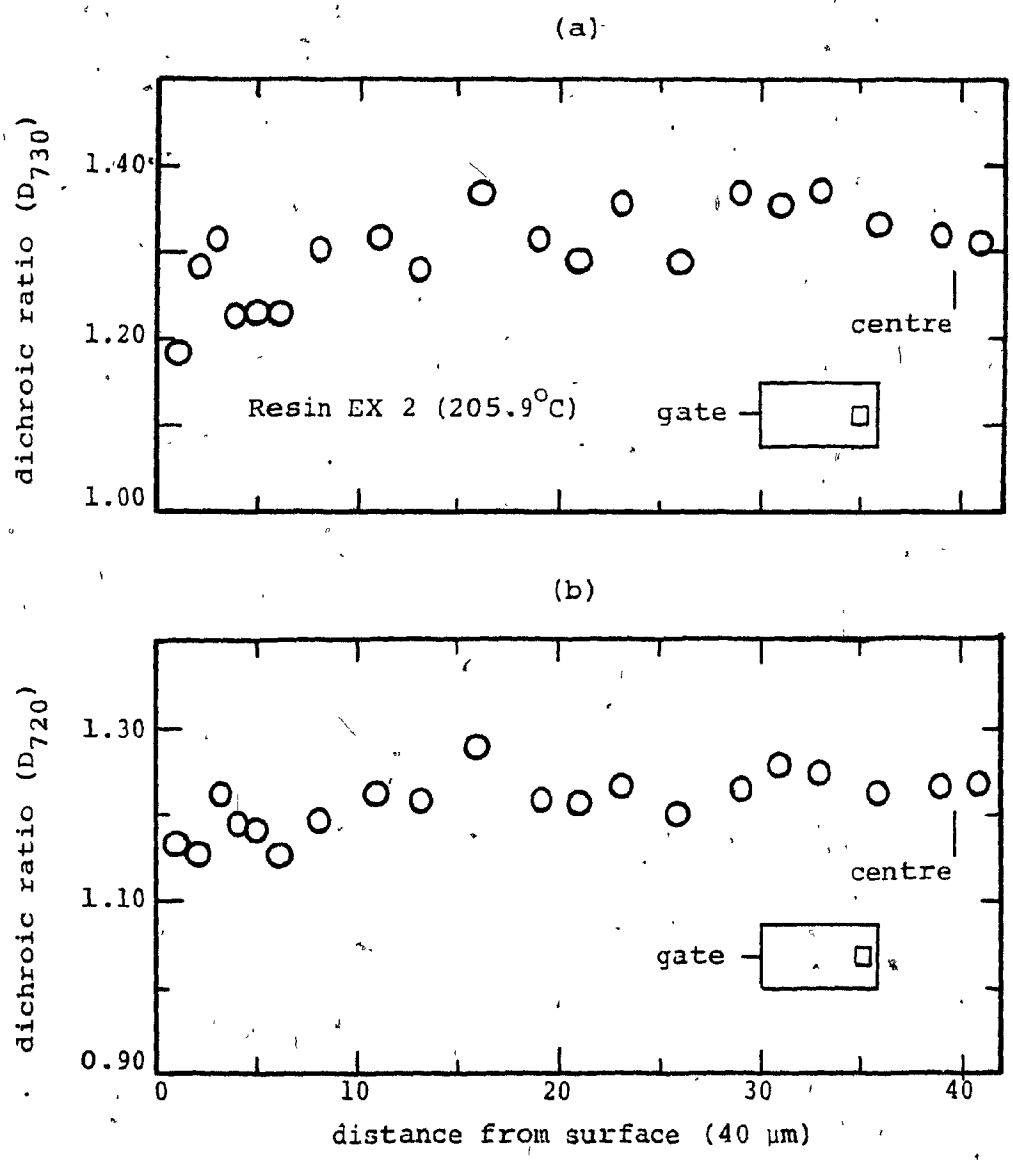


FIGURE 6.46. Variation of Dichroic Ratio in the Depth Direction

erally the dichroic ratio measurements obtained for the 720 cm^{-1} band absorption is observed to be relatively low at the surface, but increases to a maximum towards the core.

Generally, the crystalline a-axis absorption at the 730 cm^{-1} band tends to exhibit a minimum at or near the surface in all cases, as shown in Figures 6.38 to 6.46. This means that the degree of crystallite orientation tends to increase in the flow direction as distance from the surface increases. This observation is consistent with the results of wide-angle X-ray diffraction measurements, as previously discussed in Section 6.7. Similar results of infrared measurements have been reported for polyethylene injection moldings (119).

Comparison of the a-axis orientation distributions obtained by the X-ray diffraction technique and from measurement of the dichroic ratio pertaining to the 730 cm^{-1} absorption band, are shown in Figures 6.47 to 6.49 at the various locations. Figures 6.47 and 6.48 show comparisons for the two resins molded at the melt temperature of 176°C. Figure 6.49 shows comparisons at the corresponding locations for resin EX 2 molded at the high melt temperature of 205.9°C. The results show that the a-axis orientation distributions obtained by the two techniques appear to be in good agreement with each other. The two techniques show that the a-axis is oriented in the flow direction and that the degree of orientation tends to increase as distance from the surface increases.

Generally, the results of the infrared measurements may be summarized as follows:

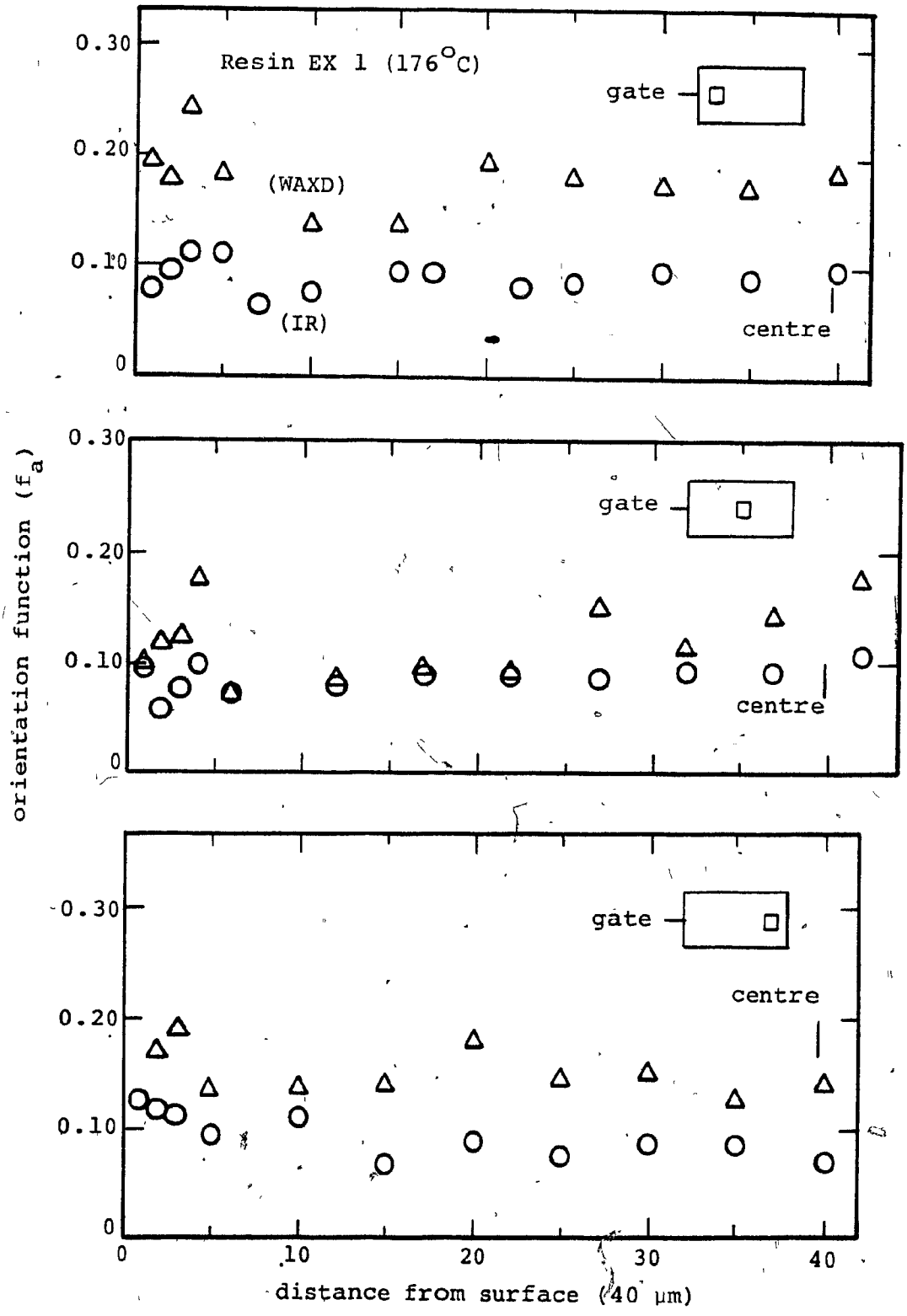


FIGURE 6.47. Comparison of f_a Obtained by X-Ray Diffraction and Infrared Dichroism

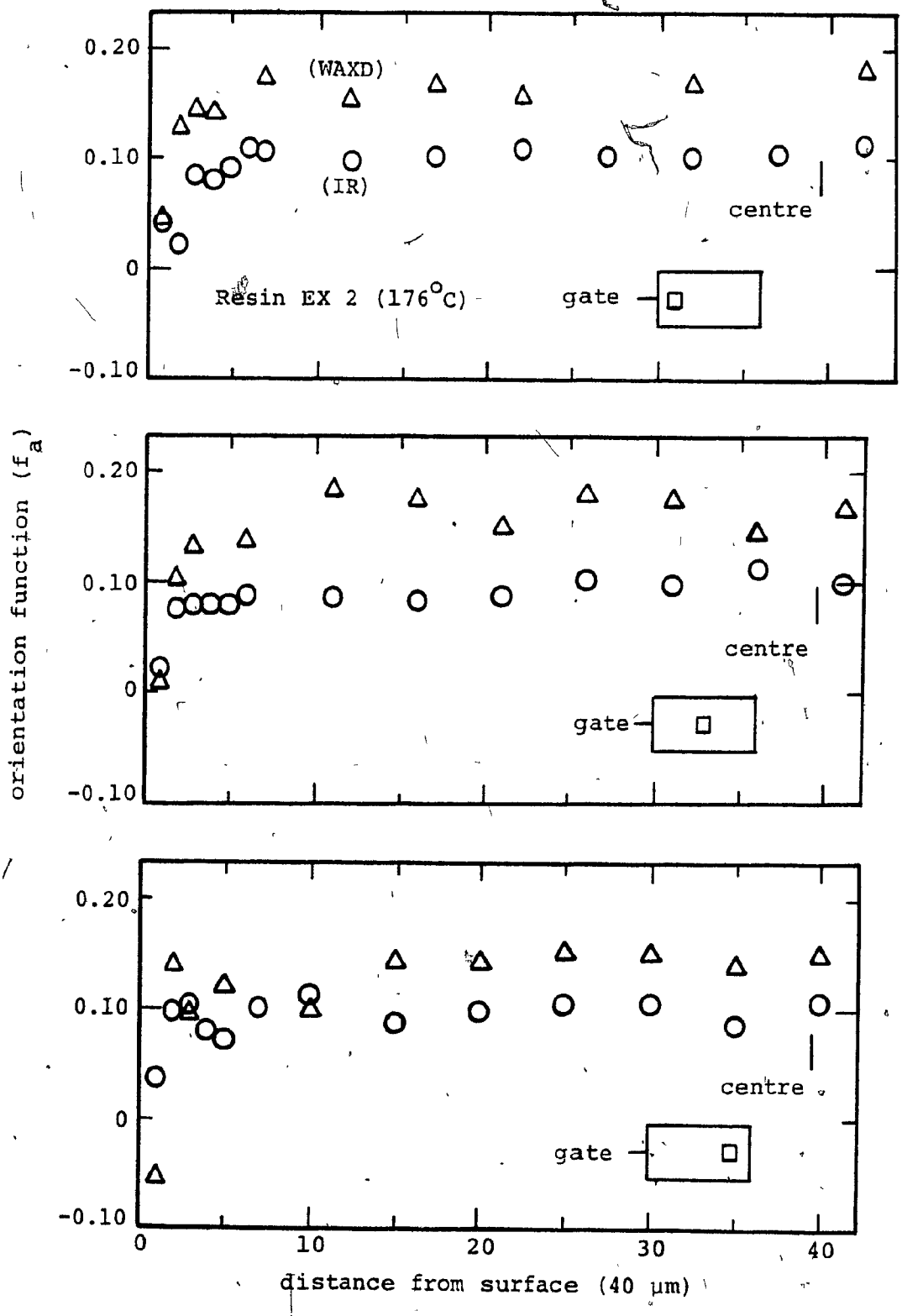


FIGURE 6.48. Comparison of f_a Obtained by X-Ray Diffraction and Infrared Dichroism

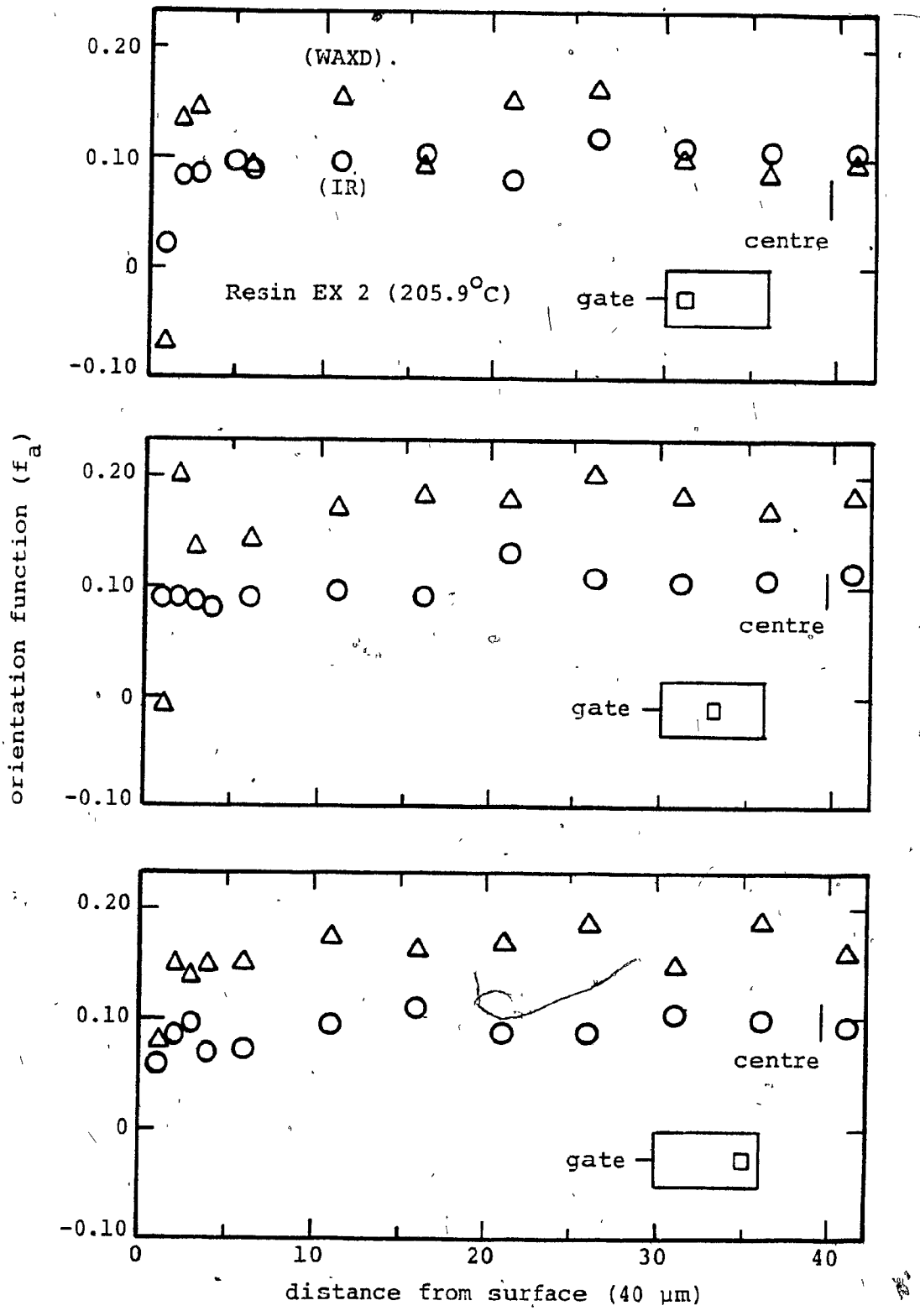


FIGURE 6.49. Comparison of f_a Obtained by X-Ray Diffraction and Infrared Dichroism

(1) The distributions of dichroic ratio measurements are in consistent agreement with the results obtained by the other techniques employed.

(2) Dichroic ratio measurements of the 730 cm^{-1} absorption band show that the a-axis tends to be oriented in the flow direction and that maximum crystallite orientation is observed at or near the surface.

(3) The a-axis orientation distributions obtained by infrared measurements are in consistent agreement with those observed from X-ray diffraction, although the latter technique appears to exhibit slightly higher values for the a-axis orientation.

It is reasonable to conclude that the results of the various techniques employed are in consistent agreement with each other. The next section discusses the results of mechanical testing in the depth direction of the molding.

6.9 Mechanical Properties

A detailed tabulation of the mechanical measurements for positions in the depth direction for the two resins molded at the melt temperature of 176°C and for resin EX 2 molded at the high melt temperature of 205.9°C, at the corresponding locations along the molding, are provided in Appendix 8. The mechanical properties measured are the nominal tensile yield stress (σ_{ny}), the elongation at yield (ε_y), and the elongation at break (ε_b). The error analysis pertaining to the measurements of the various mechanical properties is presented in Appendix 15.

Generally, all specimens exhibited high moduli, yield points, high tensile strength at yield, and large elongations at break. Two characteristic stress-strain behaviors were observed. Samples corresponding to the skin and intermediate layers tend to exhibit cold-drawing stress-strain behavior while samples from the core region tend to exhibit necking rupture behavior. The necking rupture behavior is manifested by the decrease of stress after the yield point which is contrary to the increase of the stress in the case of cold-drawing (146).

It is known that a number of factors, such as distribution of the morphological zones (111), density or degree of crystallinity (169), the spherulite sizes (168) and the state and distribution of orientation (115), affect the stress-strain behavior. Furthermore, the effects of these variables are difficult to isolate in injection molded parts. Generally, the tensile yield strength increases with the fraction of the row nucleated zones (111), with an increase in the density (167) and with an increase in the crystallite orientation (116). Although the sizes of spherulites affect the distribution of the mechanical stresses during drawing, in many cases, it is difficult to differentiate changes due to slight increases in crystallinity from changes due to an increase in spherulitic structure, since the two factors often go together (146). Generally, the elongation to break increases with molecular orientation, but decreases with increasing crystallinity (146).

Figures 6.50 and 6.51 show the variation of tensile yield stress in the depth direction at the various locations for the

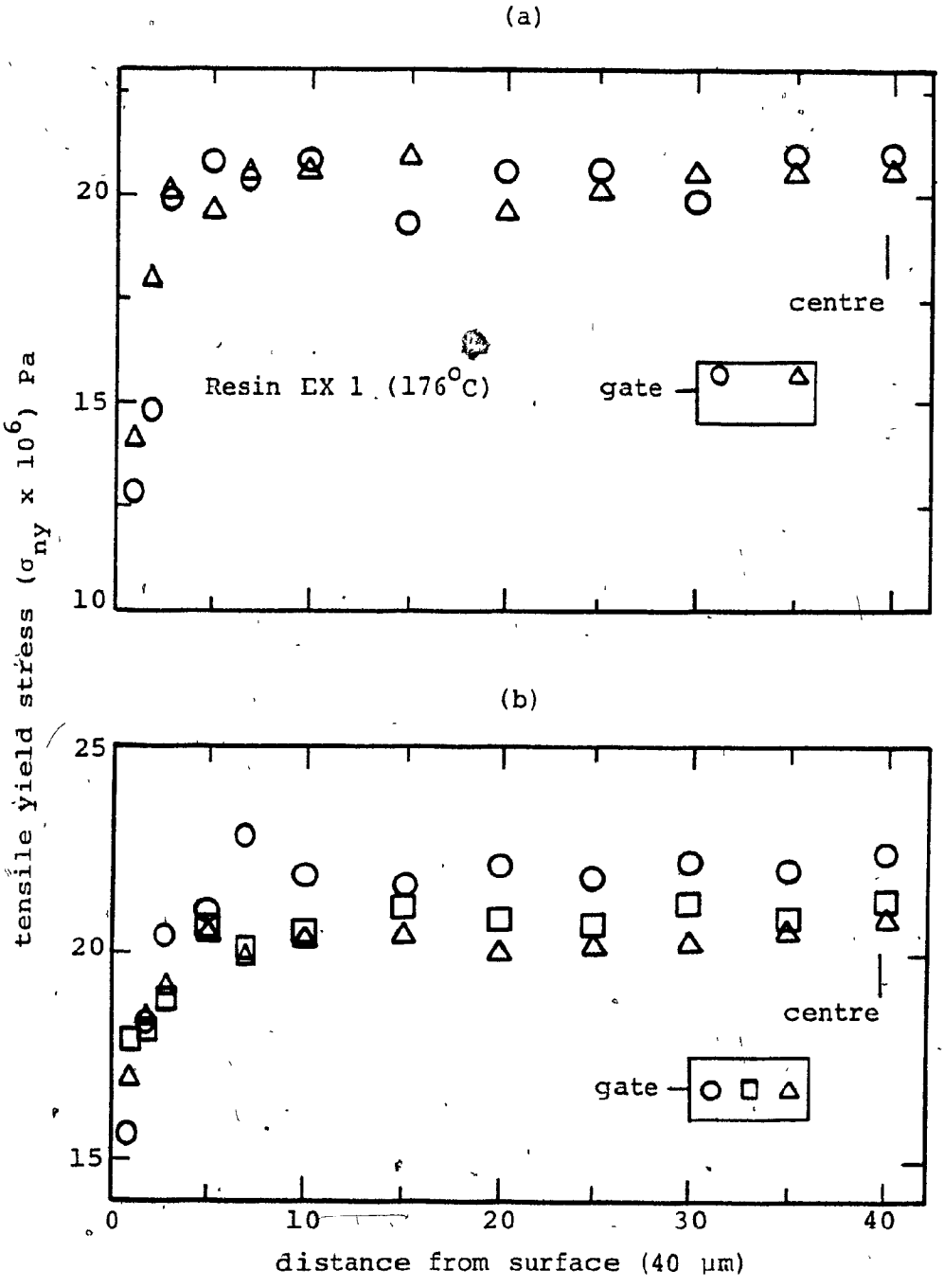


FIGURE 6.50. Variation of Nominal Tensile Yield Stress in the Depth Direction

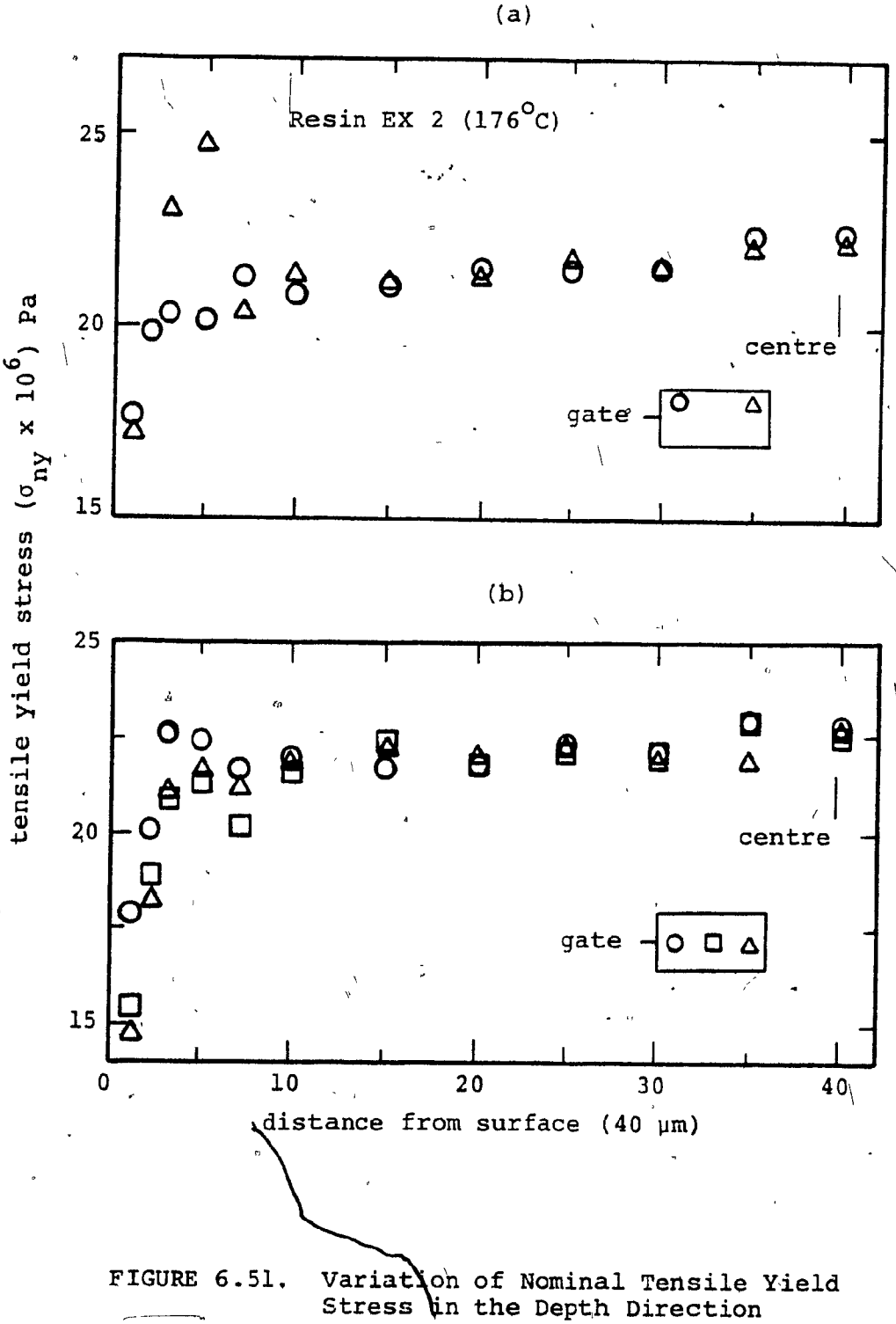


FIGURE 6.51. Variation of Nominal Tensile Yield Stress in the Depth Direction

two resins molded at the melt temperature of 176°C. Generally, the tensile yield stress tends to increase as distance from the surface increases.

Figures 6.52(a) and (b) show comparable results for yield stress measured on moldings obtained with an injection melt temperature of 205.9°C for EX 2. Figure 6.53 shows that resin EX 2 tends to exhibit higher σ_{ny} values than resin EX 1. This is attributed to the generally higher density (crystallinity) and higher crystallite orientation observed for resin EX 2, as discussed previously in Sections 6.2 and 6.7, respectively. Increasing the injection melt temperature tends to increase the tensile yield stress throughout the molded part. Similar increases in tensile yield stress are reported for injection molded polypropylene (111) and polyacetal (107).

Figures 6.54 and 6.55 show the variation of the percent elongation at yield (ε_y) in the depth direction at the various locations for the two resins molded at the melt temperature of 176°C. Generally, the ε_y values tend to increase to a maximum near the surface and gradually decrease to a constant value towards the core region. The variation is observed to be most pronounced within the first 0.40 mm (400 μm) from the surface for all locations, beyond which the ε_y values are fairly constant. The range of ε_y values observed in all cases was about 15% near the surface to about 35% towards the core region, although values of up to about 60% were observed in the case of resin EX 1, as shown in Figure 6.54. At the high melt temperature, as shown in Figures 6.56(a) and (b) for the corresponding

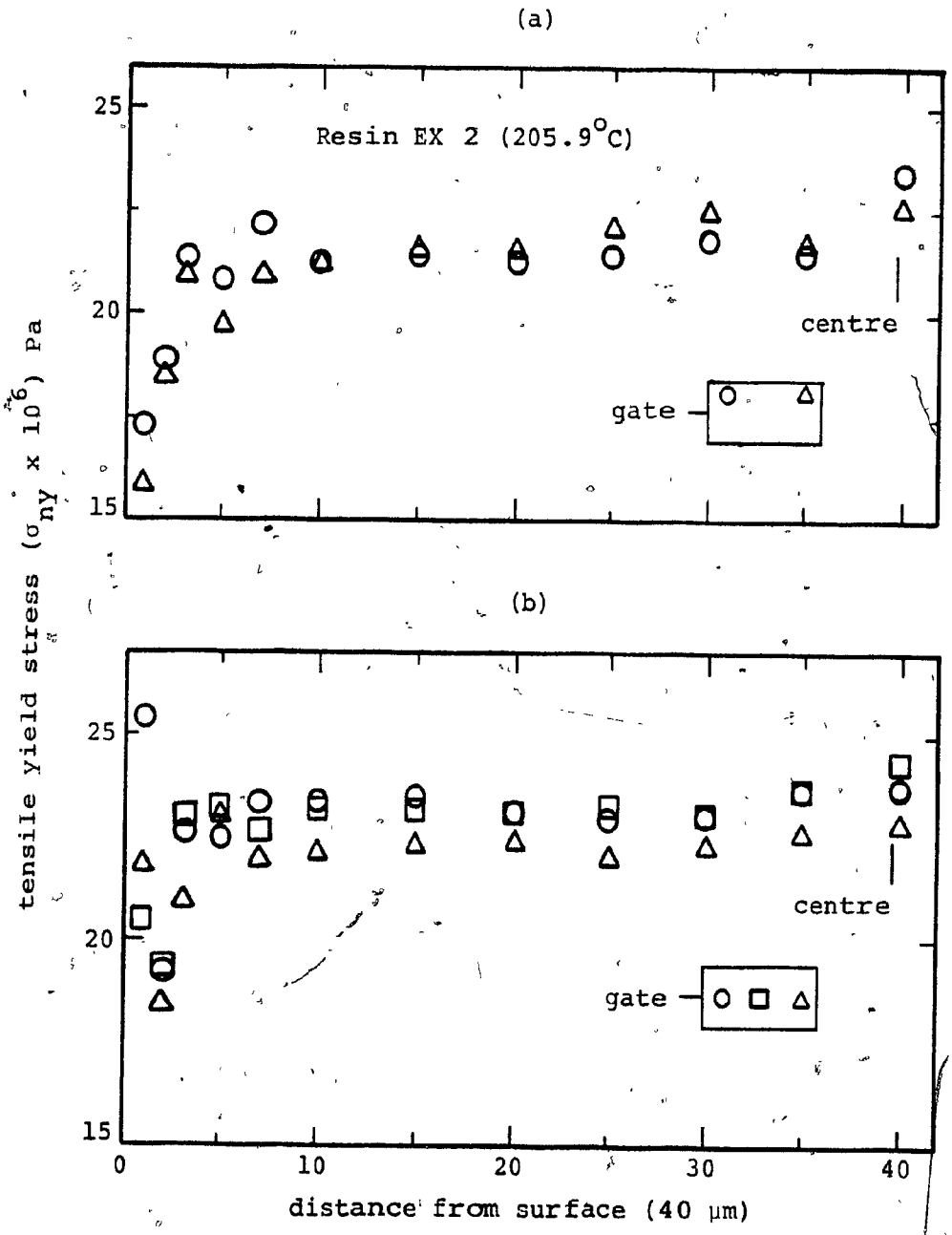


FIGURE 6.52. Variation of Nominal Tensile Yield Stress in the Depth Direction

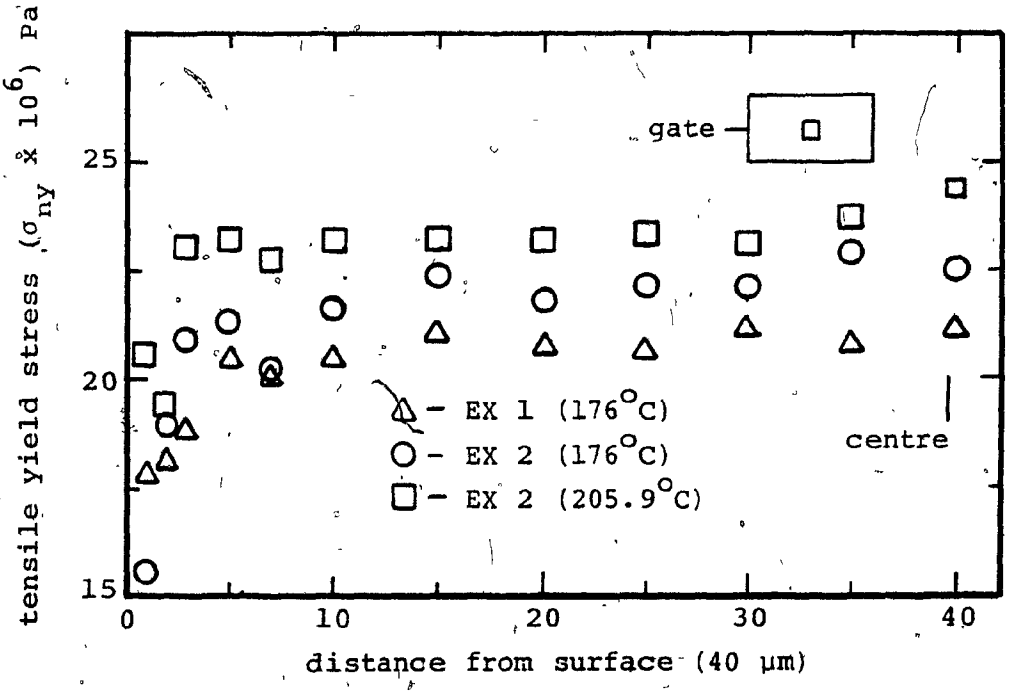


FIGURE 6.53. Typical Comparison of Nominal Tensile Yield Stress Distributions

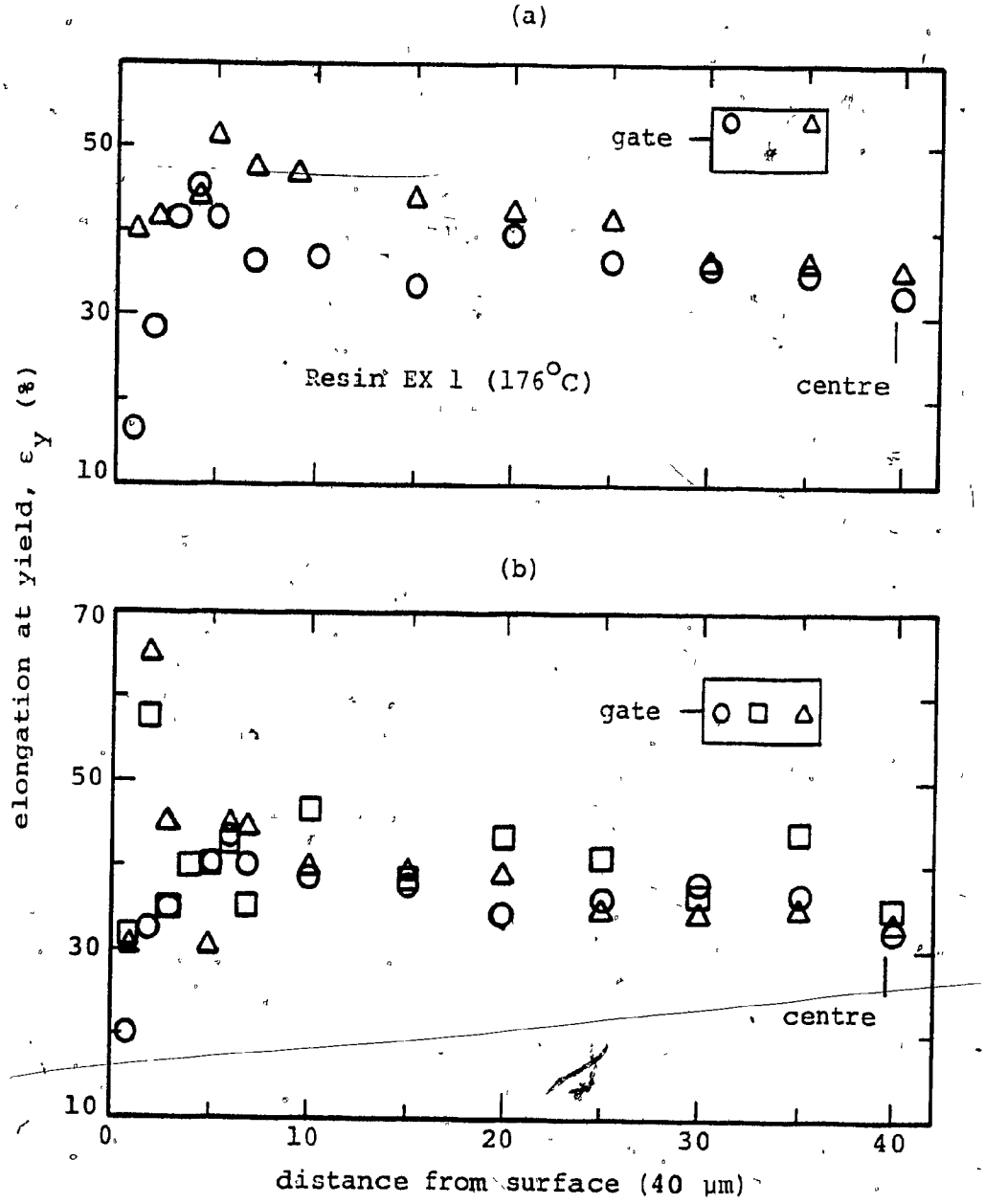


FIGURE 6.54. Variation of Percent Elongation at Yield in the Depth Direction

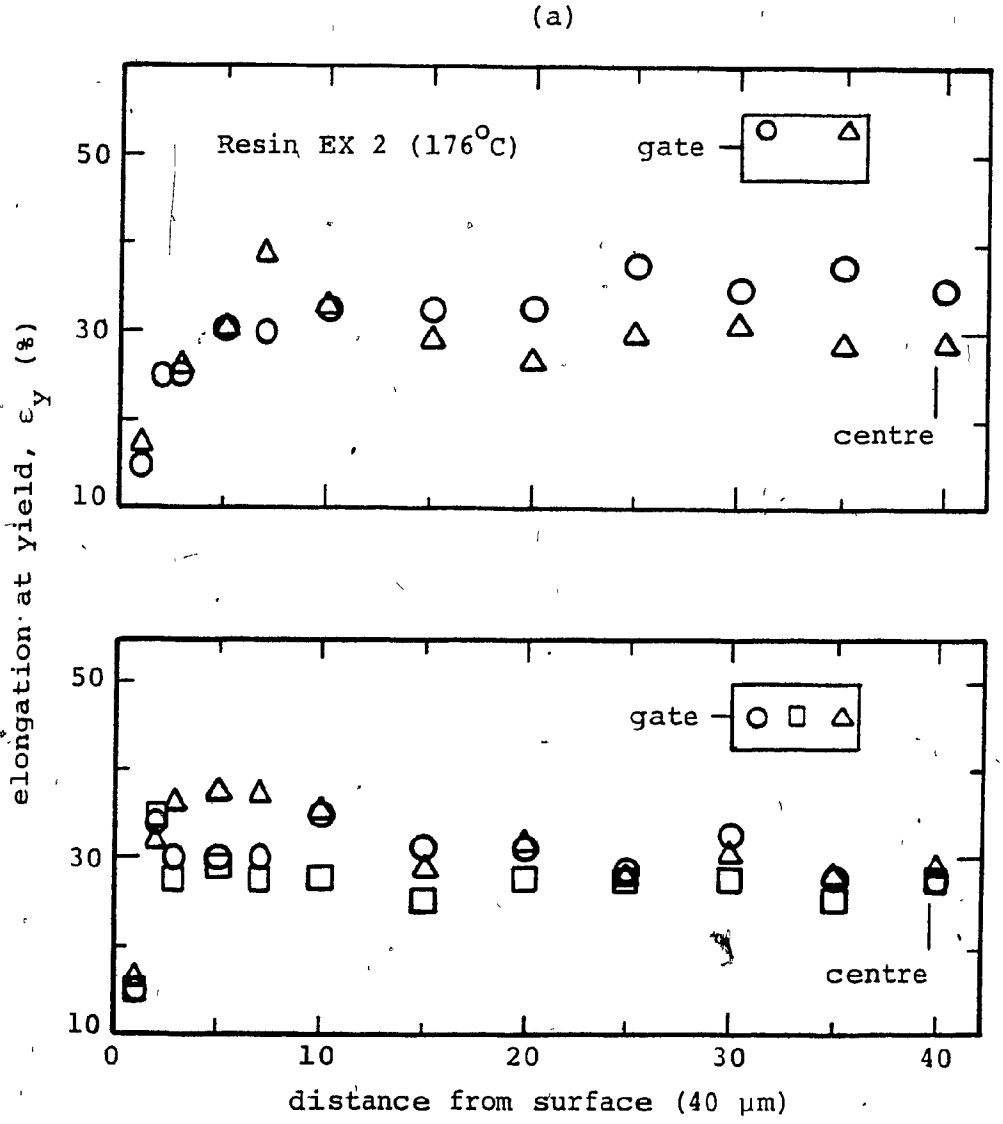


FIGURE 6.55. Variation of Percent Elongation at Yield in the Depth Direction

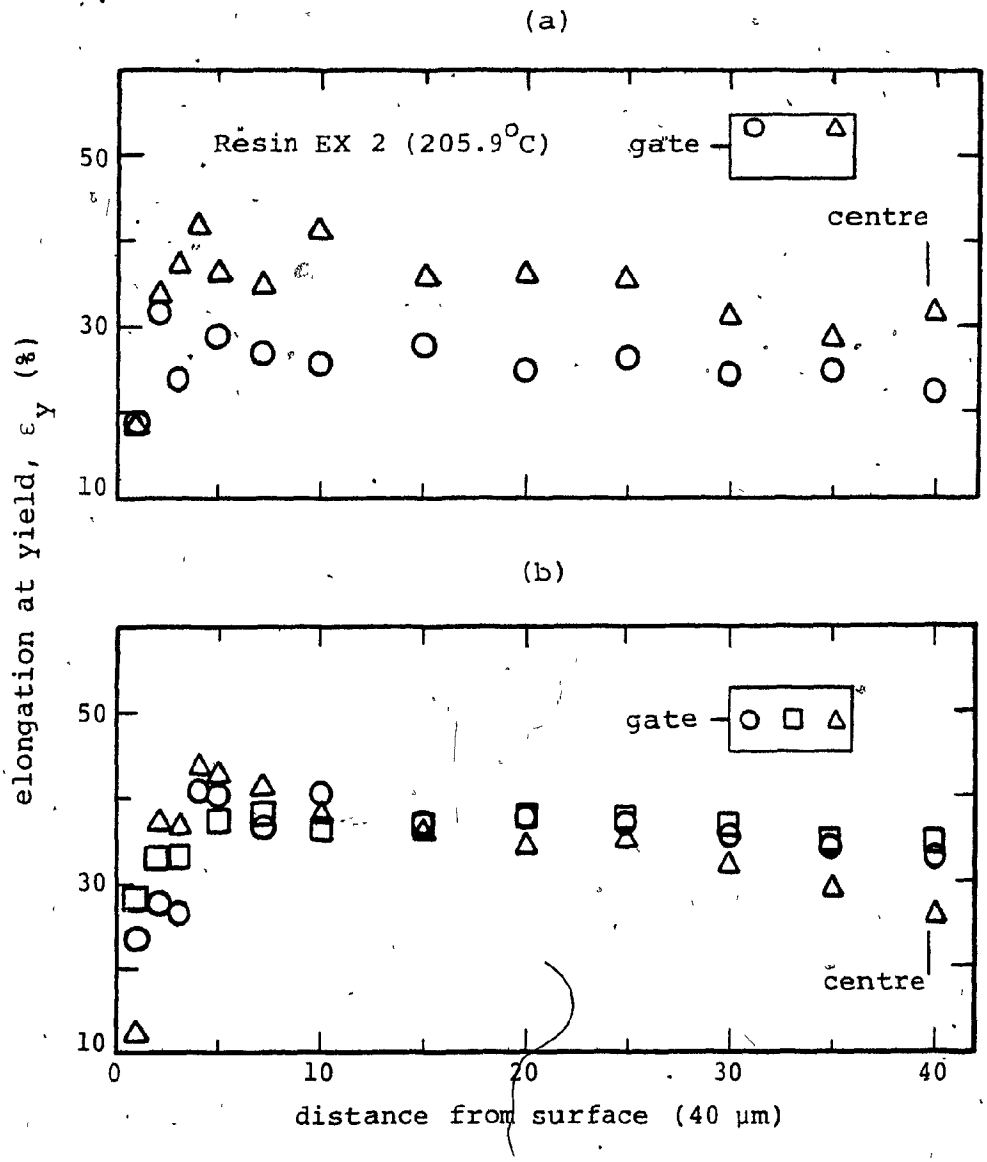


FIGURE 6.56. Variation of Percent Elongation at Yield in the Depth Direction

positions, the ε_y values also tend to increase from a value of about 20% to a maximum near the surface of about 40% and gradually decreases to a constant value of about 35% towards the core region. Figure 6.56(b) shows differences in the variation of ε_y in the depth direction for the two off-centre positions.

Figure 6.57 shows that resin EX 1 exhibits higher ε_y values than resin EX 2. Furthermore, increasing the injection melt temperature, tends to increase the elongation at yield throughout the molded part. Some results have been reported on the effect of molecular weight on the elongation at yield in injection molded parts (115). However, there has been very little reported information on the effects of processing on the elongation at yield in molded parts.

Figures 6.58 and 6.59 show the variation of the elongation to break in the depth direction at the various locations for the two resins molded at the melt temperature of 176°C. Generally, the ε_b values tend to increase to a maximum near the surface and decrease as distance from the surface increases. Again, the most pronounced variation is observed in the region (0-0.40 mm) for all locations. Beyond 0.40 mm (400 μm) from the surface, the ε_b values remain constant both with respect to the depth direction, as well as distance from the gate. Furthermore, the highest ε_b values are observed near the gate and the lowest values are far from the gate.

The higher ε_b values observed near the gate are due to the higher packing pressures which result in an increase of the fraction of row nucleated structures resulting in a substantial

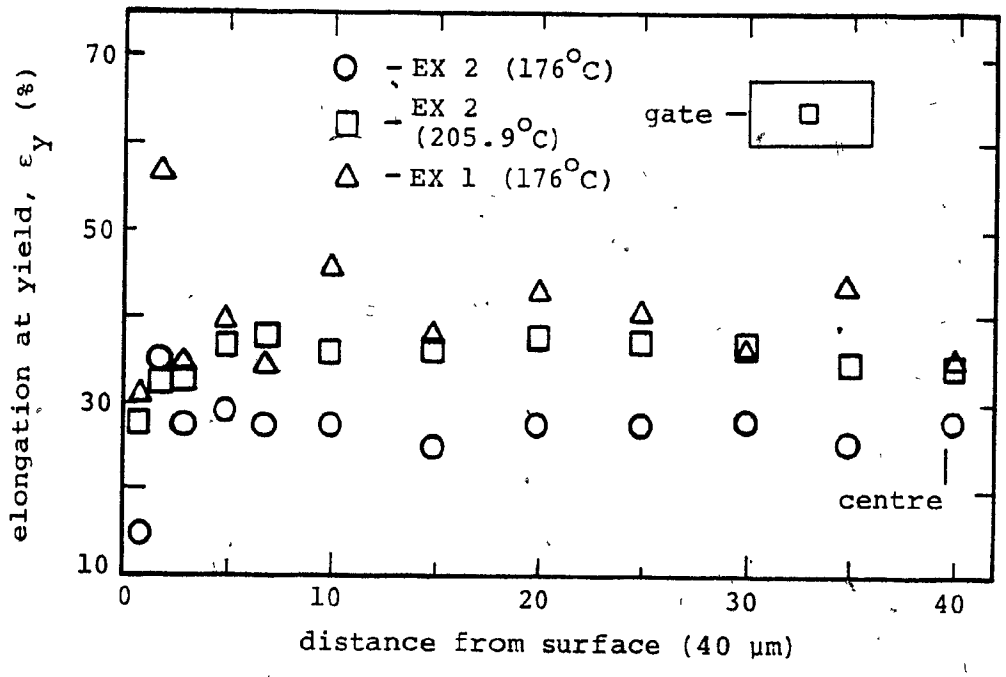


FIGURE 6.57. Typical Comparison of Percent Elongation at Yield Distributions

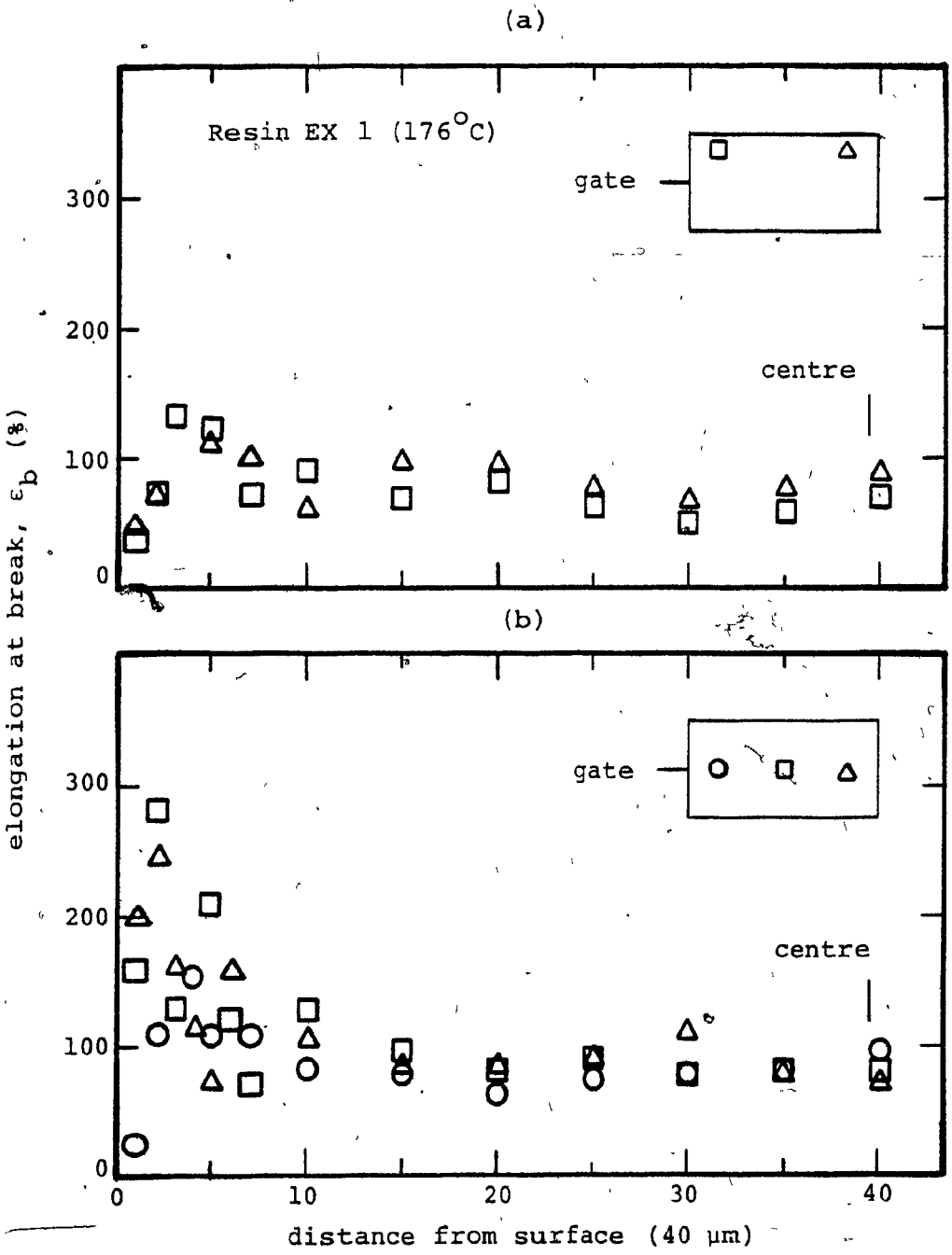


FIGURE 6.58. Variation of Percent Elongation at Break in the Depth Direction

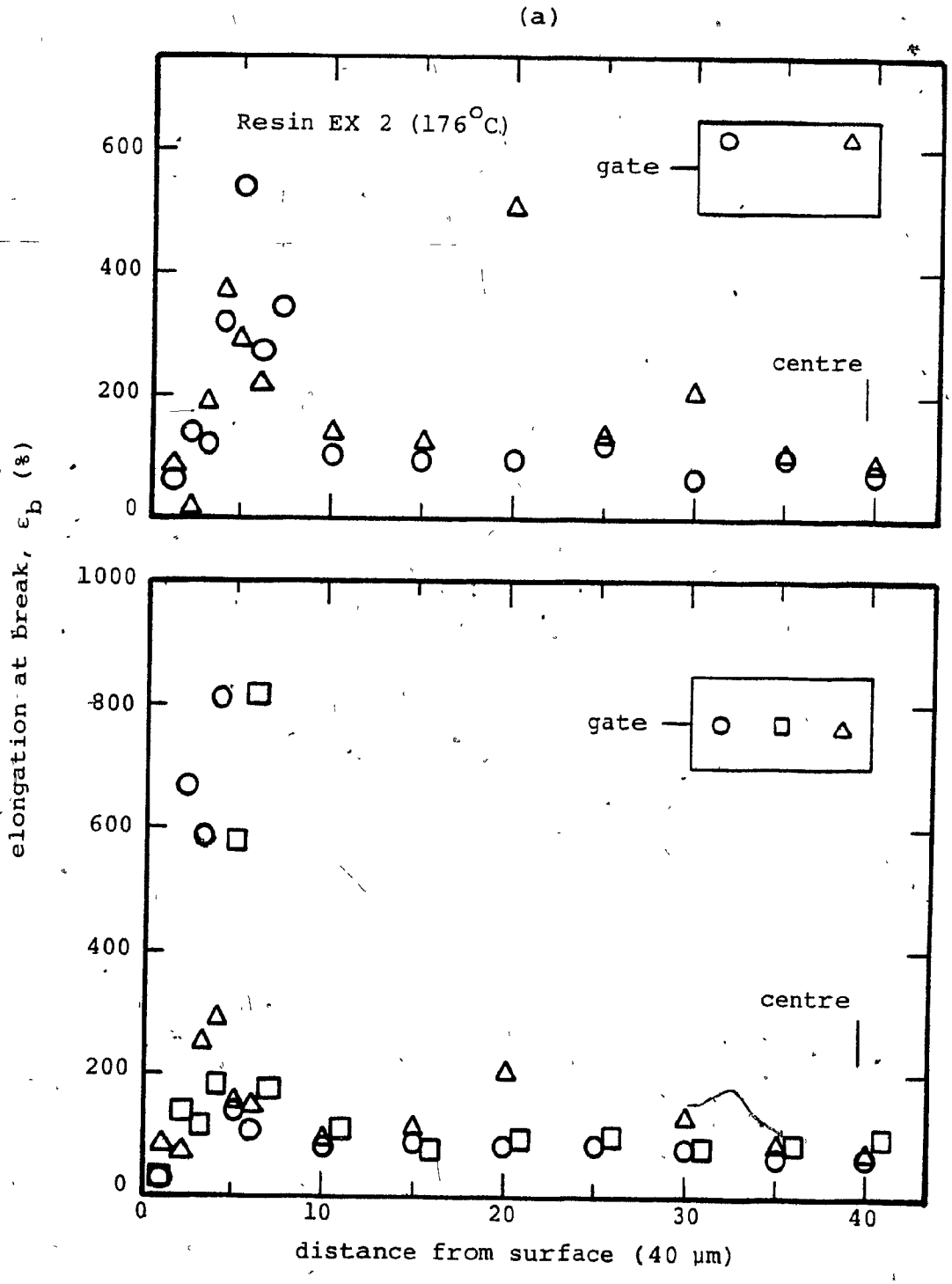


FIGURE 6.59. Variation of Percent Elongation at Break in the Depth Direction

improvement of the elongation at rupture (107, 108, 147, 169). The increased amount of these structures is due to a higher melt viscosity, giving higher shear stresses at elevated pressures resulting partly from a decrease in free volume and partly from a rise in the melting temperature (169, 170). This is consistent with the higher densities (crystallinities) observed near the gate in the region (0-0.40 mm) from the surface, as discussed in Section 6.2. Furthermore, previous DSC work (121) showed that a distribution of melting points was observed in the depth direction similar to the distribution of ε_b values observed for the two resins. Figure 6.60 shows the variation of the melting temperature in the depth direction for the two resins molded at the same melt temperature of 176°C, for the location midway from the gate. It shows that the maximum melting temperature observed near the surface corresponds to the maximum in elongation-to-break distribution. Furthermore, resin EX 2 tends to exhibit a higher maximum in the melting temperature distribution than resin EX 1. The higher ε_b values observed are attributable to the more perfect row structures of resin EX 2, since it has a higher melt viscosity during processing which tends to increase the fraction of row nucleated structures as explained earlier. Furthermore, this explanation is consistent with the observations that resin EX 2 exhibits both higher densities (crystallinities) and higher tensile yield stresses than resin EX 1.

At the high melt temperature, as shown in Figures 6.61(a) and (b), for the corresponding positions, the ε_b values in the

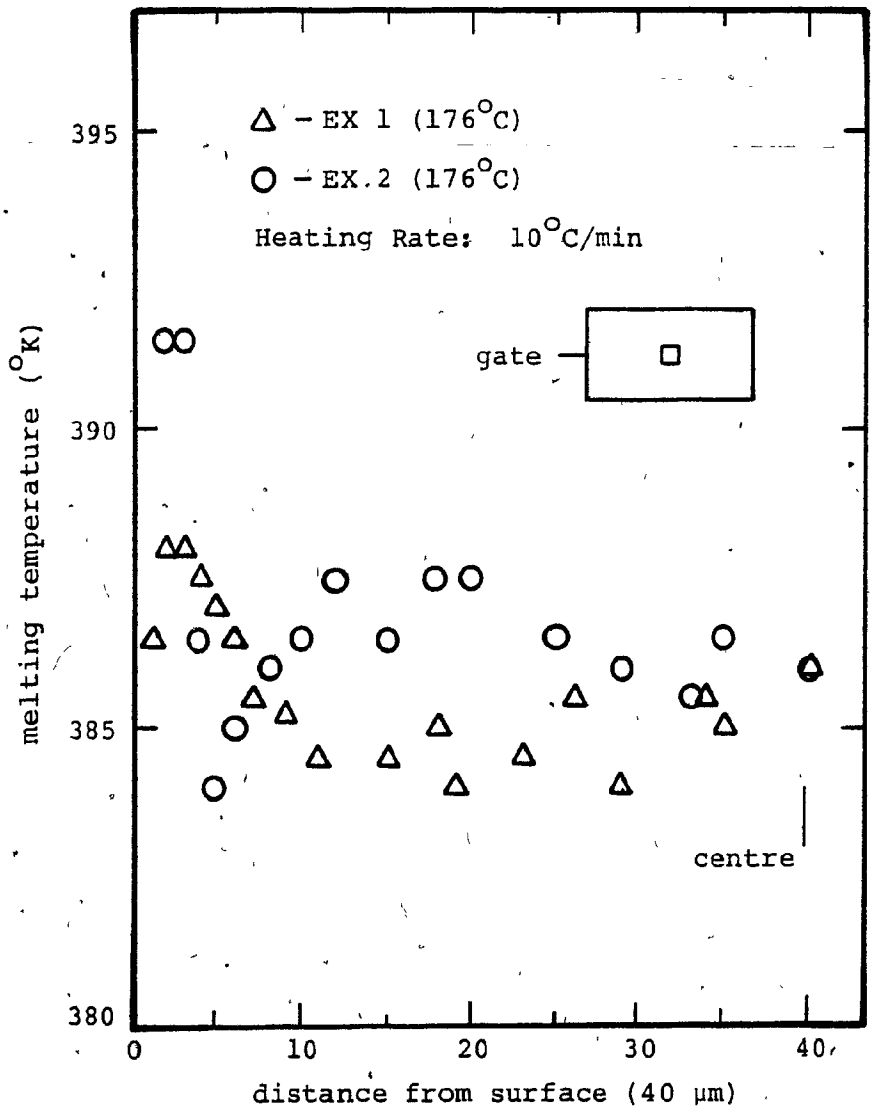


FIGURE 6.60. Variation of Melting Temperature in the Depth Direction at the Indicated Location. Unpublished Results from Reference (121).

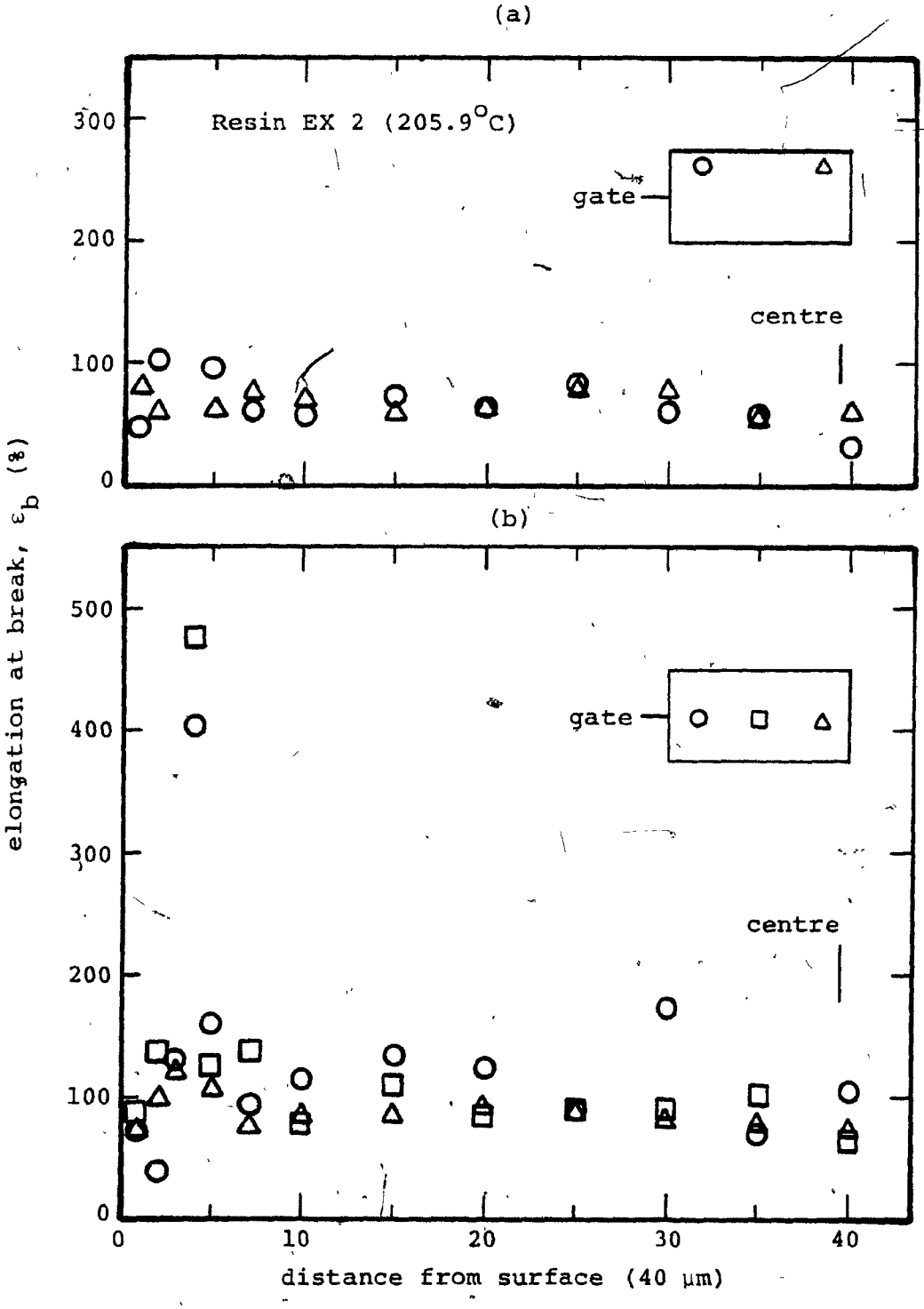


FIGURE 6.61. Variation of Percent Elongation at Break in the Depth Direction

intermediate layer decreases significantly (from 800% to 400%) so that the distribution of ε_b in the depth direction appears fairly uniform both with respect to the depth direction and distance from the gate. This is attributable to the decrease in the fraction of the row structures as a result of the lower melt viscosities during processing, as explained above. The above observation is consistent with the results reported by several workers (106, 107, 111, 115).

Figure 6.62 gives, as an example, a comparison of the distributions of ε_b for the location midway from the gate for resins EX 1 and EX 2 at an injection melt temperature of 176°C and for EX 2 at 205.9°C. These results are consistent with the observations made above.

Generally, the results of mechanical testing in the depth direction may be summarized as follows:

(1) The variations of the mechanical properties tested are most pronounced in the region (0-0.40 mm) in the depth direction of the molding. Beyond 0.40 mm (400 μm), the mechanical properties change very little with respect to the depth direction at all distances from the gate.

(2) Resin EX 2 tends to exhibit both a higher tensile yield stress and a higher elongation at break, but a lower elongation at yield than resin EX 1, molded at the melt temperature of 176°C.

(3) Increasing the injection melt temperature of resin EX 2 tends to increase both the tensile yield stress

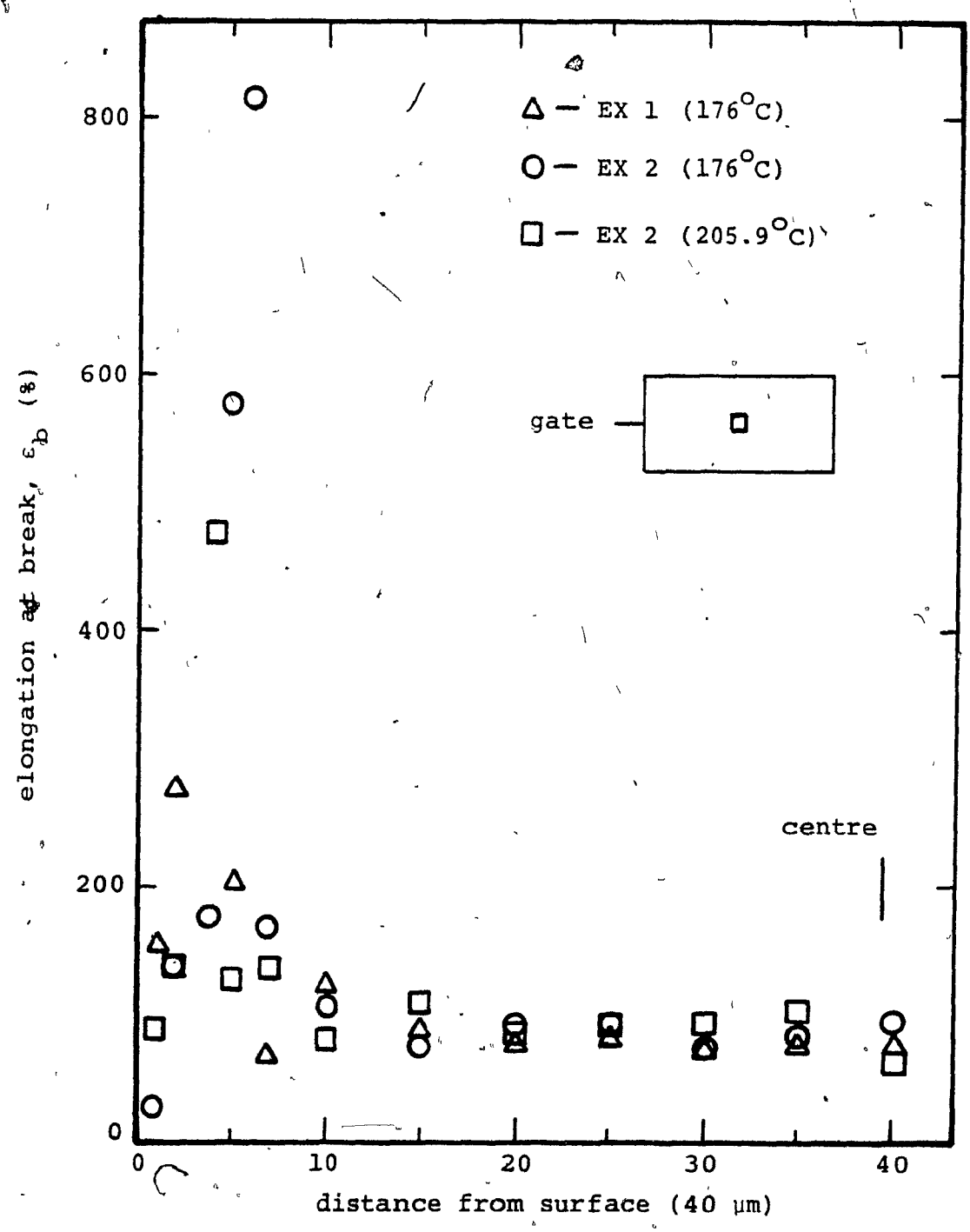


FIGURE 6.62. Typical Comparison of Percent Elongation at Break Distributions

and the elongation at yield, but decreases the elongation at break, throughout the molded part. This behavior is consistent with other reported results and with the role played by row nucleated structures.

6.10 Correlation and Integration of Results Obtained by the Various Techniques

In this section, the results of the correlation and integration of the various measurements are presented. By combining the results of density, sonic modulus and X-ray diffraction, the distribution of the degree of amorphous phase orientation (f_{am}) is obtained, as discussed previously in Section 4.6. Subsequently, the values of f_{am} are employed in the birefringence equation together with the results of density and X-ray diffraction to determine the intrinsic birefringence values for both the crystalline and amorphous phases, which in turn, are used to obtain the relative contributions of the crystalline and amorphous phases to the total orientation as measured by birefringence, in accordance with the discussion presented in Section 4.6. In addition, the results of crystallinity and orientation, obtained in the present study, are combined with the aim of predicting the sonic and tensile modulus distributions in injection moldings.

6.10.1 Amorphous Orientation

A detailed tabulation of the variation of the degree of amorphous orientation with the depth direction of the molding

for the two resins molded at the melt temperature of 176°C and for resin EX 2 molded at the high melt temperature of 205.9°C, are provided in Appendix 9. The error analysis associated with the estimation of the amorphous orientation function is presented in Appendix 15.

Figures 6.63 and 6.64 show the variation of f_{am} in the depth direction at the various locations for the two resins molded at the melt temperature of 176°C. Generally, the degree of amorphous orientation is maximum in the transverse direction near the surface, but becomes slightly oriented in the flow direction as distance from the surface increases. The transverse orientation of the amorphous phase in this region (0-0.20 mm) may be attributable to the hoop stress acting at the melt front during the filling of the mold. The transverse amorphous orientation is more distinct for the location near the gate than far from the gate, as illustrated in Figure 6.63(b) (114). It is suggested that orientation at or near the surface originates in the advancing melt front during the filling process, and this would also be the source of the transverse orientation (114, 162). The decrease of transverse amorphous orientation, resulting in higher orientation in the flow direction, is consistent with decrease of transverse (total) orientation as measured by heat shrinkage measurements reported for polystyrene injection moldings (114).

Figures 6.65(a) and (b) show the effect of increasing the injection melt temperature to 205.9°C for resin EX 2 at the various locations. Generally, the distribution of f_{am} in the

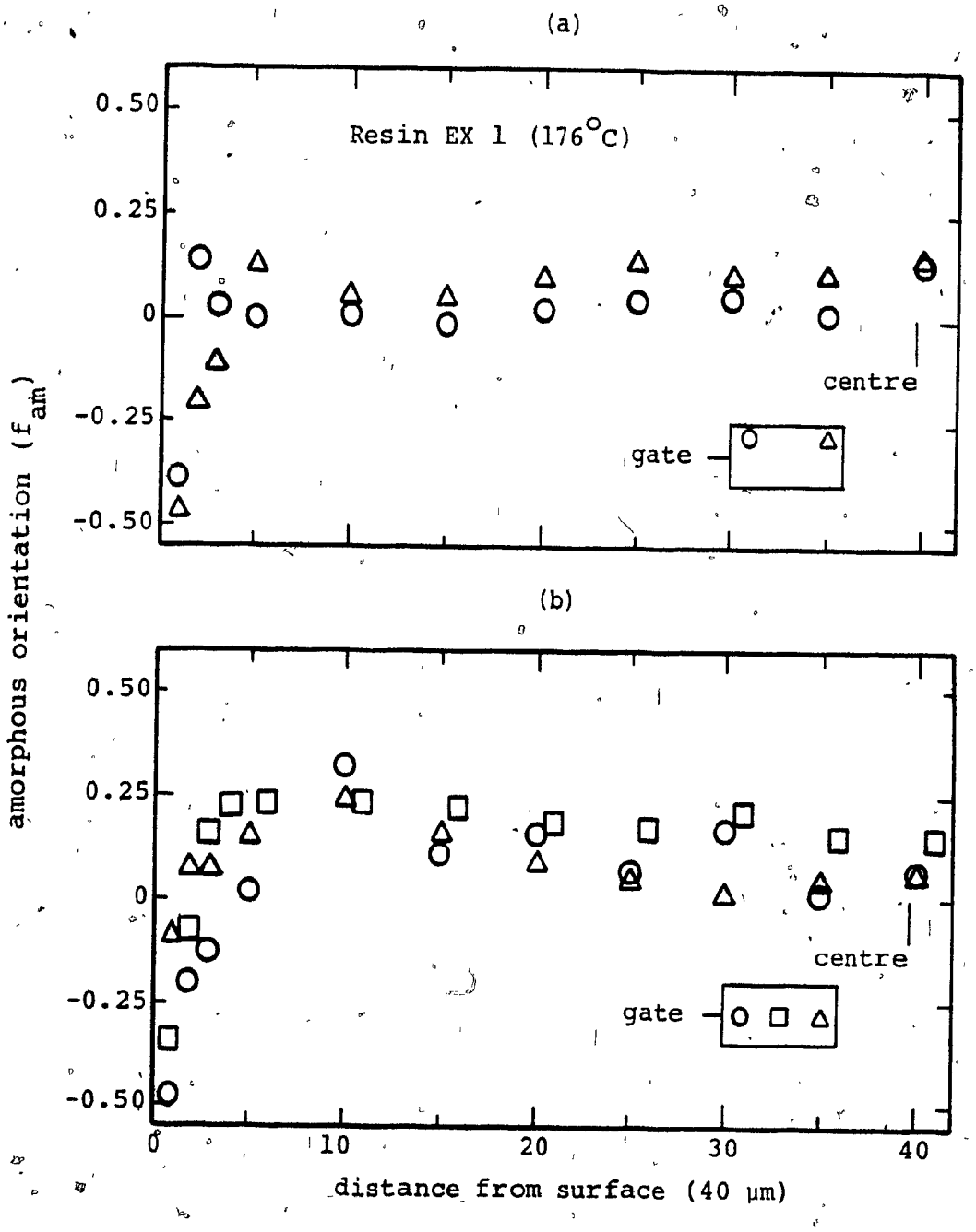


FIGURE 6.63. Variation of Amorphous Orientation Function in the Depth Direction

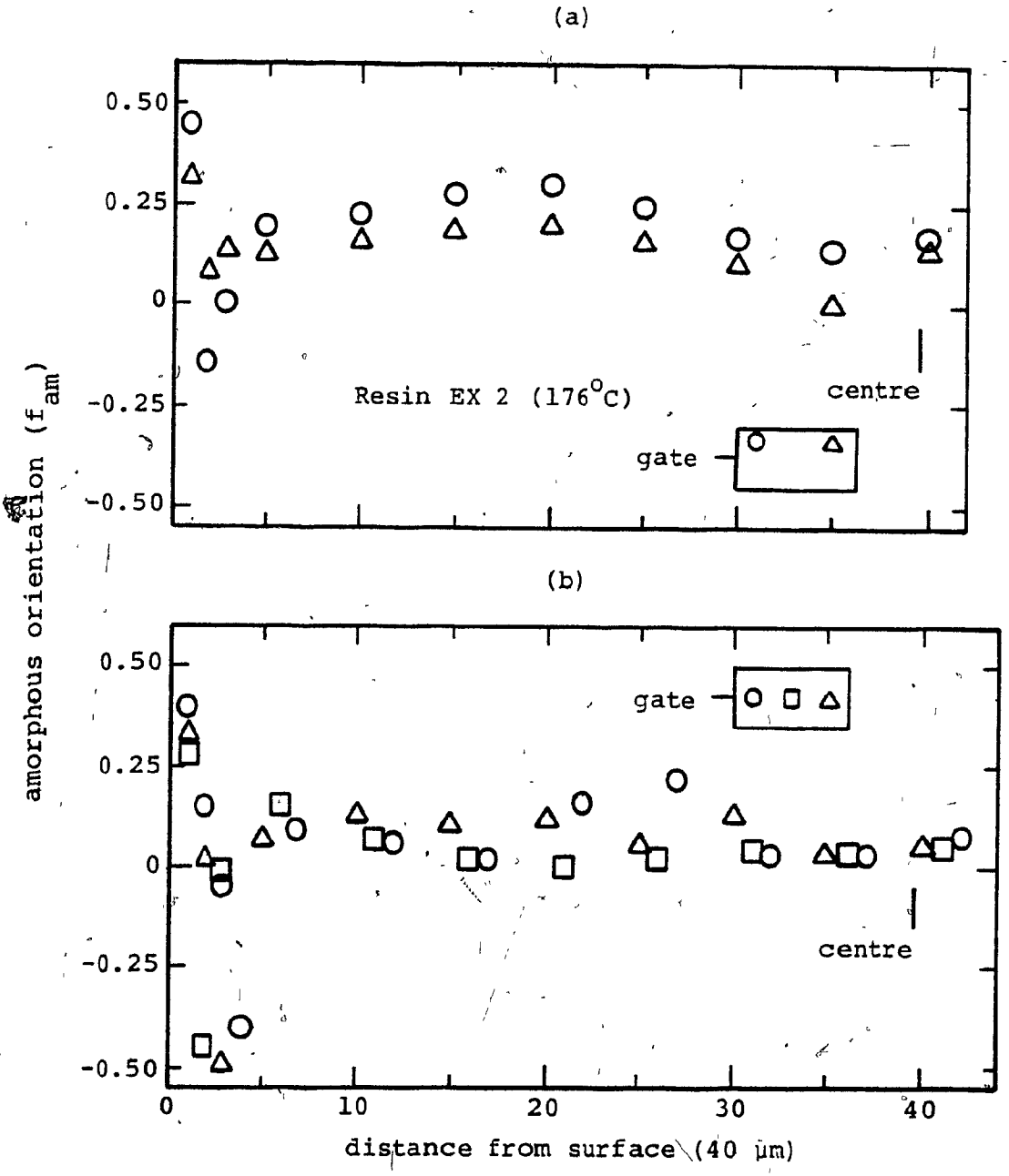


FIGURE 6.64. Variation of Amorphous Orientation Function in the Depth Direction

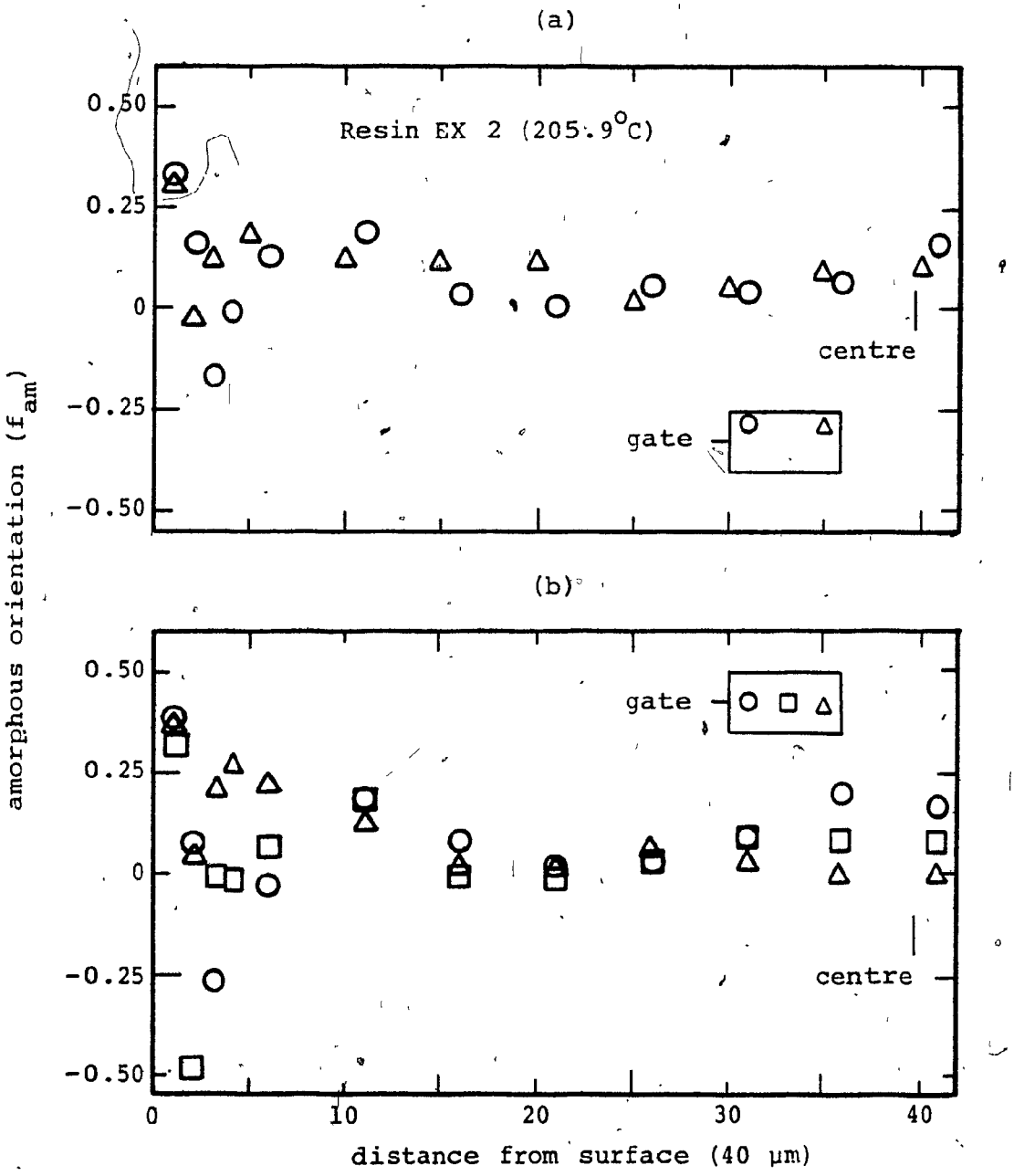


FIGURE 6.65. Variation of Amorphous Orientation Function in the Depth Direction

depth direction is essentially identical to that observed at the low melt temperature. The degree of amorphous orientation is maximum in the flow direction at the surface, but decreases to a minimum near the surface and increases only slightly in the flow direction as distance from the surface increases. The decrease of transverse orientation both with respect to the depth direction as well as away from the gate, is consistent with the observation made above for the two resins molded at the same, but lower melt temperature, as discussed above. The overall lower transverse amorphous orientation observed in the region (0-0.20 mm) near the surface is due to the generally longer cooling times.

Figure 6.66 shows that resin EX 2 tends to exhibit a maximum degree of amorphous orientation in the flow direction at the surface, regardless of melt temperature. The higher overall orientation generally observed at the surface for resin EX 2 is attributed to the faster crystallization rate under shear deformation, as discussed in Section 6.6. Furthermore, it is observed that resin EX 1 tends to exhibit generally lower degree of transverse amorphous orientation or increasingly higher longitudinal amorphous orientation in the depth direction than resin EX 2.

Generally, the results of the variation of the amorphous phase orientation in the depth direction may be summarized as follows:

(1) All moldings exhibit transverse amorphous orientation in the region (0-0.20 mm) near the surface. However,

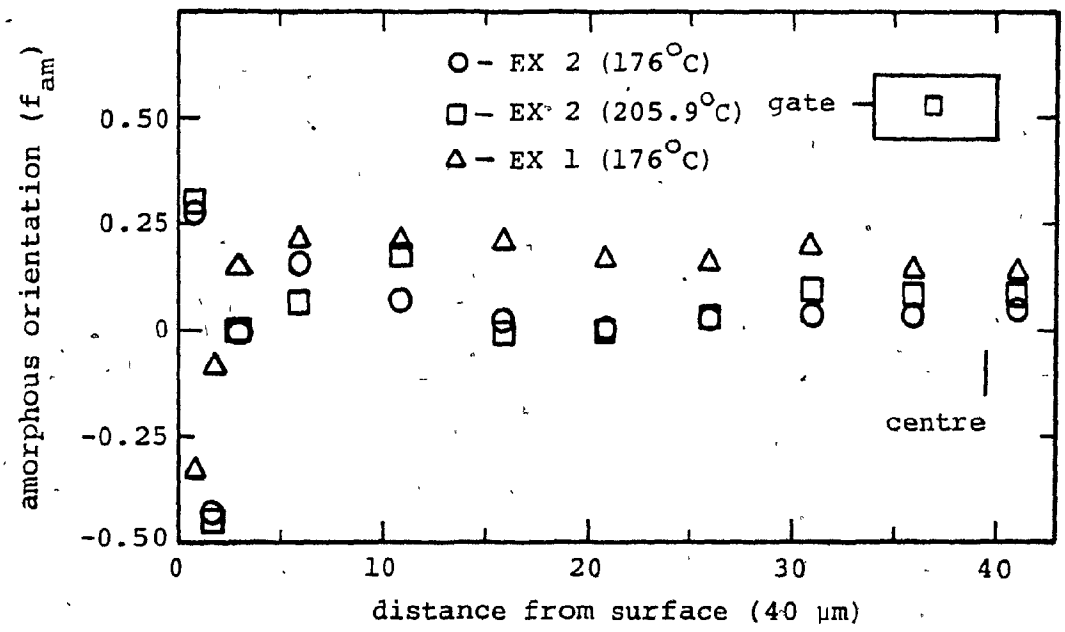


FIGURE 6.66. Typical Comparison of Amorphous Orientation Function Distributions

the variation of the amorphous phase orientation is most pronounced in the region (0-0.40 mm) which is consistent with the results of previous measurements.

(2) The transverse amorphous orientation is more distinct for the location near the gate and less for the location far from the gate.

(3) Resin EX 2 tends to exhibit maximum degree of amorphous orientation in the flow direction at the surface regardless of melt temperature, while resin EX 1 tends to show a minimum under the same molding conditions. Except at the surface, resin EX 1 tends to exhibit marginally higher longitudinal amorphous orientation than resin EX 2 towards the core region.

(4) As observed for resin EX 2, increasing the injection melt temperature tends to lower the transverse amorphous orientation observed near the surface both in the depth direction, as well as in the longitudinal direction.. The degree of amorphous orientation is marginally affected at the high melt temperature towards the core region.

6.10.2 Crystalline and Amorphous Intrinsic Birefringences

As discussed previously in Section 4.6, before the birefringence measurements could be used to establish the relative magnitudes of crystalline and amorphous orientation, it was first necessary to estimate the values of the intrinsic birefringence values for the crystalline and amorphous phases. This

is achieved by combining sonic modulus and X-ray diffraction data and making use of Equation (4-9) to obtain the amorphous orientation function using the values of the intrinsic moduli obtained from sonic modulus measurements on compression molded samples. The values of the amorphous orientation function are then combined with the degree of crystallinity from density, and the crystalline orientation function by X-ray diffraction according to the relationship shown in the birefringence equation (Equation (4-11)) to obtain the values of the intrinsic birefringence of the crystalline (Δ_c^o) and amorphous (Δ_{am}^o) phases, respectively.

Figures 6.67 to 6.69 show the plots of ($\Delta_T/X_c\ f_{cr}$) against ($1 - X_c/X_c$)(f_{am}/f_{cr}), giving rise to the estimated values of Δ_c^o and Δ_{am}^o for the two resins molded at the melt temperature of 176°C and for resin EX 2 molded at the high melt temperature of 205.9°C. Each figure shows the plot of representative data corresponding to the five locations. A detailed tabulation of the combined data using the results of the various techniques is provided in Appendix 10. A linear regression of the data, as represented in Figures 6.67 to 6.69, shows a linear relationship with correlation coefficients of 0.964 and 0.729 for resins EX 2 and EX 1, respectively. The slope of the straight line gives the value of Δ_{am}^o and the intercept gives the value of Δ_c^o. The estimated values of Δ_c^o and Δ_{am}^o are summarized and compared with the calculated values, as shown in Table 6.5.

The estimated values obtained for the crystalline and amorphous phases, respectively, appear to agree reasonably well with

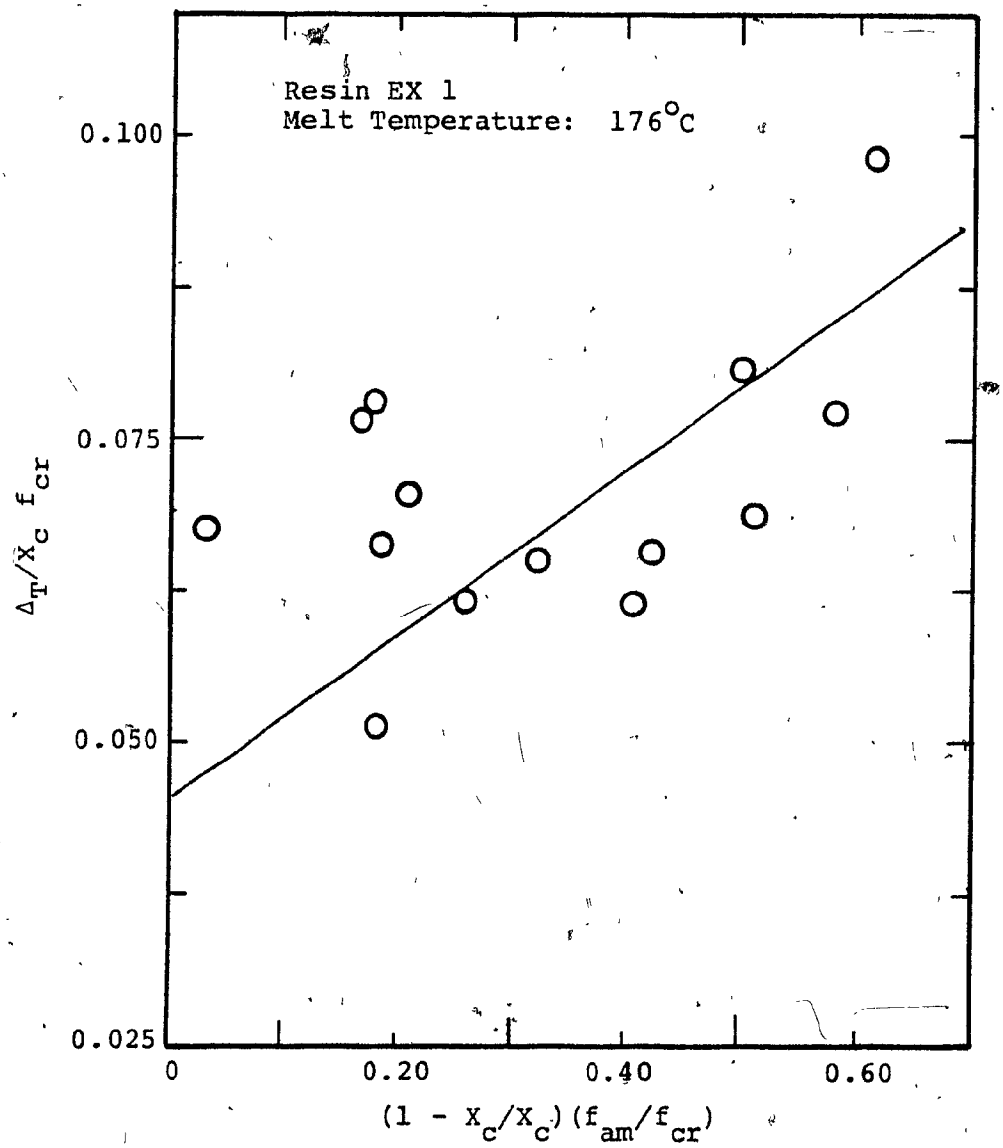


FIGURE 6.67. Plot of $(\Delta_T/X_c\ f_{cr})$ Versus $(1 - X_c/X_c)(f_{am}/f_{cr})$ for Resin EX 1 Molded at 176°C

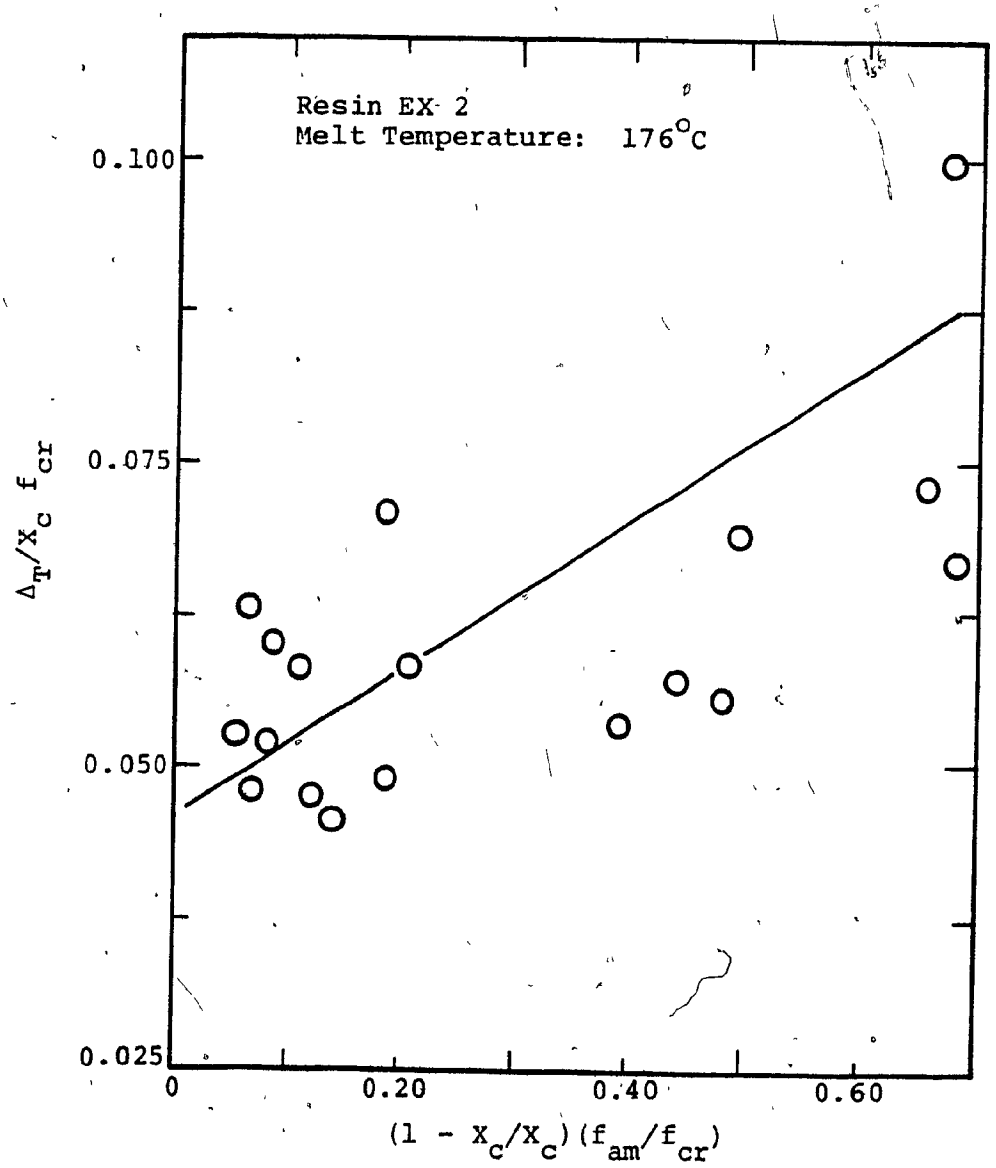


FIGURE 6.68. Plot of $(\Delta_T/X_c\ f_{cr})$ Versus $(1 - X_c/X_c)(f_{am}/f_{cr})$ for Resin EX 2 Molded at 176°C

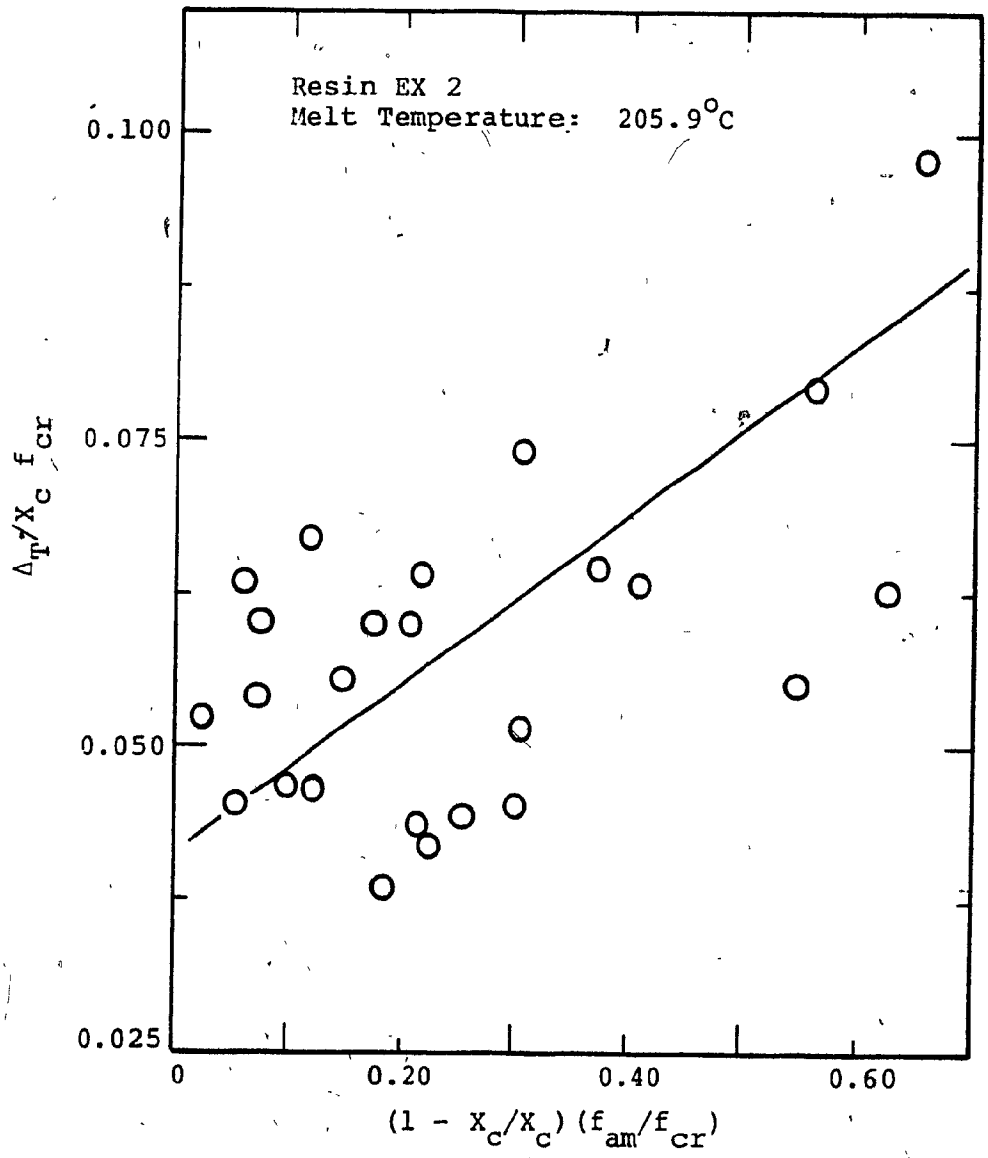


FIGURE 6.69. Plot of $(\Delta_T/X_c\ f_{cr})$ Versus $(1 - X_c/X_c)(f_{am}/f_{cr})$ for Resin EX 2 Molded at 205.9°C

TABLE 6.5. Comparison of Intrinsic Birefringence Values

Resin	Melt Temp. (°C)	Δ_c^o	Δ_{am}^o
EX 1	176	55.3×10^{-3}	58.2×10^{-3}
EX 2	176	54.9×10^{-3}	61.3×10^{-3}
EX 2	205.9	51.9×10^{-3}	72.3×10^{-3}
Experimental mean:		$(54.0 \pm 1.85) \times 10^{-3}$	$(63.9 \pm 7.41) \times 10^{-3}$
Calculated values:		58.5×10^{-3} (Ref. 54)	200×10^{-3} (Ref. 96)

each other. However, when the average estimated values of Δ_c^o and Δ_{am}^o are compared with the calculated values, it is seen that the mean value of 54.0×10^{-3} for Δ_c^o compares fairly well with the calculated value of 58.5×10^{-3} obtained by considering the crystal refractive indices (74), while the mean value of 63.9×10^{-3} for Δ_{am}^o shows a significant difference with the value of 0.2 for Δ_{am}^o (96), calculated from the Denbigh values for bond polarizabilities (171). A number of workers have indicated that the possible influence of internal field upon chain anisotropy makes the value of Δ_{am}^o, the intrinsic birefringence of completely oriented amorphous polymer, uncertain (74, 172). That is, a polyethylene chain in a solid placed in an electric field is influenced by the induced dipolar field of the neighbouring chains, which depends upon the arrangement and orientation of the neighbours and may differ considerably for crystalline and amorphous structures (74, 172). Furthermore, the effect of internal field upon K, the ratio Δ_{am}^o/Δ_c^o, casts some doubt about whether K and hence, Δ_{am}^o, is constant and independent of f_{am}, the degree of amorphous orientation. If internal field depends upon the configuration of neighbours, it is conceivable that it might change with amorphous orientation (74). A number of workers have reported that the value of K may be as high as 4 (51, 172). Furthermore, when the data are plotted by assuming a constant Δ_{am}^o value of 0.20, as shown in the example of Figure 6.70, a value of 51.3×10^{-3} for Δ_c^o is obtained. The value of Δ_c^o estimated by this procedure is in reasonably good agreement with the calculated value of 58.5×10^{-3}. A similar treatment of the data for

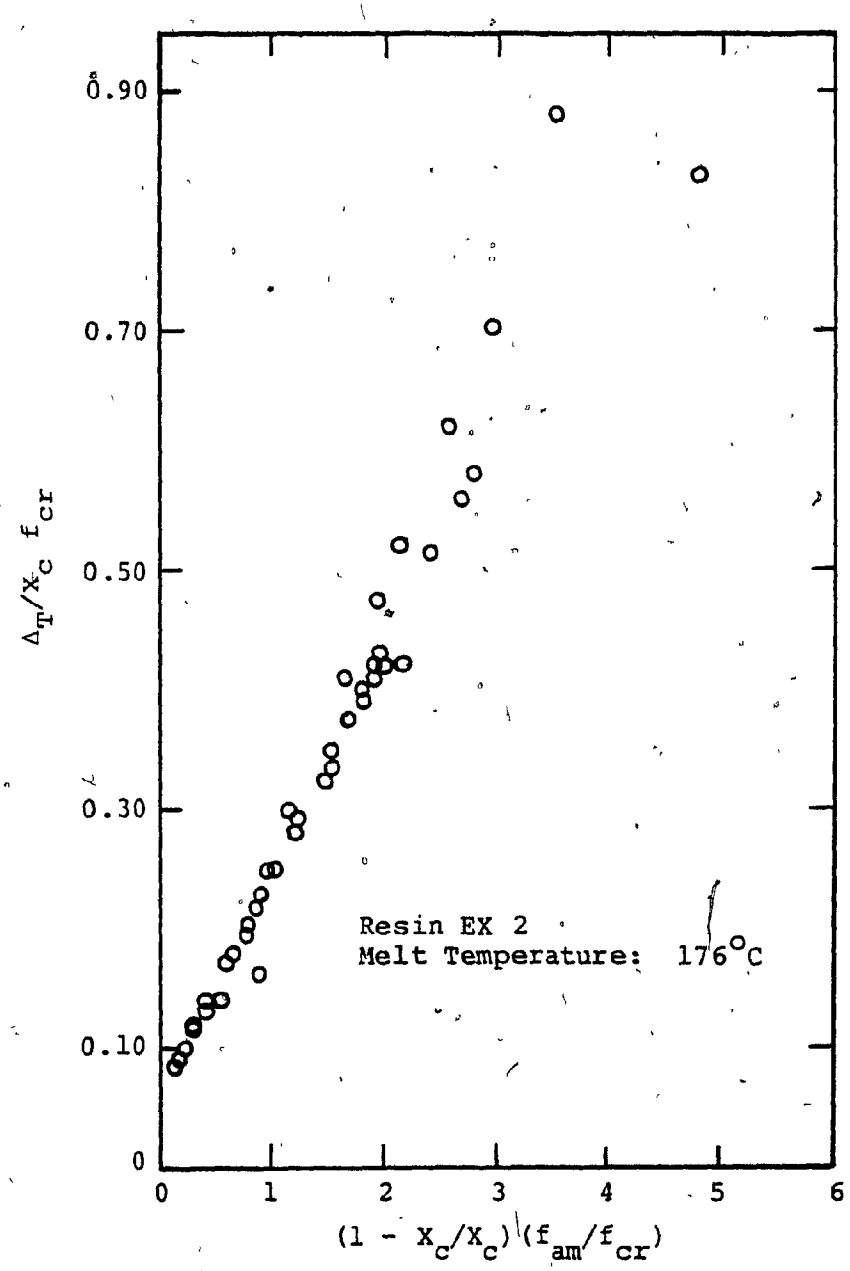


FIGURE 6.70. Plot of $(\Delta_T/X_c\ f_{cr})$ Versus $(\Delta_{am}/X_c\ f_{cr})$ for Resin EX 2 Molded at 176°C

the estimation of Δ_c^o has been reported, based on the solid-state extrusion of high density polyethylene (100). Moreover, an estimated value of 48.5×10^{-3} for Δ_{am}^o has been reported, based on the solid-state hydrostatic extrusion of polyethylene (173). The relatively low value estimated for Δ_{am}^o was attributed to the internal field effects, as discussed above. A comparison of the estimated values for Δ_c^o and Δ_{am}^o, based on other polymer processing operations, is shown in Table 6.6. As a first step, the average values of 54.0×10^{-3} for Δ_c^o and 63.9×10^{-3} for Δ_{am}^o obtained in this study, are considered fairly reasonable, in view of the scarcity of data regarding the intrinsic values, based on injection molded samples.

The intrinsic birefringence values are used in combination with birefringence, X-ray diffraction, and degree of crystallinity from density, to resolve the total birefringence of the injection molded samples into its crystalline and amorphous components. The results are discussed in the next section.

6.10.3 Relative Contributions of Crystalline and Amorphous Phases to Total Orientation

As discussed in Section 4.6, once the intrinsic birefringence values are established, the combination of density (crystallinity), birefringence, and X-ray diffraction are then used to resolve the birefringence of the injection molded specimens into its crystalline and amorphous components. A detailed tabulation of the variation of the relative amount of crystalline and amorphous orientation in the depth direction for the two

TABLE 6.6. Comparison of Estimated Intrinsic Birefringence Values for Polyethylene

Workers	$\Delta_c^o \times 10^{-3}$	$\Delta_{am}^o \times 10^{-3}$	Polymer Processing Operation
This study	54.0	63.9	Injection Molding
Porter et al. (100)	59.0	-	Solid-State Extrusion
Nakayama et al. (173)	57.2	48.5	Solid-State Extrusion
Stein et al. (54)	75.0	-	Stretched Films

resins molded at the melt temperature of 176°C and for resin EX 2 molded at the high melt temperature of 205.9°C, at the corresponding locations, is provided in Appendix 11.

Figures 6.71 to 6.80 show the distributions in the depth direction of the relative contributions of the crystalline and amorphous phases to the total orientation, as measured by birefringence, at the various locations for the two resins molded at the melt temperature of 176°C. Generally, it is the crystalline phase that makes the major contribution to the total orientation at the surface for resin EX 1, as shown in Figures 6.71 to 6.75. In the case of resin EX 2, shown in Figures 6.76 to 6.80, generally, it is the amorphous phase that makes the major contribution to the total orientation at the surface. The maximum orientation at the surface is attributable to the faster crystallization rate of resin EX 2 during the filling stage of the molding cycle, as discussed in Section 6.6.

In the region (0.08-0.20 mm) from the surface, the general tendency observed for the two resins is for both the crystalline and amorphous phases to contribute about equally to the total orientation. Towards the core region, it is the crystalline phase that makes the major contribution to the total orientation, as observed for the two resins, although resin EX 2 tends to exhibit relatively higher crystalline contribution, with respect to the total orientation, than resin EX 1.

As shown in Figures 6.81 to 6.85, increasing the injection melt temperature of resin EX 2, tends to lower the relative contribution of the amorphous phase, for example, from 86% to 49%

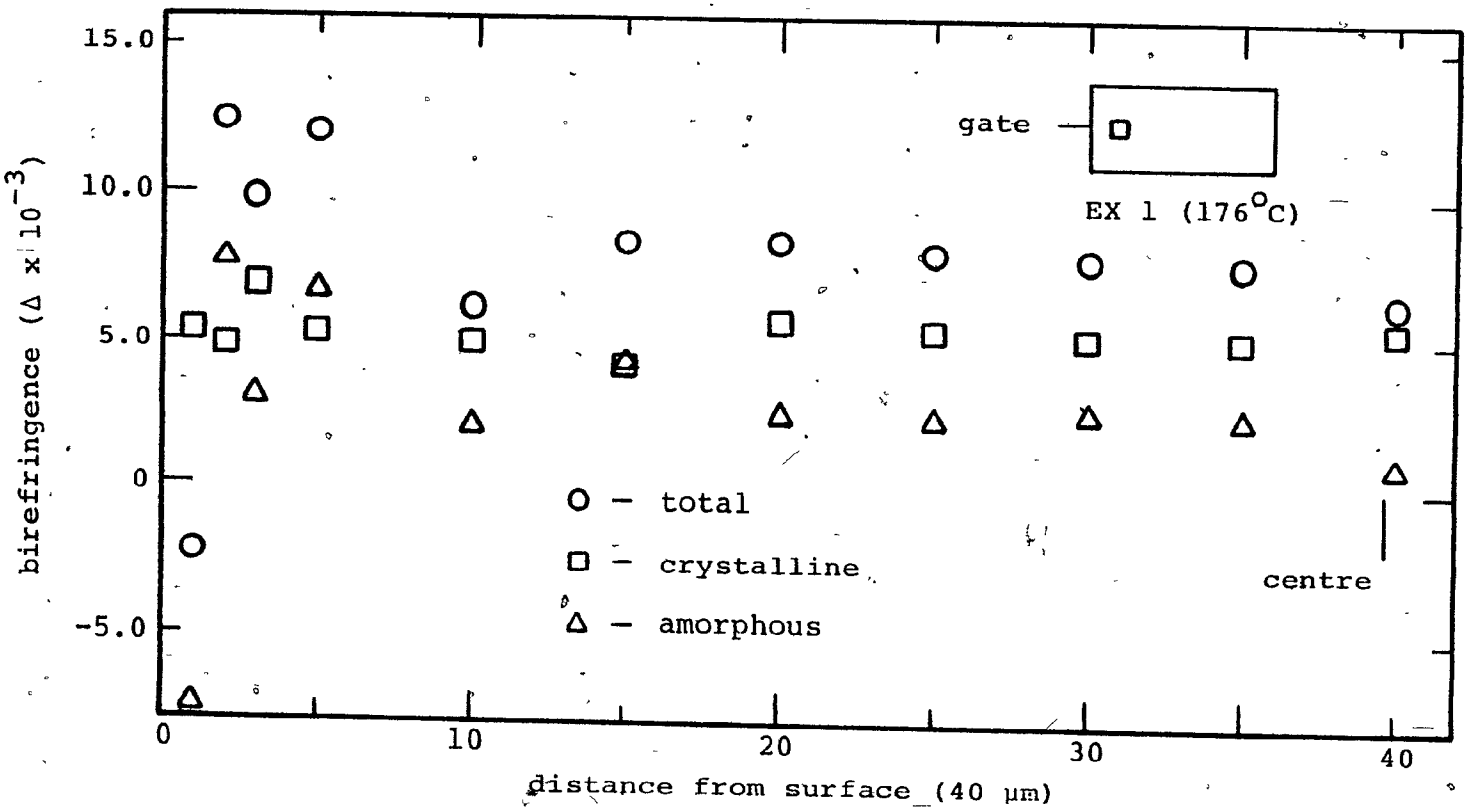


FIGURE 6.71. Crystalline and Amorphous Phase Contributions to the Total Birefringence

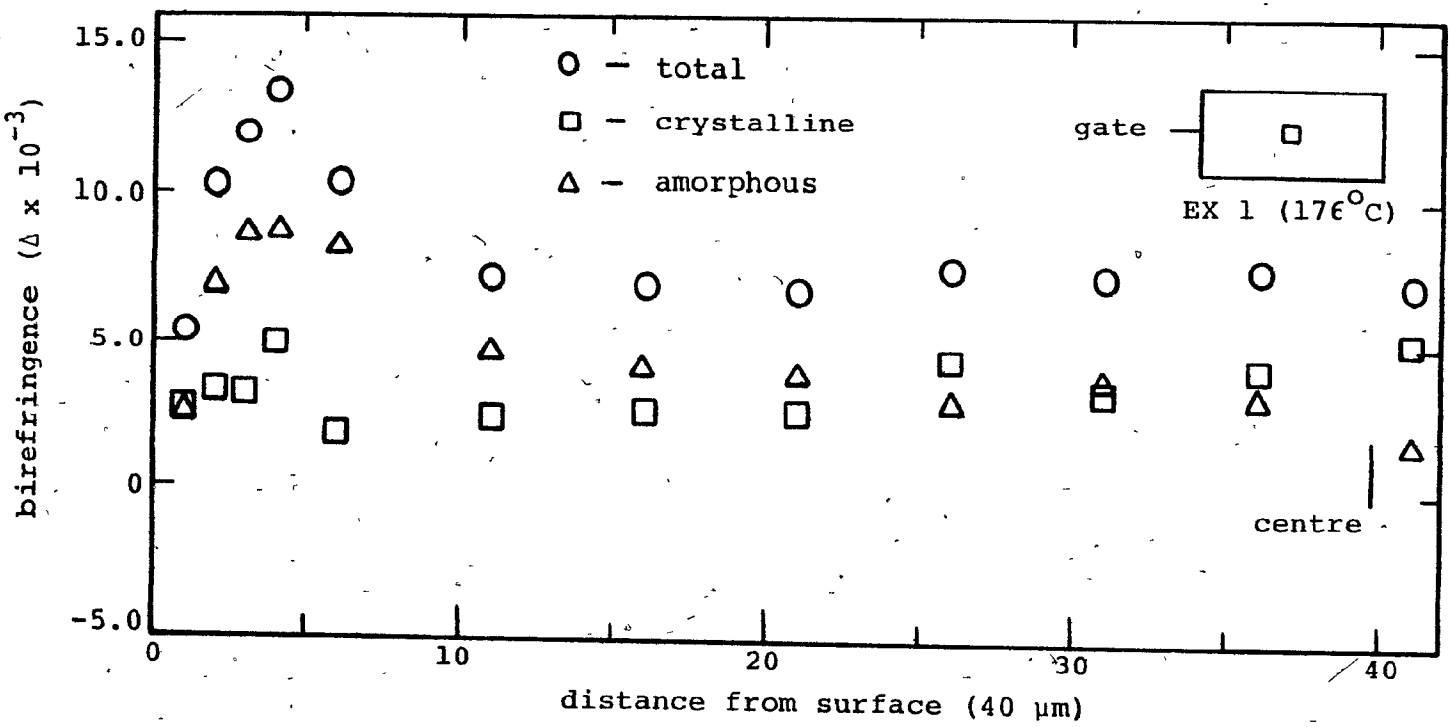


FIGURE 6.72. Crystalline and Amorphous Phase Contributions to the Total Birefringence

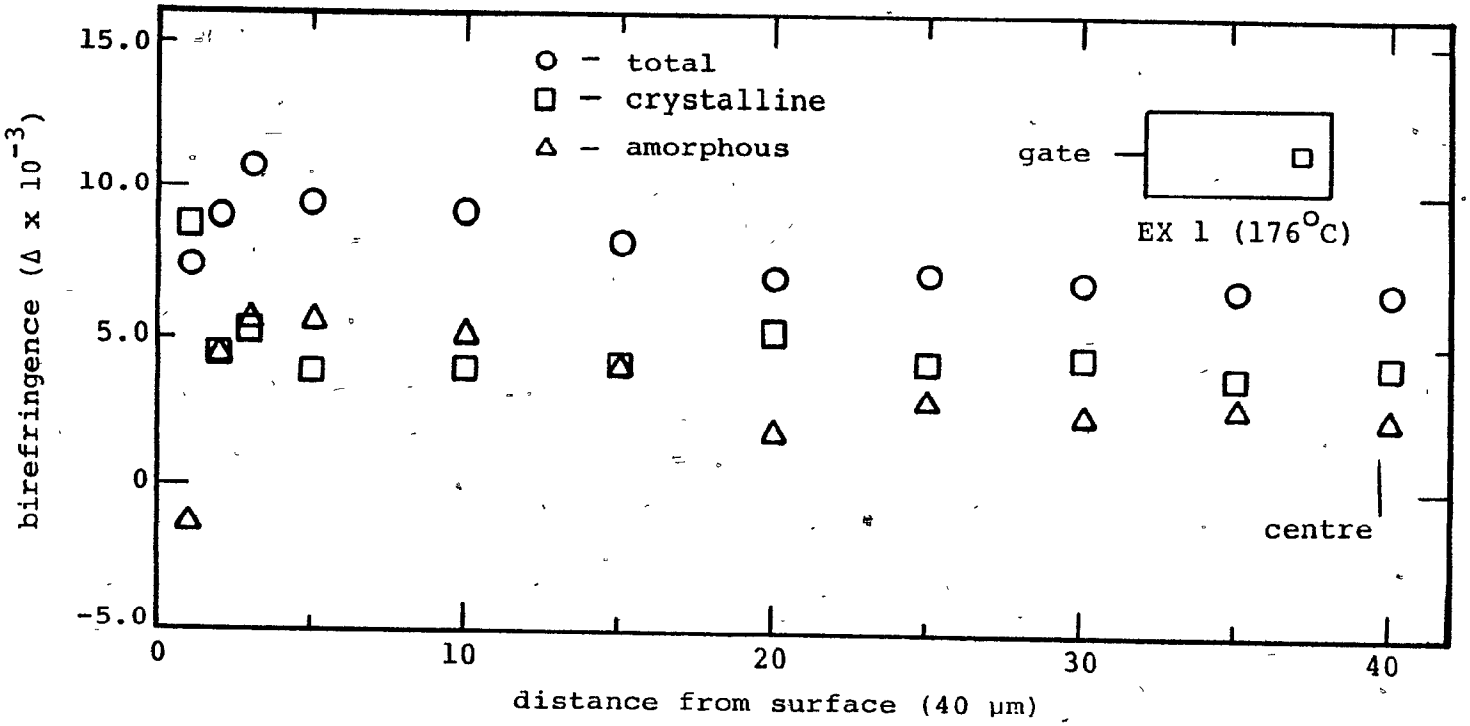


FIGURE 6.73. Crystalline and Amorphous Phase Contributions to the Total Birefringence

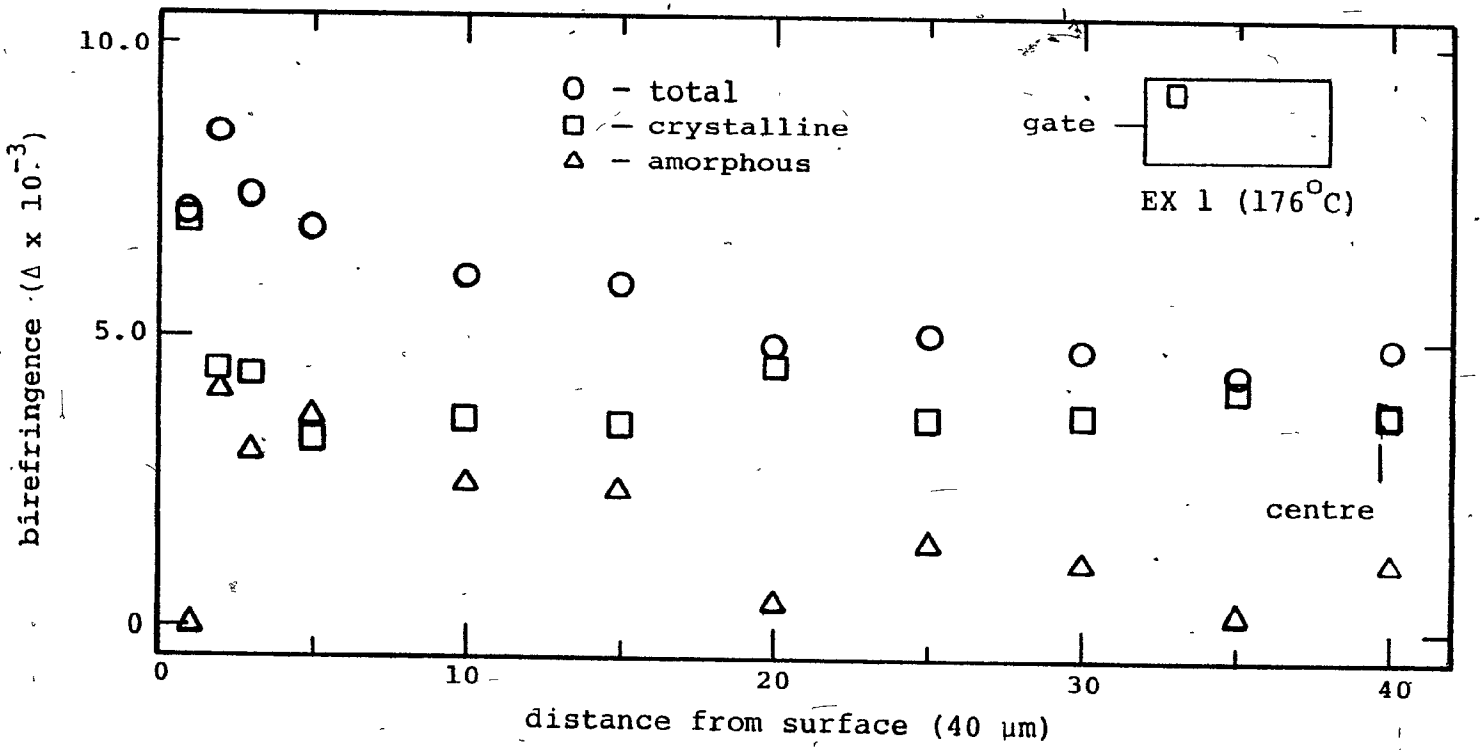


FIGURE 6.74. Crystalline and Amorphous Phase Contributions to the Total Birefringence

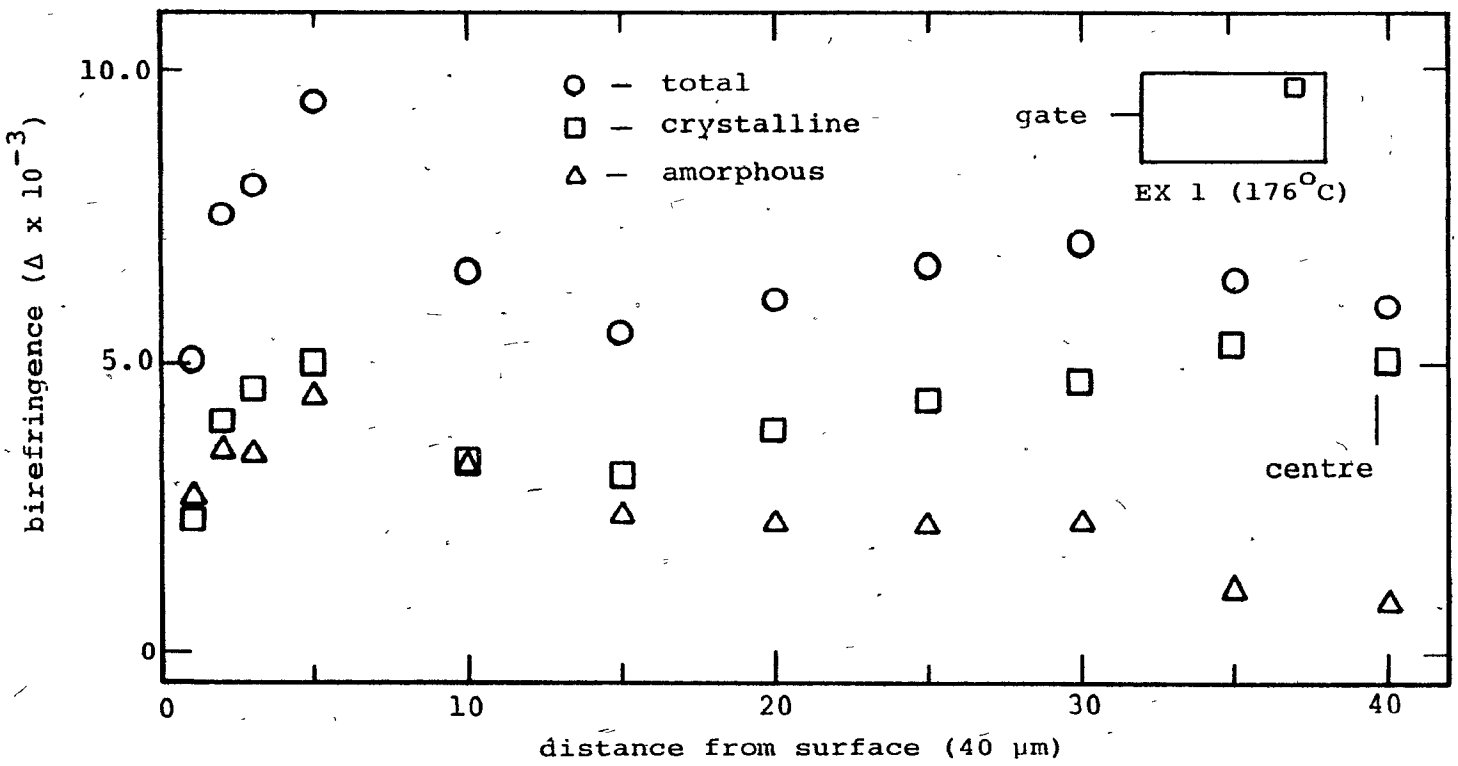


FIGURE 6.75. Crystalline and Amorphous Phase Contributions to the Total Birefringence

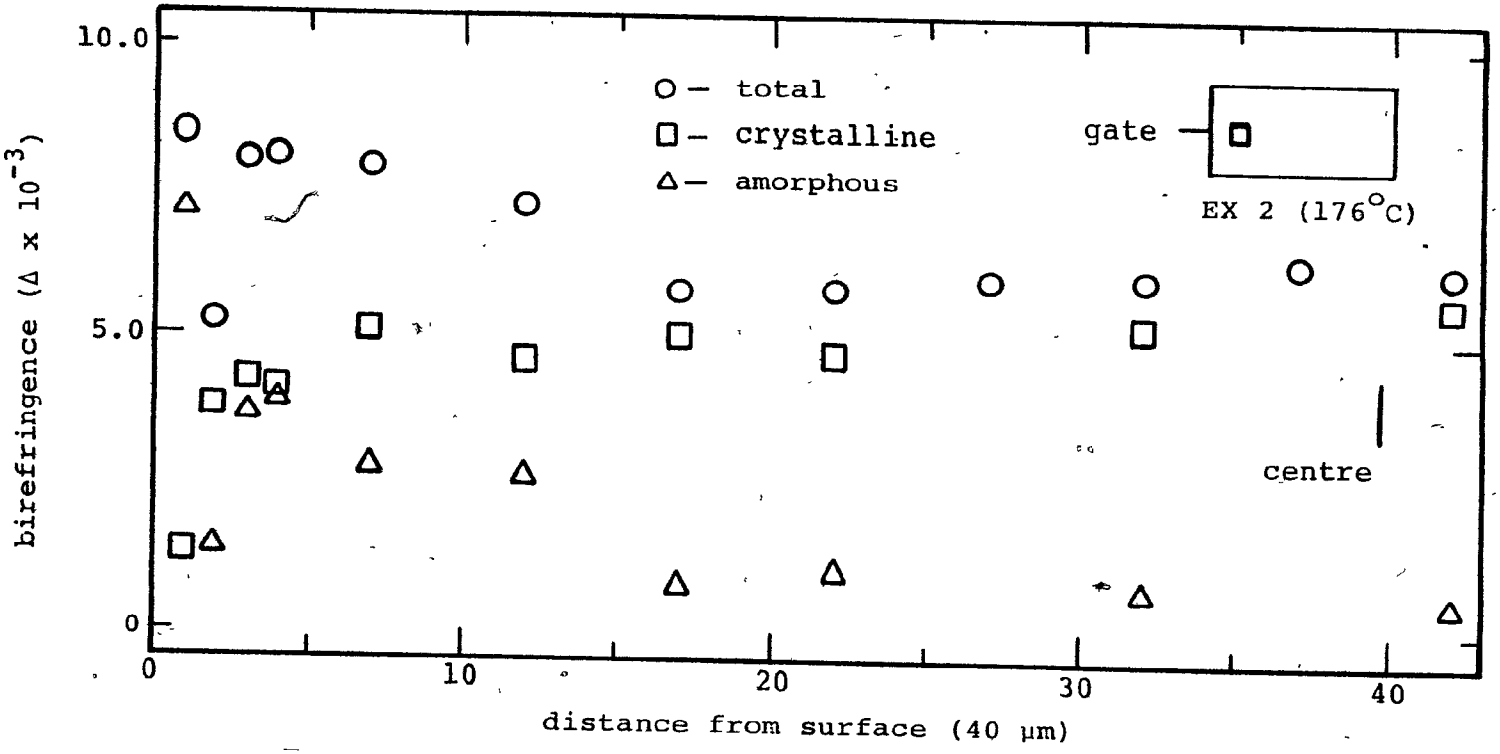


FIGURE 6.76. Crystalline and Amorphous Phase Contributions to the Total Birefringence

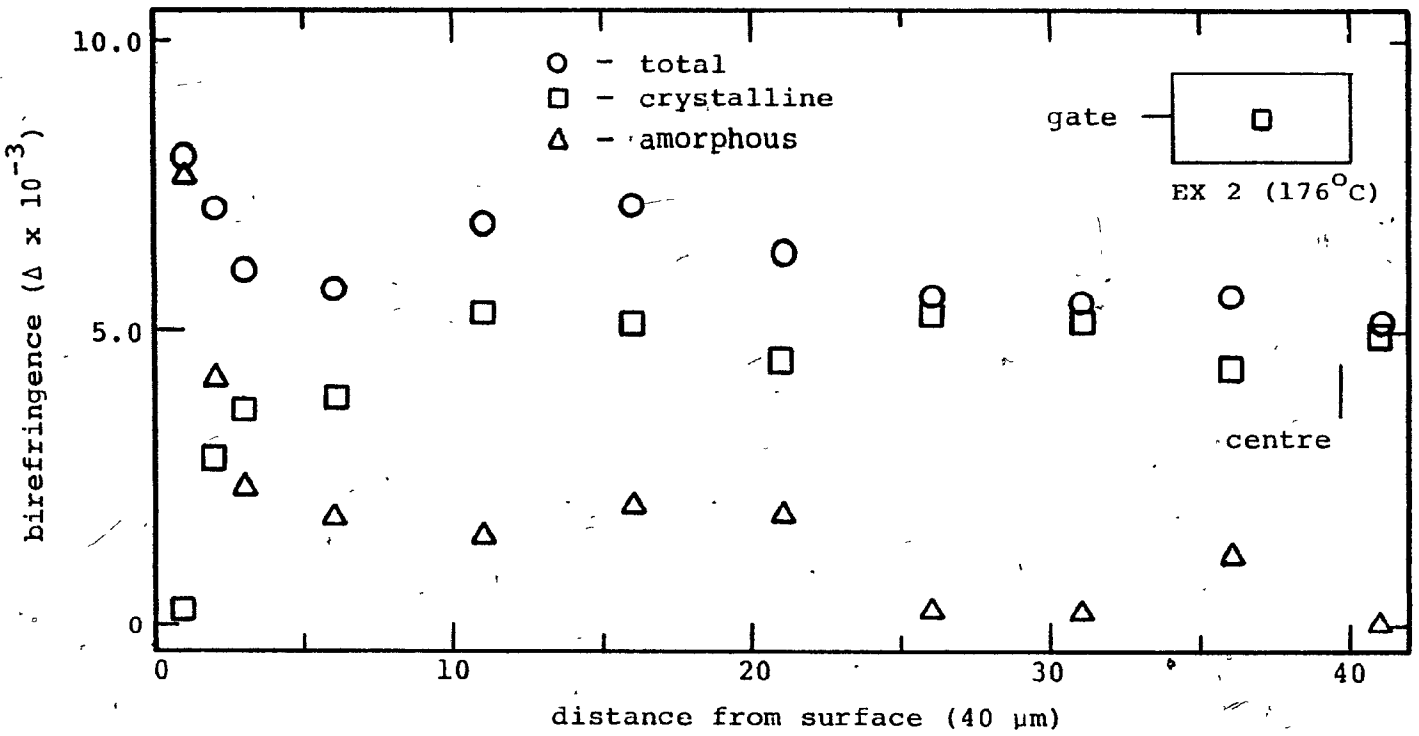


FIGURE 6.77. Crystalline and Amorphous Phase Contributions to the Total Birefringence

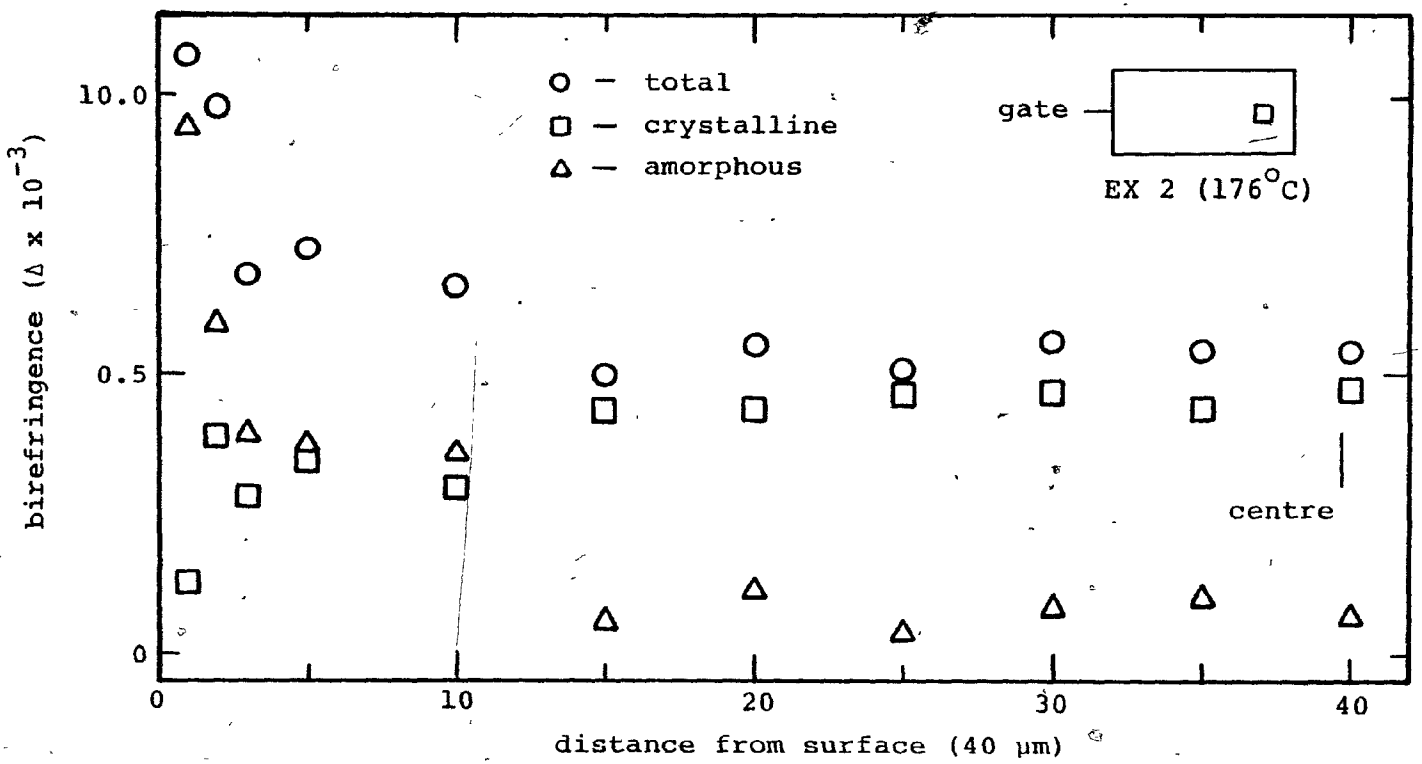


FIGURE 6.78. Crystalline and Amorphous Phase Contributions to the Total Birefringence

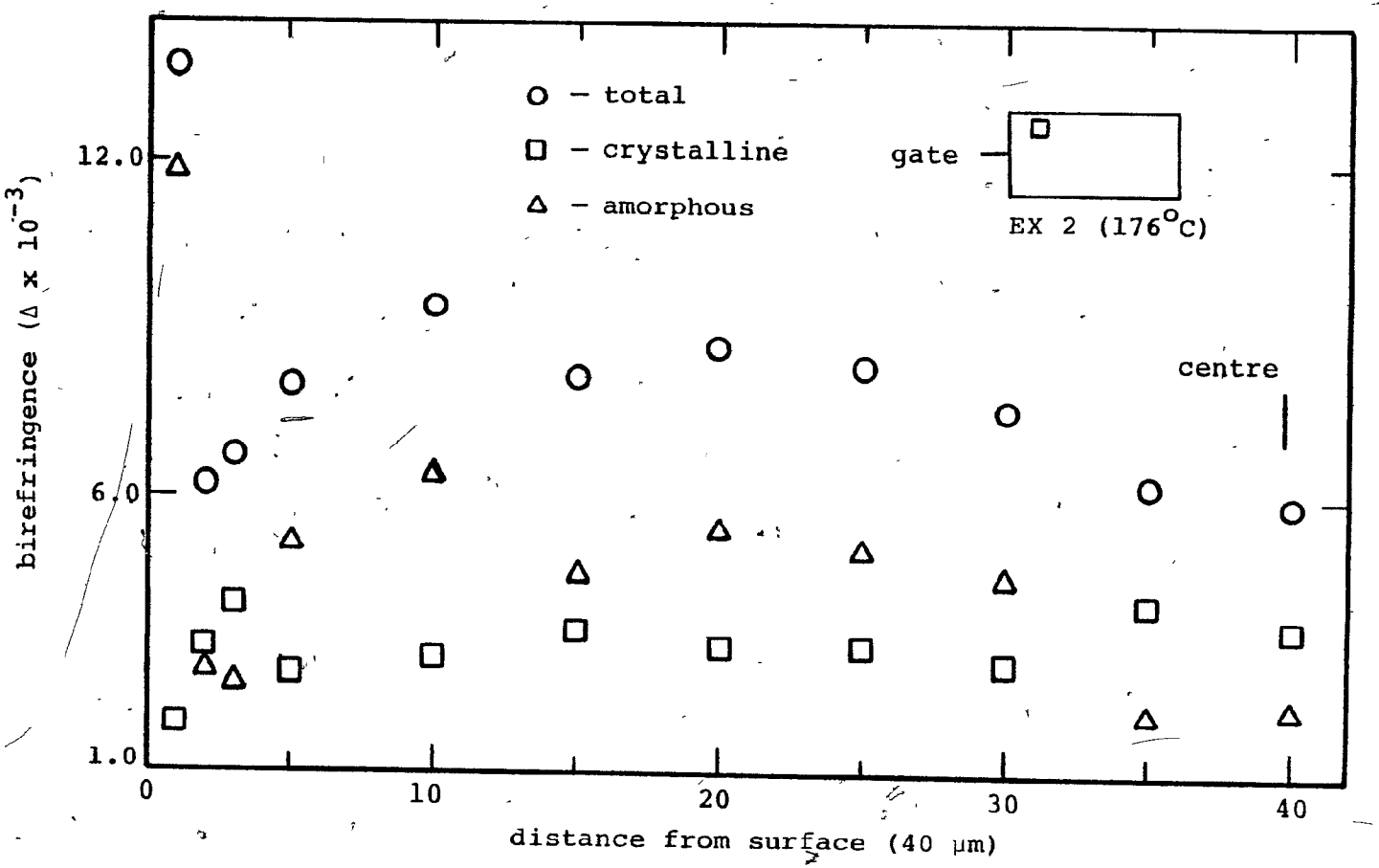


FIGURE 6.79. Crystalline and Amorphous Phase Contributions to the Total Birefringence

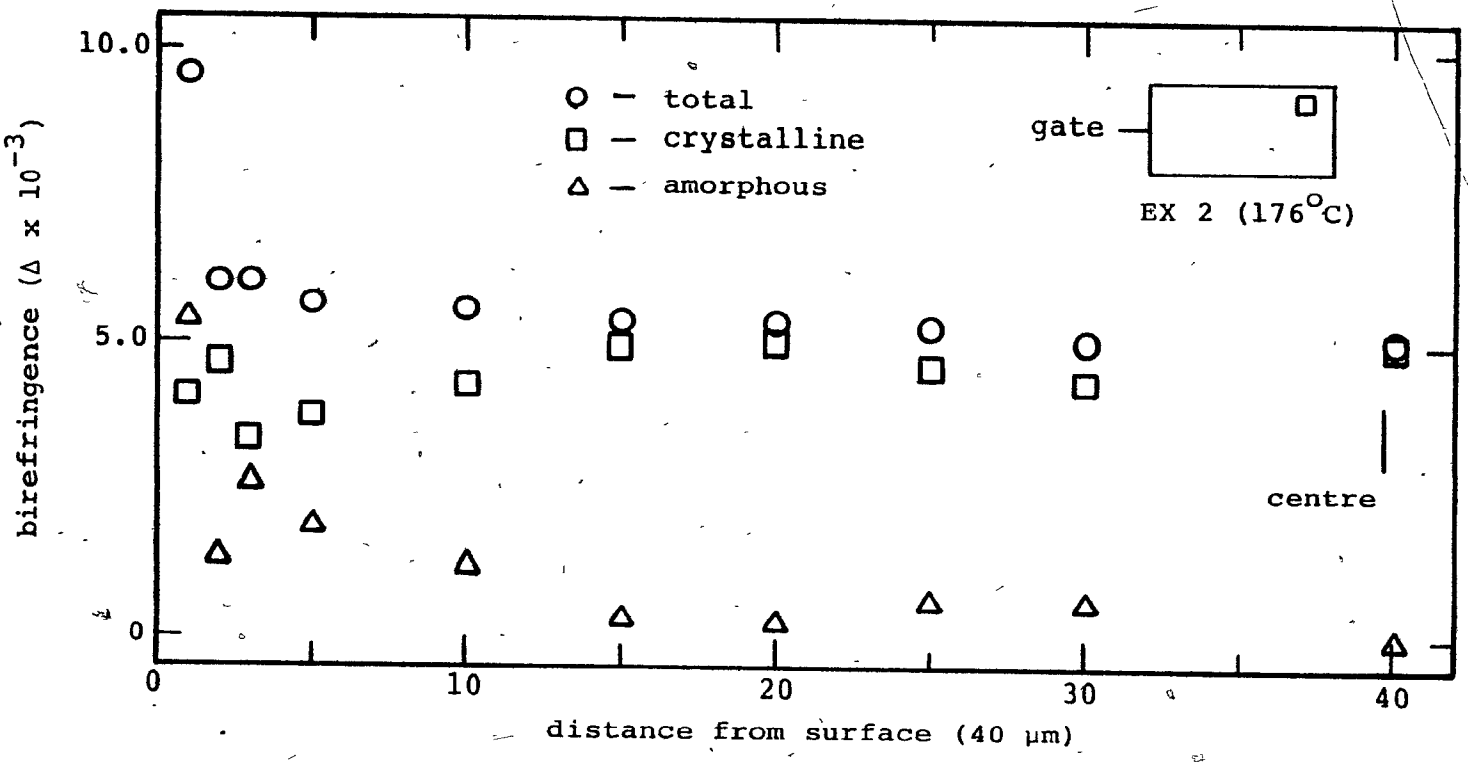


FIGURE 6.80. Crystalline and Amorphous Phase Contributions to the Total Birefringence

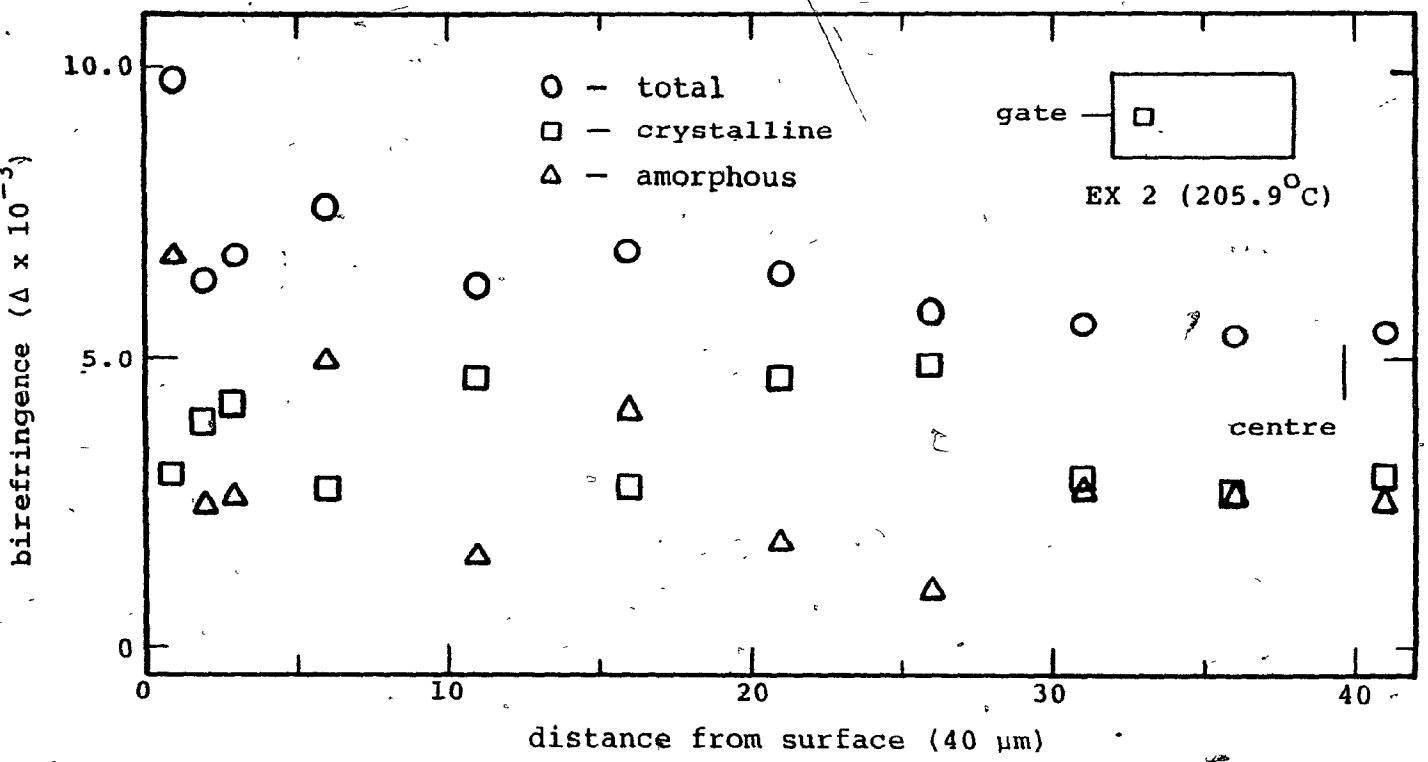


FIGURE 6.81. Crystalline and Amorphous Phase Contributions to the Total Birefringence

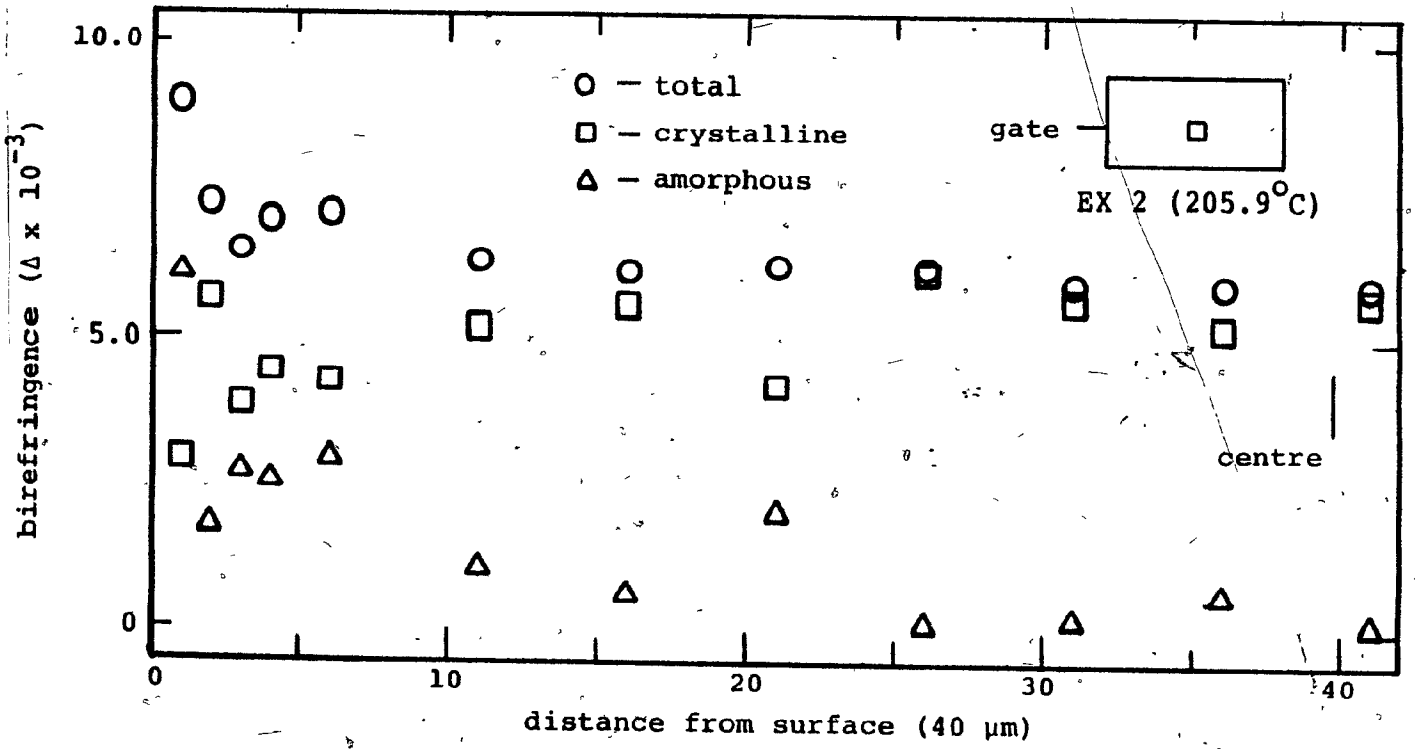


FIGURE 6.82. Crystalline and Amorphous Phase Contributions to the Total Birefringence

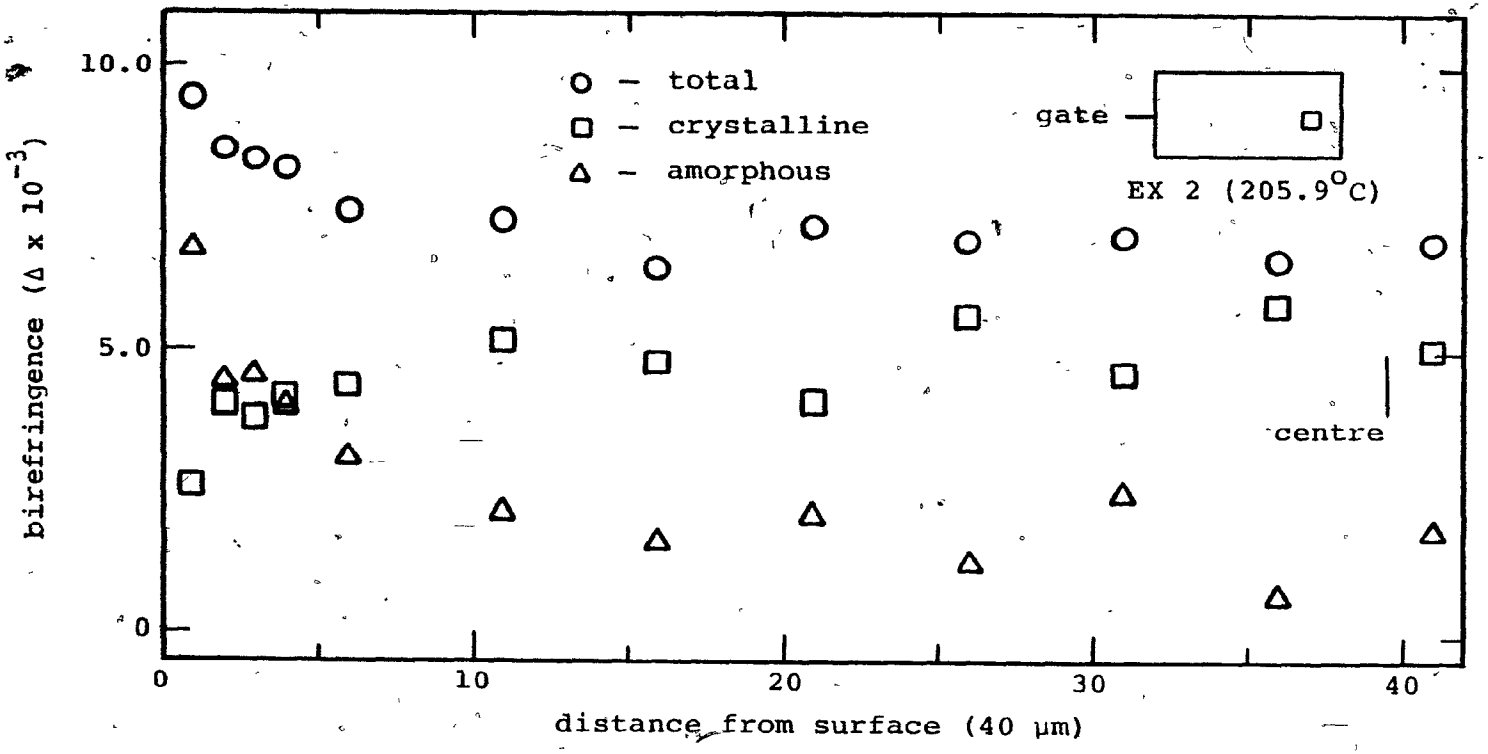


FIGURE 6.83. Crystalline and Amorphous Phase Contributions to the Total Birefringence

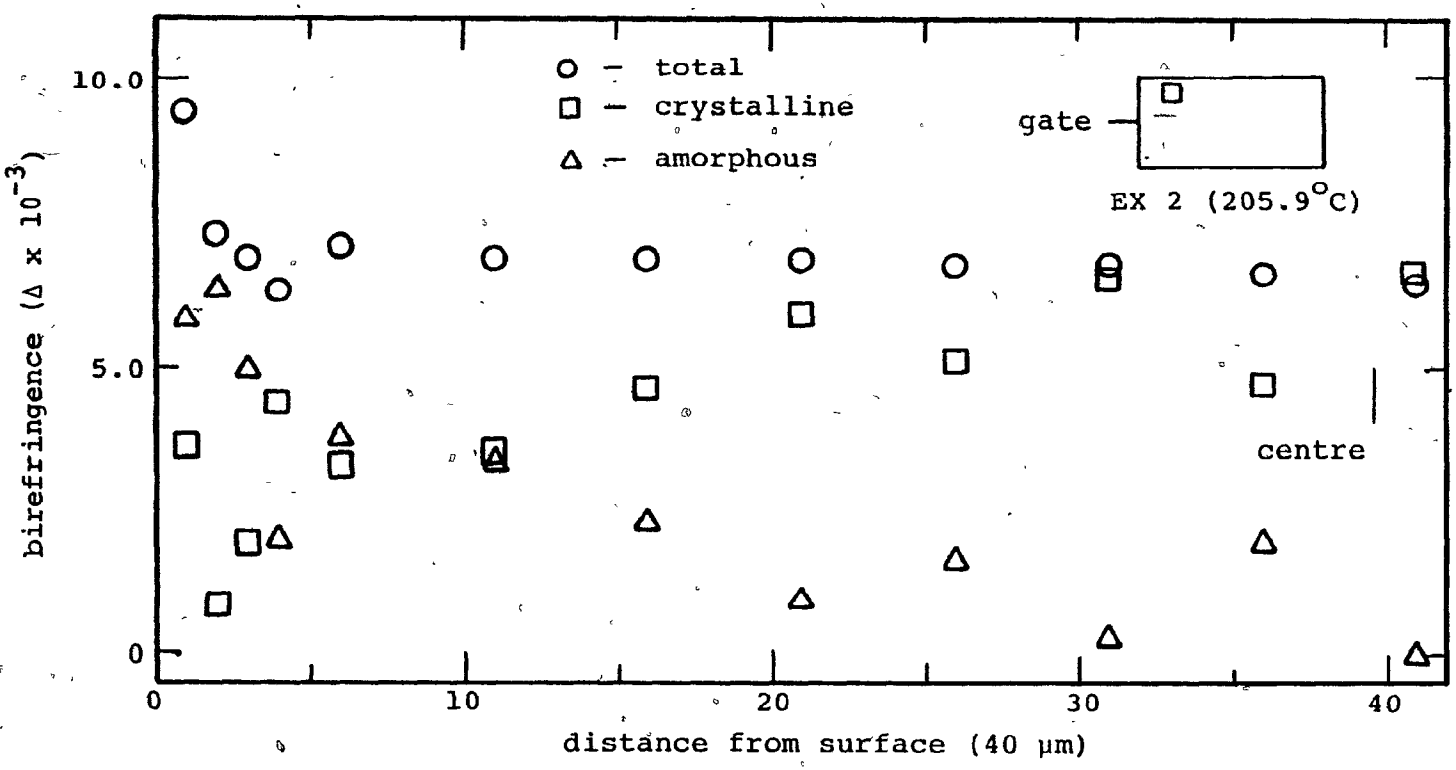


FIGURE 6.84. Crystalline and Amorphous Phase Contributions to the Total Birefringence

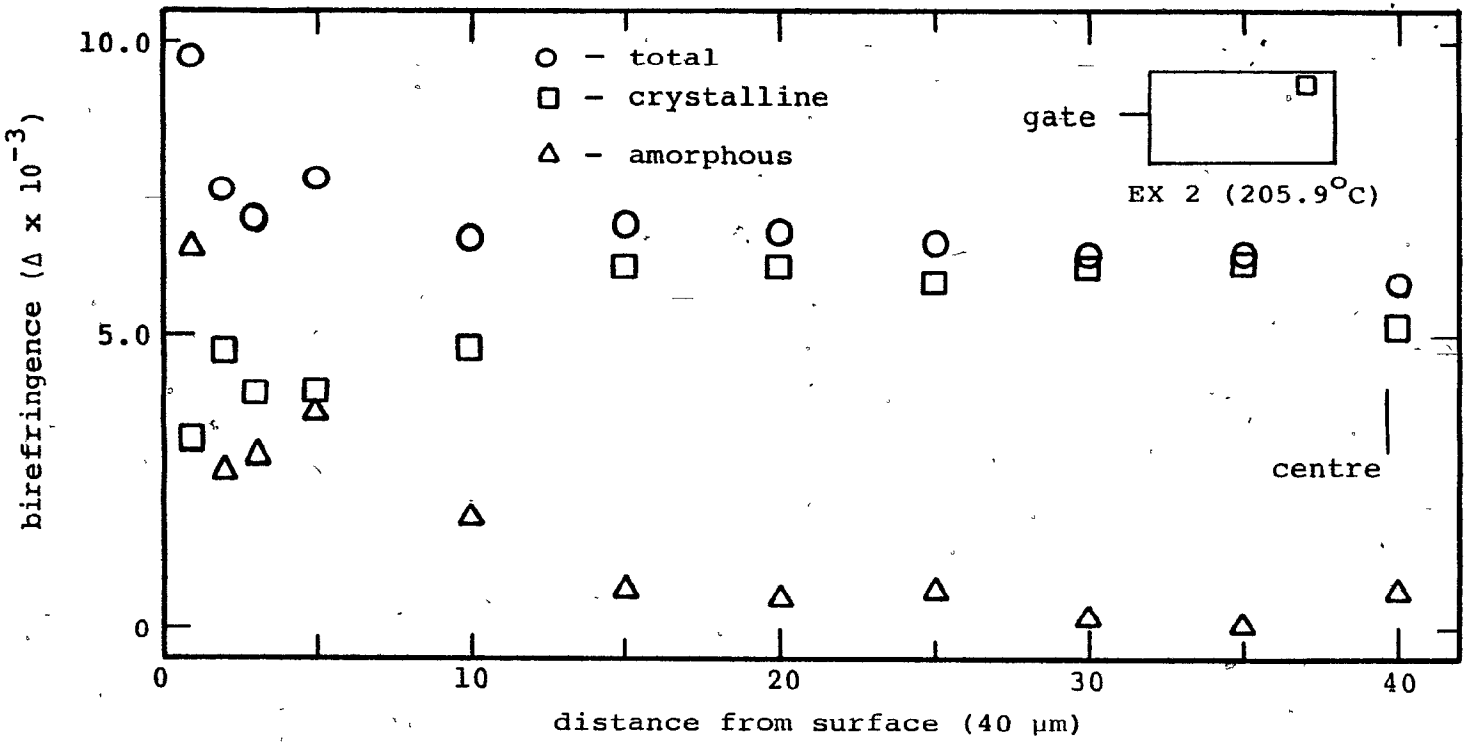


FIGURE 6.85. Crystalline and Amorphous Phase Contributions to the Total Birefringence

near the surface (0-0.08 mm), for the location midway from the gate. In the region (0.08-0.20 mm) from the surface, the general tendency is for both the crystalline and amorphous phases to contribute about equally to the total orientation, as observed for the two resins molded at the melt temperature of 176°C. Furthermore, the amorphous phase contribution to the total orientation decreases from a maximum at the surface to a minimum towards the core, while the crystalline phase contribution increases from a minimum at the surface to a maximum towards the centre of the molding.

Generally, the results of the variation of the relative contribution of the crystalline and amorphous phases to the total orientation in the depth direction, may be summarized as follows:

(1) At the surface, resin EX 1 tends to exhibit high crystalline phase orientation, while resin EX 2 tends to exhibit high amorphous phase orientation.

(2) In the intermediate region (0.08-0.40 mm), both the crystalline and amorphous phases contribute about equally to the total orientation, as observed for the two resins, regardless of melt temperature.

(3) Towards the core of the molding, the crystalline phase contribution tends towards a maximum, while the amorphous phase contribution decreases to a minimum, as observed for both resins, regardless of melt temperature.

(4) Increasing the injection melt temperature lowers the amorphous phase contribution at the surface, while

the crystalline phase contribution tends to increase.

6.10.4 Prediction of Sonic and Tensile Moduli Distributions

A detailed tabulation of the comparison between the calculated and measured sonic modulus values is listed in Appendix 12, while the calculated and measured tensile Young's moduli are listed in Appendix 13. The error associated with the prediction of sonic modulus is presented in Appendix 15.

In the calculation of the sonic modulus, according to Equation (4-28), the intrinsic values used are the reported values for $E^o_{t,c}$ and $E^o_{t,am}$ of 0.35×10^{10} Pa (159) and 0.05×10^{10} Pa (132), respectively. Furthermore, as mentioned previously in Section 4.7, the volume fraction crystallinity (X_c) was obtained from density measurements, while the crystalline and amorphous orientation functions were obtained from X-ray diffraction and sonic velocity measurements, respectively. Figure 6.86 shows typical comparisons between the calculated and measured sonic modulus values for the conditions studied at the location midway from the gate. Generally, the predicted and measured values are in good agreement for all samples tested, and the deviations between predicted and experimental values are in the same range, as shown in Figure 6.86. Other workers employing this technique have reported good agreement between the theoretically predicted and experimentally observed sonic modulus values for oriented isotactic polypropylene films (149).

The model was also extended to predict the tensile Young's modulus by using literature values for the elastic constants of

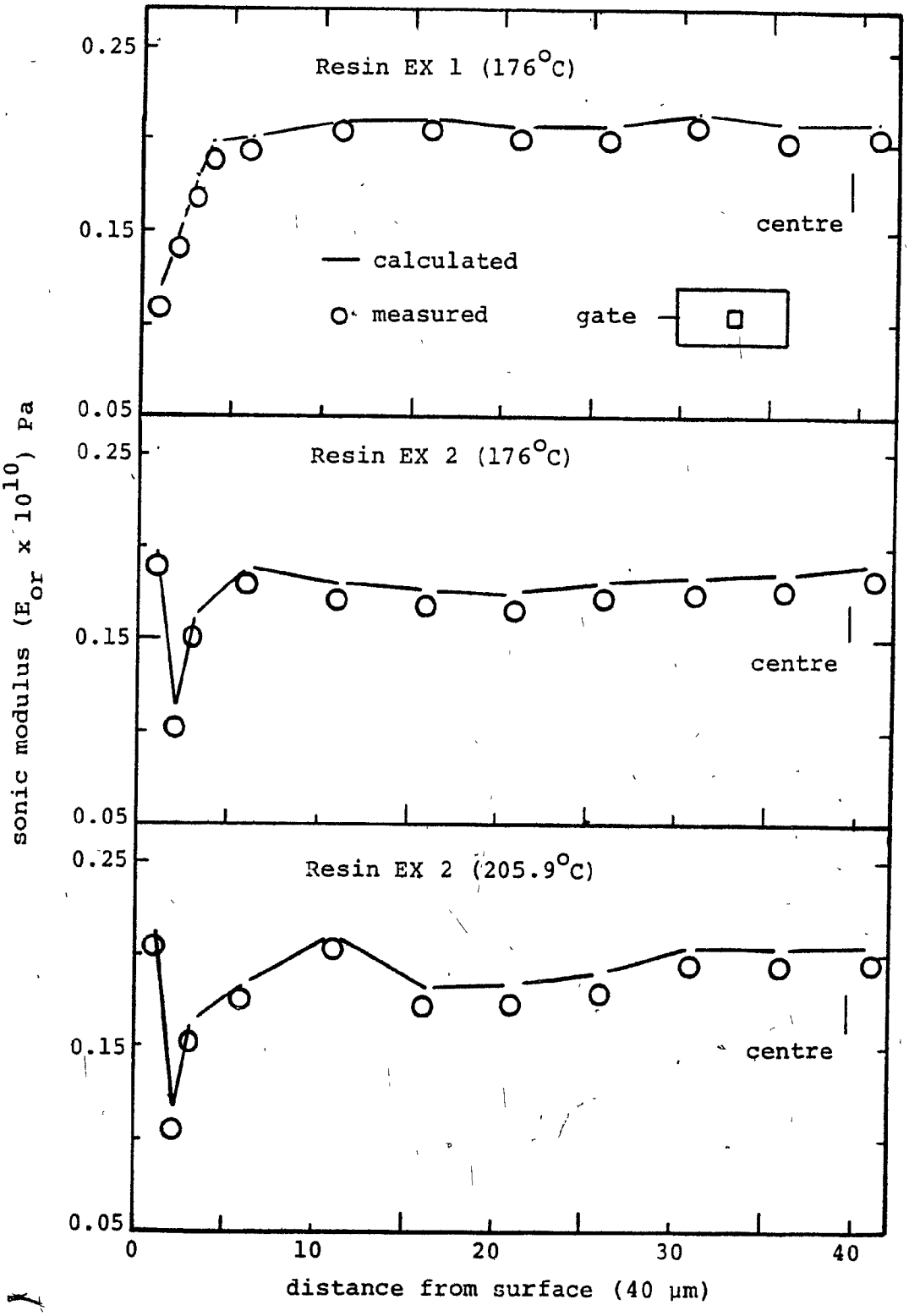


FIGURE 6.86. Typical Comparisons Between Predicted and Measured Sonic Modulus Distributions at the Indicated Location

both the crystalline and amorphous phases, respectively. The values of 24.0×10^{10} Pa and 0.01×10^{10} Pa for E_c^o and E_{am}^o, respectively, reported by Porter (174), were used in conjunction with the microstructural data obtained in the present study, to predict the tensile modulus of microtomed sections from injection moldings. Figure 6.87 shows typical comparisons between the calculated and measured tensile modulus values for the conditions studied at the location midway from the gate. The agreement between the predicted and experimentally observed values is reasonably good for all the samples tested, especially in the region near the wall which is very important. Also, the theoretical equations lead to predictions of the effects of variations in resin type and molding conditions which are consistent with observed experimental effects. This is true for both tensile and sonic modulus data. Generally, the data in Appendices 12 and 13 indicate that the noncrystalline region emerges as the controlling phase in determining the tensile modulus distribution in polyethylene injection moldings. Similar observations have been made by other workers in the study of isotactic polypropylene films (149).

In summary, it has been shown that the distributions of both sonic and tensile moduli may be predicted with reasonable accuracy by employing available models in conjunction with data on crystallinity and orientation obtained from other parts of this study.

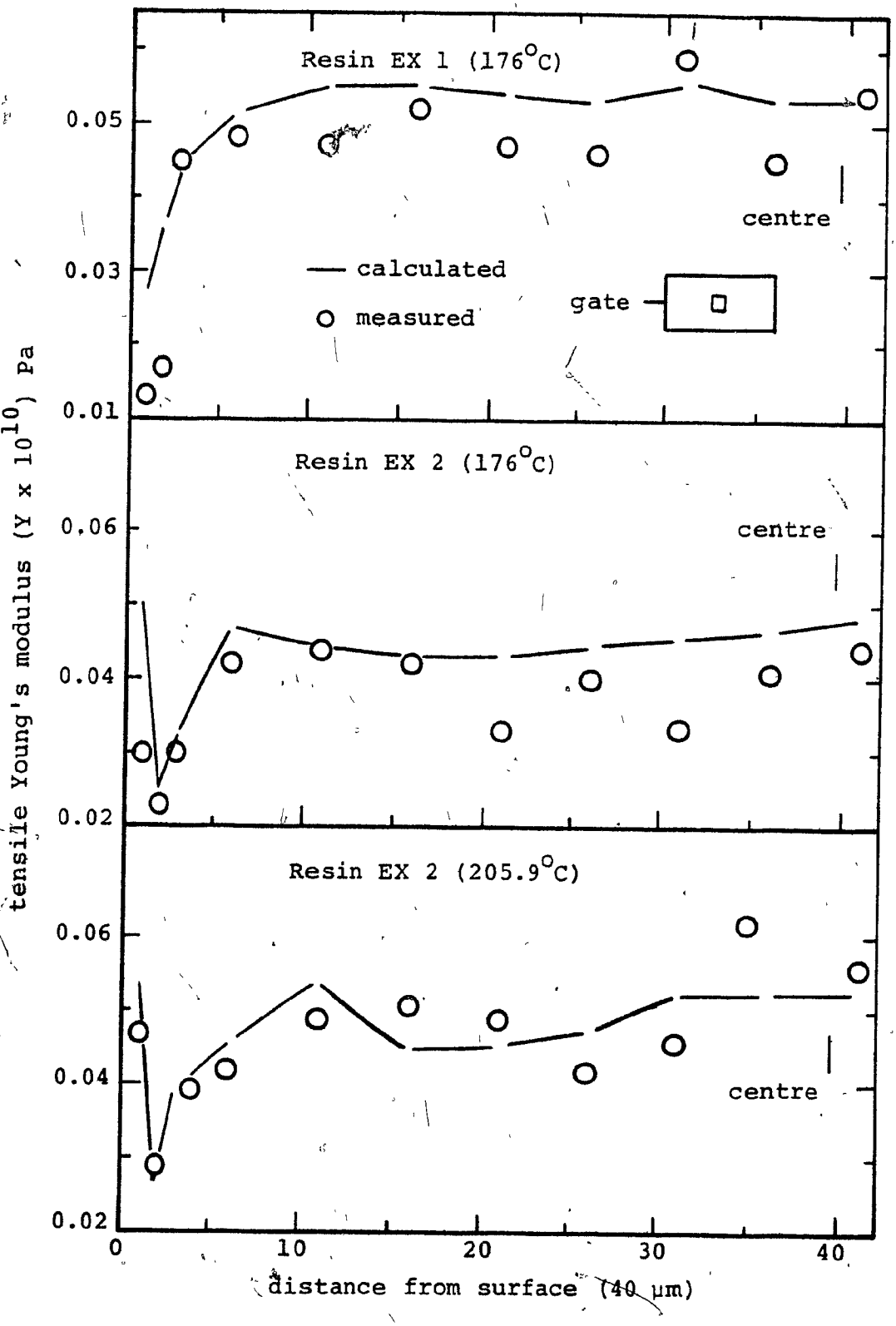


FIGURE 6.87. Typical Comparisons Between Predicted and Measured Tensile Modulus Distributions at the Indicated Location

CHAPTER 7

CONCLUSIONS, ORIGINAL CONTRIBUTIONS, AND FUTURE WORK

7.1 General Conclusions

Figures 7.1 to 7.3 give typical comparisons of the various distributions of properties in the depth direction of injection moldings with respect to both resin type and molding condition. It is intended that these figures will serve to highlight some of the general conclusions that may be made from the study.

(1) A variety of techniques were employed to quantitatively characterize the microstructure in injection molded parts.

(2) Density measurements indicate that the degree of crystallinity is a minimum near the surface, but increases to a maximum at the centre of the molding.

(3) The distributions of total orientation, as measured by both the sonic method and birefringence, showed consistent agreement with each other. Both techniques indicated that one resin (EX 2) exhibited maximum orientation at the surface, while the other resin (EX 1) exhibited minimum orientation at the surface. As observed for resin EX 2, increasing the injection melt temperature, tends to marginally increase the overall orientation throughout the molded part.

(4) The elastic constants for the crystalline ($E^{o}_{t,c}$) and amorphous ($E^{o}_{t,am}$) phases were estimated using the

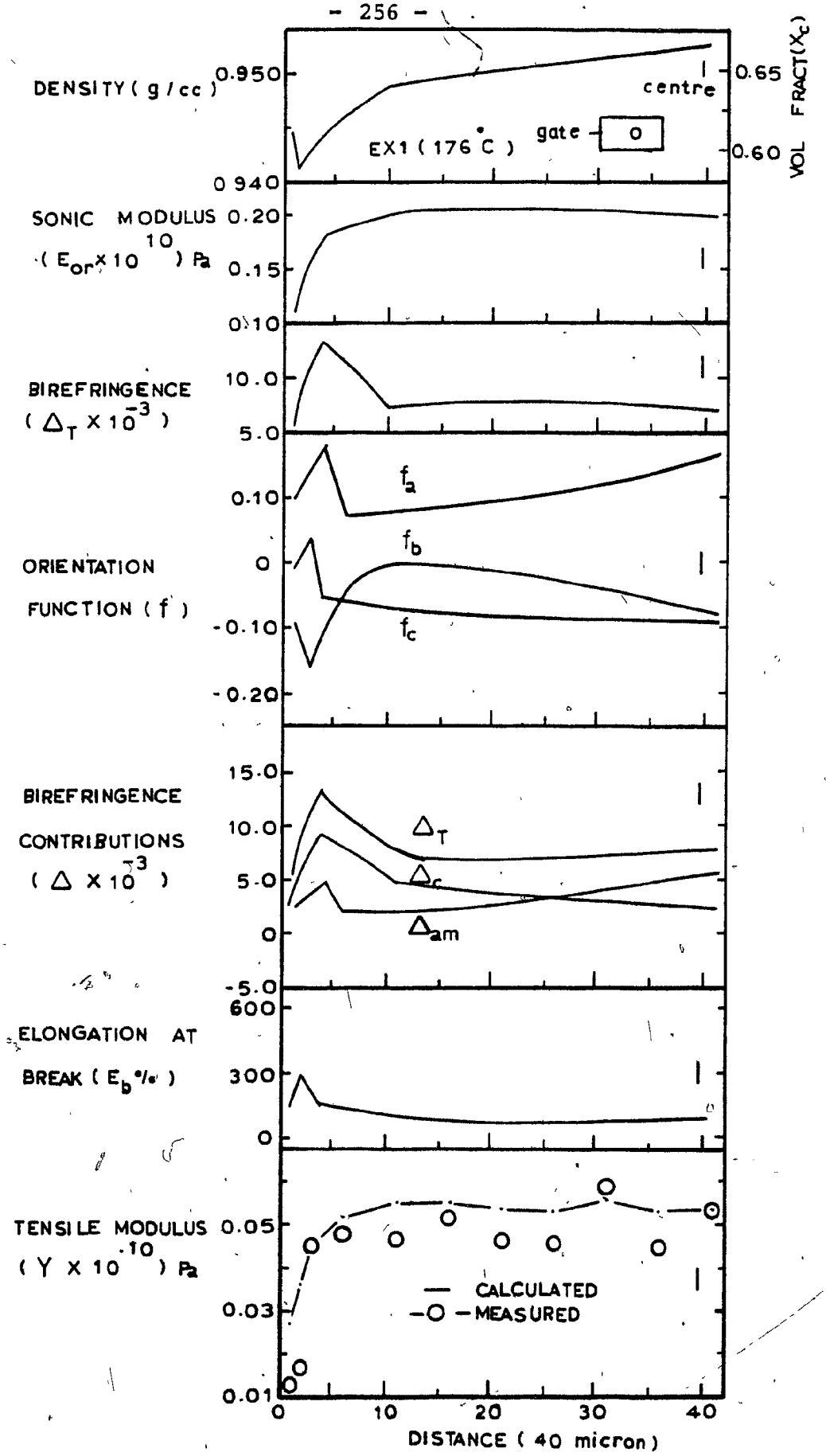


FIGURE 7.1. Distribution of Properties in the Depth Direction for Resin EX 1 Molded at 17.6°C

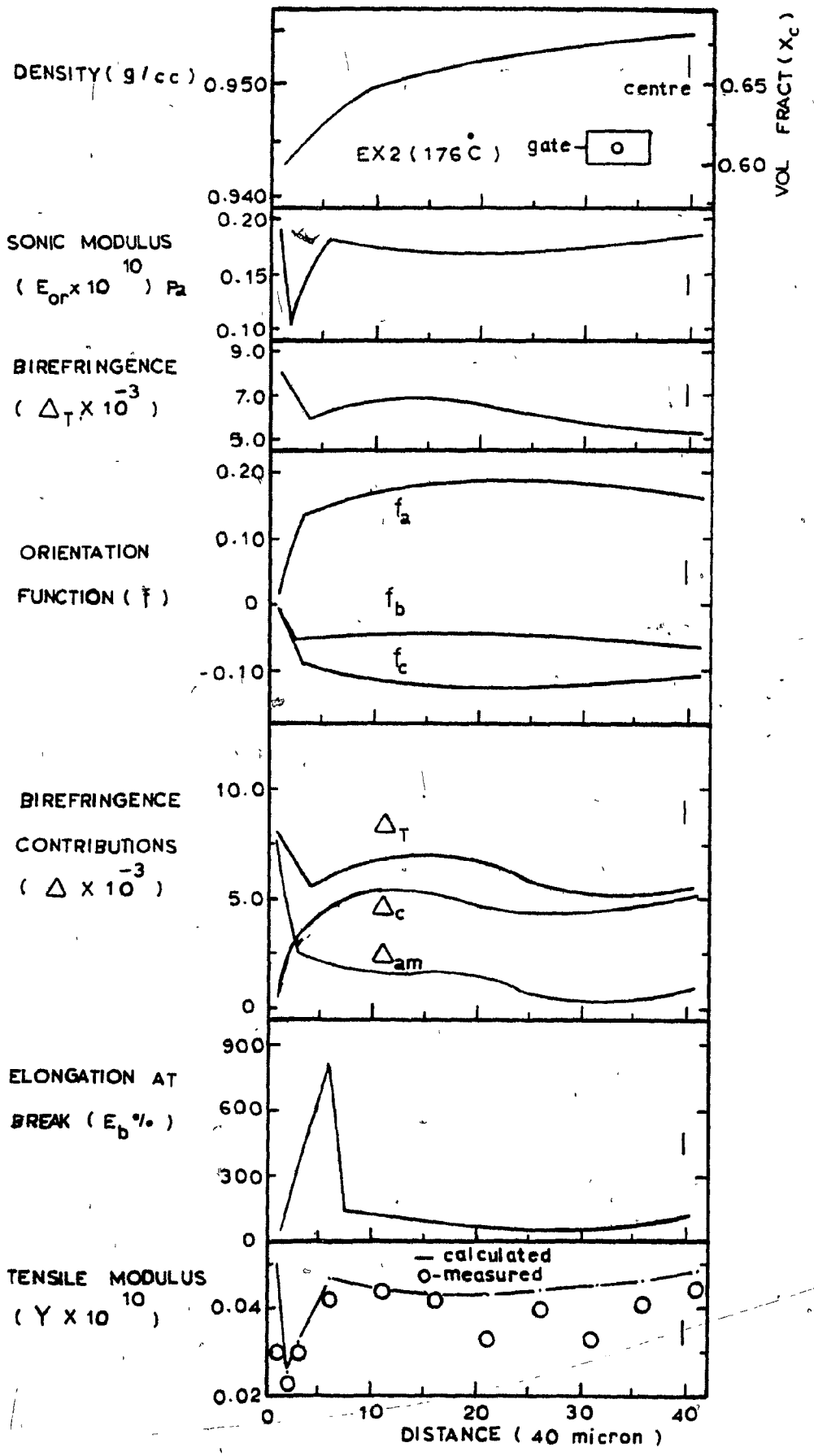


FIGURE 7.2. Distribution of Properties in the Depth Direction for Resin EX 2 Molded at 176°C

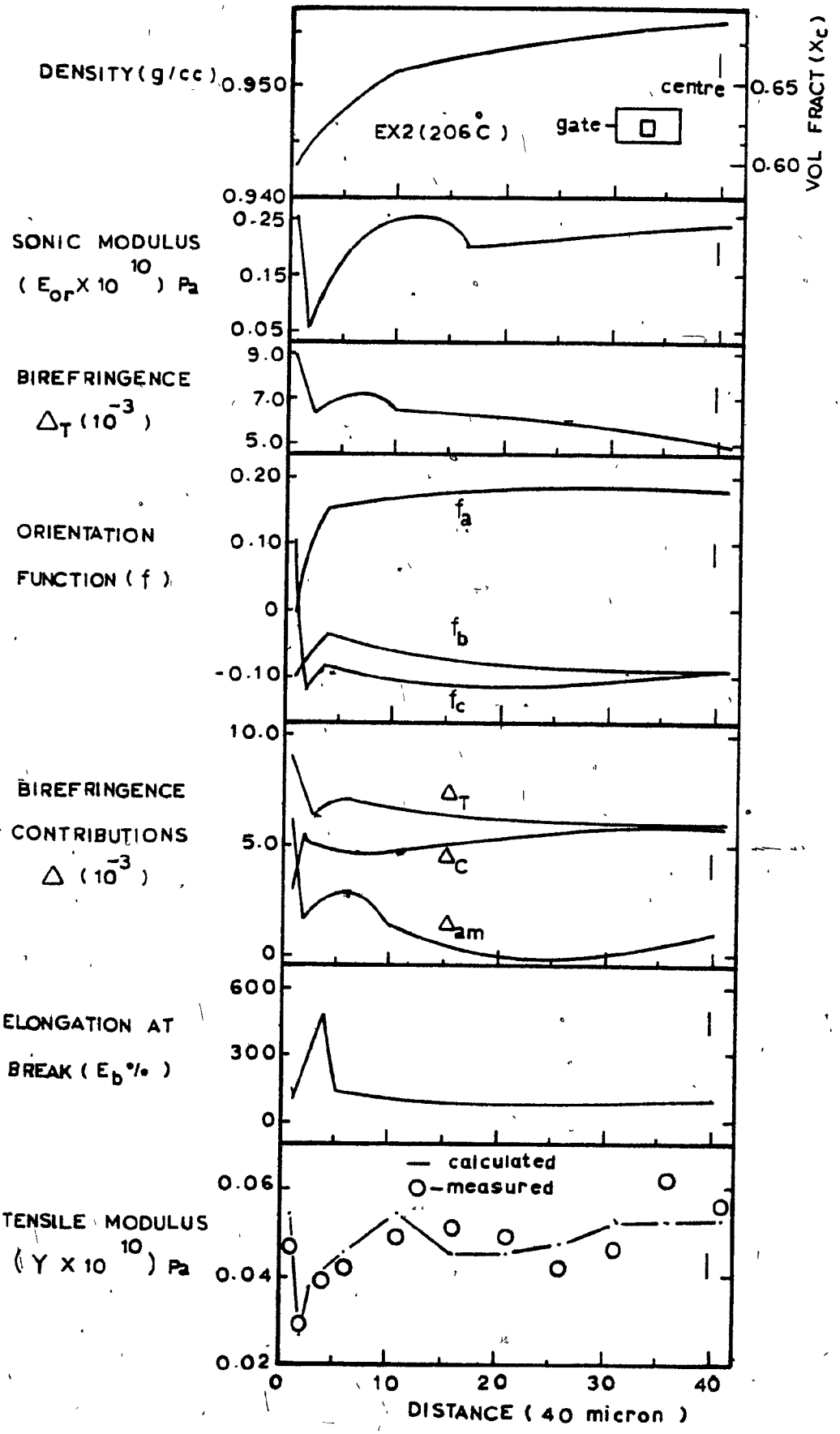


FIGURE 7.3. Distribution of Properties in the Depth Direction for Resin EX 2 Molded at 205.9°C

sonic method based on the measurement of sonic velocity of compression molded samples of varying degrees of crystallinity. The values obtained for $E^{o}_{t,c}$ and $E^{o}_{t,am}$ were 0.570×10^{10} Pa and 0.043×10^{10} Pa, respectively, which are in reasonable agreement with values reported by other investigators using different techniques.

(5) The techniques of sonic modulus were combined with X-ray diffraction and degree of crystallinity from density, together with the estimated elastic constants, to obtain the degree of orientation of the amorphous phase. It was observed that, near the surface (0-0.20 mm), the amorphous phase is oriented in the transverse to the flow direction, and that both the distribution of the amorphous phase orientation and the degree of transverse orientation were less pronounced far away from the gate.

(6) The values of the intrinsic birefringence for both the crystalline (Δ^{o}_{c}) and amorphous (Δ^{o}_{am}) phases were estimated by the combination of X-ray diffraction, degree of crystallinity from density, and the amorphous phase orientation function. By this procedure, the values of Δ^{o}_{c} and Δ^{o}_{am} were estimated to be 0.054 and 0.064, respectively, and are considered to be in reasonable agreement with calculated and estimated values reported by other workers.

(7) Wide-angle X-ray diffraction yields data regarding the details of the orientation of the crystallographic axes in relation to the flow direction.

(8) The relative contributions of the crystalline and amorphous phases to the total orientation as measured by birefringence were obtained using the estimated values of the intrinsic birefringence for the crystalline and amorphous phases, respectively. These results show that, at the surface, resin EX 1 exhibits high crystalline orientation at the surface, while resin EX 2 exhibits high amorphous phase orientation. The contribution of the crystalline phase to orientation increases as the distance from the surface increases, for both resins.

(9) The techniques of X-ray diffraction and dichroic ratio yield comparable results regarding the crystalline orientation functions.

(10) The variation of some tensile properties in the depth direction was measured at the various locations along the molding. Generally, it was observed that both the tensile yield stress and the elongation at yield, tend to increase towards the core, while the elongation at break exhibits a maximum near the surface (0-0.20 mm), but decreases rapidly as distance from the surface increases.

(11) As observed for resin EX 2, increasing the injection melt temperature, tends to marginally increase the

tensile yield stress and elongation at yield, but decreases the elongation at break, throughout the molding.

(12) Generally, resin EX 2 exhibits both higher tensile yield stress and elongation at break, but lower elongation at yield than resin EX 1.

(13) It has been shown that the distributions of both sonic and tensile moduli may be predicted with reasonable accuracy by employing available models in conjunction with data on crystallinity and orientation obtained from other parts of this study. Also, the theoretical equations lead to predictions of the effects of variations in resin type and molding conditions which are consistent with observed experimental effects. This is true for both tensile and sonic modulus data.

(14) All techniques show that the variations of properties are most pronounced within the first 0.40 mm (400 μm) from the surface, beyond which very little changes are observed. Furthermore, the variation of morphology and orientation are most pronounced for the location near the gate and least far from the gate.

(15) The mechanism that controls the development of microstructure is governed by two often competing phenomena, that is, the orientation phenomenon caused by the flow during the filling and packing stages, and the crystallization phenomenon which tends to relieve the orientation. It appears that near the skin, which is

associated with the filling stage, it is the crystallization phenomenon under shear that influences the development of microstructure in this region. In the intermediate zone, which is associated with the packing stage, it is the crystallization under pressure that influences the microstructure in this region. In the core region, the cooling times are usually longer and since the stresses are negligible, crystallization resembles that occurring under quiescent conditions.

(16) The distributions of the various properties are observed to be affected by the development of the composite morphologies in the depth direction of the molding, which in turn, are related to the properties and thermo-mechanical history of the resin material during processing, all of which, significantly influence the end-use mechanical properties of the molded part. Ideally, mathematical modeling of the injection molding process and the various phenomena considered in this study, with due consideration to all the significant interactions between material and process variables, would predict quantitatively many of the observed phenomena. The experimental results of the present study should be useful for the purposes of mathematical modeling. Obviously, useful models must incorporate considerations of crystallinity and orientation in the overall analysis.

7.2 Claims to Original Contributions

In general, it may be claimed that the totality of the effort reported in this work represents a significant contribution to the understanding of the development of morphology and orientation in injection molded parts. As such, it also represents a significant step towards the understanding of the behavior and properties of thermoplastic injection molded parts and the development of suitable mathematical models for the simulation of the development of morphology and orientation and their influence on the ultimate mechanical properties in other processing operations besides injection molding, such as blow molding and extrusion of tubular blown films.

The specific original contributions made in this work, may be summarized as follows:

(1) The overall effort represents the first complete, integrated set of experimental data employing a variety of fundamental techniques to obtain a quantitative characterization of the microstructure in injection molded parts. The consistency of these data is supported by the general agreement between sonic and birefringence measurements and between X-ray and infrared measurements.

(2) The data obtained by the X-ray diffraction method in itself represents a significant contribution since, to the best of knowledge, it represents the first set of data reported concerning the variations of the orientation functions of the crystallographic axes of

the unit cell of injection molded polyethylene.

(3) The estimated values for the elastic constants represents the first reported values for polyethylene determined by means of the sonic method.

(4) The values reported for the intrinsic birefringence represent the first estimated values for polyethylene, based on the characterization of microstructure in injection molded samples.

(5) The variation of the relative contributions of the crystalline and amorphous phases to the total orientation, as measured by birefringence, in the depth direction of the molding, represents a significant contribution towards the understanding of microstructure in injection molded parts.

(6) The data acquired through the various measurements will be useful for the development of mathematical models both for the simulation of the development of microstructure in injection molded parts, as well as for prediction of end-use mechanical properties which require the knowledge of structural parameters that describe the state of the crystalline and amorphous regions in injection molded articles.

(7) It has been shown that the distributions of both sonic and tensile moduli may be predicted with reasonable accuracy by employing available models in conjunction with data on crystallinity and orientation obtained from other parts of this study. Also, the theoretical

equations lead to predictions of the effects of variations in resin type and molding conditions which are consistent with observed experimental effects. This is true for both tensile and sonic modulus data. To our knowledge, this represents the first attempt to predict the distributions of sonic and tensile moduli in injection molded parts, employing information regarding the crystallinity and orientation as determined by other techniques.

7.3 Suggestions for Future Work

As a result of the present study, the following recommendations are proposed:

(1) The techniques developed in this work should be extended to a more systematic study of the effect of material properties and gate size, and process conditions on the development of microstructure during the filling, packing and cooling stages of the molding cycle.

(2) The techniques should also be extended and verified for the characterization of microstructure in molded parts, molded from complex geometries having sudden changes in cross-sectional area, as well as to multigated mold cavities.

(3) It has been emphasized in this study that the crystallization phenomenon plays a significant role in the development of microstructure in molded parts. There-

fore, material characterization studies must include the crystallization behavior of the material under various temperature, pressure, and velocity fields.

(4) With this in mind, it becomes necessary to develop experimental techniques for the measurement of the detailed velocity, temperature, shear stress distributions in the mold cavity. Velocity profiles may be measured using tracer techniques coupled with high-speed photography (175). Temperature profiles may be determined using infrared pyrometry or thermochromic substances (176). Flow birefringence has been used in order to determine stress distributions in mold cavities (177).

(5) The development of an on-line computer control strategy for the optimization and control of the ultimate mechanical properties and part performance of the molded part is a most important consideration.

(6) The techniques should be incorporated into the extensive blow molding program currently in progress at McGill University, to quantitatively characterize the microstructure in blow molded articles.

(7) In view of the findings of this work relating to the importance of crystallization and orientation phenomena in injection molding of thermoplastics, it appears highly desirable that the new generation of mathematical models of the injection molding process should incorporate these effects as part of the analysis.

LIST OF SYMBOLS

A	cross-sectional area at any time (mm^2)
A_c, A_{am}	relate to the intrinsic transverse moduli for the crystalline and amorphous phases, respectively
A_L, A_T	absorbances measured with radiation polarized parallel and perpendicular to the stretched (flow) direction, respectively
A_o	original cross-sectional area (mm^2)
C_l	longitudinal sonic velocity (km/sec)
C_p	average specific heat (cal/gm/^oC)
C_s	sonic velocity in sample (km/sec)
C_t	transverse sonic velocity (km/sec)
D	infrared dichroic ratio
D_{720}	measured dichroic ratio of the 720 cm^{-1} band
D_{730}	measured dichroic ratio of the 730 cm^{-1} band
$\vec{E}$	electric field vector
E_c^o, E_{am}^o	intrinsic modulus values for the crystalline and amorphous phases, respectively (Pa)
E_l^o	intrinsic longitudinal sonic modulus (Pa)
E_{or}	sonic modulus of oriented sample (Pa)
E_s	sonic modulus of sample (Pa)
E_t^o	intrinsic transverse sonic modulus (Pa)
$E_{t,am}^o$	intrinsic transverse modulus of the amorphous phase (Pa)
$E_{t,c}^o$	intrinsic transverse modulus of the crystalline phase (Pa)
E_u	sonic modulus of unoriented sample (Pa)
f_a, f_b, f_c	Hermans' orientation function for the crystallographic a, b, and c axes, respectively

f_{am}	orientation function for amorphous phase
f_{cr}	orientation function for crystalline phase
f_{χ}	orientation function for individual phase
h_a	height of density float immediately above sample (cm)
h_b	height of density float immediately below sample (cm)
h_s	height of sample (cm)
K	tensor describing the direction of the electrical polarization vector ($\vec{P}$)
k	thermal conductivity (cal/cm/^{o}C/sec)
l	measured gauge length (cm)
l_o	initial gauge length (cm)
$\bar{M}_N$	number-averaged molecular weight
$\bar{M}_W$	weight-averaged molecular weight (g/mole)
n	power law index
$\vec{P}$	electrical polarization vector
S_{33}	bulk compliance in draw direction (Pa^{-1})
T_c	crystallization temperature
T_m	equilibrium melting temperature
X_c	crystalline volume fraction
$(1 - X_c)$	amorphous volume fraction
Y	tensile Young's modulus (Pa)

Greek Symbols

α	thermal diffusivity (cm^2/sec)
$\alpha, \beta, \varepsilon$	angles measured between the x-axis (flow direction) and the a, b, and c axes, respectively

$\dot{\gamma}$	shear rate (sec^{-1})
Δ^{o}_{am}	intrinsic birefringence of amorphous phase
Δ^{o}_{c}	intrinsic birefringence of crystalline phase
Δ_{f}	form birefringence
Δ_{T}	measured total birefringence
ε	strain
ε_{b}	percent elongation at break (%)
$\varepsilon_{L}, \varepsilon_{T}$	absorbances per unit thickness of the deformed sample, measured with radiation polarized parallel and perpendicular to the stretched (flow) direction, respectively
ε_{y}	percent elongation at yield (%)
η_{T}	true shear viscosity (poise)
θ	average orientation angle (degrees)
θ_{am}	average orientation angle of amorphous phase (degrees)
θ_{c}	average orientation angle of crystalline phase (degrees)
θ_{hkl}	Bragg angle corresponding to the (hkl) plane
ρ_{a}	density of float immediately above sample (g/cc)
ρ_{am}	amorphous phase density (g/cc)
ρ_{b}	density of float immediately below sample (g/cc)
ρ_{c}	crystalline phase density (g/cc)
ρ_{s}	density of sample (g/cc)
σ	tensile stress (Pa)
σ_{b}	tensile stress at break (Pa)
σ_{ny}	nominal tensile yield stress (Pa)
σ_{y}	tensile yield stress (Pa)
χ	average orientation angle of χ-plane

REFERENCES

1. R.S. Spencer and G.D. Gilmore, Modern Plastics, 28, 97, December (1950).
2. R.S. Spencer and G.D. Gilmore, J. Colloid Sci., 6, 118 (1951).
3. G.D. Gilmore and R.S. Spencer, Modern Plastics, 28, 117, April (1951).
4. F.J. Reilly and W.L. Price, SPE Journal, 17, 1097, October (1961).
5. D.H. Harry and R.G. Parrot, Polym. Eng. Sci., 10, 4, 209 (1970).
6. J.L. Berger and C.G. Gogos, Polym. Eng. Sci., 13, 2, 107 (1973).
7. M.R. Kamal and S. Kenig, Polym. Eng. Sci., 12(4), 294 (1972).
8. M.R. Kamal and S. Kenig, Polym. Eng. Sci., 12(4), 302 (1972).
9. S. Kenig, "Injection Molding of Thermoplastics", Ph.D. Thesis, McGill University, Montreal (1972).
10. P.H. Doan, "Injection Molding of Thermoplastics in Rectangular Cavities", M.Eng. Thesis, McGill University, Montreal (1974).
11. H.A. Lord and G. Williams, Polym. Eng. Sci., 15, 569 (1975).
12. J.F. Stevenson, C.A. Hieber, A. Galskoy, and K.K. Wang, SPE Antec, 34, 282 (1972).
13. P. Thienel and G. Menges, Polym. Eng. Sci., 18, 314 (1978).
14. P.H. Geil, "Polymer Single Crystals", Interscience, New York (1963).
15. J.M. Schultz, "Polymer Materials Science", Prentice-Hall, New York (1974).
16. L. Mandelkern, "Crystallization of Polymers", McGraw-Hill, New York (1964).

17. J.D. Hoffman, G. Thomas Davis, and J.I. Lauritzen, Jr., "Treatise on Solid State Chemistry", III, N.B. Hannay, Ed., Plenum (1976).

18. A. Keller, Phil. Mag., 2, 1171 (1957).

19. E.W. Fischer, Z. Naturforsch, 12A, 753 (1957).

20. C.W. Bunn, Trans. Faraday Soc., 35, 482 (1939).

21. T. Alfrey and E.F. Gurnee, "Organic Polymers", Prentice-Hall Series in Materials Science, Prentice-Hall, Inc., New Jersey (1967).

22. E.H. Andrews, Proc. Royal Soc. (London), 277A, 562 (1963).

23. G. Schuur, Kolloid-Z., 208, 123 (1966).

24. V.M. Nadkarni, "Extensional Flow Induced Crystallization in Polyethylene Melt Spinning", Ph.D. Thesis, University of Delaware, Delaware (1974).

25. A.B. Metzner, "Flow Behavior of Thermoplastics", in "Processing of Thermoplastic Materials", E.C. Bernhardt, Ed., Van Nostrand Reinhold Co., New York (1959).

26. J.M. McKelvey, "Polymer Processing", John Wiley and Sons, New York (1962).

27. S. Middleman, "The Flow of High Polymers - Continuum and Molecular Rheology", Interscience, New York (1968).

28. J.M. Dealy, Polym. Eng. Sci., 11, 433 (1971).

29. A.J. Pennings and A.M. Kiel, Kolloid-Z., 205, 160 (1965).

30. A.J. Pennings, J.M.S.S. van der Mark, and H.C. Booij, Kolloid-Z., 236, 99 (1970).

31. F.C. Frank, A. Keller, and M.R. Mackley, Polymer, 12, 467 (1971).

32. A.J. McHugh and J.M. Schultz, Kolloid-Z., 251, 193 (1973).

33. A. Keller and F.M. Willmouth, J. Macromol. Sci. - Phys., B6, 493 (1972).

34. A.G. Wikjord, D.H. Page, and R. St. John Manley, J. Macromol. Sci. - Phys., B4, 413 (1970).

35. A.J. Pennings, J. Polym. Sci., C16, 1799 (1967).

36. E. Kobayashi, S. Okamura, and R. Signer, J. Appl. Polym. Sci., 12, 1661 (1968).

37. Z. Pelzbauer and R. St. John Manley, J. Macromol. Sci. - Phys., B4, 761 (1970).

38. A.J. Pennings, C.J.H. Schouteten, and A.M. Kiel, J. Polym. Sci., C38, 167 (1972).

39. D.A. Blackadder and P.A. Lowell, Polymer, 11, 25 (1970).

40. A. Keller and M.J. Machin, J. Macromol. Sci. - Phys., B1, 41 (1967).

41. T. Kawai, M. Iguchi, and H. Tonami, Kolloid-Z., 221, 28 (1967).

42. J.H. Southern and R.S. Porter, J. Appl. Polym. Sci., 14, 2305 (1970).

43. J.H. Southern and R.S. Porter, J. Macromol. Sci. - Phys., B4, 541 (1970).

44. E. Hellmuth and B. Wunderlich, J. Appl. Phys., 36, 3039 (1965).

45. T.W. Haas and B. Maxwell, J. Appl. Polym. Sci., 14, 2407 (1970).

46. K. Kobayashi and T. Nagasawa, J. Macromol. Sci. - Phys., B4, 331 (1970).

47. D. Krueger and G.S.Y. Yeh, J. Appl. Phys., 43, 4339 (1972).

48. A. Brown, J. Appl. Phys., 20, 552 (1949).

49. R.A. Horsley and H.A. Nancarrow, Brit. J. Appl. Phys., 2, 345 (1951).

50. D.R. Holmes, R.G. Miller, R.P. Palmer, and C.W. Bunn, Nature, 171, 1104 (1953).

51. R.S. Stein and F.H. Norris, J. Polym. Sci., 21, 381 (1956).

52. R.S. Stein, J. Polym. Sci., 31, 327 (1958).

53. R.S. Stein and M.B. Rhodes, J. Appl. Phys., 31(11), 1873 (1960).

54. S. Hoshino, J. Powers, D.G. Legrand, H. Kawai, and R.S. Stein, J. Polym. Sci., 58, 185 (1962).

55. K. Sasaguri, S. Hoshino, and R.S. Stein, J. Appl. Phys., 35(1), 47 (1964).

56. I.L. Hay and A. Keller, J. Mater. Sci., 1, 41 (1966).

57. I.L. Hay and A. Keller, J. Mater. Sci., 2, 538 (1967).

58. A. Peterlin, J. Polym. Sci.: Part C, 427 (1966).

59. A. Peterlin, J. Polym. Sci.: Part C, 123 (1967).

60. R.J. Samuels, J. Polym. Sci.: Part A, 3, 1741 (1965).

61. R.J. Samuels, J. Polym. Sci.: Part C, 253 (1967).

62. R.J. Samuels, J. Polym. Sci.: Part A-2, 6, 2021 (1968).

63. R.J. Samuels, J. Polym. Sci.: Part A-2, 6, 1101 (1968).

64. H.M. Morgan, Textiles Res. J., 32, 866 (1962).

65. J.H. Dumbleton, J. Polym. Sci.: Part A-2, 6, 795 (1968).

66. M. Takayanagi, K. Imada, and T. Kajiyama, J. Polym. Sci.: Part C, 15, 263 (1966).

67. W.R. Krigbaum, J. Polym. Sci.: Part C, 15, 251 (1966).

68. K. Kobayashi and T. Nagasawa, J. Polym. Sci.: Part C, 163 (1966).

69. H. Kawai, Proceedings 5th Intern. Congr. Rheol., 1, 97 (1969).

70. J. Clements, R. Jakeways, I.M. Ward, and G.W. Longman, Polymer, 20, 295 (1979).

71. R.S. Stein, S. Onogi, and D.A. Keedy, J. Polym. Sci., 57, 801 (1962).

72. S. Onogi and T. Asada, J. Polym. Sci.: Part C, 16, 1445 (1967).

73. Y. Fukui, T. Asada, and S. Onogi, Polymer J., 3(1), 100 (1972).

74. R.S. Stein, J. Polym. Sci.: Part C (15), 185 (1966).

75. A.J. De Vries, C. Bonnebat, and J. Beautemps, J. Polym. Sci.: Polymer Symposium, 58, 109 (1977).

76. H.J. Biangardi and H.G. Zachmann, J. Polym. Sci.: Polymer Symposium, 58, 169 (1977).

77. T. Hashimoto, H. Kawasaki, and H. Kawai, J. Polym. Sci.: Polym. Phys. Ed., 16, 271 (1978).

78. J.E. Spruiell and J.L. White, Polym. Eng. Sci., 15, 660 (1975).

79. A. Ziabicki and K. Kedzierska, J. Appl. Polym. Sci., 2, 14 (1959).

80. A. Ziabicki and K. Kedzierska, Kolloid-Z., 171, 52 (1960).

81. A. Ziabicki and K. Kedzierska, Kolloid-Z., 175, 14 (1961).

82. A. Ziabicki and K. Kedzierska, J. Appl. Polym. Sci., 6, 111 (1962).

83. A. Ziabicki and K. Kedzierska, J. Appl. Polym. Sci., 6, 361 (1962).

84. K. Katayama, T. Amano, and K. Nakamura, Kolloid-Z.-Z. Polym., 226, 125 (1968).

85. T. Kitao, S. Ohya, J. Furukawa, and S. Yamashita, J. Polym. Sci.: Polym. Phys. Ed., 11, 1091 (1973).

86. L.E. Abbott and J.L. White, Appl. Polym. Symp., 20, 247 (1973).

87. J.R. Dees and J.E. Spruiell, J. Appl. Polym. Sci., 18, 1053 (1974).

88. J.L. White, K.C. Dharod, and E.S. Clark, J. Appl. Polym. Sci., 18, 2539 (1974).

89. W.C. Sheehan and T.B. Cole, J. Appl. Polym. Sci., 8, 2339 (1964).

90. P.Y.F. Fung and S.H. Carr, J. Macromol. Sci. - Phys., B6, 621 (1972).

91. P.Y.F. Fung, E. Orlando, and S.H. Carr, Polym. Eng. Sci., 13, 295 (1973).

92. M.J. Hill and A. Keller, J. Macromol. Sci. - Phys., B3, 153 (1969).

93. A. Ziabicki, Appl. Polym. Symp., 6, 1 (1967).

94. K. Nakamura, T. Watanabe, T. Amano, and K. Katayama, J. Appl. Polym. Sci., 18, 615 (1974).

95. V.M. Nadkarni and J.M. Schultz, J. Polym. Sci.: Polym. Phys. Ed., 15, 2151 (1977).

96. C.R. Desper, J.H. Southern, R.D. Ulrich, and R.S. Porter, J. Appl. Phys., 41(11), 4284 (1970).

97. S. Kojima and R.S. Porter, J. Appl. Polym. Sci.: Appl. Polym. Symp., 33, 129 (1978).

98. S. Kojima, C.R. Desper, and R.S. Porter, J. Polym. Sci.: Polym. Phys. Ed., 16, 1721 (1978).

99. S. Kojima and R.S. Porter, J. Polym. Sci.: Polym. Phys. Ed., 16, 1729 (1978).

100. W.T. Mead, C.R. Desper, and R.S. Porter, J. Polym. Sc.: Polym. Phys. Ed., 17, 859 (1979).

101. K. Imada, T. Yamamoto, K. Shigematsu, and M. Takaganagi, J. Mater. Sci., 6, 637 (1971).

102. A.G. Gibson, I.M. Ward, B.N. Cole, and B. Parsons, J. Mater. Sci. Lett., 9, 1193 (1974).

103. S.L. Aggarwal, G.P. Tilley, and O.J. Sweeting, J. Appl. Polym. Sci., 1, 91 (1959).

104. D.R. Holmes and R.P. Palmer, J. Polym. Sci., 31, 345 (1958).

105. P.H. Lindenmeyer and S. Lustig, J. Appl. Polym. Sci., 9, 227 (1965).

106. E. Boehme, Kunststoffe, 60, 273 (1970).

107. E.S. Clark, Polymer Preprint, 14(1), 268 (1973).

108. E.S. Clark and C.A. Garber, Intern. J. Polym. Mater., 1, 31 (1974).

109. E.S. Clark, Plastics Eng., 73, March (1974).

110. D.E. Scherpereel, Plastics Eng., 46, December (1973).

111. M.R. Kantz, H.D. Newman, Jr., and F.H. Stigale, J. Appl. Polym. Sci., 16, 1249 (1972).

112. D.R. Fitchmun and Z. Mencik, J. Polym. Sci.: Polym. Phys. Ed., 11, 951, 973 (1973).

113. S.Y. Hobbs and C.F. Pratt, J. Appl. Polym. Sci., 19, 1701 (1975).

114. G. Menges and G. Wubken, SPE Antec, 19, 519, Montreal, Canada (1973).

115. M. Fleissner and E. Paschke, Kunststoffe, 61, 195 (1971).

116. W. Woebcken and B. Heise, Kunststoffe, 68, 99 (1978).

117. Z. Bakerdjian and M.R. Kamal, Polym. Eng. Sci., 17, 96 (1977).

118. V. Tan and M.R. Kamal, SPE Antec, 22, 339 (1976).

119. V. Tan and M.R. Kamal, J. Appl. Polym. Sci., 22, 2341 (1978).

120. M.R. Kamal and V. Tan, Polym. Eng. Sci., 19, 558 (1979).

121. D. Kalyon, "An Integrated Experimental Study of the Injection Molding Behavior of Polyethylene Resins", M.Eng. Thesis, McGill University, Montreal (1977).

122. F.H. Moy and M.R. Kamal, to be published in Polym. Eng. and Sci.

123. M. Jensen and R.R. Whisson, Polymer, 14, 193 (1973).

124. M. Fleissner, Kunststoffe, 63, 597 (1973).

125. T. Fett, W. Nothdurft, and H. Racké, Kunststoffe, 63, 168 (1973).

126. G. Menges, P. Thienel, and G. Wübken, Kunststoffe, 66, 42 (1976).

127. H. Keskkula and J.W. Norton, Jr., J. Appl. Polym. Sci., 11, 289 (1959).

128. H. Koda, J. Appl. Polym. Sci., 12, 2257 (1968).

129. E. Paschke, Kunststoffe, 60, 187 (1970).

130. B. Wunderlich, "Macromolecular Physics", Vol. 2, Academic Press, New York, 437 (1976).

131. S. Kavesh and J.M. Schultz, J. Polym. Sci.: Part A-2, 9, 85 (1971).

132. R.S. Stein and G.L. Wilkes, "Structure and Properties of Oriented Polymers", I.M. Ward, Ed., John Wiley and Sons, New York (1975), Chap. 3.

133. W.J. Lyons, J. Appl. Phys., 29, 1429 (1958).

134. W.W. Moseley, Jr., J. Appl. Polym. Sci., 3, 266 (1960).

135. J.W. Ballou and S. Silverman, Textile Res. J., 14, 282 (1944).

136. R.J. Samuels, "Structured Polymer Properties", John Wiley and Sons, New York (1973), Chap. 2.

137. M. Kakudo and N. Kasai, "X-Ray Diffraction by Polymers", Kodansha-Elsevier Publishing Company, New York (1972).

138. J.J. Hermans, P.H. Hermans, D. Vermass, and A. Werdinger, Rec. Trav. Chim., 65, 427 (1946).

139. A. Garton, R.F. Stepaniak, D.J. Carlsson, and D.M. Wiles, J. Polym. Sci.: Polym. Phys. Ed., 16, 599 (1978).

140. R. Zbinden, "Infra-red Spectroscopy of High Polymers", Academic Press, New York, London (1964).

141. B.E. Read and R.S. Stein, Macromolecules, 1(2), 116 (1968).

142. T. Okada and L. Mandelkern, J. Polym. Sci.: Part A-2, 5, 239 (1967).

143. S. Krimm, Fortschr. Hochpolym. - Forsch., 2, 51 (1960).

144. R.S. Stein, J. Chem. Phys., 23, 734 (1955).

145. R.G. Snydner, J. Chem. Phys., 47, 1316 (1967).

146. L.E. Nielsen, "Mechanical Properties of Polymers", Reinhold Publishing Company, New York (1962).

147. R.L. McCullough, C.T. Wu, J.C. Seferis, and P.H. Lindenmeyer, Polym. Eng. Sci., 16(5), 371 (1976).

148. J.C. Seferis, R.L. McCullough, and R.J. Samuels, Polym. Eng. Sci., 16(5), 334 (1976).

149. J.C. Seferis and R.J. Samuels, Polym. Eng. Sci., 19(14), 975 (1979).

150. M.R. Kamal, D.M. Kalyon, and J.M. Dealy, to be published in Polym. Eng. and Sci.

151. P.H. Doan, M.Eng. Thesis, McGill University, Montreal (1974).

152. Am. Soc. Testing Mater., ASTM Std. 1505-68, 482-487 (1972).

153. R.S. Stein, "New Methods of Polymer Characterization", B. Ke, Ed., Interscience, New York (1964), Chap. 4.

154. R.S. Stein, Macromolecules, 1, 116 (1968).

155. I.I. Rubin, "Injection Molding - Theory and Practice", John Wiley and Sons, New York (1972).

156. V. Tan and M.R. Kamal in "Science and Technology of Polymer Processing", The MIT Press, Cambridge, Massachusetts, and London, England, p. 665 (1977).

157. A.V. Tobolsky, "Properties and Structures of Polymers", John Wiley and Sons, New York (1960).

158. F. Kashani, "Studies About Thermal Conductivity and Thermal Diffusivity Measuring Apparatus", M.Eng. Thesis, McGill University, Montreal (1979).

159. I. Sakurada, T. Ito, and K. Nakamae, J. Polym. Sci., C15, 75 (1966).

160. A. Odajima and T. Maeda, J. Polym. Sci., 59, 55 (1966).

161. J.F. Twisleton and J.W. White, Polymer, 13, 40 (1972).

162. Z. Tadmor, J. Appl. Polym. Sci., 18, 1453 (1974).

163. T.T. Li, R.J. Volungis, and R.S. Stein, J. Polym. Sci., 20, 199 (1956).

164. C.W. Bunn and R. de P. Daubeny, Trans. Faraday Soc., 50, 1173 (1954).

165. V. Tan and C.G. Gogos, Polym. Eng. Sci., 16, 512 (1976).

166. V. Tan, private communication.

167. G.R. Williamson, B. Wright, and R.N. Haward, J. Appl. Chem., 14, 131 (1964).

168. K.M. Kulkarni, K.J. Broutman, S. Kalpakium, and D.B. Emery, Polym. Eng. Sci., 16, 1 (1976).

169. K. Djurner and M. Rigdahl, Colloid and Polym. Sci., 255, 1129 (1977).

170. K. Djurner, J. Kubát, and M. Rigdahl, Polymer, 18(10), 1068 (1977).

171. K.G. Denbigh, Trans. Faraday Soc., 36, 936 (1940).

172. D.A. Keedy, J. Powers, and R.S. Stein, J. Appl. Phys., 31, 1911 (1960).

173. K. Nakayama and H. Kanetsuna, J. Mater. Sci., 10, 1105 (1975).

174. R.S. Porter, J.H. Southern, and N. Weeks, Polym. Eng. Sci., 15(3), 213 (1975).

175. B.A. Whipple and C.T. Hill, Amer. Inst. Chem. Engrs. J., 24, 4, 664 (1978).

176. G. Mennig, Soc. Plastics Engrs. Technical Papers, 24, 529 (1978).

177. C.D. Han and C.A. Villamizar, Polym. Eng. Sci., 18, 3, 173 (1978).

178. Z. Bakerdjian, "Experimental Study of Anisotropy in Injection Molded Thermoplastic Parts", M.Eng. Thesis, McGill University, Montreal (1978).

179. A.J. Pennings, J.M.A.A. van der Mark, and A.M. Kiel, Kolloid-Z., 237, 336 (1970).

APPENDIX 1

CALCULATION OF FORM BIREFRINGENCE*

$$\Delta_f = \frac{X_c(1 - X_c)(n_1^2 - n_2^2)}{2\, n_a[(1 + X_c)n_2^2 + (1 - X_c)n_1^2]}$$

where $n_a^2 = X_c\, n_1^2 + (1 - X_c)n_2^2$

assuming $n_1 = 1.575$ (c-axis)

$n_2 = 1.514$ (a-axis)

For $X_c = 0.5868$, $\Delta_T = 8.06\times10^{-3}$

$$\Delta_f = \frac{(0.5868)(0.4132)(0.0355)}{2(1.5501)[2.2922(1.5868) + 2.4806(0.4132)]}$$

$$\Delta_f = 0.596\times10^{-3}$$

percent contribution to total birefringence $= \frac{(0.596\times10^{-3})}{(8.06\times10^{-3})} \times 100$

i.e. 7.4%

For $X_c = 0.6938$, $\Delta_T = 5.53\times10^{-3}$

$$\Delta_f = \frac{(0.6938)(0.3062)(0.0355)}{2(1.5566)[2.2922(1.6938) + 2.4806(0.3062)]}$$

---

* O. Wiener, Sachs. Ges. Wiss. Leipzig Math. - Phys. Kl. Abh., 32, 507 (1912).
W.T. Mead, C.R. Desper, and R.S. Porter, J. Polym. Sci.: Polym. Phys. Ed., 17, 859 (1979).

$$\Delta_f = 0.522 \times 10^{-3}$$

percent contribution to total birefringence $= \frac{(0.522 \times 10^{-3})}{(5.53 \times 10^{-3})} \times 100$

i.e. 9.4%

APPENDIX 2

CALIBRATION OF TRANSDUCERS

This appendix tabulates the data pertaining to the calibration of the pressure transducers.

Transducer #1		Transducer #2		Transducer #3		Transducer #4	
P (psi)	Output (mv)	P (psi)	Output (mv)	P (psi)	Output (mv)	P (psi)	Output (mv)
0	0	0	0	0	0	0	0
349.4	0.62	344.5	0.31	343.2	0.64	344.9	0.34
675.9	1.23	449.2	0.62	513.7	1.26	660.4	0.63
1159.9	2.18	1176.9	1.10	1184.7	2.23	1154.2	1.09
1772.3	3.34	1736.5	1.63	1756.3	3.32	1755.3	1.67
2311.3	4.40	2275.5	2.15	2215.8	4.25	2271.8	2.17
2810.8	5.36	2827.7	2.66	2788.2	5.32	2810.8	2.69
3369.5	6.41	3414.7	3.22	3378	6.43	3375.2	3.25
3962.2	7.58	3900.1	3.69	3934	7.52	3838	3.72
4504	8.62	4489	4.25	4385.5	8.44	4413.7	4.27

APPENDIX 3

DENSITY

Resin EX 1
Melt Temperature: 176°C

Molding #21
Mold Temperature: 35°C

Density (g/cc)

Sample	Position E4	C4	A4	E2	A2
1	0.9434	0.9412	0.9405	0.9403	0.9392
2	0.9424	0.9445	0.9403	0.9423	0.9414
3	0.9450	0.9413	0.9432	0.9436	0.9438
4	0.9463	0.9435	0.9441	0.9439	0.9455
5	0.9473	0.9453	0.9448	0.9447	0.9459
6		0.9454			
7	0.9476		0.9460	0.9462	0.9469
10	0.9482		0.9473	0.9477	0.9477
11		0.9487			
12	0.9486		0.9479	0.9492	0.9484
14		0.9495			
15	0.9490		0.9489	0.9494	0.9492
16		0.9499			
17	0.9492		0.9495	0.9495	0.9492
19		0.9505			
20	0.9495		0.9494	0.9500	0.9500
21		0.9507			
22	0.9498		0.9492	0.9499	0.9504
25	0.9496	0.9508	0.9492	0.9502	0.9499
26		0.9508			
30	0.9502		0.9501	0.9506	0.9505
31		0.9510			
35	0.9503		0.9505	0.9511	0.9505
36		0.9523			
40	0.9508		0.9509	0.9516	0.9506
41		0.9528			

Resin EX 2
Melt Temperature: 176°C

Molding #12
Mold Temperature: 35°C

Density (g/cc)

Sample	Position E4	C4	A4	E2	A2
1	0.9452	0.9405	0.9441	0.9450	0.9402
2	0.9511	0.9427	0.9432	0.9451	0.9431
3	0.9498	0.9445	0.9455	0.9476	0.9444
4	0.9495				
5			0.9464	0.9492	0.9462
6		0.9477			
7	0.9504		0.9475	0.9502	0.9473
8		0.9489			
10			0.9496	0.9509	0.9490
11		0.9502			
12	0.9512		0.9501	0.9509	0.9496
13		0.9507			
14	0.9519				
15			0.9514	0.9516	0.9509
16		0.9513			
17	0.9521				
18			0.9520	0.9518	0.9514
19		0.9517			
20			0.9521	0.9515	0.9517
21		0.9522			
22	0.9528		0.9522	0.9519	0.9520
23		0.9527			
24	0.9533				
25			0.9527	0.9521	0.9523
26		0.9529			
27	0.9536				
28			0.9534	0.9533	0.9530
29	0.9539	0.9526			
30			0.9535	0.9526	0.9532
31		0.9530			
32	0.9542				
34	0.9546				
35			0.9545	0.9535	0.9542
36		0.9546			
37	0.9548				
40			0.9550	0.9540	0.9551
41		0.9556			
42	0.9547				

Resin EX 2 Molding #16
Melt Temperature: 205.9°C Mold Temperature: 35°C

	Density (g/cc)				
	Postion				
Sample	E4	C4	A4	E2	A2
1	0.9448	0.9427	0.9433	0.9422	0.9404
2	0.9476	0.9437	0.9428	0.9408	0.9430
3	0.9482	0.9450	0.9441	0.9425	0.9451
4	0.9483	0.9464	0.9454	0.9449	0.9460
5	0.9487	0.9474	0.9466	0.9461	0.9470
6	0.9499	0.9495	0.9477	0.9480	0.9476
8	0.9497	0.9497	0.9487	0.9495	0.9491
10					0.9504
11	0.9509	0.9511	0.9502	0.9507	
12					0.9511
13	0.9512	0.9514	0.9510	0.9513	
15					0.9517
16	0.9518	0.9524	0.9517	0.9517	
18					0.9522
19	0.9530	0.9530	0.9493	0.9524	
20					0.9523
21	0.9524	0.9527	0.9528	0.9523	
22					0.9521
23	0.9527	0.9538	0.9525	0.9524	
25					0.9532
26	0.9530	0.9532	0.9530	0.9525	
28					0.9540
29	0.9533	0.9542	0.9535	0.9532	
30					0.9542
31	0.9537	0.9546	0.9535	0.9533	
35					0.9540
36	0.9548	0.9549	0.9549	0.9540	
40					0.9550
41	0.9559	0.9557	0.9558	0.9551	

APPENDIX 4

SONIC MODULUS

Resin EX 1
Melt Temperature: 176°C

Molding #21
Mold Temperature: 35°C

Position	Sample	Sonic Velocity C (km/sec)	Sonic Modulus E_{or} x 10^{-10} (Pa)
E4	1	1.06	0.105
	2	1.15	0.125
	3	1.22	0.140
	4	1.26	0.151
	5	1.31	0.163
	7	1.20	0.136
	10	1.55	0.229
	12	1.36	0.175
	15	1.38	0.181
	17	1.33	0.168
	20	1.43	0.193
	22	1.35	0.174
	25	1.37	0.177
	30	1.44	0.198
	35	1.34	0.170
	40	1.38	0.181
C4	1	1.08	0.110
	2	1.23	0.142
	3	1.34	0.169
	4	1.42	0.189
	5	1.41	0.187
	6	1.43	0.194
	11	1.47	0.205
	14	1.43	0.195
	16	1.47	0.206
	19	1.51	0.216
	21	1.45	0.200
	25	1.45	0.199
	26	1.45	0.199
	31	1.48	0.207
	36	1.44	0.198
	41	1.45	0.201

Position	Sample	Sonic Velocity C (km/sec)	Sonic Modulus E_{or} x 10^{-10} (Pa)
A4	1	1.20	0.135
	2	1.28	0.153
	3	1.31	0.161
	4	1.26	0.151
	5	1.37	0.178
	7	1.33	0.167
	10	1.47	0.205
	12	1.29	0.157
	15	1.42	0.192
	17	1.38	0.180
	20	1.38	0.180
	22	1.39	0.183
	25	1.35	0.172
	30	1.34	0.170
	35	1.36	0.175
	40	1.37	0.179
E2	1	1.11	0.115
	2	1.34	0.170
	3	1.28	0.155
	4	1.32	0.165
	5	1.27	0.153
	7	1.35	0.173
	10	1.31	0.162
	12	1.24	0.145
	15	1.31	0.163
	17	1.44	0.197
	20	1.34	0.170
	22	1.31	0.162
	25	1.35	0.174
	30	1.36	0.176
	35	1.34	0.172
	40	1.43	0.193
A2	1	1.03	0.100
	2	1.15	0.123
	3	1.21	0.138
	4	1.27	0.153
	5	1.38	0.180
	7	1.25	0.147
	10	1.34	0.170
	12	1.46	0.201
	15	1.35	0.172
	17	1.05	0.104
	20	1.39	0.184
	22	1.25	0.149
	25	1.42	0.191
	30	1.40	0.187
	35	1.40	0.187
	40	1.44	0.196

Resin EX 2
Melt Temperature: 176°C

Molding #12
Mold Temperature: 35°C

Position	Sample	Sonic Velocity C (km/sec)	Sonic Modulus E_{or} x 10^{-10} (Pa)
E4	1	1.59	0.240
	2	1.44	0.197
	3	1.29	0.159
	4	1.14	0.122
	5	1.21	0.140
	6	1.27	0.154
	7	1.39	0.183
	12	1.37	0.179
	14	1.41	0.189
	17	1.36	0.176
	22	1.46	0.203
	24	1.41	0.191
	27	1.50	0.216
	29	1.42	0.192
	32	1.39	0.183
	34	1.45	0.200
	37	1.39	0.184
	42	1.42	0.193
C4	1	1.42	0.190
	2	1.05	0.104
	3	1.27	0.151
	4	1.37	0.177
	5	1.24	0.145
	6	1.38	0.181
	8	1.33	0.167
	11	1.35	0.172
	13	1.34	0.172
	16	1.33	0.168
	19	1.33	0.167
	21	1.32	0.166
	23	1.34	0.171
	26	1.34	0.172
	29	1.31	0.164
	31	1.36	0.175
	36	1.36	0.177
	41	1.38	0.183

Position	Sample	Sonic Velocity C (km/sec)	Sonic Modulus $E_{or} \times 10^{-10}$ (Pa)
A4	1	1.50	0.212
	2	1.27	0.152
	3	1.10	0.115
	4	1.11	0.116
	5	1.33	0.168
	7	1.41	0.189
	10	1.40	0.186
	12	1.36	0.176
	15	1.41	0.189
	18	1.35	0.173
	20	1.43	0.194
	22	1.41	0.190
	25	1.39	0.184
	28	1.40	0.187
	30	1.44	0.198
	32	1.45	0.201
	35	1.39	0.184
	40	1.41	0.189
E2	1	1.59	0.240
	2	1.20	0.137
	3	1.31	0.162
	4	1.44	0.197
	5	1.45	0.200
	7	1.44	0.196
	10	1.49	0.212
	12	1.47	0.206
	15	1.55	0.227
	18	1.45	0.201
	20	1.56	0.232
	22	1.40	0.186
	25	1.52	0.219
	28	1.45	0.200
	30	1.46	0.203
	32	1.52	0.221
	35	1.45	0.200
	40	1.47	0.206

Position	Sample	Sonic Velocity C (km/sec)	Sonic Modulus $E_{or} \times 10^{-10}$ (Pa)
A2	1	1.50	0.210
	2	1.31	0.163
	3	1.37	0.176
	4	1.33	0.167
	5	1.37	0.179
	7	1.39	0.182
	10	1.43	0.194
	12	1.46	0.202
	15	1.47	0.206
	18	1.44	0.197
	20	1.48	0.210
	22	1.45	0.201
	25	1.46	0.202
	28	1.46	0.203
	30	1.42	0.193
	32	1.42	0.193
	35	1.38	0.180
	40	1.47	0.207

Resin EX 2 Molding #16
Melt Temperature: 205.9°C Mold Temperature: 35°C

Position	Sample	Sonic Velocity. C (km/sec)	Sonic Modulus $E_{or} \times 10^{-10}$ (Pa)
E4	1	1.56	0.230
	2	1.35	0.172
	3	1.18	0.131
	4	1.10	0.115
	5	1.28	0.155
	6	1.34	0.171
	8	1.23	0.144
	11	1.47	0.204
	13	1.31	0.163
	16	1.39	0.183
	19	1.43	0.195
	21	1.36	0.176
	23	1.34	0.171
	26	1.37	0.179
	29	1.41	0.189
	31	1.41	0.189
	36	1.50	0.215
	41	1.49	0.212
C4	1	1.46	0.205
	2	1.06	0.105
	3	1.27	0.153
	4	1.28	0.156
	5	1.26	0.151
	6	1.36	0.176
	8	1.29	0.157
	11	1.47	0.204
	13	1.28	0.157
	16	1.35	0.172
	19	1.36	0.176
	21	1.35	0.173
	23	1.33	0.168
	26	1.38	0.180
	29	1.41	0.189
	31	1.43	0.195
	36	1.43	0.194
	41	1.43	0.195

Position	Sample	Sonic Velocity C (km/sec)	Sonic Modulus $E_{or} \times 10^{-10}$ (Pa)
A4	1	1.53	0.220
	2	1.28	0.155
	3	1.41	0.189
	4	1.48	0.206
	5	1.43	0.193
	6	1.46	0.202
	8	1.45	0.200
	11	1.41	0.189
	13	1.44	0.197
	16	1.36	0.176
	19	1.35	0.172
	21	1.37	0.178
	23	1.37	0.178
	26	1.39	0.185
	29	1.35	0.173
	31	1.38	0.181
	36	1.34	0.171
	41	1.38	0.182
E2	1	1.53	0.220
	2	1.34	0.168
	3	1.16	0.128
	4	1.28	0.154
	5	1.37	0.178
	6	1.39	0.183
	8	1.41	0.189
	11	1.46	0.202
	13	1.43	0.193
	16	1.37	0.177
	19	1.39	0.184
	21	1.36	0.176
	23	1.36	0.177
	26	1.39	0.184
	29	1.35	0.174
	31	1.39	0.184
	36	1.41	0.189
	41	1.49	0.212

Position	Sample	Sonic Velocity C (km/sec)	Sonic Modulus E_{or} x 10^{-10} (Pa)
A2	1	1.48	0.205
	2	1.25	0.147
	3	1.36	0.175
	4	1.47	0.204
	5	1.42	0.192
	6	1.42	0.190
	8	1.41	0.188
	10	1.35	0.190
	12	1.41	0.188
	15	1.43	0.194
	18	1.43	0.194
	20	1.44	0.196
	22	1.43	0.193
	25	1.37	0.180
	28	1.35	0.173
	30	1.40	0.188
	35	1.43	0.195
	40	1.45	0.200

APPENDIX 5

BIREFRINGENCE

Resin EX 1
Melt Temperature: 176°C

Molding #21
Mold Temperature: 35°C

Measured Birefringence
$\Delta_T \times 10^3$

Sample	Position E4	C4	A4	E2	A2
1	-2.19	5.37	7.50	7.05	5.05
2	12.53	10.25	9.13	8.55	7.55
3	9.85	12.00	10.85	7.36	8.06
4	11.67	13.60	11.06	6.96	8.59
5	12.11		9.46	6.87	9.50
6		10.44			
7	7.98		9.17	5.47	9.41
9		8.16			
10	6.23		9.27	6.05	6.58
11		7.21			
12	5.54		8.16	5.32	5.75
14		7.63			
15	8.34		8.34	5.84	5.46
16		7.04			
17	8.33		7.63	5.32	6.35
19		7.46			
20	8.34		7.21	5.89	6.12
21		6.87			
22	8.16		6.55	5.03	6.27
25	7.90		7.29	5.10	6.66
26		7.63			
29		8.07			
30	7.81		7.04	4.83	7.06
31		7.38			
35	7.63		6.66	5.00	6.50
36		7.72			
40	7.63		6.66	4.90	6.50
41		7.21			

Resin EX 2
Melt Temperature: 176°C

Molding #12
Mold Temperature: 35°C

Measured Birefringence
$\Delta_T \times 10^3$

Sample	Position E4	C4	A4	E2	A2
1	8.54	8.06	10.76	13.76	9.60
2	5.28	7.15	9.85	6.18	6.10
3	8.08	6.11	6.80	6.71	6.11
4	8.16	6.27	7.89	6.82	6.11
5	7.55	6.12	7.30	7.98	5.67
6		5.82			
7	7.98		7.14	9.36	5.75
8		6.42			
9	7.47				
10			6.58	9.49	5.60
11		6.90			
12	7.29		5.89	8.34	5.53
13		7.06			
14	7.21				
15			5.50	8.15	5.39
16		7.22			
17	6.50				
18			5.31	8.59	5.02
19	5.92	6.98			
20			5.53	8.68	5.35
21		6.42			
22	6.00		5.53	8.41	5.12
23		6.35			
24	6.07				
25			5.90	8.33	5.32
26		6.50			
27	6.07				
28			5.89	7.98	5.12
29	6.31	5.75			
30			5.80	7.55	5.05
31		6.50			
32	6.40		5.38	6.66	5.05
35			5.46	6.27	5.10
36		5.67			
37	6.39				
40			5.90	5.89	5.10
41		6.25			
42	6.23				

Resin EX 2 — Molding #16
Melt Temperature: 205.9°C — Mold Temperature: 35°C

Measured Birefringence
$\Delta_T \times 10^3$

Sample	Position E4	C4	A4	E2	A2
1	9.84	8.98	9.48	9.45	9.80
2	6.33	7.26	8.60	7.27	7.47
3	6.82	6.47	8.42	6.89	6.95
4	7.59	6.95	8.25	6.34	7.55
5	7.26	7.55	8.25	7.18	7.72
6	7.64	7.14	7.50	7.10	6.82
8	6.19	6.66	7.34	8.08	6.74
10					6.66
11	6.27	6.27	7.34	6.87	
12					7.06
13	6.90	6.04	7.10	6.56	
15					6.90
16	6.90	6.12	6.48	6.87	
18					6.50
19	6.74	6.04	7.02	6.87	
20					6.80
21	6.50	6.19	7.26	6.87	
22					6.58
23	5.97	5.60	7.10	7.10	
25					6.58
26	5.89	6.19	6.95	6.79	
28					6.12
29	5.97	5.67	7.18	6.79	
30					6.42
31	5.67	5.90	7.10	6.79	
35					6.40
36	5.46	5.90	7.10	6.64	
40					5.89
41	5.53	5.90	6.95	6.60	

APPENDIX 6

X-RAY DIFFRACTION

This appendix tabulates the orientation functions corresponding to the crystallographic a, b, and c axes. The values of $\overline{\cos^2\alpha}$ and $\overline{\cos^2\beta}$ have been corrected according to the procedure outlined in Appendix 15.

Resin EX 1 — Molding #21
Melt Temperature: 176°C — Mold Temperature: 35°C

Position	Sample	$\overline{\cos^2\alpha}$	f_a	$\overline{\cos^2\beta}$	f_b	f_c
E4	1	0.464	0.196	0.327	-0.009	-0.187
	2	0.452	0.179	0.287	-0.069	-0.110
	3	0.497	0.245	0.185	-0.223	-0.023
	5	0.456	0.184	0.196	-0.206	0.022
	10	0.426	0.139	0.327	-0.010	-0.129
	15	0.427	0.140	0.296	-0.057	-0.083
	20	0.463	0.195	0.248	-0.128	-0.068
	25	0.455	0.183	0.257	-0.115	-0.068
	30	0.449	0.174	0.309	-0.036	-0.138
	35	0.448	0.172	0.294	-0.058	-0.114
	40	0.458	0.186	0.248	-0.128	-0.058
C4	1	0.400	0.100	0.275	-0.088	-0.013
	2	0.413	0.120	0.236	-0.146	0.026
	3	0.415	0.123	0.229	-0.157	0.035
	4	0.451	0.176	0.260	-0.110	-0.066
	6	0.381	0.072	0.315	-0.028	-0.044
	11	0.392	0.087	0.336	0.004	-0.084
	16	0.397	0.096	0.334	0.002	-0.094
	21	0.395	0.092	0.314	-0.030	-0.063
	26	0.434	0.150	0.331	-0.004	-0.147
	31	0.412	0.118	0.309	-0.037	-0.081
	36	0.429	0.143	0.312	-0.032	-0.110
	41	0.450	0.174	0.286	-0.070	-0.104

Position	Sample	$\overline{\cos^2\alpha}$	f_a	$\overline{\cos^2\beta}$	f_b	f_c
A4	1	0.556	0.333	0.239	-0.141	-0.192
	2	0.447	0.171	0.225	-0.163	-0.008
	3	0.461	0.192	0.265	-0.103	-0.089
	5	0.426	0.139	0.289	-0.067	-0.072
	10	0.427	0.140	0.311	-0.034	-0.106
	15	0.428	0.142	0.313	-0.031	-0.112
	20	0.454	0.180	0.258	-0.114	-0.067
	25	0.431	0.147	0.293	-0.061	-0.086
	30	0.435	0.153	0.303	-0.046	-0.107
	35	0.419	0.129	0.300	-0.050	-0.079
	40	0.429	0.143	0.298	-0.053	-0.091
E2	1	0.510	0.265	0.283	-0.076	-0.189
	2	0.443	0.164	0.280	-0.080	-0.085
	3	0.439	0.158	0.289	-0.067	-0.091
	5	0.411	0.117	0.293	-0.060	-0.057
	10	0.416	0.124	0.308	-0.038	-0.086
	15	0.413	0.119	0.275	-0.088	-0.031
	20	0.435	0.153	0.244	-0.135	-0.019
	25	0.414	0.121	0.283	-0.076	-0.045
	30	0.415	0.123	0.278	-0.083	-0.040
	35	0.426	0.138	0.281	-0.079	-0.059
	40	0.416	0.123	0.265	-0.103	-0.021
A2	1	0.392	0.088	0.298	-0.054	-0.035
	2	0.434	0.151	0.287	-0.070	-0.081
	3	0.445	0.168	0.295	-0.058	-0.110
	5	0.452	0.178	0.239	-0.142	-0.035
	10	0.409	0.114	0.307	-0.039	-0.074
	15	0.403	0.104	0.323	-0.016	-0.089
	20	0.420	0.131	0.296	-0.057	-0.074
	25	0.433	0.150	0.277	-0.085	-0.064
	30	0.440	0.160	0.276	-0.086	-0.074
	35	0.453	0.180	0.255	-0.118	-0.062
	40	0.447	0.170	0.261	-0.108	-0.062

Resin EX 2
Melt Temperature: 176°C

Molding #12
Mold Temperature: 35°C

Position	Sample	$\overline{\cos^2\alpha}$	f_a	$\overline{\cos^2\beta}$	f_b	f_c
E4	1	0.365	0.048	0.316	-0.026	-0.022
	2	0.420	0.129	0.334	0.002	-0.131
	3	0.432	0.147	0.308	-0.037	-0.110
	4	0.429	0.143	0.295	-0.057	-0.086
	7	0.450	0.175	0.269	-0.097	-0.077
	12	0.437	0.156	0.279	-0.082	-0.073
	17	0.446	0.169	0.269	-0.097	-0.072
	22	0.439	0.158	0.281	-0.079	-0.079
	27	0.405	0.107	0.280	-0.080	-0.027
	32	0.448	0.172	0.286	-0.071	-0.101
	37	0.437	0.156	0.282	-0.077	-0.079
	42	0.455	0.183	0.280	-0.080	-0.120
C4	1	0.341	0.011	0.328	-0.008	-0.003
	2	0.404	0.106	0.296	-0.056	-0.050
	3	0.422	0.133	0.301	-0.049	-0.084
	6	0.427	0.140	0.306	-0.042	-0.099
	11	0.457	0.186	0.298	-0.054	-0.133
	16	0.452	0.177	0.302	-0.047	-0.130
	21	0.437	0.155	0.299	-0.051	-0.104
	26	0.454	0.181	0.290	-0.065	-0.116
	31	0.451	0.177	0.297	-0.054	-0.123
	36	0.432	0.148	0.276	-0.086	-0.062
	41	0.446	0.169	0.301	-0.049	-0.120
A4	1	0.301	-0.048	0.336	0.004	0.045
	2	0.428	0.143	0.302	-0.047	-0.096
	3	0.400	0.099	0.311	-0.033	-0.066
	5	0.415	0.123	0.306	-0.041	-0.081
	10	0.400	0.100	0.296	-0.056	-0.044
	15	0.431	0.147	0.261	-0.109	-0.038
	20	0.430	0.145	0.275	-0.087	-0.058
	25	0.437	0.155	0.285	-0.073	-0.082
	30	0.436	0.154	0.284	-0.074	-0.080
	35	0.429	0.143	0.286	-0.071	-0.072
	40	0.436	0.154	0.276	-0.086	-0.068

Position	Sample	$\overline{\cos^2\alpha}$	f_a	$\overline{\cos^2\beta}$	f_b	f_c
E2	1	0.379	0.068	0.273	-0.090	0.022
	2	0.412	0.118	0.308	-0.039	-0.079
	3	0.428	0.142	0.337	0.005	-0.147
	5	0.398	0.096	0.304	-0.045	-0.052
	10	0.403	0.104	0.283	-0.076	-0.028
	15	0.412	0.118	0.222	-0.167	0.049
	20	0.406	0.109	0.261	-0.109	0.001
	25	0.406	0.109	0.250	-0.126	0.016
	30	0.399	0.099	0.255	-0.118	0.019
	35	0.423	0.134	0.282	-0.077	-0.057
	40	0.412	0.118	0.259	-0.112	-0.006
A2	1	0.438	0.157	0.298	-0.053	-0.103
	2	0.448	0.172	0.317	-0.025	-0.146
	3	0.415	0.123	0.285	-0.073	-0.050
	5	0.422	0.133	0.295	-0.057	-0.076
	10	0.433	0.149	0.293	-0.061	-0.088
	15	0.446	0.169	0.300	-0.050	-0.118
	20	0.445	0.168	0.276	-0.085	-0.083
	25	0.436	0.154	0.282	-0.078	-0.076
	30	0.429	0.144	0.278	-0.083	-0.061
	35	0.472	0.208	0.301	-0.049	-0.159
	40	0.442	0.163	0.280	-0.080	-0.084

Resin EX 2 Molding #16
Melt Temperature: 205.9°C Mold Temperature: 35°C

Position	Sample	$\overline{\cos^2\alpha}$	f_a	$\overline{\cos^2\beta}$	f_b	f_c
E4	1	0.289	-0.067	0.307	-0.040	0.107
	2	0.423	0.135	0.302	-0.048	-0.087
	3	0.430	0.145	0.334	0.000	-0.146
	6	0.394	0.091	0.338	0.007	-0.097
	11	0.437	0.156	0.317	-0.025	-0.131
	16	0.394	0.091	0.291	-0.063	-0.028
	21	0.435	0.153	0.292	-0.063	-0.091
	26	0.441	0.162	0.273	-0.090	-0.072
	31	0.396	0.094	0.292	-0.062	-0.033
	36	0.392	0.087	0.283	-0.076	-0.012
	41	0.397	0.095	0.273	-0.091	-0.004
C4	1	0.329	-0.007	0.267	-0.099	0.106
	2	0.469	0.203	0.276	-0.086	-0.117
	3	0.423	0.135	0.303	-0.045	-0.090
	4	0.437	0.156	0.309	-0.037	-0.119
	6	0.429	0.143	0.307	-0.039	-0.104
	11	0.449	0.173	0.296	-0.056	-0.117
	16	0.430	0.183	0.284	-0.074	-0.109
	21	0.455	0.182	0.274	-0.089	-0.093
	26	0.469	0.203	0.285	-0.073	-0.130
	31	0.455	0.183	0.281	-0.079	-0.104
	36	0.446	0.170	0.292	-0.062	-0.108
	41	0.431	0.183	0.271	-0.094	-0.089
A4	1	0.280	-0.080	0.324	-0.014	0.094
	2	0.433	0.150	0.331	-0.004	-0.146
	3	0.426	0.139	0.323	-0.016	-0.123
	4	0.433	0.149	0.307	-0.039	-0.111
	6	0.435	0.152	0.294	-0.060	-0.093
	11	0.450	0.174	0.306	-0.041	-0.133
	16	0.441	0.161	0.285	-0.073	-0.088
	21	0.446	0.169	0.256	-0.116	-0.053
	26	0.457	0.186	0.286	-0.071	-0.114
	31	0.433	0.150	0.278	-0.083	-0.068
	36	0.460	0.190	0.279	-0.082	-0.109
	41	0.441	0.162	0.276	-0.087	-0.075

Position	Sample	$\overline{\cos^2\alpha}$	f_a	$\overline{\cos^2\beta}$	f_b	f_c
E2	1	0.422	0.134	0.319	-0.022	-0.111
	2	0.354	0.031	0.302	-0.046	0.015
	3	0.379	0.069	0.294	-0.059	-0.010
	4	0.437	0.156	0.315	-0.028	-0.128
	6	0.409	0.114	0.268	-0.098	-0.015
	11	0.411	0.117	0.295	-0.057	-0.060
	16	0.436	0.154	0.295	-0.057	-0.097
	21	0.464	0.195	0.231	-0.070	-0.125
	26	0.446	0.169	0.271	-0.094	-0.075
	31	0.477	0.215	0.244	-0.135	-0.081
	36	0.435	0.152	0.268	-0.099	-0.054
	41	0.480	0.221	0.231	-0.154	-0.067
A2	1	0.414	0.121	0.324	-0.014	-0.107
	2	0.449	0.174	0.309	-0.037	-0.137
	3	0.428	0.141	0.281	-0.079	-0.063
	5	0.427	0.141	0.305	-0.043	-0.098
	10	0.441	0.161	0.290	-0.065	-0.096
	15	0.471	0.207	0.296	-0.057	-0.150
	20	0.471	0.206	0.241	-0.138	-0.068
	25	0.463	0.194	0.296	-0.057	-0.137
	30	0.468	0.202	0.277	-0.085	-0.116
	35	0.471	0.206	0.289	-0.067	-0.140
	40	0.444	0.166	0.270	-0.095	-0.070

APPENDIX 7

INFRARED SPECTROSCOPY

Resin EX 1
Melt Temperature: 176°C

Molding #21
Mold Temperature: 35°C

Position	Sample	D_{720}	D_{730}	f_a (IR)
E4	1	1.20	1.26	0.079
	2	1.12	1.32	0.095
	3	1.10	1.38	0.113
	4	1.07	1.33	0.099
	5	1.06	1.38	0.111
	7	1.13	1.21	0.064
	10	1.19	1.25	0.077
	12	1.17	1.31	0.093
	15	1.17	1.31	0.094
	17	1.19	1.31	0.094
	22	1.16	1.26	0.081
	25	1.14	1.29	0.087
	30	1.19	1.32	0.097
	35	1.15	1.30	0.090
	40	1.18	1.33	0.098
C4	1	1.18	1.31	0.095
	2	1.13	1.18	0.057
	3	1.14	1.24	0.075
	4	1.06	1.33	0.098
	5	1.15	1.22	0.069
	6	1.13	1.23	0.072
	7	1.17	1.23	0.072
	9	1.17	1.23	0.071
	11	1.17	1.25	0.078
	14	1.18	1.28	0.086
	16	1.19	1.30	0.089
	19	1.14	1.27	0.083
	21	1.15	1.29	0.088
	26	1.17	1.28	0.086
	29	1.18	1.30	0.090
	31	1.18	1.31	0.092
	34	1.18	1.30	0.089
	36	1.15	1.31	0.093
	39	1.17	1.28	0.086
	41	1.22	1.36	0.108

Position	Sample	D_{720}	D_{730}	f_a (IR)
A4	1	1.21	1.44	0.127
	2	1.17	1.40	0.117
	3	1.26	1.38	0.113
	4	1.22	1.32	0.097
	5	1.19	1.32	0.095
	7	1.26	1.36	0.107
	10	1.28	1.38	0.112
	12	1.13	1.24	0.073
	15	1.14	1.22	0.069
	17	1.19	1.29	0.088
	20	1.19	1.29	0.089
	22	1.15	1.26	0.080
	25	1.15	1.25	0.076
	30	1.18	1.29	0.087
	35	1.16	1.28	0.086
	40	1.17	1.23	0.071

Resin EX 2
Melt Temperature: 176°C

Molding #12
Mold Temperature: 35°C

Position	Sample	D_{720}	D_{730}	f_a (IR)
E4	1	1.16	1.13	0.043
	2	1.02	1.07	0.024
	3	1.17	1.28	0.085
	4	1.22	1.27	0.082
	5	1.19	1.30	0.092
	6	1.20	1.36	0.108
	7	1.24	1.36	0.107
	9	1.19	1.30	0.090
	12	1.21	1.33	0.099
	14	1.26	1.32	0.097
	17	1.03	1.34	0.102
	20	1.22	1.32	0.095
	22	1.17	1.37	0.110
	24	1.24	1.31	0.094
	27	1.25	1.35	0.104
	30	1.22	1.31	0.093
	32	1.25	1.34	0.102
	34	1.24	1.38	0.111
	37	1.29	1.35	0.106
	40	1.25	1.37	0.109
	42	1.28	1.39	0.115
C4	1	1.08	1.07	0.024
	2	1.15	1.25	0.078
	3	1.17	1.26	0.080
	4	1.20	1.26	0.080
	5	1.19	1.26	0.080
	6	1.19	1.30	0.091
	8	1.17	1.29	0.087
	11	1.18	1.29	0.087
	13	1.24	1.33	0.099
	16	1.18	1.28	0.085
	18	1.21	1.31	0.093
	21	1.21	1.29	0.089
	23	1.21	1.32	0.096
	26	1.25	1.35	0.104
	28	1.26	1.35	0.105
	31	1.23	1.33	0.099
	33	1.16	1.28	0.087
	36	1.24	1.39	0.114
	38	1.17	1.29	0.087
	41	1.24	1.34	0.101

Position	Sample	D_{720}	D_{730}	f_a (IR)
A4	1	1.11	1.13	0.041
	2	1.24	1.33	0.100
	3	1.23	1.35	0.105
	4	1.20	1.27	0.082
	5	1.23	1.24	0.075
	6	1.20	1.27	0.082
	7	1.23	1.34	0.103
	10	1.27	1.39	0.115
	12	1.22	1.34	0.103
	15	1.19	1.29	0.089
	18	1.22	1.34	0.102
	20	1.23	1.33	0.100
	22	1.20	1.34	0.101
	25	1.23	1.36	0.106
	28	1.26	1.36	0.106
	30	1.25	1.36	0.107
	35	1.21	1.29	0.088
	40	1.25	1.37	0.110

Resin EX 2 — Molding #16
Melt Temperature: 205.9°C — Mold Temperature: 35°C

Position	Sample	D_{720}	D_{730}	f_a (IR)
E4	1	1.09	1.07	0.023
	2	1.21	1.27	0.083
	3	1.21	1.28	0.085
	4	1.24	1.30	0.092
	5	1.22	1.32	0.095
	6	1.24	1.29	0.088
	8	1.25	1.35	0.106
	11	1.20	1.32	0.096
	13	1.24	1.32	0.096
	16	1.24	1.34	0.103
	19	1.23	1.33	0.100
	21	1.19	1.26	0.080
	23	1.23	1.37	0.111
	26	1.25	1.40	0.118
	29	1.24	1.36	0.108
	31	1.23	1.37	0.111
	33	1.23	1.36	0.107
	36	1.25	1.35	0.106
	39	1.27	1.40	0.117
	41	1.28	1.35	0.105
C4	1	1.15	1.30	0.091
	2	1.20	1.30	0.090
	3	1.22	1.29	0.087
	4	1.21	1.26	0.081
	5	1.24	1.28	0.086
	6	1.26	1.30	0.090
	8	1.21	1.28	0.085
	11	1.27	1.32	0.096
	13	1.21	1.30	0.092
	16	1.21	1.30	0.091
	19	1.22	1.30	0.090
	21	1.33	1.45	0.131
	23	1.24	1.40	0.117
	26	1.22	1.37	0.109
	29	1.24	1.32	0.096
	31	1.23	1.35	0.104
	33	1.21	1.30	0.090
	36	1.24	1.36	0.107
	39	1.25	1.36	0.107
	41	1.28	1.39	0.114

Position	Sample	D_{720}	D_{730}	f_a (IR)
A4	1	1.17	1.19	0.059
	2	1.16	1.28	0.086
	3	1.23	1.32	0.095
	4	1.19	1.23	0.070
	5	1.18	1.23	0.071
	6	1.15	1.23	0.071
	8	1.19	1.30	0.091
	11	1.23	1.32	0.096
	13	1.22	1.28	0.085
	16	1.28	1.37	0.109
	19	1.22	1.32	0.095
	21	1.21	1.29	0.089
	23	1.23	1.35	0.106
	26	1.20	1.29	0.087
	29	1.23	1.37	0.110
	31	1.26	1.35	0.105
	33	1.25	1.37	0.110
	36	1.22	1.33	0.099
	39	1.23	1.32	0.096
	41	1.24	1.31	0.093

APPENDIX 8

MECHANICAL PROPERTIES

Resin EX 1
Melt Temperature: 176°C

Molding #8
Mold Temperature: 35°C

Position	Sample	$\sigma_{ny} \times 10^{-6}$ (Pa)	ε_y (%)	ε_b (%)
E4	1	15.6	20.0	27.5
	2	18.3	32.5	111.0
	3	20.4	35.0	70.5
	4	21.7	38.8	156.5
	5	20.9	40.0	111.5
	6	21.7	43.2	99.0
	7	22.8	40.0	109.0
	8	22.7	36.3	79.5
	9	22.4	37.9	75.0
	10	21.9	38.5	84.5
	12	22.6	36.9	70.0
	15	21.6	37.5	79.0
	17	22.1	36.7	82.0
	20	22.1	33.8	67.0
	22	22.0	33.2	70.5
	25	21.8	35.7	76.5
	27	22.0	36.3	72.0
	30	22.2	37.5	80.5
	32	21.8	36.3	73.0
	35	22.0	36.5	84.5
	37	22.9	35.0	69.5
	40	22.4	31.9	101.5

Position	Sample	$\sigma_{ny} \times 10^{-6}$ (Pa)	ε_y (%)	ε_b (%)
C4	1	17.9	31.3	158.0
	2	18.1	57.5	283.0
	3	18.9	34.8	129.0
	4	20.2	40.0	130.0
	5	20.5	40.0	209.5
	6	20.6	42.5	118.0
	7	20.1	35.0	72.5
	8	20.9	45.0	111.5
	9	20.7	41.3	102.5
	11	20.5	46.3	129.0
	13	20.8	40.0	88.5
	16	21.1	38.2	93.0
	18	21.2	40.3	95.5
	21	20.8	43.2	83.0
	23	21.0	39.5	95.5
	26	20.7	40.7	86.5
	28	21.1	41.3	90.0
	31	21.2	36.3	79.5
	33	21.1	38.8	75.0
	36	20.8	43.8	79.5
	38	21.2	38.2	82.0
	41	21.2	35.0	79.5
A4	1	17.0	30.5	203.0
	2	18.1	65.0	250.0
	3	19.2	45.0	166.0
	4	19.2	47.5	118.0
	5	20.5	30.2	77.5
	6	19.6	45.3	162.5
	7	19.9	44.4	117.5
	8	19.6	45.0	124.0
	9	20.2	30.3	108.0
	10	20.4	39.8	111.5
	12	20.3	37.5	98.0
	15	20.5	38.8	87.0
	17	19.6	40.0	85.0
	20	20.0	38.8	89.0
	22	19.3	38.8	89.0
	25	20.2	34.7	94.5
	27	19.7	36.3	98.0
	30	20.3	34.4	114.0
	32	19.4	35.0	92.5
	35	20.5	35.0	79.0
	37	19.1	33.8	92.0
	40	20.8	33.2	75.5

Position	Sample	$\sigma_{ny} \times 10^{-6}$ (Pa)	ε_y (%)	ε_b (%)
E2	1	12.86	16.3	37.0
	2	14.8	28.2	75.0
	3	19.9	41.3	132.0
	4	20.2	45.0	127.0
	5	20.8	41.3	124.0
	6	19.6	41.3	88.0
	7	20.4	36.3	72.0
	8	20.6	41.3	114.0
	9	19.8	35.7	65.0
	10	20.8	36.9	90.0
	12	20.9	37.5	83.0
	15	19.3	33.2	71.5
	17	20.6	36.3	82.5
	20	20.6	39.4	82.5
	22	20.6	36.3	62.0
	25	20.6	36.3	66.5
	27	20.6	38.8	75.0
	30	19.8	35.7	52.0
	32	20.7	36.3	62.0
	35	21.0	35.0	61.5
	37	20.6	29.4	50.0
	40	21.0	32.5	72.5
A2	1	14.1	40.5	51.5
	2	18.0	41.3	74.5
	3	20.1	36.3	58.5
	4	19.8	43.8	79.0
	5	19.6	51.5	116.5
	6	20.2	46.3	82.5
	7	20.6	47.5	105.0
	8	19.9	31.3	31.3
	9	19.7	46.9	105.0
	10	20.6	31.9	65.5
	12	21.4	35.7	79.0
	15	20.9	43.8	99.0
	17	21.2	41.3	109.0
	20	19.6	42.5	97.0
	22	20.9	40.7	96.5
	25	20.0	41.3	78.0
	27	20.6	45.0	129.5
	30	20.5	36.3	67.5
	32	20.9	38.2	85.0
	35	20.5	36.3	77.5
	37	21.1	36.9	96.5
	40	20.6	35.7	92.5

Resin EX 2
Melt Temperature: 176°C

Molding #13
Mold Temperature: 35°C

Position	Sample	$\sigma_{ny} \times 10^{-6}$ (Pa)	ε_y (%)	ε_b (%)
E4	1	17.9	15.0	24.0
	2	20.1	34.2	668.4
	3	22.6	30.0	585.0
	4	21.4	35.0	812.5
	5	22.4	30.0	136.0
	6	22.1	32.5	110.0
	7	21.7	30.0	95.0
	8	22.3	31.0	82.5
	9	21.5	32.5	81.0
	10	22.0	35.0	81.0
	12	21.7	31.0	85.0
	15	21.7	31.0	88.0
	17	21.3	32.5	71.0
	20	21.8	31.0	85.0
	22	22.1	30.0	80.0
	25	22.3	28.5	85.5
	27	22.3	27.0	77.3
	30	22.1	32.5	80.0
	32	22.4	27.5	65.0
	35	22.9	27.5	66.0
	37	22.7	35.0	77.5
	40	22.7	27.5	65.0
C4	1	15.5	15.0	30.0
	2	18.9	35.0	140.0
	3	20.9	27.5	115.0
	4	21.3	27.5	182.5
	5	21.3	29.0	581.0
	6	21.6	27.5	819.0
	7	20.2	27.5	172.5
	8	21.4	25.5	91.0
	9	21.7	26.0	107.5
	11	21.6	27.5	110.0
	13	21.3	27.5	71.0
	16	22.4	25.0	79.0
	18	21.6	27.5	92.5
	21	21.8	27.5	94.0
	23	21.8	30.0	90.0
	26	22.1	27.5	97.5
	28	22.2	25.0	95.0
	31	22.1	27.5	80.5
	33	22.4	31.0	107.5
	36	22.9	25.0	90.0
	38	22.2	29.0	86.0
	41	22.5	27.5	102.5

Position	Sample	$\sigma_{ny} \times 10^{-6}$ (Pa)	ε_y (%)	ε_b (%)
A4	1	14.7	16.3	83.8
	2	18.3	32.0	71.0
	3	21.1	36.5	250.0
	4	21.9	34.5	290.5
	5	21.8	37.5	156.5
	6	21.6	37.5	146.5
	7	21.2	37.5	109.5
	8	22.1	32.5	101.5
	9	21.2	32.5	101.5
	10	21.9	35.5	95.0
	12	21.4	35.0	132.0
	15	22.3	28.8	113.5
	17	21.5	31.3	125.0
	20	22.0	31.9	206.0
	22	21.5	30.0	109.5
	25	22.2	28.2	95.5
	27	21.0	30.7	153.0
	30	21.9	30.7	134.5
	32	21.4	29.4	95.0
	35	21.9	28.2	84.0
	37	21.8	28.2	74.5
	40	22.6	29.4	74.5
E2	1	17.6	15.0	65.0
	2	19.8	25.0	139.0
	3	20.3	25.0	120.0
	4	20.4	27.0	319.0
	5	20.2	30.3	539.0
	6	21.2	30.0	272.5
	7	21.3	30.0	346.0
	8	21.3	32.5	147.5
	9	21.1	31.0	111.5
	10	20.8	32.5	105.0
	12	21.2	35.0	115.0
	15	21.1	32.5	92.5
	17	21.7	35.0	107.5
	20	21.5	32.5	95.0
	22	21.7	35.0	94.0
	25	21.5	37.5	125.0
	27	21.9	32.5	111.0
	30	21.6	35.0	70.0
	32	22.5	37.5	100.0
	35	22.4	37.5	100.0
	37	22.8	32.5	81.5
	40	22.5	35.0	77.5

Position	Sample	$\sigma_{ny} \times 10^{-6}$ (Pa)	ε_y (%)	ε_b (%)
A2	1	17.3	17.5	80.5
	2	21.1	10.0	11.3
	3	23.1	26.3	186.5
	4	19.9	35.0	371.8
	5	24.8	30.7	291.5
	6	20.4	31.9	220.0
	7	20.4	39.0	76.5
	8	20.5	34.4	107.5
	9	21.0	33.8	201.5
	10	21.4	33.2	140.0
	12	20.8	33.8	213.0
	15	21.2	29.4	125.0
	17	20.8	31.5	264.5
	20	21.3	26.9	513.0
	22	20.3	30.7	154.0
	25	21.8	30.0	146.5
	27	20.4	28.2	89.5
	30	21.6	31.3	211.3
	32	21.3	30.7	287.5
	35	22.1	28.8	104.5
	37	21.2	31.9	127.5
	40	22.2	28.8	81.5

Resin EX 2 — Molding #17
Melt Temperature: 205.9°C — Mold Temperature: 35°C

Position	Sample	σ_{ny} x 10^{-6} (Pa)	ε_y (%)	ε_b (%)
EA	1	25.4	25.5	73.8
	2	19.3	26.9	38.8
	3	22.6	25.7	131.5
	4	22.7	40.3	406.5
	5	22.5	40.0	161.5
	6	24.0	38.2	89.0
	7	23.4	36.3	94.5
	8	23.5	35.0	254.5
	9	23.1	33.8	97.0
	11	23.4	39.8	114.5
	13	23.4	36.3	71.5
	16	23.5	36.3	137.5
	18	23.2	35.0	212.0
	21	23.5	36.9	126.5
	23	23.7	30.7	66.5
	26	23.0	36.3	90.0
	28	23.2	33.2	132.5
	31	23.0	35.0	175.0
	33	23.6	33.8	121.5
	36	23.7	33.8	69.5
	38	24.1	32.5	72.5
	41	23.8	32.5	107.0
C4	1	20.5	23.1	90.0
	2	19.4	32.5	139.0
	3	23.0	32.5	138.0
	4	21.7	33.8	477.0
	5	23.2	36.9	127.5
	6	22.2	40.7	137.0
	7	22.7	37.5	140.0
	8	22.3	38.2	115.5
	9	23.3	35.0	94.0
	11	23.2	35.7	81.5
	13	23.2	36.3	103.0
	16	23.2	36.3	111.5
	18	22.7	35.0	89.0
	21	23.2	37.5	89.0
	23	23.1	36.3	79.5
	26	23.3	36.9	92.5
	28	22.8	37.5	86.5
	31	23.1	36.6	94.5
	33	23.3	33.8	95.0
	36	23.7	34.4	104.5
	38	23.9	36.3	70.0
	41	24.4	34.2	66.5

Position	Sample	$\sigma_{ny} \times 10^{-6}$ (Pa)	ε_y (%)	ε_b (%)
A4	1	21.9	12.5	76.3
	2	18.5	36.9	102.5
	3	21.0	36.3	124.0
	4	22.4	43.2	79.0
	5	23.1	42.5	109.0
	6	21.6	43.2	92.0
	7	22.0	41.0	81.5
	8	22.4	40.9	83.0
	9	22.1	45.0	120.5
	11	22.2	37.5	87.5
	13	21.6	34.4	78.1
	16	22.4	35.7	86.5
	18	21.8	37.2	83.0
	21	22.5	34.0	96.5
	23	22.6	33.8	84.0
	26	22.1	35.0	90.5
	28	22.4	33.8	81.5
	31	22.4	31.9	87.0
	33	22.6	33.2	74.0
	36	22.7	28.8	83.0
	38	22.8	24.5	50.0
	41	22.9	25.7	74.5
E2	1	17.3	18.8	51.5
	2	18.9	31.9	103.5
	3	21.4	24.0	109.5
	4	20.3	31.3	102.0
	5	20.9	28.8	97.0
	6	20.3	26.9	79.0
	7	22.2	26.9	63.0
	8	20.2	27.5	64.5
	9	21.4	25.7	75.0
	11	21.3	25.7	59.0
	13	21.4	28.2	70.5
	16	21.5	27.9	75.0
	18	21.0	26.9	69.5
	21	21.3	25.0	65.0
	23	21.3	30.0	97.5
	26	21.5	26.3	82.0
	28	21.3	25.7	88.8
	31	21.9	24.4	62.5
	33	21.7	27.5	63.0
	36	21.5	25.0	60.0
	38	21.6	24.4	70.5
	41	23.5	22.5	33.8

Position	Sample	$\sigma_{ny} \times 10^{-6}$ (Pa)	ε_y (%)	ε_b (%)
A2	1	19.2	18.8	85.0
	2	18.5	33.8	63.5
	3	20.9	37.5	66.0
	4	19.8	41.9	64.0
	5	19.8	36.3	65.0
	6	19.8	36.3	65.0
	7	21.0	35.0	82.5
	8	21.6	40.7	70.5
	9	21.4	33.8	67.5
	10	21.3	41.3	72.5
	12	22.2	36.3	63.5
	15	21.6	35.7	62.0
	17	22.0	32.5	65.0
	20	21.6	36.3	66.5
	22	21.6	28.2	62.5
	25	22.2	35.7	84.5
	27	22.6	28.8	66.5
	30	22.6	31.5	80.0
	32	22.7	31.3	77.5
	35	21.8	28.8	56.0
	37	22.8	31.9	74.0
	40	22.7	31.9	62.0

APPENDIX 9

AMORPHOUS ORIENTATION FUNCTION

Resin EX 1
Melt Temperature: 176°C

Molding #21
Mold Temperature: 35°C

Position	Sample	X_c	f_{am}
E4	1	0.6070	-0.478
	2	0.6000	-0.204
	3	0.6180	-0.128
	5	0.6340	0.015
	10	0.6403	0.321
	15	0.6458	0.103
	20	0.6493	0.151
	25	0.6500	0.063
	30	0.6542	0.167
	35	0.6549	0.010
	40	0.6583	0.085
C4	1	0.5916	-0.342
	2	0.6146	-0.084
	3	0.5924	0.155
	4	0.6076	0.219
	6	0.6208	0.226
	11	0.6438	0.230
	16	0.6521	0.217
	21	0.6576	0.181
	26	0.6583	0.169
	31	0.6597	0.207
	36	0.6688	0.145
	41	0.6722	0.145
A4	1	0.5868	-0.087
	2	0.5854	0.071
	3	0.6055	0.072
	5	0.6167	0.148
	10	0.6340	0.241
	15	0.6452	0.159
	20	0.6486	0.086
	25	0.6473	0.044
	30	0.6535	0.016
	35	0.6562	0.044
	40	0.6591	0.058

Position	Sample	X_c	f_{am}
E2	1	0.5854	-0.276
	2	0.5993	0.138
	3	0.6083	0.029
	5	0.6159	0.000
	10	0.6369	0.007
	15	0.6486	-0.012
	20	0.6528	0.018
	25	0.6542	0.045
	30	0.6570	0.051
	35	0.6604	0.013
	40	0.6639	0.132
A2	1	0.5778	-0.431
	2	0.5931	-0.196
	3	0.6097	-0.106
	5	0.6243	0.138
	10	0.6369	0.062
	15	0.6473	0.051
	20	0.6528	0.106
	25	0.6521	0.138
	30	0.6562	0.112
	35	0.6562	0.109
	40	0.6570	0.154

Resin EX 2
Melt Temperature: 176°C

Molding #12
Mold Temperature: 35°C

Position	Sample	X_c	f_{am}
E4	1	0.6195	5.159
	2	0.6604	0.615
	3	0.6514	-0.193
	4	0.6493	-1.494
	7	0.6556	0.268
	12	0.6611	0.185
	17	0.6673	0.051
	22	0.6722	0.483
	27	0.6778	0.954
	32	0.6820	0.079
	37	0.6861	0.083
	42	0.6861	0.192
C4	1	0.5868	18.412
	2	0.5979	-2.856
	3	0.6146	-0.057
	6	0.6196	0.682
	11	0.6365	0.204
	16	0.6439	0.062
	21	0.6500	0.004
	26	0.6547	0.067
	31	0.6554	0.122
	36	0.6662	0.110
	41	0.6729	0.140
A4	1	0.6118	-4.369
	2	0.6055	0.090
	3	0.6216	-3.033
	5	0.6278	0.335
	10	0.6500	0.675
	15	0.6625	0.377
	20	0.6673	0.439
	25	0.6716	0.186
	30	0.6771	0.393
	35	0.6840	0.117
	40	0.6875	0.165
E2	1	0.6180	0.399
	2	0.6188	-0.142
	3	0.6361	0.008
	5	0.6473	0.198
	10	0.6591	0.231
	15	0.6639	0.280
	20	0.6653	0.298
	25	0.6673	0.246
	30	0.6708	0.172
	35	0.6771	0.139
	40	0.6806	0.165

Position	Sample	X_c	f_{am}
A2	1	0.5847	0.349
	2	0.6049	0.084
	3	0.6139	0.146
	5	0.6264	0.131
	10	0.6458	0.165
	15	0.6591	0.195
	20	0.6646	0.201
	25	0.6688	0.163
	30	0.6750	0.107
	35	0.6820	0.007
	40	0.6883	0.147

Resin EX 2
Melt Temperature: 205.9°C

Molding #16
Mold Temperature: 35°C

Position	Sample	X_c	f_{am}
E4	1	0.6167	0.387
	2	0.6361	0.072
	3	0.6403	-0.267
	6	0.6521	0.032
	11	0.6591	0.189
	16	0.6653	0.078
	21	0.6694	0.019
	26	0.6736	0.025
	31	0.6785	0.084
	36	0.6861	0.200
	41	0.6938	0.171
C4	1	0.6021	0.316
	2	0.6091	-0.488
	3	0.6180	-0.009
	4	0.6278	-0.017
	6	0.6493	0.065
	11	0.6604	0.183
	16	0.6694	-0.012
	21	0.6716	-0.011
	26	0.6750	0.024
	31	0.6847	0.089
	36	0.6868	0.083
	41	0.6924	0.076
A4	1	0.6063	0.372
	2	0.6028	0.043
	3	0.6118	0.212
	4	0.6208	0.269
	6	0.6369	0.219
	11	0.6542	0.121
	16	0.6646	0.024
	21	0.6722	0.019
	26	0.6736	0.058
	31	0.6771	0.028
	36	0.6868	-0.000
	41	0.6931	0.000

Position	Sample	X_c	f_{am}
E2	1	0.5986	0.361
	2	0.5889	0.168
	3	0.6007	-0.169
	4	0.6174	-0.007
	6	0.6389	0.132
	11	0.6576	0.185
	16	0.6646	0.036
	21	0.6688	0.010
	26	0.6702	0.060
	31	0.6757	0.044
	36	0.6806	0.070
	41	0.6883	0.161
A2	1	0.5862	0.331
	2	0.6042	-0.021
	3	0.6188	0.129
	5	0.6319	0.187
	10	0.6556	0.126
	15	0.6646	0.124
	20	0.6688	0.125
	25	0.6750	0.021
	30	0.6820	0.054
	35	0.6806	0.095
	40	0.6875	0.111

APPENDIX 10

ESTIMATION OF INTRINSIC BIREFRINGENCES

Resin EX 1
Melt Temperature: 176°C

Molding #21
Mold Temperature: 35°C

Position	Sample	$\frac{\Delta_T}{X_c f_{cr}}$	$\left(\frac{1 - X_c}{X_c}\right)\left(\frac{f_{am}}{f_{cr}}\right)$
E4	1	-0.0184	-1.5827
	2	0.1169	0.7626
	3	0.0650	0.3223
	5	0.1038	0.0483
	10	0.0701	1.2996
	15	0.0924	0.4048
	20	0.0658	0.4191
	25	0.0666	0.1853
	30	0.0686	0.5085
	35	0.0676	0.0297
	40	0.0515	0.1823
C4	1	0.0904	-2.3488
	2	0.1392	-0.4376
	3	0.1253	0.8709
	4	0.1269	0.8014
	6	0.2333	1.9164
	11	0.1284	1.4593
	16	0.1126	1.2078
	21	0.1134	1.0250
	26	0.0771	0.5819
	31	0.0951	0.9072
	36	0.0808	0.5039
	41	0.0615	0.4060
A4	1	0.0383	-0.1835
	2	0.0913	0.2936
	3	0.0934	0.2434
	5	0.1108	0.6642
	10	0.1044	0.9925
	15	0.0984	0.6160
	20	0.0617	0.2583
	25	0.0767	0.1648
	30	0.0121	0.0568
	35	0.0788	0.1782
	40	0.0706	0.2082

Position	Sample	$\frac{\Delta_T}{X_c f_{cr}}$	$\left(\frac{1 - X_c}{X_c}\right)\left(\frac{f_{am}}{f_{cr}}\right)$
E2	1	0.0455	-0.7385
	2	0.0868	0.5600
	3	0.0766	0.1175
	5	0.0957	0.0021
	10	0.0767	0.0318
	15	0.0757	-0.0528
	20	0.0599	0.0628
	25	0.0645	0.1950
	30	0.0600	0.2163
	35	0.0548	-0.0469
	40	0.0599	0.5403
A2	1	0.0989	-3.5659
	2	0.0842	-0.8893
	3	0.0787	-0.4038
	5	0.0857	0.4673
	10	0.0910	0.3099
	15	0.0808	0.2657
	20	0.0717	0.4314
	25	0.0683	0.4910
	30	0.0672	0.3651
	35	0.0550	0.3159
	40	0.0582	0.4724

Resin EX 2
Melt Temperature: 176°C

Molding #12
Mold Temperature: 35°C

Position	Sample	$\frac{\Delta_T}{X_c f_{cr}}$	$\left(\frac{1 - X_c}{X_c}\right)\left(\frac{f_{am}}{f_{cr}}\right)$
E4	1	0.2902	5.1593
	2	0.0618	0.6149
	3	0.0843	-0.1927
	4	0.0879	-1.4938
	7	0.1292	0.2676
	12	0.0709	0.1846
	17	0.0577	0.0514
	22	0.0565	0.4827
	27	0.0839	0.9543
	32	0.0547	0.0786
	37	0.0597	0.0827
	42	0.0498	0.1918
C4	1	1.2718	18.4124
	2	0.1128	-2.8563
	3	0.0747	-0.0565
	6	0.0670	0.6818
	11	0.0583	0.2038
	16	0.0632	0.0618
	21	0.0099	0.0035
	26	0.0547	0.0666
	31	0.0560	0.1220
	36	0.0577	0.1101
	41	0.0551	0.1398
A4	1	-0.3664	-4.3689
	2	0.1140	0.0904
	3	0.1103	-3.0327
	5	0.0948	0.3351
	10	0.1009	0.6754
	15	0.0566	0.3767
	20	0.0571	0.4385
	25	0.0568	0.1859
	30	0.0556	0.3927
	35	0.0558	0.1173
	40	0.0558	0.1646

Position	Sample	$\frac{\Delta_T}{X_c f_{cr}}$	$\left(\frac{1 - X_c}{X_c}\right)\left(\frac{f_{am}}{f_{cr}}\right)$
E2	1	0.3265	3.6163
	2	0.0849	-0.7437
	3	0.0744	0.0315
	5	0.1282	1.1237
	10	0.1387	1.1500
	15	0.1040	1.2026
	20	0.1203	1.3808
	25	0.1142	1.1240
	30	0.1138	0.8535
	35	0.0692	0.4936
	40	0.0735	0.6575
A2	1	0.1049	1.5849
	2	0.0587	0.3203
	3	0.0811	0.7498
	5	0.0679	0.5857
	10	0.0583	0.6089
	15	0.0485	0.5998
	20	0.0479	0.6046
	25	0.0518	0.5259
	30	0.0520	0.3573
	35	0.0359	0.0157
	40	0.0454	0.4079

Resin EX 2 — Molding #16
Melt Temperature: 205.9°C — Mold Temperature: 35°C

Position	Sample	$\frac{\Delta_T}{X_c f_{cr}}$	$\left(\frac{1 - X_c}{X_c}\right)\left(\frac{f_{am}}{f_{cr}}\right)$
E4	1	-0.2374	-3.5766
	2	0.0739	0.3047
	3	0.0733	-1.0304
	6	0.1292	0.1906
	11	0.0610	0.6257
	16	0.1140	0.4285
	21	0.0634	0.0622
	26	0.0541	0.0734
	31	0.0886	0.4216
	36	0.0911	1.0475
	41	0.0842	0.7969
C4	1	-2.162	-30.294
	2	0.0587	-1.5420
	3	0.0778	-0.0395
	4	0.0712	-0.0648
	6	0.0770	0.2443
	11	0.0548	0.5439
	16	0.0500	-0.0313
	21	0.0507	-0.0293
	26	0.0451	0.0568
	31	0.0472	0.2248
	36	0.0507	0.2225
	41	0.0466	0.1843
A4	1	-0.1957	-3.0208
	2	0.0951	0.1883
	3	0.0992	0.9692
	4	0.0890	1.0985
	6	0.0774	0.8197
	11	0.0644	0.3670
	16	0.0606	0.0760
	21	0.0640	0.0553
	26	0.0556	0.1506
	31	0.0699	0.0896
	36	0.0543	0.0007
	41	0.0619	0.0003

Position	Sample	$\frac{\Delta_T}{X_c f_{cr}}$	$\left(\frac{1 - X_c}{X_c}\right)\left(\frac{f'_{am}}{f_{cr}}\right)$
E2	1	0.1182	1.8094
	2	0.3932	3.7261
	3	0.1658	-1.6215
	4	0.0660	-0.0267
	6	0.0977	0.6542
	11	0.0895	0.8263
	16	0.0671	0.1189
	21	0.0526	0.0248
	26	0.0601	0.1743
	31	0.0467	0.0990
	36	0.0641	0.2165
	41	0.0435	0.3298
A2	1	0.1385	1.9382
	2	0.0713	-0.0800
	3	0.0794	0.5598
	5	0.0867	0.7711
	10	0.0631	0.4099
	15	0.0502	0.3018
	20	0.0494	0.3011
	25	0.0503	0.0527
	30	0.0467	0.1238
	35	0.0456	0.2159
	40	0.0517	0.3048

APPENDIX 11

RELATIVE CONTRIBUTIONS OF CRYSTALLINE AND AMORPHOUS PHASES TO TOTAL BIREFRINGENCE

Resin EX 1 — Molding #21
Melt Temperature: 176°C — Mold Temperature: 35°C

Position	Sample	$X_c \Delta_c (10^{-3})$	$(1 - X_c)\Delta_{am} (10^{-3})$
E4	1	6.42	4.23
	2	5.79	6.74
	3	8.19	1.66
	5	6.30	5.81
	10	4.80	1.43
	15	4.87	3.47
	20	6.84	1.50
	25	6.41	1.49
	30	6.15	1.66
	35	6.09	1.54
	40	6.62	1.01
C4	1	3.21	2.16
	2	3.98	6.27
	3	3.93	8.08
	4	5.79	7.81
	6	2.42	8.02
	11	3.03	4.18
	16	3.38	3.66
	21	3.27	3.60
	26	5.35	2.28
	31	4.19	3.19
	36	5.16	2.56
	40	6.33	0.88
A4	1	10.57	-3.07
	2	5.40	3.73
	3	6.28	4.58
	5	4.61	4.85
	10	4.79	4.48
	15	4.96	3.38
	20	6.31	0.90
	25	5.13	2.16
	30	5.40	1.64
	35	4.56	2.10
	40	5.09	1.57

Position	Sample	$X_c \Delta_c (10^{-3})$	$(1 - X_c)\Delta_{am} (10^{-3})$
E2	1	7.00	0.05
	2	5.32	3.23
	3	5.19	2.17
	5	3.88	2.99
	10	4.26	1.79
	15	4.17	1.67
	20	5.40	0.49
	25	4.27	0.83
	30	4.35	0.48
	35	4.93	0.18
	40	4.42	0.48
A2	1	2.76	2.29
	2	4.84	2.71
	3	5.53	2.53
	5	5.99	3.51
	10	3.90	2.68
	15	3.65	1.81
	20	4.61	1.51
	25	5.26	1.40
	30	5.67	1.39
	35	6.38	0.12
	40	6.04	0.46

Resin EX 2
Melt Temperature: 176°C

Molding #12
Mold Temperature: 35°C

Position	Sample	$X_c \Delta_c (10^{-3})$	$(1 - X_c)\Delta_{am} (10^{-3})$
E4	1	1.59	6.95
	2	4.61	0.67
	3	5.18	2.90
	4	5.16	3.00
	7	6.18	1.80
	12	5.55	1.74
	17	6.09	0.41
	22	5.74	0.27
	27	3.91	2.16
	32	6.32	0.08
	37	5.78	0.61
	42	5.66	0.57
C4	1	0.34	7.72
	2	3.42	3.73
	3	4.42	1.69
	6	4.69	1.13
	11	6.40	0.50
	16	6.17	1.06
	21	5.43	0.99
	26	6.41	0.09
	31	6.27	0.23
	36	5.31	0.36
	41	6.13	0.12
A4	1	1.47	9.29
	2	4.67	5.18
	3	3.33	3.47
	5	4.16	3.14
	10	3.52	3.06
	15	5.25	0.25
	20	5.23	0.30
	25	5.61	0.29
	30	5.63	0.17
	35	5.28	0.18
	40	5.71	0.19

Position	Sample	$X_c \Delta_c (10^{-3})$	$(1 - X_c)\Delta_{am} (10^{-3})$
E2	1	2.28	11.48
	2	3.93	2.25
	3	4.87	1.84
	5	3.36	4.62
	10	3.69	5.80
	15	4.23	3.92
	20	3.90	4.78
	25	3.94	4.39
	30	3.58	3.97
	35	4.90	1.37
	40	4.33	1.56
A2	1	4.94	4.66
	2	5.61	0.49
	3	4.07	2.04
	5	4.51	1.16
	10	5.19	0.41
	15	5.02	0.37
	20	5.05	0.30
	25	4.64	0.68
	30	4.39	0.66
	35	6.42	-1.32
	40	5.08	0.02

Resin EX 2
Melt Temperature: 205.9°C

Molding #16
Mold Temperature: 35°C

Position	Sample	$X_c \Delta_c (10^{-3})$	$(1 - X_c)\Delta_{am} (10^{-3})$
E4	1	3.56	6.28
	2	4.62	1.71
	3	5.03	1.79
	6	3.19	4.45
	11	5.55	0.72
	16	3.27	3.63
	21	5.54	0.96
	26	5.88	0.01
	31	3.46	2.22
	36	3.24	2.22
	41	3.55	1.98
C4	1	3.45	5.53
	2	6.67	0.59
	3	4.49	1.98
	4	5.28	1.68
	6	5.01	2.13
	11	6.18	0.09
	16	5.54	0.58
	21	4.16	2.03
	26	6.20	-0.01
	31	5.65	0.25
	36	5.26	0.64
	41	5.73	0.17
A4	1	3.07	6.41
	2	4.89	3.71
	3	4.59	3.83
	4	5.01	3.25
	6	5.23	2.27
	11	6.16	1.18
	16	5.77	0.71
	21	6.12	1.14
	26	6.75	0.20
	31	5.49	1.61
	36	7.06	0.04
	41	6.06	0.89

Position	Sample	$X_c \Delta_c (10^{-3})$	$(1 - X_c)\Delta_{am} (10^{-3})$
E2	1	4.32	5.13
	2	1.00	6.27
	3	2.25	4.65
	4	5.19	1.15
	6	3.92	3.18
	11	4.14	2.73
	16	5.53	1.34
	21	5.91	0.96
	26	6.10	0.69
	31	6.58	0.21
	36	5.59	1.05
	41	6.86	-0.26
A2	1	3.82	5.98
	2	5.66	1.81
	3	4.73	2.23
	5	4.81	2.91
	10	5.70	0.96
	15	6.22	0.68
	20	6.22	0.58
	25	5.91	0.67
	30	6.21	0.21
	35	6.35	0.05
	40	5.15	0.74

APPENDIX 12

PREDICTION OF SONIC MODULUS

Resin EX 1
Melt Temperature: 176°C

Molding #21
Mold Temperature: 35°C

Position	Sample	$X_c(1 - f_{cr})A_{cr}(10^{10})$	$(1 - X_c)(1 - f_{am})A_{am}(10^{10})$	Predicted $E_{or} \times 10^{-10}$ (Pa)	Measured $E_{or} \times 10^{-10}$ (Pa)
E4	1	0.930	7.746	0.115	0.105
	2	0.939	6.423	0.136	0.125
	3	0.889	5.744	0.151	0.140
	5	0.985	4.805	0.173	0.163
	10	1.051	3.256	0.232	0.229
	15	1.058	4.236	0.189	0.181
	20	0.996	3.968	0.202	0.193
	25	1.012	4.373	0.186	0.177
	30	1.029	3.839	0.205	0.198
	35	1.033	4.556	0.179	0.170
	40	1.021	4.258	0.189	0.181
C4	1	1.014	7.305	0.120	0.110
	2	1.031	5.568	0.152	0.142
	3	0.990	4.591	0.179	0.169
	4	0.953	4.087	0.198	0.189
	6	1.097	3.912	0.200	0.194
	11	1.120	3.656	0.209	0.205
	16	1.123	3.632	0.210	0.206
	21	1.137	3.738	0.205	0.200
	26	1.066	3.788	0.206	0.199
	31	1.109	3.598	0.213	0.207
	36	1.092	3.774	0.206	0.198
	41	1.057	3.736	0.209	0.201

Position	Sample	$X_c(1 - f_{cr})A_{cr}(10^{10})$	$(1 - X_c)(1 - f_{am})A_{am}(10^{10})$	Predicted $E_{or} \times 10^{-10}$ (Pa)	Measured $E_{or} \times 10^{-10}$ (Pa)
A4	1	0.745	5.988	0.149	0.135
	2	0.925	5.136	0.165	0.153
	3	0.932	4.883	0.172	0.161
	5	1.012	4.354	0.186	0.178
	10	1.039	3.705	0.211	0.205
	15	1.054	3.976	0.199	0.192
	20	1.013	4.283	0.189	0.180
	25	1.052	4.494	0.180	0.172
	30	1.054	4.544	0.179	0.170
	35	1.089	4.383	0.183	0.175
	40	1.076	4.283	0.187	0.179
E2	1	0.820	7.053	0.127	0.115
	2	0.954	4.607	0.180	0.170
	3	0.976	5.072	0.165	0.155
	5	1.037	5.119	0.162	0.153
	10	1.063	4.808	0.170	0.162
	15	1.089	4.739	0.172	0.163
	20	1.053	4.545	0.179	0.170
	25	1.096	4.405	0.182	0.174
	30	1.098	4.341	0.184	0.176
	35	1.084	4.471	0.180	0.172
	40	1.109	3.891	0.200	0.193
A2	1	1.004	8.057	0.110	0.100
	2	0.959	6.488	0.134	0.123
	3	0.967	5.755	0.149	0.138
	5	0.978	4.318	0.189	0.180
	10	1.076	4.542	0.178	0.170
	15	1.104	4.463	0.180	0.172
	20	1.082	4.138	0.192	0.184
	25	1.057	4.000	0.198	0.191
	30	1.050	4.073	0.195	0.187
	35	1.025	4.086	0.196	0.187
	40	1.039	3.869	0.204	0.196

Resin EX 2
Melt Temperature: 176°C

Molding #12
Mold Temperature: 35°C

Position	Sample	$X_c(1 - f_{cr})A_{cr}(10^{10})$	$(1 - X_c)(1 - f_{am})A_{am}(10^{10})$	Predicted $E_{or} \times 10^{-10}$ (Pa)	Measured $E_{or} \times 10^{-10}$ (Pa)
E4	1	1.124	3.049	0.240	0.240
	2	1.096	3.828	0.203	0.197
	3	1.058	4.894	0.168	0.159
	4	1.060	6.525	0.132	0.122
	7	1.031	4.184	0.192	0.183
	12	1.064	4.265	0.188	0.179
	17	1.057	4.359	0.185	0.176
	22	1.078	3.687	0.210	0.203
	27	1.153	3.375	0.221	0.216
	32	1.076	4.117	0.193	0.183
	37	1.103	4.067	0.193	0.184
	42	1.069	3.865	0.203	0.193
C4	1	1.106	3.953	0.198	0.190
	2	1.018	7.775	0.114	0.104
	3	1.015	5.200	0.161	0.151
	6	1.015	4.282	0.189	0.181
	11	0.987	3.945	0.181	0.172
	16	1.009	4.654	0.177	0.168
	21	1.047	4.662	0.175	0.166
	26	1.021	4.499	0.181	0.172
	31	1.027	4.406	0.184	0.175
	36	1.082	4.306	0.186	0.177
	41	1.066	4.150	0.192	0.183

Position	Sample	$X_c(1 - f_{cr})A_{cr}(10^{10})$	$(1 - X_c)(1 - f_{am})A_{am}(10^{10})$	Predicted $E_{or} \times 10^{-10}$ (Pa)	Measured $E_{or} \times 10^{-10}$ (Pa)
A4	1	1.114	3.522	0.216	0.212
	2	0.989	5.156	0.163	0.152
	3	1.067	7.538	0.116	0.115
	5	1.049	4.619	0.176	0.168
	10	1.114	4.079	0.193	0.186
	15	1.077	4.012	0.197	0.189
	20	1.087	3.869	0.202	0.194
	25	1.082	4.121	0.192	0.184
	30	1.091	3.759	0.206	0.198
	35	1.117	4.060	0.193	0.184
	40	1.108	3.934	0.198	0.189
E2	1	1.097	3.061	0.241	0.240
	2	1.040	5.805	0.146	0.137
	3	1.040	4.814	0.171	0.162
	5	1.115	3.770	0.205	0.200
	10	1.125	3.496	0.216	0.212
	15	1.116	3.225	0.230	0.227
	20	1.130	3.134	0.235	0.232
	25	1.132	3.343	0.224	0.219
	30	1.152	3.634	0.209	0.203
	35	1.117	3.708	0.207	0.200
	40	1.144	3.556	0.213	0.206
A2	1	0.940	3.604	0.220	0.210
	2	0.955	4.824	0.173	0.163
	3	1.026	4.394	0.185	0.176
	5	1.034	4.329	0.187	0.179
	10	1.047	3.942	0.200	0.194
	15	1.044	3.657	0.213	0.206
	20	1.053	3.571	0.216	0.210
	25	1.079	3.696	0.209	0.202
	30	1.101	3.871	0.201	0.193
	35	1.029	4.210	0.191	0.180
	40	1.097	3.545	0.215	0.207

Resin EX 2
Melt Temperature: 205.9°C

Molding #16
Mold Temperature: 35°C

Position	Sample	$X_c(1 - f_{cr})A_{cr}(10^{10})$	$(1 - X_c)(1 - f_{am})A_{am}(10^{10})$	Predicted $E_{or} \times 10^{-10}$ (Pa)	Measured $E_{or} \times 10^{-10}$ (Pa)
E4	1	1.050	3.242	0.233	0.230
	2	1.049	4.504	0.180	0.172
	3	1.042	6.075	0.141	0.131
	6	1.130	4.488	0.178	0.171
	11	1.060	3.688	0.211	0.204
	16	1.152	4.117	0.190	0.183
	21	1.080	4.323	0.185	0.176
	26	1.076	4.245	0.188	0.179
	31	1.171	3.927	0.196	0.189
	36	1.193	3.348	0.220	0.215
	41	1.197	3.384	0.218	0.212
C4	1	1.025	3.696	0.212	0.205
	2	0.925	7.753	0.115	0.105
	3	1.019	5.137	0.163	0.153
	4	1.010	5.047	0.165	0.156
	6	1.060	4.374	0.184	0.176
	11	1.040	3.698	0.211	0.204
	16	1.042	4.459	0.182	0.172
	21	1.047	4.426	0.183	0.173
	26	1.025	4.229	0.190	0.180
	31	1.066	3.829	0.204	0.195
	36	1.087	3.831	0.203	0.194
	41	1.078	3.790	0.205	0.195

Position	Sample	$X_c(1 - f_{cr})A_{cr}(10^{10})$	$(1 - X_c)(1 - f_{am})A_{am}(10^{10})$	Predicted $E_{or} \times 10^{-10}$ (Pa)	Measured $E_{or} \times 10^{-10}$ (Pa)
A4	1	1.047	3.404	0.225	0.220
	2	0.976	5.069	0.165	0.155
	3	1.004	4.078	0.197	0.189
	4	1.006	3.698	0.213	0.206
	6	1.029	3.782	0.208	0.202
	11	1.029	4.053	0.197	0.189
	16	1.063	4.364	0.184	0.176
	21	1.065	4.287	0.187	0.178
	26	1.045	4.101	0.194	0.185
	31	1.096	4.184	0.189	0.181
	36	1.059	4.177	0.191	0.171
	41	1.107	4.091	0.192	0.182
E2	1	0.988	3.422	0.227	0.220
	2	1.087	4.562	0.177	0.168
	3	1.065	6.222	0.137	0.128
	4	0.993	5.135	0.163	0.154
	6	1.079	4.181	0.190	0.183
	11	1.107	3.720	0.207	0.202
	16	1.071	4.309	0.186	0.177
	21	1.025	4.372	0.185	0.176
	26	1.061	4.135	0.193	0.184
	31	1.010	4.132	0.195	0.184
	36	1.099	3.960	0.198	0.189
	41	1.022	3.488	0.222	0.212

Position	Sample	$X_c(1 - f_{cr})A_{cr}(10^{10})$	$(1 - X_c)(1 - f_{am})A_{am}(10^{10})$	Predicted $E_{or} \times 10^{-10}$ (Pa)	Measured $E_{or} \times 10^{-10}$ (Pa)
A2	1	0.982	3.689	0.214	0.205
	2	0.951	5.389	0.158	0.147
	3	1.012	4.430	0.184	0.175
	5	1.034	3.992	0.199	0.192
	10	1.048	4.015	0.198	0.190
	15	1.004	3.918	0.203	0.194
	20	1.012	3.863	0.205	0.196
	25	1.037	4.241	0.190	0.180
	30	1.038	4.013	0.198	0.188
	35	1.029	3.854	0.205	0.195
	40	1.093	3.704	0.209	0.200

APPENDIX 13

PREDICTION OF TENSILE MODULUS

Resin EX 1
Melt Temperature: 176°C

Molding #8
Mold Temperature: 35°C

Position	Sample	$X_c(1 - f_{cr})A_{cr}(10^{10})$	$(1 - X_c)(1 - f_{am})A_{am}(10^{10})$	Predicted $Y \times 10^{-10}$ (Pa)	Measured $Y \times 10^{-10}$ (Pa)
E4	1	0.014	38.734	0.026	0.029
	2	0.014	32.115	0.031	0.042
	3	0.013	28.724	0.035	0.049
	5	0.014	24.024	0.042	0.045
	10	0.015	16.280	0.061	0.041
	15	0.016	21.179	0.047	0.047
	20	0.015	19.840	0.050	0.054
	25	0.015	21.868	0.046	0.058
	30	0.015	19.194	0.052	0.045
	35	0.015	22.784	0.044	0.044
	40	0.015	21.290	0.047	0.051
C4	1	0.015	36.527	0.027	0.013
	2	0.015	27.841	0.036	0.017
	3	0.014	22.953	0.044	0.045
	4	0.014	21.225	0.047	0.067
	6	0.016	19.562	0.051	0.048
	11	0.016	18.285	0.055	0.047
	16	0.016	18.158	0.055	0.052
	21	0.017	18.672	0.054	0.047
	26	0.016	18.939	0.053	0.046
	31	0.016	17.991	0.056	0.059
	36	0.016	18.872	0.053	0.045
	41	0.015	18.680	0.054	0.054

Position	Sample	$X_c(1 - f_{cr})A_{cr}(10^{10})$	$(1 - X_c)(1 - f_{am})A_{am}(10^{10})$	Predicted $Y \times 10^{-10}$ (Pa)	Measured $Y \times 10^{-10}$ (Pa)
A4	1	0.011	29.941	0.033	0.024
	2	0.014	25.683	0.039	0.023
	3	0.014	24.414	0.041	0.021
	5	0.015	21.772	0.046	0.037
	10	0.015	18.527	0.054	0.040
	15	0.015	19.883	0.050	0.038
	20	0.015	21.414	0.047	0.055
	25	0.015	22.470	0.045	0.053
	30	0.015	22.721	0.044	0.051
	35	0.016	21.916	0.046	0.046
	40	0.016	21.418	0.047	0.050
E2	1	0.012	35.269	0.028	0.030
	2	0.014	23.038	0.043	0.029
	3	0.014	25.361	0.039	0.037
	5	0.015	25.597	0.039	0.047
	10	0.016	24.040	0.042	0.052
	15	0.016	23.699	0.042	0.034
	20	0.015	22.728	0.044	0.043
	25	0.016	22.025	0.045	0.045
	30	0.016	21.705	0.046	0.041
	35	0.016	22.355	0.045	0.051
	40	0.016	19.458	0.051	0.051
A2	1	0.015	40.289	0.025	0.027
	2	0.014	32.444	0.031	0.036
	3	0.014	28.776	0.035	0.039
	5	0.014	21.593	0.046	0.039
	10	0.016	22.713	0.044	0.045
	15	0.016	22.317	0.045	0.044
	20	0.016	20.693	0.048	0.048
	25	0.015	20.002	0.050	0.053
	30	0.015	20.365	0.049	0.059
	35	0.015	20.431	0.049	0.057
	40	0.015	19.348	0.052	0.064

Resin EX 2
Melt Temperature: 176°C

Molding #13
Mold Temperature: 35°C

Position	Sample	$X_c(1 - f_{cr})A_{cr}(10^{10})$	$(1 - X_c)(1 - f_{am})A_{am}(10^{10})$	Predicted $Y \times 10^{-10}$ (Pa)	Measured $Y \times 10^{-10}$ (Pa)
E4	1	0.016	15.245	0.066	0.036
	2	0.016	19.140	0.052	0.024
	3	0.015	24.472	0.041	0.034
	4	0.016	32.627	0.031	0.021
	7	0.015	20.919	0.048	0.035
	12	0.016	21.328	0.047	0.032
	17	0.015	21.794	0.046	0.042
	22	0.016	18.436	0.054	0.044
	27	0.017	16.875	0.059	0.056
	32	0.016	20.587	0.049	0.048
	37	0.016	20.337	0.049	0.038
	42	0.016	19.326	0.052	0.038
C4	1	0.016	19.768	0.051	0.030
	2	0.015	38.875	0.026	0.023
	3	0.015	37.261	0.027	0.030
	6	0.015	21.409	0.047	0.042
	11	0.014	22.624	0.044	0.044
	16	0.015	23.270	0.043	0.042
	21	0.015	23.310	0.043	0.033
	26	0.015	22.493	0.044	0.040
	31	0.015	22.029	0.045	0.033
	36	0.016	21.532	0.046	0.041
	41	0.016	20.749	0.048	0.044

Position	Sample	$X_c(1 - f_{cr})A_{cr}(10^{10})$	$(1 - X_c)(1 - f_{am})A_{am}(10^{10})$	Predicted $Y \times 10^{-10}$ (Pa)	Measured $Y \times 10^{-10}$ (Pa)
A4	1	0.016	17.611	0.057	0.058
	2	0.014	25.779	0.039	0.037
	3	0.016	37.694	0.027	0.047
	5	0.015	23.094	0.043	0.045
	10	0.016	20.398	0.049	0.051
	15	0.016	20.061	0.050	0.056
	20	0.016	19.348	0.052	0.053
	25	0.016	20.606	0.049	0.045
	30	0.016	18.795	0.053	0.046
	35	0.016	20.302	0.049	0.046
	40	0.016	19.673	0.051	0.047
E2	1	0.016	15.306	0.065	0.028
	2	0.015	29.025	0.034	0.019
	3	0.015	24.071	0.042	0.031
	5	0.016	18.848	0.053	0.043
	10	0.016	17.481	0.057	0.031
	15	0.016	16.126	0.062	0.033
	20	0.017	15.669	0.064	0.034
	25	0.017	16.715	0.060	0.033
	30	0.017	18.172	0.055	0.033
	35	0.016	18.543	0.054	0.037
	40	0.017	17.782	0.056	0.039
A2	1	0.014	18.019	0.056	0.038
	2	0.014	24.122	0.041	0.020
	3	0.015	21.972	0.046	0.045
	5	0.015	21.647	0.046	0.040
	10	0.015	19.713	0.051	0.039
	15	0.015	18.286	0.055	0.044
	20	0.015	17.857	0.056	0.049
	25	0.016	18.481	0.054	0.045
	30	0.016	19.355	0.052	0.044
	35	0.015	21.052	0.048	0.046
	40	0.016	17.725	0.056	0.049

Resin EX 2
Melt Temperature: 205.9°C

Molding #17
Mold Temperature: 35°C

Position	Sample	$X_c(1 - f_{cr})A_{cr}(10^{10})$	$(1 - X_c)(1 - f_{am})A_{am}(10^{10})$	Predicted $Y \times 10^{-10}$ (Pa)	Measured $Y \times 10^{-10}$ (Pa)
E4	1	0.015	16.211	0.062	0.033
	2	0.015	22.521	0.044	0.023
	3	0.015	30.376	0.033	0.036
	6	0.017	22.442	0.045	0.042
	11	0.016	18.441	0.054	0.044
	16	0.017	20.584	0.049	0.053
	21	0.016	21.615	0.046	0.054
	26	0.016	21.227	0.047	0.046
	31	0.017	19.635	0.051	0.053
	36	0.017	16.739	0.060	0.049
	41	0.018	16.923	0.059	0.057
C4	1	0.015	18.479	0.054	0.047
	2	0.014	38.764	0.026	0.029
	3	0.015	25.686	0.039	0.053
	4	0.015	25.235	0.040	0.036
	6	0.016	21.870	0.046	0.042
	11	0.015	18.492	0.054	0.049
	16	0.015	22.296	0.045	0.051
	21	0.015	22.132	0.045	0.049
	26	0.015	21.147	0.047	0.042
	31	0.016	19.145	0.052	0.046
	36	0.016	19.153	0.052	0.052
	41	0.016	18.950	0.053	0.056

Position	Sample	$X_c(1 - f_{cr})A_{cr}(10^{10})$	$(1 - X_c)(1 - f_{am})A_{am}(10^{10})$	Predicted $Y \times 10^{-10}$ (Pa)	Measured $Y \times 10^{-10}$ (Pa)
A4	1	0.015	17.021	0.059	0.035
	2	0.014	25.344	0.039	0.027
	3	0.015	20.394	0.049	0.034
	4	0.015	18.492	0.054	0.036
	6	0.015	18.913	0.053	0.038
	11	0.015	20.264	0.049	0.042
	16	0.016	21.819	0.046	0.043
	21	0.016	21.434	0.047	0.044
	26	0.015	20.505	0.049	0.045
	31	0.016	20.920	0.048	0.038
	36	0.016	20.886	0.048	0.043
	41	0.016	20.458	0.049	0.048
E2	1	0.014	17.113	0.058	0.049
	2	0.016	22.813	0.044	0.036
	3	0.016	31.114	0.032	0.056
	4	0.015	25.678	0.039	0.048
	6	0.016	20.905	0.048	0.048
	11	0.016	18.599	0.054	0.048
	16	0.016	21.548	0.046	0.049
	21	0.015	21.864	0.046	0.046
	26	0.016	20.674	0.048	0.046
	31	0.015	20.660	0.048	0.049
	36	0.016	19.799	0.051	0.050
	41	0.015	17.443	0.057	0.054

Position	Sample	$X_c(1 - f_{cr})A_{cr}(10^{10})$	$(1 - X_c)(1 - f_{am})A_{am}(10^{10})$	Predicted $Y \times 10^{-10}$ (Pa)	Measured $Y \times 10^{-10}$ (Pa)
A2	1	0.014	18.445	0.054	0.041
	2	0.014	26.946	0.037	0.022
	3	0.015	22.148	0.045	0.029
	5	0.015	19.963	0.050	0.021
	10	0.015	20.074	0.050	0.022
	15	0.015	19.592	0.051	0.037
	20	0.015	19.316	0.052	0.038
	25	0.015	21.207	0.047	0.039
	30	0.015	20.066	0.050	0.038
	35	0.015	19.273	0.052	0.035
	40	0.016	18.519	0.054	0.036

APPENDIX 14

REPRODUCIBILITY MEASUREMENTS

The measurements of density, sonic modulus, birefringence, and tensile properties are repeated employing moldings from the two resins. Representative results are tabulated below.

Resin EX 1
Melt Temperature: 176°C

Molding #6
Mold Temperature: 35°C

Density

	Density (g/cc)		
Sample	E4	C4	A4
1	0.9395	0.9399	0.9377
2	0.9403	0.9408	0.9396
3	0.9410	0.9419	0.9409
4	0.9436	0.9433	0.9433
5	0.9443	0.9446	0.9439
6	0.9446	0.9453	0.9444
7	0.9450	0.9459	0.9454
10	0.9465	0.9472	0.9464
20	0.9477	0.9492	0.9483
30	0.9485	0.9497	0.9500
40	0.9494	0.9515	0.9522

Sonic Modulus

	Position					
	E4		C4		A4	
Sample	C (km/s)	$E_{or} x10^{-10}$ (Pa)	C (km/s)	$E_{or} x10^{-10}$ (Pa)	C (km/s)	$E_{or} x10^{-10}$ (Pa)
1	1.27	0.152	1.19	0.133	1.29	0.156
2	1.29	0.157	1.22	0.140	1.29	0.156
3	1.47	0.203	1.78	0.298	1.38	0.179
4	1.41	0.188	1.22	0.140	1.33	0.167
5	1.36	0.175	1.30	0.160	1.40	0.185
6	1.36	0.175	1.40	0.185	1.34	0.170
7	1.40	0.185	1.47	0.204	1.38	0.180
10	1.31	0.162	1.36	0.175	1.42	0.191
15	1.40		1.46		1.33	
20	1.42	0.191	1.33	0.168	1.34	0.170
25	1.31		1.43		1.38	
30	1.41	0.189	1.40	0.186	1.38	0.181
35	1.39		1.31		1.46	
40	1.48	0.208	1.39	0.184	1.34	0.171

Birefringence

	$\Delta_T \times 10^3$		
Sample	E4	C4	A4
1	6.47	6.68	8.90
2	8.64	7.40	10.85
3	10.83	8.41	10.91
4	10.66	8.95	11.22
5	7.26	8.77	10.95
7	6.48	7.42	10.85
10	5.75	6.95	9.30
15	6.56	6.87	7.62
20	6.32	6.87	6.85
25	5.96	7.75	7.62
30	6.48	7.83	7.08
35	6.64	8.00	6.32
40	6.64	8.00	5.82

Mechanical Properties

Sample	Position C4			
	$E \times 10^{-10}$ (Pa)	$\sigma_{ny} \times 10^{-6}$ (Pa)	ε_y (%)	ε_b (%)
1	0.028	14.6	7.50	85.0
2	0.044	20.8	32.5	92.5
3	0.049	20.1	50.0	142.5
4	0.039	20.6	45.0	145.0
5	0.064	20.6	50.0	90.0
6	0.036	20.7	42.5	90.0
7	0.051	22.0	45.0	100.0
10	0.055	20.2	35.0	62.5
15	0.048	21.2	40.0	70.0
20	0.034	20.2	40.0	60.0
25	0.027	20.9	40.0	55.0
30	0.039	20.0	35.0	55.0
35	0.059	20.5	22.5	37.5
40	0.042	21.1	31.5	50.0

Resin EX 2
Melt Temperature: 176°C

Molding #21
Mold Temperature: 35°C

Density

Sample	Density (g/cc)		
	E4	C4	A4
1	0.9257	0.9400	0.9390
2	0.9420	0.9410	0.9405
3	0.9449	0.9438	0.9428
5	0.9484	0.9462	0.9452
7	0.9487	0.9475	0.9471
10	0.9504	0.9474	0.9488
20	0.9520	0.9503	0.9519
30	0.9540	0.9546	0.9537
40	0.9547	0.9551	0.9553

Sonic Modulus

	Position					
	E4		C4		A4	
Sample	C (km/s)	$E_{or} \times 10^{-10}$ (Pa)	C (km/s)	$E_{or} \times 10^{-10}$ (Pa)	C (km/s)	$E_{or} \times 10^{-10}$ (Pa)
1	1.50	0.208	1.55	0.226	1.45	0.197
2	1.20	0.136	1.39	0.182	1.33	0.166
3	1.41	0.188	1.38	0.180	1.44	0.196
4	1.37		1.38		1.44	
5	1.36	0.175	1.40	0.186	1.42	0.191
6	1.38		1.49		1.43	
7	1.44	0.197	1.46	0.202	1.37	0.178
10	1.41	0.189	1.54	0.225	1.32	0.165
15	1.40		1.53		1.38	
20	1.35	0.174	1.48	0.208	1.38	0.181
25	1.43		1.39		1.45	
30	1.50	0.215	1.51	0.218	1.35	0.174
35	1.40		1.38		1.39	
40	1.47	0.206	1.49	0.212	1.42	0.193

Birefringence

	$\Delta_T \times 10^3$		
Sample	E4	C4	A4
1	13.80	9.60	16.24
2	8.48	6.51	8.89
3	9.06	6.71	8.78
4	8.77	7.10	8.08
5	11.19	7.02	9.04
7	8.51	7.26	9.49
10	7.10	7.67	9.50
15	6.48	8.17	8.25
20	5.82	7.50	5.53
25	5.89	6.48	5.89
30	6.04	6.64	5.75
35	5.89	5.39	5.26
40	5.53	5.82	5.89

Mechanical Properties

	Position C4			
Sample	Y x 10^{-10} (Pa)	σ_{ny} x 10^{-6} (Pa)	ε_y (%)	ε_b (%)
1	0.049	12.6	7.50	150.0
2	0.044	26.0	20.0	380.0
3	0.092	23.2	25.0	125.0
4	0.092	25.4	27.5	120.0
5	0.088	23.6	25.0	75.0
6	0.088	24.5	20.0	52.5
7	0.041	22.4	25.0	71.0
10	0.075	22.9	30.0	77.5
15	0.054	23.4	22.5	56.0
20	0.046	23.9	25.0	52.5
25	0.040	24.1	27.5	60.0
30	0.041	25.0	30.0	60.0
40	0.046	25.9	22.5	25.0

Resin EX 2
Melt Temperature: 205.9°C

Molding #14
Mold Temperature: 35°C

Density

	Density (g/cc)		
Sample	E4	C4	A4
1	0.9359	0.9408	0.9402
2	0.9430	0.9436	0.9421
3	0.9459	0.9449	0.9448
5	0.9483	0.9482	0.9459
7	0.9511	0.9501	0.9472
10	0.9504	0.9498	0.9477
20	0.9515	0.9519	0.9509
30	0.9539	0.9528	0.9533
40	0.9552	0.9555	0.9552

Sonic Modulus

	Position					
	E4		C4		A4	
Sample	C (km/s)	$E_{or} x10^{-10}$ (Pa)	C (km/s)	$E_{or} x10^{-10}$ (Pa)	C (km/s)	$E_{or} x10^{-10}$ (Pa)
1	1.50	0.211	1.53	0.220	1.45	0.198
2	1.29	0.157	1.34	0.169	1.35	0.172
3	1.48	0.207	1.49	0.210	1.34	0.170
4	1.47		1.38		1.40	
5	1.38	0.181	1.48	0.208	1.48	0.207
6	1.40		1.50		1.38	
7	1.41	0.189	1.36	0.176	1.40	0.186
10	1.36	0.176	1.44	0.197	1.39	0.183
15	1.36		1.46		1.36	
20	1.41	0.189	1.44	0.197	1.42	0.192
25	1.42		1.47		1.53	
30	1.44	0.198	1.29	0.159	1.47	0.206
35	1.47		1.38		1.52	
40	1.46	0.204	1.50	0.215	1.44	0.198

Birefringence

	$\Delta_T \times 10^3$		
Sample	E4	C4	A4
1	14.24	8.82	18.66
2	12.20	7.81	11.64
3	10.54	6.95	10.61
4	12.19	6.56	10.90
5	13.13	6.87	10.57
7	12.19	6.56	8.36
10	10.99	6.64	8.44
15	10.42	5.46	7.47
20	9.67	5.96	7.71
25	9.95	5.67	6.92
30	7.83	6.26	6.47
35	5.39	6.64	6.02
40	55.26	6.32	5.89

Mechanical Properties

	Position C4			
Sample	Y x 10^{-10} (Pa)	σ_{ny} x 10^{-6} (Pa)	ε_y (%)	ε_b (%)
1	0.041	16.9	10.0	315.0
2	0.031	24.5	20.0	108.5
3	0.052	25.8	25.0	80.0
4	0.049	24.8	25.0	57.5
5	0.055	26.4	25.0	55.0
6	0.046	24.6	25.0	55.0
7	0.060	24.9	25.0	55.0
10	0.062	25.6	25.0	50.0
15	0.062	25.7	26.0	55.0
20	0.075	24.8	26.0	55.0
25	0.060	25.0	26.0	55.0
30	0.074	25.4	27.5	57.5
35	0.073	25.5	26.0	62.5
40	0.057	25.7	26.5	55.5

APPENDIX 15

KNIFE-EFFECTS, CORRECTION FACTORS, AND ERROR ANALYSIS

This appendix is divided into three sections. The first section (A.15.1) documents the correction factors used in some of the techniques to account for the influence of the cutting action of the microtome knife. The second section (A.15.2) documents the correction factors used in the calculation of the orientation functions of the crystallographic a, b, and c-axes. The third section (A.15.3) presents the error analysis involved in the various measurements.

A.15.1 Knife-Effects

Although precautionary measures were taken to minimize knife-effects during sample preparation, it was evident that the cutting action of the knife would affect the measurements made on the microtomed sections. Previous studies have attempted to evaluate the influence of the knife-effect on the measurements of density and birefringence using annealed polystyrene compression moldings (120, 178). Furthermore, the evaluation of knife-effects on the measurement of birefringence in polyethylene microtomed sections is difficult since one must attempt to separate the contributions due to the knife and the polycrystalline character of polyethylene. Consequently, while acknowledging a knife-effect, the polyethylene birefringence results were left uncorrected. However, in the present study, an attempt was made

to evaluate the influence of the knife-effect on microtomed polyethylene sections, employing the sonic velocity method.

Compression-molded samples with different densities (crystallinities) were prepared by employing the procedure described in Section 5.3.5. The density and sonic velocity of each specimen were measured according to the procedures described in Sections 5.3.3 and 5.3.4, respectively. Density and sonic velocity measurements were made on both un-microtomed and microtomed specimens. The results are summarized in Table A.15.1. The standard deviations pertaining to the measurements on both un-microtomed and microtomed compression-molded samples, for each sample-set, are indicated in brackets. For the un-microtomed thin films, each sample-set constitutes four independent specimens, while for the thin films obtained by microtoming, each sample-set contains seven independent specimens. The results of sonic modulus and crystalline volume fraction for both un-microtomed and microtomed specimens are plotted as shown in Figure A.15.1. It can be seen that the sonic modulus of the microtomed sections is lower than that of the un-microtomed sections. This may be attributed to void formation during microtoming, which tends to lower the density and/or sonic velocity observed for the microtomed specimen.

A linear regression was performed on the two sets of data which yielded the following expressions:

for the un-microtomed sections,

$$E_{um} = (- 0.168 + 0.587\ X_c) \times 10^{10}\ Pa$$

TABLE A.15.1. Summary of Results for Studying Knife-Effects

	Sample Set	Density ρ (g/cc)	Vol. Fract. X_c	Sonic Velocity C (km/sec)	Sonic Modulus $E_s \times 10^{10}$ (Pa)
Un-microtomed	A	0.9344 (±0.10%)	0.5407	1.273 (±0.8%)	0.151
	B	0.9429 (±0.06%)	0.5993	1.378 (±0.8%)	0.179
	C	0.9514 (±0.17%)	0.6579	1.537 (±3%)	0.225
	D	0.9598 (±0.02%)	0.7159	1.613 (±3.8%)	0.250
Microtomed	E	0.9450 (±0.21%)	0.6183	1.422 (±5.7%)	0.191
	F	0.9486 (±0.27%)	0.6385	1.444 (±4.1%)	0.198
	G	0.9530 (±0.19%)	0.6690	1.492 (±3.7%)	0.212
	H	0.9585 (±0.06%)	0.7066	1.547 (±3.8%)	0.229

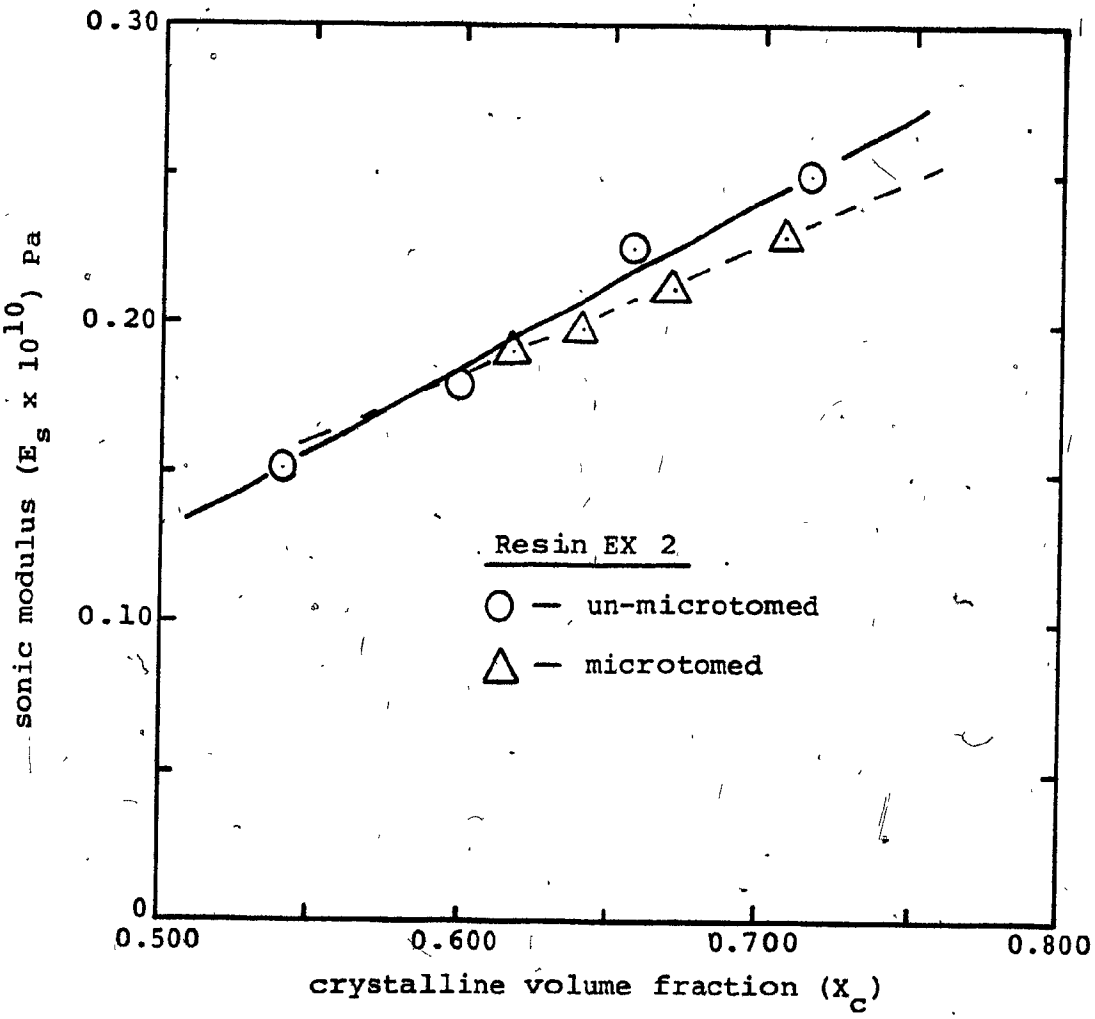


FIGURE A.15.1. Plot of Sonic Modulus of Compression Molded Samples Versus Crystalline Volume Fraction

and for the microtomed sections,

$$E_m = (- 0.079 + 0.436\ X_c) \times 10^{10}\ Pa$$

where E_{um} and E_m are the sonic modulus pertaining to the unmicrotomed and microtomed sections, respectively, in (Pa), and X_c is the crystalline volume fraction. The regression coefficients obtained for the two expressions were 0.994 and 0.999, respectively.

Since the density of the microtomed sections from the injection moldings fall within the range (0.9452-0.9559 g/cc), the "negative" contribution of the knife-effect to the sonic modulus was estimated to vary from 0.58% to 6.8% of the measured values. Therefore, in order to simplify the correction due to the knife-effect, an average value of 3.7% of the observed sonic modulus was used. That is, the measured sonic modulus was multiplied by the factor 1.037 to account for the knife-effect.

Furthermore, previous density measurements (178) on annealed compression-molded polyethylene samples, before and after microtoming, have shown that the microtomed sections exhibited slightly lower density and that a correction factor of 0.0044 g/cc must be added to the density of microtomed sections cut from the injection moldings. Due to the very small magnitude of this correction factor, it was not applied in the present study.

A.15.2 Correction of the Azimuthal Intensity, $I(\psi)$, Distribution Data Corresponding to the (200) and (020) Reflected Planes

Since the azimuthal intensity distributions, $I(\psi)$, as obtained from radial scans on a flat-film photograph, gives an apparent $\overline{\cos^2\psi_{hkl}}$, a suitable correction must be made in order to obtain the total orientation sphere surface (137, 138). The correction factors derived for the (200) and (020) reflected planes are as follows:

For the (200) reflected plane, the Hermans' orientation function (f) is defined as

$$f_{200} = (3\,\overline{\cos^2\alpha} - 1)/2 \qquad \text{(A.15-1)}$$

where α is the angle between the (200) plane normal and the stretch (or flow) direction.

Polanyi's equation from spherical trigonometry gives

$$\cos\alpha = \cos\theta_{200} \cdot \sin\psi_{200} \qquad \text{(A.15-2)}$$

where θ_{200} is the Bragg angle for the (200) plane, and ψ_{200} is the azimuthal angle obtained from a flat-film photograph.

Taking averaged values and squaring, Equation (A.15-2) gives,

$$\overline{\cos^2\alpha} = \cos^2\theta_{200} \cdot \overline{\sin^2\psi_{200}} \qquad \text{(A.15-3)}$$

where $\overline{\sin^2\psi_{200}}$ is defined as,

$$\overline{\sin^2\psi_{200}} = \frac{\int_0^{\pi/2} I(\psi)_{200}\ \sin^2\psi_{200}\ \cos\psi_{200}\ \cdot\ d\psi_{200}}{\int_0^{\pi/2} I(\psi)_{200}\ \cos\psi_{200}\ \cdot\ d\psi_{200}} \qquad \text{(A.15-4)}$$

From Equation (A.15-2), one obtains by rearrangement,

$$\sin\psi_{200} = \frac{\cos\alpha}{\cos\theta_{200}} \qquad \text{(A.15-5)}$$

Similarly, from Equation (A.15-3), one obtains,

$$\overline{\sin^2\psi_{200}} = \frac{\overline{\cos^2\alpha}}{\cos^2\theta_{200}} \qquad \text{(A.15-6)}$$

Also, differentiating both sides of Equation (A.15-2) gives,

$$-\sin\alpha\ \cdot\ d\alpha = \cos\theta_{200}\ \cdot\ \cos\psi_{200}\ \cdot\ d\psi_{200} \qquad \text{(A.15-7)}$$

By substituting Equations (A.15-5), (A.15-6), and (A.15-7) into Equation (A.15-4), one obtains,

$$\frac{\overline{\cos^2\alpha}}{\cos^2\theta_{200}} = \frac{\int I(\alpha)\ \frac{\cos^2\alpha}{\cos^2\theta_{200}}\left(-\frac{\sin\alpha}{\cos\theta_{200}}\right)d\alpha}{\int I(\alpha)\left(-\frac{\sin\alpha}{\cos\theta_{200}}\right)d\alpha} \qquad \text{(A.15-8)}$$

Substituting the limits,

at $\psi = 90^\circ$, $\alpha = \theta_{200}$

and $\psi = 0^\circ$, $\alpha = \pi/2$

one obtains

$$\overline{\cos^2\alpha} = \frac{\int_{\alpha=\theta_{200}}^{\alpha=\pi/2} I(\alpha)\,\cos^2\alpha \cdot \sin\alpha \cdot d\alpha}{\int_{\alpha=\theta_{200}}^{\alpha=\pi/2} I(\alpha)\cdot \sin\alpha \cdot d\alpha} \qquad \text{(A.15-9)}$$

Now, in order to complete the orientation sphere one must obtain $\overline{\cos^2\alpha}$, according to Equation (A.15-9). However, since one cannot obtain the intensity distributions for weak reflections on a flat-film X-ray pattern, between $\alpha = \theta$ and $\alpha = 0^\circ$, one must extrapolate the $I(\psi)$ values obtained by azimuthal scans on the film by setting $I(\alpha)$ equal to $I(\theta)$ in this range. The combined procedure would then yield $\overline{\cos^2\alpha}$ as expressed by Equation (A.15-9). Therefore, to compute $\overline{\cos^2\alpha}$ according to Equation (A.15-9), one must compute,

$$\overline{\cos^2\alpha} = \frac{\int_0^{\theta} I(\theta_{200})\,\cos^2\alpha\cdot\sin\alpha\cdot d\alpha + \int_{\theta}^{\pi/2} I(\alpha)\,\cos^2\alpha\cdot\sin\alpha\cdot d\alpha}{\int_0^{\theta} I(\theta_{200})\,\sin\alpha\cdot d\alpha + \int_{\theta}^{\pi/2} I(\alpha)\,\sin\alpha\cdot d\alpha}$$

(A.15-10)

where $I(\theta_{200}) = I(\alpha = 0^\circ) = I(\psi = 90^\circ)$. By assuming $I(\theta_{200}) = I(\alpha = 0^\circ) = I(\psi = 90^\circ)$ = constant, between the range $\alpha = 0^\circ$ to

$\alpha = \theta^{o}_{200}$, then Equation (A.15-10) simplifies to give

$$\overline{\cos^2\alpha} = \frac{I(\theta_{200}) \int_0^{\theta} \cos^2\alpha \cdot \sin\alpha \cdot d\alpha + \int_{\theta}^{\pi/2} I(\alpha)\, \cos^2\alpha \cdot \sin\alpha \cdot d\alpha}{I(\theta_{200}) \int_0^{\theta} \sin\alpha \cdot d\alpha + \int_{\theta}^{\pi/2} I(\alpha)\, \sin\alpha \cdot d\alpha} \qquad \text{(A.15-11)}$$

that is,

$$\overline{\cos^2\alpha} = \frac{I(\theta_{200}) \left[- \frac{\cos^{m+1}\alpha}{m+1} \right]_0^{\theta} + \int_{\theta}^{\pi/2} I(\alpha)\, \cos^2\alpha \cdot \sin\alpha \cdot d\alpha}{I(\theta_{200}) \left[- \cos\alpha \right]_0^{\theta} + \int_{\theta}^{\pi/2} I(\alpha)\, \sin\alpha \cdot d\alpha} \qquad \text{(A.15-12)}$$

where $m = 2$, so that,

$$\overline{\cos^2\alpha} = \frac{\frac{1}{3}\left[1 - \cos^3\theta_{200}\right] I(\theta_{200}) + \int_{\theta}^{\pi/2} I(\alpha)\, \cos^2\alpha \cdot \sin\alpha \cdot d\alpha}{(1 - \cos\theta_{200})\, I(\theta_{200}) + \int_{\theta}^{\pi/2} I(\alpha) \cdot \sin\alpha \cdot d\alpha} \qquad \text{(A.15-13)}$$

For the (200) plane, $\theta_{200} = 12.04^{o}$, so that,

$$\overline{\cos^2\alpha} = \frac{0.0214\, I(\theta_{200}) + \int_{\theta}^{\pi/2} I(\alpha)\, \cos^2\alpha \cdot \sin\alpha \cdot d\alpha}{0.0219\, I(\theta_{200}) + \int_{\theta}^{\pi/2} I(\alpha)\, \sin\alpha \cdot d\alpha} \qquad \text{(A.15-14)}$$

In terms of $I(\psi)$, one obtains

$$\overline{\cos^2\alpha} = \frac{0.0214\, I(\psi_{200}-90^\circ) + \int_{0}^{\pi/2} I(\psi)_{200}\, \cos^2\psi_{200} \cdot \sin\psi_{200} \cdot d\psi_{200}}{0.0219\, I(\psi_{200}-90^\circ) + \int_{0}^{\pi/2} I(\psi)_{200}\, \sin\psi_{200} \cdot d\psi_{200}} \qquad \text{(A.15-15)}$$

Similarly, for the (020) plane, $\theta_{020} = 18.29^\circ$ and one obtains

$$\overline{\cos^2\beta} = \frac{0.0480\, I(\theta_{020}) + \int_{\theta}^{\pi/2} I(\alpha)\, \cos^2\alpha \cdot \sin\alpha \cdot d\alpha}{0.0505\, I(\theta_{020}) + \int_{\theta}^{\pi/2} I(\alpha)\, \sin\alpha \cdot d\alpha} \qquad \text{(A.15-16)}$$

and in terms of $I(\psi)$, one obtains

$$\overline{\cos^2\beta} = \frac{0.0480\, I(\psi_{020}-90^\circ) + \int_{0}^{\pi/2} I(\psi)_{020}\, \cos^2\psi_{020} \cdot \sin\psi_{020} \cdot d\psi_{020}}{0.0505\, I(\psi_{020}-90^\circ) + \int_{0}^{\pi/2} I(\psi)_{020}\, \sin\psi_{020} \cdot d\psi_{020}} \qquad \text{(A.15-17)}$$

Therefore, it is apparent that the region not sampled comprises 2% for the (200) plane and 5% for the (020) plane of the total orientation sphere surface. For simplicity, the corrected averaged cosine squared values pertaining to the (200) and (020) reflected planes are given as:

For the (200) plane,

$$\overline{\cos^2\alpha} = 1.02\ \overline{\sin^2\psi_{200}} \qquad \text{(A.15-18)}$$

and for the (020) plane,

$$\overline{\cos^2\beta} = 1.05\ \overline{\sin^2\psi_{020}} \qquad \text{(A.15-19)}$$

where $\overline{\sin^2\psi_{200}}$ and $\overline{\sin^2\psi_{020}}$ are obtained by azimuthal scans of the (200) and (020) reflected planes, respectively.

A.15.3 Error Analysis

If a calculated result, y, is dependent on the variables $x_1, x_2, \ldots, x_n$, then the uncertainty, ε_y, in the calculated result is given by:

$$\varepsilon_y = \left[\left(\frac{\partial y}{\partial x_1}\varepsilon_1\right)^2 + \left(\frac{\partial y}{\partial x_2}\varepsilon_2\right)^2 + \ldots \left(\frac{\partial y}{\partial x_n}\varepsilon_n\right)^2\right]^{0.5}$$

where $\varepsilon_1, \varepsilon_2, \ldots, \varepsilon_n$ are the uncertainties in the variables $x_1, x_2, \ldots, x_n$.

The above equation is applied to the appropriate expres-

sions employed in the calculation of the various measured quantities shown in the following sections.

A.15.3.1 Density

The experimental errors in the various measured quantities were estimated to be:

Variable	Error
Float density	0.1%
Float and sample position	0.1%
Temperature	±0.1%

$$\text{Density of PE sample} = \rho_s = \rho_T + \frac{(\rho_B - \rho_T)(h_T - h_B)}{(h_T - h_B)}$$

$$\varepsilon_{\rho_s} = \left[\left(\left\{ 1 + \frac{(h_T - h_s)}{(h_T - h_B)} (-\rho_T) \right\} \varepsilon_{\rho_T} \right)^2 + \left\{ \frac{(h_T - h_s)}{(h_T - h_B)} \rho_B \varepsilon_{\rho_B} \right\}^2 \right.$$

$$+ \left\{ \frac{(\rho_B - \rho_T)}{(h_T - h_B)} \varepsilon_{(h_T - h_s)} \right\}^2$$

$$\left. + \left\{ - \frac{(\rho_B - \rho_T)(h_T - h_s)}{(h_T - h_B)} \varepsilon_{(h_T - h_s)} \right\}^2 \right]^{1/2}$$

$$\varepsilon_{\rho_s} = \left[\left(\left\{ 1 + \frac{5}{11} (-0.955) \right\} 0.000955 \right)^2 + \left(\frac{5}{11} (0.965)(0.000965) \right)^2 + \left\{ \frac{(0.01)(0.005)}{11} \right\}^2 + \left\{ \frac{(0.01)(5)(0.011)}{121} \right\}^2 \right]^{1/2}$$

$\varepsilon = 5.5 \times 10^{-4}$ g/cm^3

% Density error = 0.05%

A.15.3.2 Sonic Modulus

The experimental errors in the various measured quantities were estimated to be:

Variable	Error
Sonic velocity (C)	1%
Density (ρ_s)	0.05%

Sonic modulus, $E = \rho_s C^2$

$$\varepsilon_E = \left[(C^2 \cdot \varepsilon_{\rho_s})^2 + (2 C \cdot \rho_s \cdot \varepsilon_C)^2 \right]^{1/2}$$

$$\varepsilon_E = \left[\left((1.560)^2 (0.0005) \right)^2 + \left(2(1.56)(0.9448)(0.01) \right)^2 \right]^{1/2}$$

$\varepsilon_E = 0.0295 \times 10^{10}$ dynes/cm^2 or 0.00295×10^{10} Pa

Percent error = 1.28%

The reproducibility of the sonic velocity measurement was found to be 3.93%.

A.15.3.3 Birefringence

The experimental errors in the various measured quantities were estimated to be:

Variable	Error
Phase difference (R_o)	7.0×10^{-5} μm
Thickness (t)	2.5 μm

Birefringence, $\Delta n = \frac{R_o}{t}$

$$\varepsilon_{\Delta n} = \left[\left(\frac{1}{t} \cdot \varepsilon_{R_o} \right)^2 + \left(- \frac{R_o}{t^2} \varepsilon_t \right)^2 \right]^{1/2}$$

$$\varepsilon_{\Delta n} = \left[\left(\frac{1}{(45.7)} (7.0 \times 10^{-5}) \right)^2 + \left(- \frac{(284.65 \times 10^{-3})}{(45.7)^2} (2.5) \right)^2 \right]^{1/2}$$

$$\varepsilon_{\Delta n} = 0.341 \times 10^{-3}$$

$$\text{Percent error} = \frac{0.341 \times 10^{-3}}{6.23 \times 10^{-3}} \times 100$$

Percent error = 5.5%

The reproducibility of the birefringence measurement was found to be 2.7%.

A.15.3.4 X-Ray Diffraction

The experimental errors in the various measured quantities for the measurement of $\overline{\cos^2\alpha}$ were estimated to be:

Variable	Error
Azimuthal intensity, $I(\psi)$	0.5 mm
Azimuthal angle, (ψ)	0.05°

$$\overline{\cos^2\alpha} = \frac{0.0214\ I(\psi_{200}-90^\circ) + \int_0^{0.05^\circ} I(\psi)_{200}\cos^2\psi_{200}\cdot\sin\psi_{200}\cdot d\psi_{200}}{0.0219\ I(\psi_{200}-90^\circ) + \int_0^{0.05^\circ} I(\psi)_{200}\sin\psi_{200}\cdot d\psi_{200}}$$

that is,

$$\overline{\cos^2\alpha} = \frac{0.0214\ I(\psi_{200}-90^\circ) + I(\psi)_{200}\left[-\frac{\cos^{m+1}\psi_{200}}{(m+1)}\right]_0^{0.05^\circ}}{0.0219\ I(\psi_{200}-90^\circ) + I(\psi)_{200}\left[-\cos\psi_{200}\right]_0^{0.05^\circ}}$$

where $m = 2$.

Substituting the limits and simplifying, gives

$$\overline{\cos^2\alpha} = 0.978$$

Error in measurement of $\overline{\cos^2\alpha} = 1 - 0.978 = 0.022$

Percent error = 2.2%

Similarly, the experimental errors in the various measured

quantities for the measurement of $\overline{\cos^2\beta}$ are equal to that shown for $\overline{\cos^2\alpha}$. However,

$$\overline{\cos^2\beta} = \frac{0.0480\, I(\psi_{020}=90^\circ) + \int_0^{0.05^\circ} I(\psi)_{020}\, \cos^2\psi_{020} \cdot \sin\psi_{020} \cdot d\psi_{020}}{0.0505\, I(\psi_{020}=90^\circ) + \int_0^{0.05^\circ} I(\psi)_{020}\, \sin\psi_{020} \cdot d\psi_{020}}$$

so that,

$$\overline{\cos^2\beta} = \frac{0.0480\, I(\psi_{020}=90^\circ) + I(\psi)_{020}\left[-\frac{\cos^{m+1}\psi_{020}}{(m+1)}\right]_0^{0.05^\circ}}{0.0505\, I(\psi_{020}=90^\circ) + I(\psi)_{020}\left[-\cos\psi_{020}\right]_0^{0.05^\circ}}$$

where $m = 2$.

Substituting the limits and simplifying, gives

$$\overline{\cos^2\beta} = 0.951$$

Error in measurement of $\overline{\cos^2\beta} = 1 - 0.951 = 0.0495$

Percent error = 4.95% ≈ 5%

Therefore, the errors in the measurements of f_a and f_b pertaining to the (200) and (020) reflected planes are estimated to be 2.2% and 5%, respectively. The reproducibility of the azimuthal scans for the (200) and (020) reflected planes was found to be 3.5% and 8.2%, respectively.

A.15.3.5 Infrared Spectroscopy

The experimental errors in the various measured quantities for the measurement of dichroic ratio were estimated to be:

Variable	Error
Parallel absorption, A_P	0.5 mm
Transverse Absorption, A_T	0.5 mm

Dichroic ratio, $D = \frac{A_P}{A_T}$

$$\varepsilon_D = \left[\left(\frac{1}{A_T} \cdot \varepsilon_P \right)^2 + \left(- \frac{A_P}{A_T^2} \cdot \varepsilon_T \right)^2 \right]^{1/2}$$

$$\varepsilon_D = \left[\left(\frac{1}{57.2} \cdot (0.5) \right)^2 + \left(- \frac{(78.2)}{(57.2)^2} \cdot (0.5) \right)^2 \right]^{1/2}$$

$$\varepsilon_D = 0.015$$

Percent error = 1.1%

Similarly, the error associated with the determination of the degree of a-axis orientation (f_a) from the dichroic ratio measurement is estimated to be:

Variable	Error
Dichroic ratio, (D)	0.015

Orientation function, $f_a = \frac{D - 1}{D + 2}$

or $f_a = \frac{u}{v}$

$$\varepsilon_f = \left[\left(\frac{1}{v} \cdot \varepsilon_u \right)^2 + \left(- \frac{u}{v^2} \cdot \varepsilon_v \right)^2 \right]^{1/2}$$

$$\varepsilon_f = \left[\left(\frac{0.015}{3.367} \right)^2 + \left(- \frac{(0.367)}{(3.367)^2} \cdot (0.015) \right)^2 \right]^{1/2}$$

$$\varepsilon_f = 0.0045$$

$$\text{Percent error} = \frac{0.0045}{0.1090} \times 100 = 4.1\%$$

A.15.3.6 Tensile Young's Modulus

The experimental errors in the various measured quantities were estimated to be:

Variable	Error
Initial slope (s)	0.03%
Initial length (l_o)	0.1 mm
Width (w)	0.0025 mm
Thickness (t)	0.0025 mm

$$\text{Tensile Young's modulus, } Y = \left[\frac{s \times l_o}{w \times t} \right] (9.80 \times 10^6) \text{ N/m}^2$$

$$\varepsilon_Y = \left[\left(\frac{s}{w\,t} \cdot \varepsilon_{l_o} \right)^2 + \left(\frac{l_o}{w\,t} \cdot \varepsilon_s \right)^2 + \left(- \frac{s\,l_o}{w^2\,t} \cdot \varepsilon_w \right)^2 + \left(- \frac{s\,l_o}{w\,t^2} \cdot \varepsilon_t \right)^2 \right]^{1/2}$$

$$\varepsilon_Y = \left[\left(\frac{0.350}{(3.5509)(0.0508)}\cdot(0.1)\right)^2 + \left(\frac{20}{(3.5509)(0.0508)}\cdot(0.01)\right)^2 + \left(-\frac{(0.350)(20)}{(3.5509)^2(0.0508)}\cdot(0.0025)\right)^2 + \left(-\frac{(0.350)(20)}{(3.5509)(0.0508)^2}\cdot(0.0025)\right)^2\right]^{1/2}$$

$$\varepsilon_Y = 2.22 \times 9.80 \times 10^6 \text{ N/m}^2$$

$$\varepsilon_Y = 2.18 \times 10^7 \text{ N/m}^2 \text{ or Pa}$$

Percent error = 5.7%

A.15.3.7 Tensile Strength

The experimental errors in the various measured quantities were estimated to be:

Variable	Error
Force (F)	0.049 Newtons
Width (w)	0.0025 mm
Thickness (t)	0.0025 mm

Tensile strength, $\sigma = \frac{F}{w\,t} \times 10^6$

$$\varepsilon_\sigma = \left[\left(\frac{1}{w\,t}\,\varepsilon_F\right)^2 + \left(-\frac{F}{w\,t^2}\,\varepsilon_t\right)^2 + \left(-\frac{F}{w^2\,t}\,\varepsilon_w\right)^2\right]^{1/2}$$

$$\varepsilon_\sigma = \left[\left(\frac{1}{(3.5509)(0.0508)}\cdot(0.049)\right)^2 + \left(-\frac{4.096}{(3.5509)(0.0508)^2}\cdot(0.0025)\right)^2 + \left(-\frac{4.096}{(3.5509)^2(0.0508)}\cdot(0.0025)\right)^2\right]^{1/2}$$

$$\varepsilon_\sigma = 1.15\times10^6 \text{ N/m}^2$$

Percent error = 5.1%

A.15.3.8 Strain

The experimental errors in the various measured quantities were estimated to be:

Variable	Error
Length (initial), l_o	0.1 mm
Length (final), l	0.5 mm

Elongation at yield, $\varepsilon_y = \frac{l}{l_o}$

$$\varepsilon_{\varepsilon_y} = \left[\left(\frac{1}{l_o}\cdot\varepsilon_l\right)^2 + \left(-\frac{1}{l_o^2}\cdot\varepsilon_{l_o}\right)^2\right]^{1/2}$$

$$\varepsilon_{\varepsilon_y} = \left[\left(\frac{1}{20}\cdot(0.5)\right)^2 + \left(-\frac{5.5}{(20)^2}\cdot(0.1)\right)^2\right]^{1/2}$$

$$\varepsilon_{\varepsilon_y} = 0.025$$

Percent error = 9.1%

Similarly, the error associated with the measurement of the percent elongation at break (ε_b) is estimated to be:

$$\varepsilon_{\varepsilon_b} = \left[\left(\frac{1}{20} \cdot (0.5)\right)^2 + \left(-\frac{13}{(20)^2} \cdot (0.1)\right)^2\right]^{1/2}$$

$$\varepsilon_{\varepsilon_b} = 0.025$$

Percent error = 3.9%

A.15.3.9 Amorphous Orientation Function

From Chapter 4, Equation (4-9) gives

$$\frac{3}{2}(\Delta E)^{-1} = \frac{X_c f_{cr}}{E^o_{t,c}} + \frac{(1 - X_c) f_{am}}{E^o_{t,am}}$$

rearranging and simplifying, gives for f_{am},

$$f_{am} = \frac{\left(\frac{3}{2}(\Delta E)^{-1} E^o_{t,am}\right)}{(1 - X_c)} - \frac{X_c f_{cr} E^o_{t,am}}{(1 - X_c) E^o_{t,c}}$$

substituting the estimated values for $E^o_{t,c}$ and $E^o_{t,am}$ gives,

$$f_{am} = \frac{\frac{3}{2}(\Delta E)^{-1}(0.043 \times 10^{10})}{(1 - X_c)} - \frac{X_c f_{cr}(0.043 \times 10^{10})}{(1 - X_c)(0.570 \times 10^{10})}$$

$$f_{am} = \frac{(0.0645 \times 10^{10})(\Delta E)^{-1}}{(1 - X_c)} - \frac{(0.0754) X_c f_{cr}}{(1 - X_c)}$$

or

$$f_{am} = (0.0645 \times 10^{10})A - 0.0754\ B$$

where

$$A = \frac{(\Delta E)^{-1}}{(1 - X_c)} \quad \text{and} \quad B = \frac{X_c\ f_{cr}}{(1 - X_c)}$$

that is, the error in estimating f_{am} is given as,

$$\varepsilon_{f_{am}} = (0.0645 \times 10^{10})\varepsilon_A - 0.0754\ \varepsilon_B$$

however,

$$(\Delta E)^{-1} = \frac{1}{E_u} - \frac{1}{E_{or}}$$

Since the error in sonic modulus = 1.38%, then

$$\varepsilon_{\Delta E} = \left[\left(-\frac{1}{E_u^2} \cdot \varepsilon_{E_u}\right)^2 + \left(-\frac{1}{E_{or}^2} \cdot \varepsilon_{E_{or}}\right)^2\right]^{1/2}$$

$$\varepsilon_{\Delta E} = \left[\left(-\frac{1}{(0.1525)^2}(0.002)\right)^2 + \left(-\frac{1}{(0.24)^2}(0.003)\right)^2\right]^{1/2}$$

$$\varepsilon_{\Delta E} = 0.101 \times 10^{-10}\ Pa^{-1}$$

$$\text{Percent error} = \frac{(0.101 \times 10^{-10})}{(2.391 \times 10^{-10})} \times 100 = 4.2\%$$

Now, the error in A is estimated as,

$$\varepsilon_A = \left[\left(\frac{1}{(1 - X_c)} \cdot \varepsilon_{\Delta E} \right)^2 + \left(- \frac{(\Delta E)^{-1}}{(1 - X_c)^2} \cdot \varepsilon_{(1-X_c)} \right)^2 \right]^{1/2}$$

$$= \left[\left(\frac{(0.101 \times 10^{-10})}{(1 - 0.6195)} \right)^2 + \left(- \frac{2.391 \times 10^{-10}}{(1 - 0.6195)^2} (0.00019) \right)^2 \right]^{1/2}$$

$$\varepsilon_A = (0.2655 \times 10^{-10}) \text{ Pa}^{-1}$$

$$\text{Percent error in A} = \frac{(0.2655 \times 10^{-10})}{(6.2831 \times 10^{-10})} \times 100 = 4.23\%$$

Similarly, the error in B is estimated as,

$$\varepsilon_B = \left[\left(\frac{f_{cr}}{(1 - X_c)} \cdot \varepsilon_{X_c} \right)^2 + \left(\frac{X_c}{(1 - X_c)} \cdot \varepsilon_{f_{cr}} \right)^2 + \left(- \frac{X_c \, f_{cr}}{(1 - X_c)^2} \cdot \varepsilon_{(1-X_c)} \right)^2 \right]^{1/2}$$

$$\varepsilon_B = \left[\left(\frac{0.0475}{(1 - 0.6195)} \cdot (0.0003) \right)^2 + \left(\frac{0.6195}{(1 - 0.6195)} \cdot (0.00095) \right)^2 + \left(- \frac{0.6195(0.0475)}{(1 - 0.6195)^2} \cdot (0.00019) \right)^2 \right]^{1/2}$$

$$\varepsilon_B = \left[(1.4 \times 10^{-9}) + (2.392 \times 10^{-9}) + (1.4 \times 10^{-9}) \right]^{1/2}$$

$\varepsilon_B = 15.475 \times 10^{-4}$

Percent error in B $= \frac{0.00155}{0.07734} \times 100 = 2.0\%$

That is,

$\varepsilon_{f_{am}} = (0.0645 \times 10^{10})(0.2655 \times 10^{-10}) - (0.0754)(0.00155)$

$\varepsilon_{f_{am}} = 0.0170$

Percent error $= \frac{0.0170}{0.3990} \times 100 = 4.3\%$

A.15.3.10 Prediction of Sonic Modulus

The experimental errors in the various measured quantities were estimated to be:

Variable	Error
X_c	0.05%
$(1 - X_c)$	0.05%
f_{cr}	2%
f_{am}	4.3%

$$\frac{1}{E_{or}} = X_c(1 - f_{cr})A_c + (1 - X_c)A_{am}(1 - f_{am})$$

where $A_c = \frac{10}{15}\left(\frac{1}{E^o_{t,c}}\right)$

and $A_{am} = \frac{10}{15}\left(\frac{1'}{E^o_{t,am}}\right)$

substituting for $E^{o}_{t,c} = 0.350 \times 10^{10}$ Pa

and $E^{o}_{t,am} = 0.05 \times 10^{10}$ Pa

then,

$$A_c = \frac{10}{15}\left(\frac{1}{0.350 \times 10^{10}}\right) = 1.9048 \times 10^{-10}\ \text{Pa}^{-1}$$

and

$$A_{am} = \frac{10}{15}\left(\frac{1}{0.05 \times 10^{10}}\right) = 13.333 \times 10^{-10}\ \text{Pa}^{-1}$$

substituting for A_c and A_{am}, gives

$$\left(\frac{1}{E_{or}}\right) = (1.9048 \times 10^{-10}) X_c (1 - f_{cr}) + (13.333 \times 10^{-10})(1 - X_c)(1 - f_{am})$$

Again, let $P = X_c(1 - f_{cr})$

and $Q = (1 - X_c)(1 - f_{am})$

so that the error in $(1/E_{or})$ is,

$$\varepsilon_{(1/E_{or})} = (1.9048 \times 10^{-10})\varepsilon_P + (13.333 \times 10^{-10})\varepsilon_Q$$

Now, error in P is estimated to be:

$$\varepsilon_P = \left[\left((1 - f_{cr}) \varepsilon_{X_c} \right)^2 + \left(- X_c \cdot \varepsilon_{(1-f_{cr})} \right)^2 \right]^{1/2}$$

$$\varepsilon_P = \left[\left((1 - 0.0475) \cdot 0.0003 \right)^2 + \left(- (0.6195) \cdot 0.01905 \right)^2 \right]^{1/2}$$

$$\varepsilon_P = 0.0118$$

Now, error in Q is estimated to be:

$$\varepsilon_Q = \left[\left((1 - f_{am}) (- \varepsilon_{(1-X_c)}) \right)^2 + \left((1 - X_c) (- \varepsilon_{(1-f_{am})}) \right)^2 \right]^{1/2}$$

$$\varepsilon_Q = \left[\left((1 - 0.3990) (- 0.00019) \right)^2 + \left(- (1 - 0.6195) (0.0258) \right)^2 \right]^{1/2}$$

$$\varepsilon_Q = 0.00982$$

Therefore, error in $(1/E_{or})$ is estimated to be:

$$\varepsilon_{(1/E_{or})} = (1.9048 \times 10^{-10}) 0.0118 + (13.333 \times 10^{-10}) (0.00982)$$

$$\varepsilon_{(1/E_{or})} = (0.0225 \times 10^{-10}) + (0.1309 \times 10^{-10})$$

$$\varepsilon_{(1/E_{or})} = 0.1534 \times 10^{-10} \text{ Pa}^{-1}$$

Percent error in prediction of $(1/E_{or})$ is

$$= \frac{0.1534 \times 10^{-10}}{4.1680 \times 10^{-10}} \times 100$$

$$= 3.68\% \simeq 3.7\%$$